



Université
de Toulouse

THÈSE

En vue de l'obtention du

DOCTORAT DE L'UNIVERSITÉ DE TOULOUSE

Délivré par :

Université Toulouse 3 Paul Sabatier (UT3 Paul Sabatier)

Cotutelle internationale avec :

University of Iceland, Islande

Présentée et soutenue par :
Snorri GUDBRANDSSON

Le mercredi 30 octobre 2013

Titre :

Experimental weathering rates of aluminium-silicates
(Vitesses d'altération expérimentales des silicates d'aluminium)

École doctorale et discipline ou spécialité :

ED SDU2E : Sciences de la Terre et des Planètes Solides

Unité de recherche :

Géosciences Environnement Toulouse (GET)

Directeur(s) de Thèse :

OELKERS, Dr. Eric H.

GISLASON, Dr. Sigurdur Reynir

Rapporteurs :

GODARD, Dr. Marguerite

AAGAARD, Prof. Per

Autre(s) membre(s) du jury :

WOLFF-BOENISCH, Dr. Domenik,
BURTON, Prof. Kevin, et ARNÓRSSON, Prof. Stefán

Résumé

L'altération chimique des roches primaires et des minéraux dans les systèmes naturels a un impact majeur sur la formation des sols et leur composition. L'altération chimique est largement pilotée par la dissolution des minéraux. Les éléments chimiques libérés dans les eaux souterraines par la dissolution des minéraux réagissent facilement pour former des minéraux secondaires comme les argiles, zéolites et carbonates. Les carbonates se forment par réaction des cations divalents (Ca, Fe et Mg) avec CO₂ dissous tandis que la formation des kaolins et de la gibbsite est attribuée à l'altération des minéraux riches en aluminium, le plus souvent les feldspaths.

Le projet Carbfix à Hellisheiði (sud-ouest de l'Islande) a pour but d'utiliser les processus d'altération naturelle pour former des minéraux carbonatés par réinjection dans les roches basaltiques environnantes de CO₂ provenant d'une centrale géothermique. Ce processus trouve son origine dans la dissolution des roches basaltiques riches en cations divalents (Ca, Fe et Mg) qui se combinent au CO₂ injecté pour former des minéraux carbonatés.

Cette thèse est centrée sur la dissolution du basalte cristallin de Stapafell qui est composé essentiellement de trois phases minérales (plagioclase, pyroxène et olivine) et qui est riche en cations divalents. La vitesse de libération des éléments du basalte à l'état stationnaire et loin de l'équilibre a été mesurée dans des réacteurs à circulation à des pH de 2 à 12 et des températures de 5 à 75°C. Les vitesses de libération de Si et Ca à l'état stationnaire présentent une variation en fonction du pH en forme de U avec une diminution des vitesses lorsque le pH augmente en conditions acides et une augmentation avec le pH en conditions alcalines. Les vitesses de libération du silicium par le basalte cristallin sont comparables à celles par le verre basaltique de même composition chimique aux faibles pH et aux températures ≥ 25°C mais elles sont plus lentes aux pH alcalins et aux températures ≥ 50°C. Par contre, les vitesses de libération de Mg et Fe diminuent de manière monotone avec l'accroissement du pH à toutes les températures. Ce comportement a pour cause les variations contrastées, en fonction du pH, des vitesses de dissolution des trois minéraux constitutifs du basalte: plagioclase, olivine et pyroxène. Les vitesses de libération des éléments déduites de la somme des vitesses de dissolution du plagioclase, pyroxène et olivine normalisées à la fraction volumique de ces minéraux sont, à un ordre de grandeur près, les mêmes que celles mesurées dans cette étude. En outre, les résultats expérimentaux montrent que, durant l'injection d'eaux chargées en CO₂ de pH proche de 3.6, le basalte cristallin libère préférentiellement Mg et Fe en solution par rapport à Ca. L'injection de fluides acides chargés en CO₂ dans des roches cristallines basaltiques peut donc favoriser la formation de carbonates de Mg et Fe aux dépends de la calcite aux conditions de pH acides à neutres.

Le plagioclase, qui est la phase la plus abondante du basalte, influence fortement la réactivité de ce dernier. La vitesse de dissolution du plagioclase, basée sur la libération de la silice, présente une variation en forme de U en fonction du pH, diminuant lorsque le pH augmente aux conditions acides mais augmentant avec le pH aux conditions alcalines. En accord avec les données de la littérature, la vitesse de dissolution du plagioclase à pH constant, en conditions acides, augmente avec sa teneur en anorthite. L'interprétation et le fit

des données obtenues suggèrent que la vitesse de dissolution du plagioclase est contrôlée par la décomposition d'un complexe activé riche en silice, formé par le départ de Al de la structure du minéral. Le plus remarquable, par comparaison aux hypothèses antérieures, est que la vitesse de dissolution du plagioclase en conditions alcalines est indépendante de sa teneur en anorthite – e.g. les vitesses de dissolution des plagioclases riches en anorthite augmentent avec le pH aux conditions alcalines. A ces conditions, il est probable que la vitesse de dissolution rapide du plagioclase domine, en raison de sa forte teneur en Ca, la libération vers la phase fluide des cations divalents du basalte cristallin.

La gibbsite est généralement le premier minéral qui précipite lors de la dissolution du plagioclase. C'est un hydroxyde d'aluminium que l'on trouve dans divers sols et qui est aussi la phase principale des minéraux de bauxite. Les vitesses de précipitation de la gibbsite ont été mesurées dans des réacteurs fermés, en conditions alcalines à 25 et 80°C, en fonction de l'état de saturation du fluide. Les analyses des solides après réaction ont démontré que la précipitation de gibbsite s'est produite dans toutes les expériences. L'interprétation de l'évolution dans le temps de la chimie du fluide réactif fournit des vitesses de précipitation de la gibbsite qui sont près des vitesses de dissolution du plagioclase. En plus, des vitesses de précipitation de la gibbsite diminuent plus rapidement que des vitesses de dissolution du plagioclase quand le pH descend. Ceci suggère que l'étape limitant de l'altération du plagioclase sur la surface de la Terre est plutôt la consommation d'Al par formation de la gibbsite que la dissolution même du plagioclase.

La kaolinite est en général le second minéral formé après la gibbsite lors de la dissolution du plagioclase à basse température. Les vitesses de précipitation de la kaolinite ont été mesurées dans des réacteurs à circulation à pH = 4 et t = 25°C, en fonction de l'état de saturation du fluide. Au total, 8 expériences de précipitation de longues durées ont été réalisées dans des fluides légèrement supersaturés par rapport à la kaolinite, en utilisant comme germes pour la précipitation une quantité connue de kaolinite de Géorgie (KGa-1b) contenant peu de défauts et préalablement nettoyée. Les vitesses de précipitation de kaolinite mesurées sont relativement lentes comparées aux vitesses de dissolution du plagioclase. Cette observation suggère que la formation de kaolinite lors de l'altération est limitée par sa vitesse de précipitation plutôt que par la disponibilité en Al et Si issus de la dissolution du plagioclase.

L'ensemble des résultats de cette étude fournit un certain nombre de principes scientifiques de base nécessaires à la prédiction des vitesses et des conséquences de la dissolution du basalte cristallin et du plagioclase à la surface de la Terre et lors de l'injection du CO₂ à proximité de la surface dans le cadre des efforts de stockage du carbone. Les résultats obtenus indiquent, bien que les vitesses de précipitation de la gibbsite soient relativement rapides, que la vitesse de précipitation relativement lente de la kaolinite peut être le processus contrôlant la formation de ce minéral à la surface de la Terre. Cette observation souligne la nécessité de poursuivre la quantification de la précipitation de ce minéral secondaire aux conditions typiques de la surface de la Terre. En outre, comme les proportions des différents métaux divalents libérés par les basaltes cristallins varient sensiblement avec le pH, la carbonatation des basaltes doit produire un changement systématique de l'identité des minéraux carbonatés et des zéolites précipités en fonction de la distance au puits d'injection. Cette dernière conclusion pourra être directement testée dans le cadre du projet CarbFix actuellement conduit à Hellisheiði en Islande.

Abstract

The chemical weathering of primary rocks and minerals in natural systems has a major impact on soil development and its composition. Chemical weathering is driven to a large extent by mineral dissolution. Through mineral dissolution, elements are released into groundwater and can readily react to precipitate secondary minerals such as clays, zeolites, and carbonates. Carbonates form from divalent cations (e.g. Ca, Fe and Mg) and CO₂, and kaolin clay and gibbsite formation is attributed to the weathering of aluminium-rich minerals, most notably the feldspars.

The CarbFix Project in Hellisheiði SW-Iceland aims to use natural weathering processes to form carbonate minerals by the re-injection of CO₂ from a geothermal power plant back into surrounding basaltic rocks. This process is driven by the dissolution of basaltic rocks, rich in divalent cations, which can combine with injected CO₂ to form and precipitate carbonates.

This thesis focuses on the dissolution behaviour of Stapafell crystalline basalt, which consists of three major phases (plagioclase, pyroxene, and olivine) and is rich in divalent cations. Steady-state element release rates from crystalline basalt at far-from-equilibrium conditions were measured at pH from 2 to 11 and temperatures from 5° to 75° C in mixed-flow reactors. Steady-state Si and Ca release rates exhibit a U-shaped variation with pH, where rates decrease with increasing pH at acid condition but increase with increasing pH at alkaline conditions. Silicon release rates from crystalline basalt are comparable to Si release rates from basaltic glass of the same chemical composition at low pH and temperatures $\geq 25^{\circ}\text{C}$ but slower at alkaline pH and temperatures $\geq 50^{\circ}\text{C}$. In contrast, Mg and Fe release rates decrease continuously with increasing pH at all temperatures. This behaviour is interpreted to stem from the contrasting dissolution behaviours of the three major minerals comprising the basalt: plagioclase, pyroxene, and olivine. Element release rates estimated from the sum of the volume fraction normalized dissolution rates of plagioclase, pyroxene, and olivine are within one order of magnitude of those measured in this study. In addition, these experimental results show that during injection of CO₂-charged waters with pH close to 3.6, crystalline basalt preferentially releases Mg and Fe relative to Ca to the fluid phase. The injection of acidic CO₂-charged fluids into crystalline basaltic rocks may therefore favour the formation of Mg and Fe carbonates rather than calcite at acidic to neutral conditions.

Plagioclase is the most abundant phase in crystalline basalts and thus influences strongly its reactivity. Plagioclase dissolution rates based on Si release show a common U-shaped behaviour as a function of pH where rates decrease with increasing pH at acid condition but increase with increasing pH at alkaline conditions. Constant pH plagioclase dissolution rates increase with increasing anorthite content at acid conditions, in agreement with literature findings. Interpretation and data fitting suggests that plagioclase dissolution rates are consistent with their control by the detachment of Si-rich activated complexes formed by the removal of Al from the mineral framework. Most notably, compared with previous assumptions, plagioclase dissolution rates are independent of plagioclase composition at alkaline conditions, e.g. anorthite-rich plagioclase dissolution rates increase with increasing pH at alkaline conditions. At such conditions rapid plagioclase dissolution rates likely

Abstract

dominate divalent metal release from crystalline basalts to the fluids phase due to its high Ca content.

Gibbsite is commonly the first mineral formed during low temperature dissolution of plagioclase. Gibbsite is an aluminium-hydroxide that is found in various soils as well as the dominant phase in many bauxite ores. Gibbsite precipitation rates were measured in closed system reactors at alkaline condition, both at 25 °C and 80 °C as a function of fluid saturation state. Analyses of the solids demonstrate that gibbsite precipitation occurred in all experiments. The comparison of gibbsite precipitation to the dissolution rates of plagioclase at pH 11 shows that the rates are close to equal. The precipitation rates of gibbsite, however, decrease faster with decreasing pH than plagioclase dissolution rates. As such it seem likely that plagioclase dissolution is faster than gibbsite precipitation at near to neutral pH, and the relatively slow rate of gibbsite precipitation influences plagioclase weathering in many Earth surface systems.

Kaolinite is commonly the second secondary mineral formed during low temperature dissolution of plagioclase. Kaolinite precipitation rates were measured in mixed flow reactors as a function of fluid saturation state at pH=4 and 25 °C. In total eight long-term precipitation experiments were performed in fluids mildly supersaturated with respect to kaolinite, together with a known quantity of cleaned low defect Georgia Kaolinite as seeds. Measured kaolinite precipitation rates are relatively slow compared with plagioclase dissolution rates. This observation suggests that kaolinite formation during weathering is limited by its precipitation rates rather than by the availability of aqueous species sourced from plagioclase dissolution.

Taken together the results of this study provide some of the fundamental scientific basic for predicting the rates and consequences of crystalline basalt and plagioclase dissolution at both the Earth's surface and during the near surface injection of CO₂ as part of carbon storage efforts. Results indicate that although gibbsite precipitation rates are relatively rapid, the relatively slow precipitation rates of kaolinite may be the process controlling the formation of this mineral at the Earth's surface. This observation highlights the need to further quantify this secondary mineral precipitation rates at conditions typical at the Earth's surface. Moreover, as the composition of divalent metals released from crystalline basalts varies significantly with pH, CO₂ carbonation in basalt should yield a systematic variation in the identity of carbonate and zeolite minerals precipitated with distance from the injection site. This latter conclusion can be tested directly as part of the currently on-going CarbFix project in Hellisheiði, Iceland.

Útdráttur

Leysing frumsteinda er einn meginþáttur efnaveðrunar bergs. Við leysingu berast ýmis efni úr bergeninu í grunnvatn og yfirborðsvatn. Þessi uppleystu efni hafa áhrif á steindasamsetningu ummyndaðs bergs og jarðvegs, því þau mynda síðsteindir í bergrunninum, svo sem geislasteina, leirsteindir og karbónöt. Karbónöt myndast oftast úr tvígildum katjónum, einkum kalsíum (Ca), járni (Fe) og magnesíum (Mg), sem bindast koltvíoxíði (CO_2) úr lausn. Álsteindirnar kaólínít og gibbsít myndast við veðrun álrikra frumsteinda, einkum plagióklasa.

Losun koltvíoxíðs til andrúmslofts er eitt alvarlegasta umhverfismál samtímans. Miklu skiptir, að unnt verði að þróa aðferðir til að binda það varanlega í jörðu, þannig að hverfandi hætta sé á að það sleppi aftur til yfirborðs. Markmið CarbFix verkefnisins, samstarfsverkefnis Háskóla Íslands, Orkuveitu Reykjavíkur, CNRS í Toulouse í Frakklandi og Columbia háskólans í New York í Bandaríkjunum, er einmitt að dæla CO_2 úr Hellisheiðarvirkjun niður í basaltlög í nágrenni virkjunarinnar. Þar er þess vænst, að Fe, Mg og Ca leysist úr basaltinu og felli karbónöt úr vökvánnum, og bindi þannig koltvíoxíðið til frambúðar. Aðferðin þykir vænleg vegna þess að basalt leysist miklu hraðar en kísilríkara berg, vegna þess hversu auðugt basalt er af tvígildum katjónum, og vegna þess hve holrými er mikið í basalti.

Í þessari ritgerð er fjallað um leysnihraða kristallaðs basalts. Kristallað basalt er ríkt af tvígildum katjónum og samanstendur aðallega af þremur steindum, ólivíni (Mg, Fe), plagióklasi (Ca) og pýroxeni (Ca, Mg, Fe). Leysnihraði var ákvarðaður í hvarfakúti úr títanmálmi við pH-gildi frá 2 til 11 og hita frá 5° til 75°C. Leysniferill kísils (Si) og kalsíums sem fall af pH-gildi í kristölluðu basalti er U-laga, líkt og leysniferlar basaltglers og albítríks plagióklass. Leysnihraði minnkar með hækandi pH-gildi í súrri lausn ($\text{pH} < 7$), en eykst með hækandi pH-gildi í basískri. Þessi hegðun sýnir, að ólivín og pýroxen leysast mun hraðar en plagióklas ef vökvinn er súr. Í basískum vökva er þessu öfugt farið, og þá verður leysing plagióklas ríkjandi, leysnihraði Ca og Al meiri, og því verður hlutfallslegur styrkur Ca og Al í lausn einnig meiri.

Niðurstöður rannsóknanna sýna, að í kolsýrðu vatni við pH 3,6 er hlutfall leysni Fe og Mg við leysni Ca mun hærra en sem nemur hlutfalli þessara málma í basalti. Af þeim sökum má leiða að því líkur, að styrkur Mg og Fe verði mikill í vökva með þessu pH-gildi, sem dælt yrði niður í kristallað basalt. Þessi efni gætu því fallið út sem karbónöt. Þessi rannsókn sýnir einnig að plagióklas, sem er ríkjandi frumsteind (um 50%) í kristölluðu basalti, leggur til megnið af áli og alkalí- og jarðalkalímálum við myndun síðsteinda þegar basalt veðrast og ummyndast við hátt pH-gildi í grunnvatni og jarðhitakerfum.

Í ritgerðinni eru birtar niðurstöður mælinga á leysnihraða plagióklasa með efnasamsetningu sem spannar röðina frá albíti að anortíti. Tilraunirnar voru gerðar í hvarfakútum við stofuhita (22°C) og pH-gildi frá 2 til 11. Niðurstöðurnar sýna að plagióklas leysist því hraðar sem meira kalsíum er í steindinni ef vökvinn er súr. Í basískri lausn leysast hins vegar öll plagióklös jafnhrott upp, óháð efnasamsetningu. Þessi niðurstaða kann að virðast óvænt, að Na:Ca hlutfall plagióklasa hafi engin áhrif á leysnihraða þeirra í basískri lausn. Öll plagióklösin sýna sömu hegðun og albít, en leysniferill allra er U-laga. Þetta er í

samræmi við áður birt gögn um Na-rík plagióklös og skýrist af því að Si-jón losnar úr grind steindarinnar eftir að Al-jónin hefur losnað úr grindinni.

Gibbsít, sem er algeng álsteind í jarðvegi, er talið myndast við efnaveðrun plagióklass við lágan hita og nægan raka. Gibbsít er ein álsteindanna í báxíti, sem er helsta hráefni í álframleiðslu. Tilraunir voru gerðar með útfellingu gibbsíts í lokuðum hvarfakútum með "kími" gibbsítkristalla til að hvetja útfellingu. Þessar tilraunir voru gerðar sem fall af mettunarstigi við 22°C og pH=11 annars vegar og við 80°C og pH=9 hins vegar. Könnun á kristalkíminu með rafeindasmásjá leiddi í ljós útfellingar í öllum tilraununum. Hraði útfellingar gibbsíts sem fall af mettun var ákvarðaður, og reyndist hann vera álika mikill og leysnihraði plagióklas við sama pH. Á hinn bóginn minnkar útfellingahraði gibbsíts meira með lækkandi pH-gildi en leysnihraði plagióklass. Þetta bendir til þess, að myndun gibbsíts í náttúrunni við hlutlaust pH stjórnist fremur af litlum útfellingahraða gibbsíts en af leysnihraða plagióklasanna.

Kaólínít er algeng Al-síðsteind sem myndast úr plagióklasi við lághitaveðrun, líkt og gibbsít. Hlutfall Al við Si er jafnt í kaólíníti (2:2), en það er talið myndast á síðari stigum plagióklasveðrunar þegar kísillinn stendur enn eftir. Gerðar voru tilraunir með útfellingu kaólíníts í hvarfakút við 25°C og pH=4 með kristalkími sem hvata, og var hraði mældur sem fall af mettunarstigi. Alls voru gerðar átta tilraunir, en ekki reyndist unnt að greina breytingar á kíminu. Vatnslausninar gefa hins vegar til kynna, að mjög hægar útfellingar eigi sér stað. Þetta bendir til þess að við lágan hita sé það í reynd útfellingahraði kaólíníts sem stjórni vexti þess fremur en leysnihraði plagióklasa.

Niðurstöður þeirra rannsókna, sem hér eru kynntar, gefa ýmsar vísbendingar um leysingu kristallaðs basalts og plagióklass, bæði við náttúrulegar aðstæður og þegar koltvioxíði er dælt í basalt, eins og í CarbFix verkefninu á Hellisheiði. Þó að plagióklös leysist hægt upp við hlutlaust pH, fellur gibbsít þó líklega hægar út, og hið sama á við um kaólínít við pH=4. Pannig er útfellingahraði álríkra síðsteinda gildur þáttur í þróun jarðvegs. Þessar niðurstöður gefa til kynna, að frekari rannsókna á útfellingahraða álríkra síðsteinda sé þörf til þess að öðlast dýpri skilning á veðrun á yfirborði jarðar. Niðurstöðurnar sýna einnig, að líklega muni karbónöt, sem falla út við dælingu á kolsýrðu vatni með lágt pH-gildi niður í basaltlög, verða sundurleitari en þau sem finnast í náttúrunni vegna þess hve leysing kristallaðs bergs er háð pH-gildi. Þessi sundurleitni mun líklega koma fram í CarbFix verkefninu á Hellisheiði.

Acknowledgements

There are many people who have helped me along the way during my PhD. First of all I would like to thank my family, my girlfriend Sólveig Lilja Snæbjörnsdóttir and my son Snæbjörn Flóki for their support and their patience during the time of the project and the time I have spent away from them during my work in France.

I started the PhD-project as a part of the CarbFix project, where the aim is to store CO₂ in basaltic formations in Hellisheiði area in SW-Iceland. But after the collapse of the Icelandic economy the funding of my project became difficult, I was fortunate enough to be offered a Marie-Curie early training grant with the Delta-Min initial Training Network of the EU seventh framework. This grant meant that I was able to go to Toulouse and work at the GET/CNRS lab where I enjoyed myself, apart from being away from my family.

I have had a good relationship with my supervisors Eric Hermann Oelkers at the GET/CNRS in Toulouse and Sigurður Reynir Gislason at the University of Iceland, during my project. They are not only good scientists but more importantly they are also good persons who have helped me a lot during my time. Also on my team are Domenik Wolff-Boenisch and Vasileios Mavromatis. Both of them have been a great help and I have learned a lot from them in the laboratory and they have also helped me improve my writing skills. In Toulouse I had the privilege to work with Jacques Schott and for me that has been a steep learning curve but also really nice experience. I would also like to thank him for telling me about rugby and the beans to make cassoulet. Clare Desplats has been a tremendous help with all practical things in France. Without her I guess I would not have managed in France.

As I have mentioned I have worked in two places during this project so there are many people to thank. In Iceland I have worked with the geochemistry group at the university of Iceland and I would like to thank all of them for their time and help: Eydis S. Eiríksdóttir, Helgi Arnar Alfreðsson, Gabrielle Jarvik Stockmann, Iwona Monica Galeczka, Mahnaz Rezvani Khalilabad, Alexander Gysi, Morgan Jones, Sandra Ósk Snæbjörnsdóttir, Kiflom G. Mesfin, Júlia Katrín Björke, Sigurður Hafsteinn Markússon, Nicole Keller, Hanna Kaasalinen, Stefán Arnórsson, Jón Örn Bjarnason and Þorsteinn Jónsson. It is also worth mentioning special thanks to several people at the University of Iceland for their extraordinary help they have given me and the time they have spent on me because of their kindness, Níels Óskarsson and Ingvi Gunnarsson. Ásgeir Einarsson, Sigurjón B. Þórarinsson, Esther Ruth Guðmundsdóttir, Þorbjörg Ágústsdóttir, Hreggviður Norðahl, Ólafur Ingólfsson and probably some other people have helped me pick my pace up during a known situation called writers block (Upper, 1974).

All the time I stayed in France I was without my family there, so first of all I would like to thank Andri Stefánsson and his family for helping me in various ways and by taking me into their home when I first arrived in Toulouse and the apartment, I thought I had rented, had been rented to someone else. For this I am extremely grateful and also for all the times they invited me to dinner to their apartment in Saouzelong. Also in Toulouse where Quentin Gautier and his girlfriend Olga, Julien Declercq, Oliver Bosc, Tamara Dietrich, Sophie Demouy and Vasileios Mavromatis who all helped me during my stay as well as Melanie

Acknowledgements

Louterbach who was kind enough to lend me her flat at Place du Capitol, dead centre in Toulouse. The staff at GET/CNRS has been really helpful and patient to me (as has everybody in Toulouse) and special thanks have to go to Carole Causserand, Stephanie Mounic, Alain Castillo, Pascale Gisquet, Philippe de Parseval, Thierry Aigouy and Sophy Gouy.

In the year 2009 I had the opportunity to spend few months at the NanoGeoScience laboratory in Copenhagen. This was made financially possible for me by Susan Stipp and the NanoGeoScience lab and Erasmus exchange program. In Copenhagen I met a brilliant group of people and really enjoyed my time there. From there I would like to mention specially Susan Stipp, Kjeld West, Nicolas Bovet, Sorin Nedel, Tue Hassenkam, Bo Christiansen, Caroline Hem, Iván S. Pasarin, Lone Skovbjerg and Karina Sand.

The work I have done has been financed by several grants over the time. The Environmental Fund of Reykjavík Energy through the CarbFix Project, Delta-Min (Mechanism of Mineral Replacement Reactions: Grant PITN-GA-2008-215360) and the CarbFix (Collaborative Project-FP7-469 ENERGY-2011-1-283148) and for these grants I am grateful and know that without them this would not have been possible. I have also to thank the late Nordisk Mineralogical Network who I have received several small grants from, for a short course in Gothenburg, Sweden, and visits to Copenhagen and Helsinki. From them I would like to mention the head of the Network Tonci Balic Zunic at the University of Copenhagen, Denmark, and David Cornell at the University of Gothenburg, Sweden. I have received several in-house travel grants from the Earth Science institute. These grants have helped me to introduce my work at international conferences and I am grateful for that.

And my friends who I have hardly met since 2009.

Preface

This PhD study has been carried out at the Faculty of Earth Sciences, University of Iceland and the Geosciences Environnement Toulouse/Centre National de la Recherche Scientifique (GET/CNRS), Midi-Pyrénées Laboratory in Toulouse, France and is presented for a joint degree in geology between the University of Iceland and Paul Sabatier Université Toulouse. This project aims to quantify the dissolution rate of crystalline basalt and plagioclase and the precipitation rates of aluminium secondary phases. The work and main results are presented here in the form of four articles, I-IV. The papers are at different stages, paper I is published, paper II has been submitted to *Geochimica et Cosmochimica Acta*, III is to be submitted to a peer-reviewed (*Chemical Geology*) upon completion of work and paper IV will be submitted to a peer-reviewed international journal late 2013.

Paper I

Gudbrandsson, S., Wolff-Boenisch, D., Gislason, S.R. and Oelkers, E.H., (2011) *An experimental study of crystalline basalt dissolution from $2 \leq pH \leq 11$ and temperature from 5 to 75 degrees C*, **Geochimica et Cosmochimica Acta** Vol 75, pp. 5469-5509.

Paper II

Gudbrandsson, S., Wolff-Boenisch, D., Gislason, S.R. and Oelkers, E.H., *Experimental characterisation of plagioclase dissolution rates as a function of their composition and pH at 22° C*, Submitted to **Geochimica et Cosmochimica Acta**.

Paper III

Gudbrandsson, S., Mavromatis, V. and Oelkers, E.H. *Gibbsite precipitation at pH 11 at 25 °C and pH 9 at 80 °C*. To be submitted to **Chemical Geology**.

Paper IV

Gudbrandsson, S., Mavromatis, V., Gautier, Q., Bovet, N., Schott, J., and Oelkers, E.H. *Kaolinite precipitation rates at pH 4 and 25 °C*. To be submitted to **Chemical Geology**.

Table of Contents

Résumé	i
Abstract	iii
Útdráttur	v
Acknowledgements	vii
Preface	ix
1 Introduction	1
<i>1.1 Research project</i>	2
<i>1.2 Chemical Weathering rates</i>	3
<i>1.3 Primary rocks and minerals</i>	8
<i>1.4 Methods</i>	14
<i>1.5 Thesis outline:</i>	17
2 Chapter An experimental study of crystalline basalt dissolution from $2 \leq \text{pH} \leq 11$ and temperatures from 5 to 75 °C	19
<i>2.1 Introduction</i>	23
<i>2.2 Theoretical background</i>	24
<i>2.3 Material and methods</i>	25
<i>2.4 Results</i>	29
<i>2.5 Discussion</i>	30
<i>2.6 Conclusions</i>	33
3 Chapter Experimental characterization of plagioclase dissolution rates as a function of their composition and pH at 22° C	37
<i>3.1 Introduction</i>	42
<i>3.2 Theoretical background</i>	43
<i>3.3 Sample preparation and experimental methods</i>	47
<i>3.4 Results</i>	50
<i>3.5 Discussion</i>	52
<i>3.6 Conclusions</i>	59
4 Chapter Precipitation of gibbsite at pH 11 at 22°C and pH 9 at 80 °C as a function of saturation degree	83
<i>4.1 Introduction</i>	88
<i>4.2 Theoretical background</i>	90
<i>4.3 Methods and materials</i>	91
<i>4.4 Results</i>	93

Table of Contents

4.5 Discussion	95
4.6 Summary	97
5 Chapter <i>An experimental study of kaolinite precipitation kinetics as a function of fluid saturation state at pH 4 and 25 °C</i>	109
5.1 Introduction	114
5.2 Theoretical background	115
5.3 Materials and Methods	118
5.4 Results	121
5.5 Discussion	123
5.6 Conclusions	127
6 Conclusions and implications	141
6.1 Implications	142
6.2 The future	143
7 References	147
8 Appendices	157
Appendix 1	158
8.1 Appendix 2	163
8.2 Appendix 3	168
8.3 Appendix 4	187
8.4 Appendix 5	198

1 Introduction

Weathering at Earth's surface is largely divided into two mechanisms, depending on the forces that are attributed:

1. Physical weathering, where the Earth's surface is moulded by external factors such as glaciations and bioprocesses that grind and break rocks into smaller pieces without changing the mineral composition or the chemical attributes of the rock.
2. Chemical weathering where a rock or a mineral is chemically altered due to exposure to water, gas, and/or pressure.

Over the past decades major efforts within the geochemistry community have been made to measure the dissolution and precipitation rates of various minerals in the laboratory. This effort has the aim of better understanding Earth's surface chemical weathering processes.

In this dissertation I focus on two steps in the chemical weathering of primary rocks and minerals:

- a) The dissolution rates of multi-mineral rocks and plagioclase feldspars.
- b) The precipitation rates of aluminium-rich secondary minerals.

This study was originally motivated by the lack of knowledge of chemical weathering rates and mechanisms of multi-phase rocks, such as crystalline basalt, as a function of pH and temperature. This information is essential to predict the fate and consequences of the CarbFix carbon-storage project, which aims to inject CO₂ from the Hellisheiði Geothermal Power plant into SW-Iceland basalts. As this thesis evolved, its emphasis evolved into a fundamental experimental study, motivated by the apparent lack in published data on the dissolution behaviour of plagioclases, the most abundant mineral in the Earth's crust (Nesbitt and Young, 1984; Gudbrandsson et al., 2011) as well as a major component in crystalline basalts (Gudbrandsson et al., 2011). These experiments were performed at the Earth Science Institute, University of Iceland.

The second part of this thesis focuses on the experimental characterization of precipitation rates of the aluminium rich secondary minerals: kaolinite and gibbsite. This work was done within DELTA-MIN, a Marie Curie Initial Training Network of the EU Seventh Framework Programme and performed at the GET/CNRS laboratory in Toulouse, France. The overall research aim of DELTA-MIN was to better understand mineral replacement reactions. Formation of both gibbsite and kaolinite is generally attributed to plagioclase weathering and both phases are common on the Earth's surface in soils. Each mineral is also found in large economically important deposits: kaolinite in extensive kaolin clay formations; and gibbsite in bauxite formations. The formation rates of aluminium-rich secondary phases in nature are poorly defined and are still a scientific challenge owing to their slow precipitation rates and limits of experimental/analytical methods.

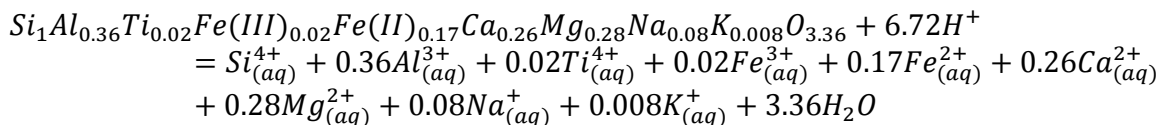
1.1 Research project

The chemical weathering of minerals is an on-going process that affects the daily lives of Earth's habitants and their future. For example, chemical weathering influences climate through the CO₂ content of the atmosphere, the chemical composition of the oceans, ore deposit formation, geothermal energy harvesting and exploration, secondary mineral formation, and bedrock porosity. In recent times contamination from the mining industry and CO₂ emission into atmosphere and its effect on the global climate have been of growing concern to both the scientific community and the general public. Methods to control these processes are being actively researched at present. Much of this effort is aimed at an improved understanding of weathering cycles to provide insight into nature's response to anthropogenically induced hazards.

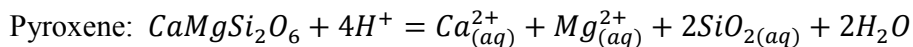
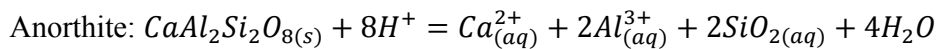
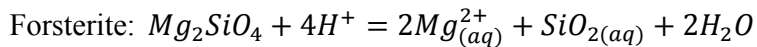
The CarbFix project is collaboration, originally between Reykjavík Energy, University of Iceland, Centre National de la Recherche Scientifique, Paul Sabatier University in Toulouse, France, and the Earth Institute at Columbia University in New York, USA. The project aim is to find a long-term solution to re-inject CO₂ from the Hellisheiði Powerplant and store it as carbonate minerals. Hellisheiði is a basaltic formation in SW-Iceland. The formations found are both basaltic glass, as well as crystalline basalts. The alteration of the bedrock increases with depth (Alfredsson et al., 2013). The area has been extensively researched for geothermal exploration and over 100 boreholes have been drilled in the area, both for geothermal harvesting as well as for re-injection of geothermal waters and cold water.

Annually more than 40,000 tons of CO₂ is released in a gas mixture from the power plant. Other gases in the mixture include H₂S, H₂, Ar, CH₄, and N₂. The aim is to separate the CO₂ from the mixture and re-inject, dissolved in water, into the groundwater aquifers in the area. The CO₂-rich waters will form carbonic acid and have a pH close to 3.6, depending on the partial pressure of CO₂. When injected into the basaltic terrain it will dissolve the basalt, releasing divalent cations into solution making them available for secondary mineral formation. Over time, the injected waters will react with the basalt and mix with present groundwater causing the pH to rise from 3.6 to surrounding pH of close 8 - 10. This will result in the following behaviour of the solution

- 1) Dissolution of basaltic glass:

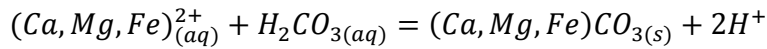


- 2) Dissolution of crystalline basalt:



The divalent cations released during the injection are all potentially available for carbonate precipitation, although one cannot neglect the possibility of other secondary phases, such as clay minerals precipitating.

3) Precipitation of carbonates:



As suggested by Stockmann (2012), the crystal structure of primary minerals is important for calcium carbonate growth. Apart from growing on calcite surface the preferred mineral structure for carbonate growth in basalts, is found to be in the order: orthorhombic > monoclinic > triclinic, suggesting that carbonates are likely to form on minerals in the order olivine > pyroxene > plagioclase. The slowest calcite growth was found to be on basaltic glass, the non-structured phase. This suggests that when injecting into fresh basalts it is more efficient to target a crystalline structure rather than basaltic glass for formation of calcium carbonates, assuming no calcite is present in the basalt. If carbonates are already present, calcite precipitates readily from supersaturated solutions. After injecting the CO₂-charged water into the basaltic formations nature takes control of the process. What minerals form and in which order and quantities is controlled by the abundance of constituent metallic aqueous species in the groundwater after dissolution. Models have shown that possible minerals are kaolinite and gibbsite along with other clay minerals and zeolites (Gysi and Stefánsson, 2012; Alfredsson et al., 2013).

The goal of this thesis is to improve our ability to quantify, in real time, the chemical weathering rates and fluid-rock interactions occurring on and near to the Earth's surface. Towards this goal I have measured the dissolution rates of multi-phase rocks and minerals as a function of fluid composition and the precipitation rates of common aluminium rich secondary phases that are likely to form during weathering of silicate rocks (Helgeson et al., 1984).

The dissolution experiments focused on the reactivity of crystalline basalt and plagioclase feldspars as a function of fluid composition. Additionally, in the crystalline basalt experiments the effects of temperature was assessed while in the plagioclase experiments mineral composition effects were explored. These experiments were carried out within the CarbFix project with the aim of better understanding the release of divalent cations for CO₂ storage into basaltic formations.

The weathering reaction path of plagioclase feldspars to secondary minerals has been suggested to follow the order gibbsite > kaolinite > clays > zeolites (e.g. Bricker and Garrels, 1967; Helgeson et al., 1969; Berner and Berner, 2012). The latter half of this thesis focuses on gibbsite and kaolinite precipitation experiments, with the aim of assessing the influence of precipitation kinetics on the overall rate of natural water-rock processes, which commonly involve a close coupling of dissolution and precipitation reactions. The experiments were compared to albite dissolution rates at equal pH to assess if the rate limiting mechanism in nature is the dissolution of albite or the rates at which secondary minerals precipitate.

1.2 Chemical Weathering rates

Considerable experimental effort has been made to quantify the weathering rates of silicate minerals (Brantley, 2003, and references therein) and glass (e.g. Oelkers and Gislason, 2001;

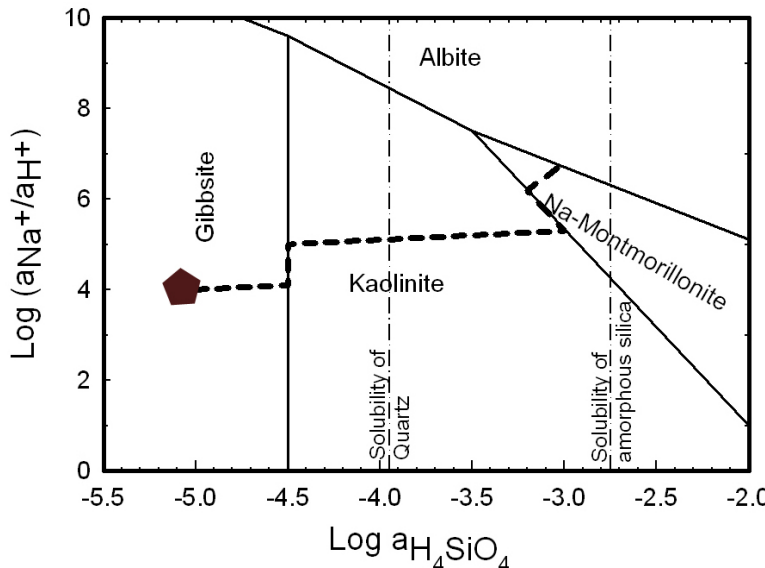
Gislason and Oelkers, 2003; Wolff-Boenisch et al., 2004; Stockmann et al., 2008) over the last few decades. Numerous questions remain on the dissolution behaviour of minerals, especially at alkaline conditions. This may be attributed to the fact that the majority of the fluids on the Earth's continents are somewhat acidic due to CO₂ dissolution and the presence of organic acids. Also alkaline conditions are usually more difficult to control experimentally due to the challenge of avoiding secondary mineral precipitation during experiments.

The plagioclase feldspars have been studied extensively at acid conditions (e.g. Chou and Wollast, 1984; Chou and Wollast, 1985; Blum and Lasaga, 1991; Oxburgh et al., 1994; Blum and Stillings, 1995; Stillings and Brantley, 1995; Brantley and Stillings, 1996; Hamilton et al., 2000; Oelkers, 2001b; Ganor et al., 2005; Hellmann and Tisserand, 2006; Hellmann et al., 2010). Dissolution rates of pyroxene have also been extensively studied in the laboratory (e.g. Schott and Berner, 1985; Gislason and Arnorsson, 1993; Knauss et al., 1993; Brantley and Chen, 1995; Chen and Brantley, 1998; Stockmann et al., 2008; Zakaznova-Herzog et al., 2008) and so have olivines (e.g. Grandstaff, 1977; Wogelius and Walther, 1992; Wasklewicz et al., 1993; Chen and Brantley, 2000; Pokrovsky and Schott, 2000a; Pokrovsky and Schott, 2000b; Rosso and Rimstidt, 2000; Kobayashi et al., 2001; Hanchen et al., 2006; Liu et al., 2006; Stopar et al., 2006; Hanchen et al., 2007; Velbel, 2009; King et al. 2010; Daval et al., 2011). Also available are several studies on basalt weathering (e.g. Eggleton et al., 1987; Gislason and Eugster, 1987a; 1987b; Nesbitt and Wilson, 1992; Gislason et al., 1993; Gislason et al., 1996; Daux et al., 1997; Oelkers and Gislason, 2001; Arnorsson et al., 2002; Gislason and Oelkers, 2003; Eiriksdottir et al., 2008; Flaathen et al., 2008; Schaef and McGrail, 2009).

However, little is known about precipitation rates and mechanisms of secondary aluminium rich phases and experimental studies of the precipitation rates of secondary aluminium rich phases are relatively rare. There are only three main studies on kaolinite precipitation rates at temperatures below 100°C, (Nagy and Lasaga, 1990; Devidal et al., 1997; Yang and Steefel, 2008). This contrasts to the numerous studies of kaolinite dissolution rates (Nagy and Lasaga, 1990; Nagy et al., 1991; Oelkers et al., 1994; Ganor et al., 1995; Maurice et al., 2001; Cama et al., 2002). Likewise, only a few experimental studies have strived to determine gibbsite precipitation rates (e.g. Nagy and Lasaga, 1992; Nagy and Lasaga, 1993; Nagy et al., 1999; Benézeth et al., 2001; Palmer et al., 2001; Bénézeth et al., 2008; Wang et al., 2010).

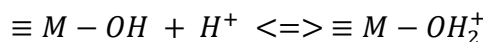
Chemical weathering involves the breakdown of rocks and minerals via chemical reactions driven by rainwater and/or biogenic processes. These processes can be enhanced by the presence of natural or manmade pollutants and chemicals (Berner and Berner, 2012). Chemical weathering of silicates involves mineral dissolution, where the mineral is leached of its elements until the final Si-O bond is broken and the mineral destroyed (Oelkers, 2001b). Mineral dissolution produces dissolved metals which can either form secondary phases or remain dissolved in groundwater, where they can be transported by natural forces far from their origin (Garrels and Mackenzie, 1971). Mineral replacement in situ is also a natural phenomenon, e.g. albitionisation (Putnis, 2009). The weathering reaction path of plagioclase feldspars to secondary minerals has been suggested to follow the order gibbsite > kaolinite > clays > zeolites (e.g. Bricker and Garrels, 1967; Helgeson et al., 1969; Berner and Berner, 2012). Berner and Berner (2012) showed the reaction path of aqueous solution during dissolution of albite feldspar (Fig. 1). The first phase to be supersaturated as albite dissolves and as the concentration of released elements, Na, Al and Si increases is gibbsite. As the fluid

becomes more concentrated other minerals can form. Due to the lack thermodynamic data on zeolites, the clay - zeolites boundary in Fig. 1 is poorly constrained.

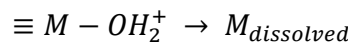


(line from gibbsite to montmorillonite). (Figure remade from Drever 1997).

The rates and mechanism of dissolution and precipitation are commonly described with the aid of Transition State Theory. Although originally Transition State Theory was developed to describe the mixing of gases it has also been used extensively to describe the dissolution of silicate minerals (Aagaard and Helgeson, 1982; Oelkers, 2001b; Schott et al., 2009). When applied to silicate mineral dissolution, the simplest assumption for single oxide minerals that an adsorbed proton on a mineral surface will weaken the adjacent cation-oxygen bonds. As more protons adsorb, the rate at which cations are released into solution will increase. This can be described in two steps, where the first step shows the adsorption of the proton to a metal surface:



where \equiv is the mineral bond and M is a metal. This step is assumed to be fast and reversible and is the first step of the mineral dissolution/precipitation process. The second step is the slow and irreversible detachment of the metal to the fluid phase:



where again the \equiv is the mineral bond, M is the metal and $M_{dissolved}$ stands for the dissolved metal in solution. Minerals that contain a number of distinct metal-oxygen bonds are dissolved by one or more steps (figure 2).

In agreement with the Transition State Theory dissolution or precipitation of minerals has been described using (Aagaard and Helgeson, 1982):

$$r = r_+(1 - \exp(-A/\sigma RT)) \quad (1)$$

Figure 1 Stability diagram of the system $Na_2O-Al_2O_3-SiO_2-H_2O$ at $25^\circ C$. The logarithmic activities of aqueous silica are displayed on the horizontal axis and that of Na over hydrogen on the vertical axis. During weathering of albite, both Si and Na concentration increases. The first phase to reach saturation is gibbsite (pentagon) and it is likely to precipitate until the Si concentration is enough to reach the saturation of kaolinite (line from pentagon to vertical line). At that point the gibbsite is converted into kaolinite until all the gibbsite is consumed (line up on the vertical line). The kaolinite precipitates from solution until it reaches montmorillonite saturation

where r refers to the overall rate, r_+ stands for the forward rate, A designates the chemical affinity, σ the Temkin's average stoichiometric number equal to the number of moles of mineral destroyed by one mole of each elementary reaction, and R and T refer to the gas constant and temperature in Kelvin, respectively.

Chemical affinity is the driving force for the reaction and can be computed from this relation between the equilibrium constant of a mineral and the activities of the aqueous species in solution:

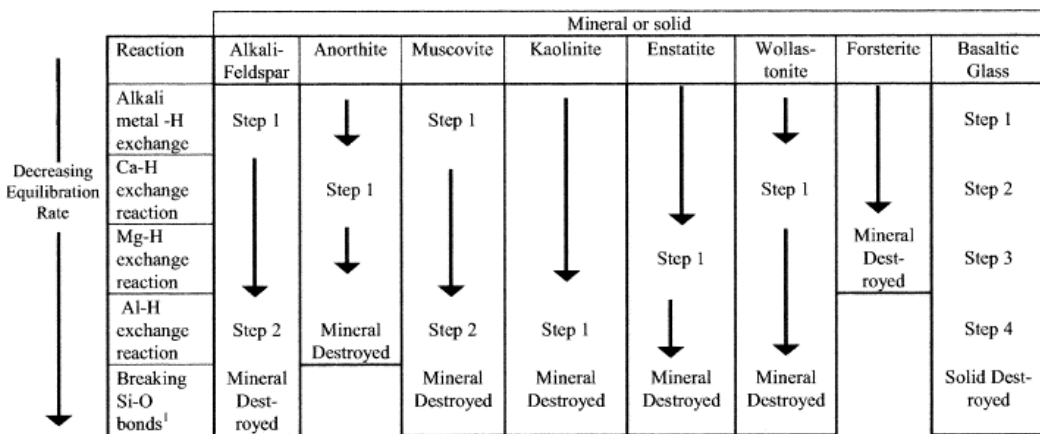
$$A = RT \ln(Q/K_{eq}) \quad (2)$$

where the K stands for equilibrium constant and Q symbolizes the reaction quotient of the chemical reaction.

At far from equilibrium A is much greater than σRT and therefore the rate r is equal to the forward dissolution rate r_+ as the reverse reaction is negligible. As $(-A/\sigma RT)$ approaches 0, the dissolution rate decreases to zero at equilibrium. At equilibrium $K = Q$ and as $K > Q$ the solution is supersaturated with respect to the mineral and precipitation takes place, i.e. the reaction is reversed.

1.2.1.1 Dissolution

Dissolution rates are commonly based on measurement of Si release from a silicate mineral or glass (Chou and Wollast, 1985; Knauss and Wolery, 1986; Knauss et al., 1993; Gislason and Oelkers, 2003). Si is used because most rock-forming minerals have a Si-O bonded framework, and Si-O bonds are typically that which holds the mineral structure together. In Fig. 2 the steps of dissolution leading to the destruction of some multi oxide minerals and glasses are shown. The first step is the breaking of alkali-metal-H bonds, followed by Ca-H bonds, Mg-H bonds, Al-H bonds, and finally Si-O bonds, with the latter destroying the mineral. Dissolution is considered to be stoichiometric if the elemental ratio in the reactive fluid increases in a proportion equivalent to that in the mineral; otherwise it is termed non-stoichiometric. Non-stoichiometry can be due to several reasons, e.g. formation of secondary phases, more than one mineral present or a formation of a surface layer enriched in an element (Oelkers, 2001b).



1) The breaking of Si-O bonds most likely involves H_2O absorption rather than an Si for H exchange reaction (see Dove and Crerar, 1990).

Figure 2: This figure displays the steps during dissolution towards complete destruction of the mineral/glass at acid conditions. The number of steps depends on the structure of the mineral and composition (Oelkers, 2001b).

1.2.1.2 Precipitation

Precipitation can occur via a number of mechanisms. One is via mineral replacement where a new mineral is formed directly on another (Putnis, 2009). Another mechanism is the nucleation of a crystal phase from aqueous solution and its subsequent growth where elements from solution are attached onto the nuclei composition (Benning and Waychunas, 2008). In this study precipitation refers to the addition of material from supersaturated aqueous fluids onto seed crystals of the same mineral.

In natural systems mineral dissolution is commonly coupled to secondary mineral precipitation. During low grade metamorphism in the basaltic regions of Iceland the dominating secondary minerals are clays, zeolites and calcite (Walker, 1960; Kristmannsdottir and Tomasson, 1978; Neuhoff et al., 1997; Neuhoff et al., 2000; Fridriksson et al., 2001; Neuhoff et al., 2006; Rogers et al., 2006; Arnorsson and Neuhoff, 2007). Such secondary minerals have chemical compositions that reflect the composition of the altered parent rock. In geothermal areas, this is of interest because these secondary phases can be used as indicators of alteration temperature (Kristmannsdottir and Tomasson, 1978) and can influence the geothermal productivity of an area as secondary minerals can fill pore space and therefore decrease rock permeability.

In large scale weathering, the parent rock can be altered into economically exploitable deposits of secondary phases. For example, large kaolinite formations are likely to have originated from the alteration of feldspar-rich parent rocks such as granite, where increasing temperature and humidity promoted kaolinite rather than illite or smectite precipitation (Sherman and Uehara, 1956; Hay and Jones, 1972). Bauxite is formed when large aluminium rich formations are leached of silica leaving only aluminium to precipitate.

Mineral precipitation rates are commonly described as a function of fluid saturation state using a variant of Eqn. (1):

$$r = r_+(\Omega_i - 1)^n \quad (3)$$

where r_+ represents the forward reaction rate which may itself depend on the fluid composition (e.g. Saldi et al., 2009; Saldi et al., 2012) and Ω_i represents the saturation degree with respect to the i th mineral.

$$\Omega_i = Q/K_{eq} = \exp(-A_i/RT) \quad (4)$$

The parameter n in Eqn. (3) is representative of the precipitation mechanism. When $n=1$ it is consistent with mineral surface growth by adsorption processes, $n=2$ is consistent with mineral spiral growth and when $n>2$ mineral growth is controlled by nucleation (Gratz et al., 1993; Nielsen, 1964; Nielsen, 1984; Shiraki and Brantley, 1995; Teng et al., 2000). As emphasized by Temkin (1963), however, the chemical affinity of an overall reaction needs to be normalized to that of the elementary reaction to accurately use reaction orders based on these elementary reaction mechanisms. In the case of gibbsite the only metal is aluminium and the chemical formula contains one mole of Al; it thus seems likely that the elementary reaction for gibbsite precipitation contains one mole of gibbsite. In the case of kaolinite the elemental formula has two Si and two Al moles per one mole of kaolinite. This suggests that the elemental reaction for kaolinite precipitation contains less than one mole of kaolinite.

1.2.1.3 Rate expressions

Dissolution and precipitation rates are commonly reported in units of moles of mineral over the normalized surface area and time, i.e. mol/m²/s. The rates refer to moles of the mineral based on the release rates of a chosen element. Also found commonly in literature are rates based on changes in concentration of an element. These rates can be referred to as elemental release rates. The simplified formula of dissolution/precipitation rates for a flow-through system can be expressed as:

$$r_{i,j} = \left(\frac{FR \times \Delta C_i}{S_j m} \right) / \sigma_i \quad (5)$$

where r_i represents the rate based on the changes of the i th element, FR signifies the flow rate, ΔC_i stands for the change of the i th element concentration between the inlet solution and the reactive fluid, S_j stands for the specific surface area of the mineral in denoted format, per mass and m is the mass of the mineral, σ is the stoichiometric coefficient of the i th element in the mineral.

1.3 Primary rocks and minerals

1.3.1 Igneous rock

The textbook definition of igneous rock is that it forms when magma (or lava) solidifies. This can either happen below the surface, where the magma intrusion will slowly cool and solidify and form coarse grained rocks such as gabbros or at the surface where the cooling process is faster and the rock will consist of smaller crystals and/or glass to form finer grained rocks such as basalt or basaltic glass. Igneous rocks are commonly divided into groups from low to high silica content from ultramafic, mafic, and intermediate to silicic (felsic), a generalized overview of this can be seen in Figure 3. With changing chemical composition the mineral

assemblage and compositions also change. For example plagioclase becomes Na-richer and Al-poorer as the Si content increases in the parent magma. Forsterite olivine (Mg-rich) is present in mafic rocks whereas fayalite (Fe-rich) is more common in felsic rocks. The most abundant mineral in igneous rocks is plagioclase, which is present in all rock types. Basalt is a mafic rock that forms as primitive magma cools. It is found on the Earth's surface as either basaltic glass that is formed by rapid cooling of the magma or as crystalline basalt that forms by the slower cooling of the magma. Crystalline basalt tends to be dominated by three main silicate-minerals: pyroxene, plagioclase and olivine. Minor minerals such as Fe-Ti-oxides and glass are commonly present as interstitial components.

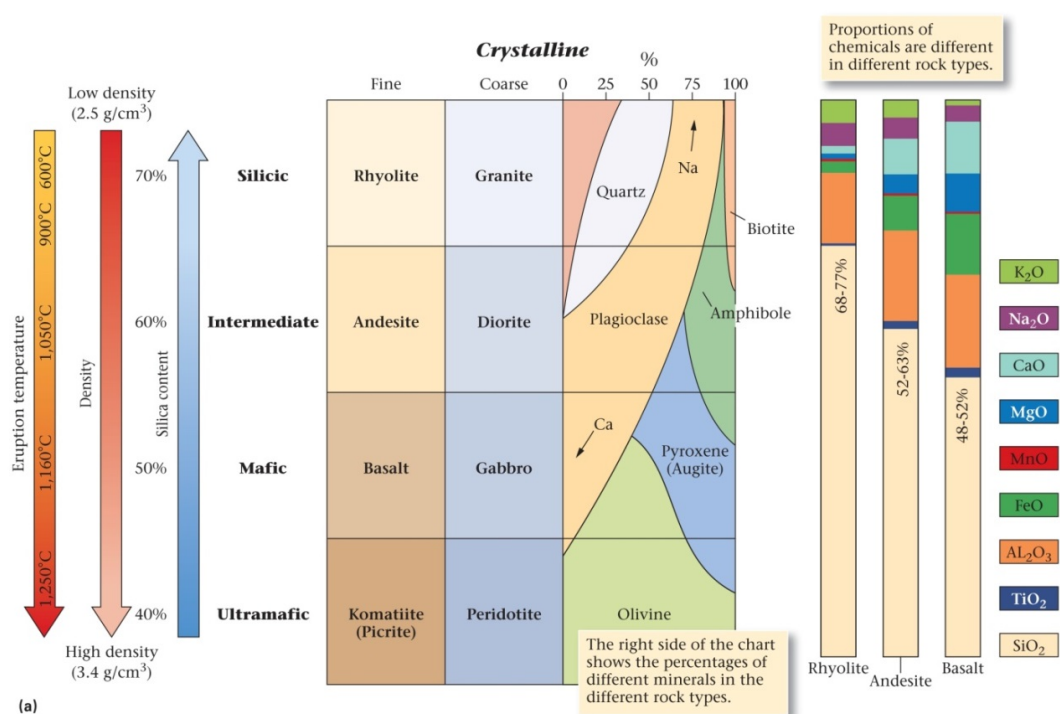


Figure 3: This figure shows the mineral composition, the silica percent and the element percent of crystalline igneous rocks. The Staphell basalt has the silica concentration of ~50% and the three main minerals present in the crystalline basalt are Ca-rich plagioclases, olivine and pyroxene. (Figure from Marshak and Prothero, 2008)

1.3.1.1 Mid-Ocean Ridge Basalts (MORB)

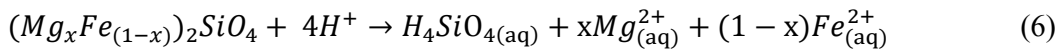
The oceans cover approx. 70% of the Earth's surface. They cover some of the most active volcanic zones on Earth, e.g. Mid-Atlantic Ridge and The Pacific Ring (Ring of Fire) as well as some of the most active onshore basaltic regions (Iceland and Hawaii). The igneous ocean floor is basaltic with pillow basalts as well as lava flows in the top 1-2 km followed below by mafic dykes (1-2 km) and then gabbroic formations. The oceans also cover some of the plate boundaries, e.g. the Mid-Atlantic Ridge that is the rift between the Eurasian and N-American plates. Perched on this rift sits Iceland. The average whole rock chemical formula of a MORB is comparable to the Staphell crystalline basalt of this study (Albarède 2005; Gislason and Oelkers, 2003; Gudbrandsson et al., 2011).

1.3.1.2 Staphafell Basalt

Stapafell Mountain is one of the first formations in the rift zone between the North-American and Eurasian plate after coming on shore in SW-Iceland. The formation is a hyaloclastite made of basaltic glass that also features pillow basalts at lower elevations. Several dykes are visible and easily accessible. This mountain is an exceptionally good location to access fresh basaltic material for experiments for several reasons. First, the mountain has been used as a quarry for several decades and therefore one can access material that has recently been exposed, and has few visible alteration and weathering features. Second, the basaltic glass from the location has been well characterized (Oelkers and Gislason, 2001; Gislason and Oelkers, 2003; Wolff-Boenisch et al., 2004; Stockmann et al., 2011; Galeczka et al., 2013). Third, Stapafell is chemically and mineralogically comparable to the basaltic formation at Hellisheiði and therefore ideal to assess CO₂-water-basalt interaction at the CarbFix injection site (Gudbrandsson et al., 2011; Alfredsson et al., 2013). Fourth, it is chemically comparable to Mid-Ocean-Ridge basalt (Albarède, 2005).

The bulk chemical composition of Stapafell basaltic glass and crystalline basalt is comparable (Chapter 2, Table 1). The mineral composition of the Stapafell crystalline basalt was analysed using XRD (see material and methods section below). The three main minerals present are olivine (17%), clinopyroxene (39%) and plagioclase (44%). Other minor phases are glass and iron oxides occurring interstitially.

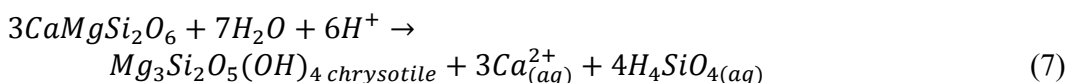
Olivine is a common mineral in mafic igneous rocks (Fig 3). The general chemical formula of olivine is (Mg,Fe)₂SiO₄. The crystal structure of olivine minerals is orthorhombic and they appear in igneous rocks such as gabbros and basalts as well as ultramafic. The olivine found in the Stapafell crystalline basalt is 85% forsterite (Fo₈₅), its dissolution can be described by:



where $0 \leq x \leq 1$

where x refers to the Mg content of the olivine. The dissolution rates of olivine have been studied extensively (Pokrovsky and Schott, 2000b; Kobayashi et al., 2001; Oelkers, 2001a; Giammar et al., 2005; Hanchen et al., 2006) and decrease with increasing pH.

The pyroxenes can be divided into two major groups based on their crystal structure: orthopyroxenes, with orthorhombic structure and clinopyroxene with monoclinic crystal structure. The pyroxene found in the Stapafell crystalline basalt is a clinopyroxene called augite with the chemical formula of Mg_{0.73}Ca_{0.76}Fe_{0.38}Na_{0.02}Al_{0.25}Si_{1.79}O₆. Pyroxenes are an important mineral in igneous rocks that have 40-60% SiO₂ content and are a major mineral in basalts such as that from Stapafell. The weathering of Fe-poor clinopyroxene can be described by:



Pyroxene saturation state in natural waters and dissolution rates have also been extensively studied and like olivine the dissolution rates decrease with increasing pH (Gislason and Arnorsson, 1993; Knauss et al., 1993; Brantley and Chen, 1995; Chen and

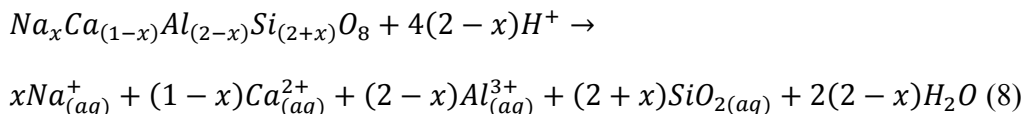
Brantley, 1998; Arnorsson et al., 2002). While proportionally clinopyroxene is the second most abundant component in the studied crystalline basalt, its influence on dissolution at the temperatures in this study, is likely to be minor as clinopyroxene is found to resist alteration. During the dissolution of crystalline basalts in natural systems, the fast dissolution rates of olivine releases Mg^{2+} and Fe^{2+} into the fluid leading it to become nearly saturated with respect to pyroxene, i.e. for Eqn (4), $Q_{cpx} \leq K_{cpx}$ while $Q_{ol} \ll K_{ol}$. (Arnórsson et al., 2002). This has been observed in nature (Gustavson, 2006; Neuhoff et al., 2006) where the olivine and plagioclases are altered or dissolved by weathering while the pyroxenes tend to be less weathered.

The plagioclase present in the Stapafell basalt is a Ca-rich plagioclase of labradorite composition (An_{65}).

1.3.1.3 Plagioclases

Plagioclase is part of the feldspar mineral-group. It is the most common mineral in the Earth's crust and present in nearly all crystalline crustal igneous rocks (Nesbitt and Young, 1984; Mc Birney, 1993). Plagioclase range from a pure Na end-member, albite, ($NaAlSi_3O_8$), to a pure Ca end-member called anorthite ($CaAl_2Si_2O_8$).

The dissolution of the plagioclase can be described by:



where $0 \leq x \leq 1$

1.3.1.3.1 Intermediate plagioclases

The plagioclase feldspars are arbitrarily divided into six compositional ranges: albite, oligoclase, andesine, labradorite, bytownite and anorthite, with anorthite percentage of 0-10, 10-30, 30-50, 50-70, 70-90 and 90-100, respectively (Fig. 4).

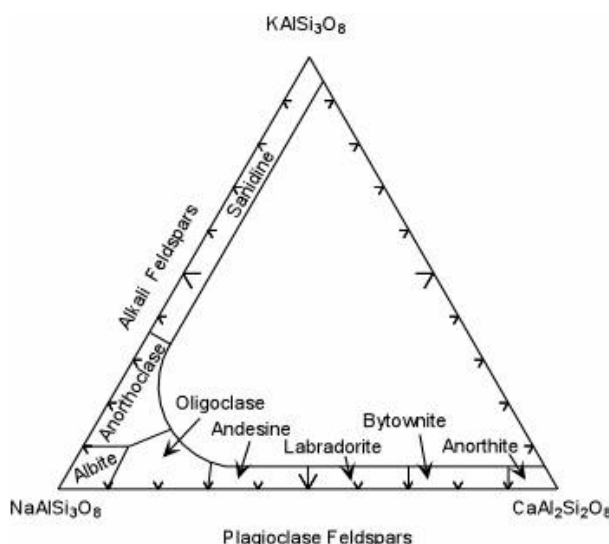


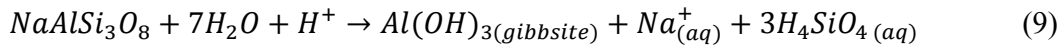
Figure 4: A ternary feldspar plot showing its chemical composition and classification. (Mc Birney, 1993)

Plagioclases are present, both in igneous as well as metamorphic rock and are commonly referred to their origin by high or low, for igneous and metamorphic respectively. The most common metamorphism in plagioclases refers to albitization, that is, when the chemical attributes of the plagioclase changes from more Ca rich to more Na rich (Ramseyer et al., 1992). In many plagioclases intergrowths can be found. There are three well known regions of plagioclase intergrowths: i) Peristerite intergrowths, An₂-An₁₆, with the lamella of An₀ and An₂₅ composition, ii) Bøggild intergrowths, An₄₃-An₅₈, comprised of An₃₉₋₄₉ and An₅₃₋₆₄ intergrowths, and iii) Huttenlocher intergrowth, An₆₇-An₉₀, composed of the intergrowths having the composition An₆₇₋₉₅. (Smith and Brown, 1988). These intergrowths are commonly not visible in optical microscope and in this study we assume that all plagioclases are a homogeneous solid.

1.3.2 Secondary phases

1.3.2.1 Gibbsite

Gibbsite is an aluminium hydroxide and one of three main aluminium minerals that form bauxite, the ore rock for aluminium production. It is named after American mineral collector Col. George Gibbs. Gibbsite is commonly found in soils, especially in warm climates. Gibbsite formation is found in nature, besides other minerals such as kaolinite and illite. Gibbsite forms monoclinic crystals and can result from albite weathering according to the equation:



Bauxite formations are largely attributed to plagioclase weathering in wet and warm climates where the Si of the parent rock is leached, leaving an Al-rich phase behind. The largest bauxite deposits are found in East-Asia, S-America and W-Africa (see Fig. 6).



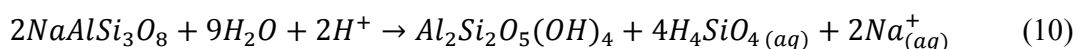
Figure 5: Darkened areas show the location of major bauxite formations. Note these are mainly in warmer regions of the world. The bauxite is mined and shipped to the aluminium smelters such as those located throughout Iceland. Source: www.pinepacific.com.

More than 160 million tons of bauxite are mined annually for aluminium production globally (European Aluminium Association webpage) making aluminium one of the most important metal for industrial use on earth. The production of aluminium has increased since 1950 from approx. 2,000,000 tons per year in 1950 to close to 50,000,000 tons in the year 2012 (European Aluminium Association webpage). This increase can be attributed to several reasons but one of the main reasons is that aluminium is a much lighter metal than previously used in the auto and aviation industry. Aluminium is extracted from the crude material bauxite by the Bayer Process and the Hall-Heroult process (Hind et al., 1999) wherein one step is precipitation of gibbsite.

In Iceland, due to relatively cheap energy, there are three aluminium smelters. The total production capacity in 2012 was approx. 800,000 tons or just over 1.5% of the world production; this number has increased since 1990 by more than 700,000 tons. The production of aluminium releases CO₂ into the atmosphere and the increased production resulted in increased CO₂-emission in Iceland by 71%, from 570,000 tons in 1991 to 978,000 tons in 2007. The CO₂ released per ton Al produced has decreased by approx 75% during the same time (Davíðsdóttir et al., 2009). Although the production of aluminium releases CO₂ into the atmosphere the metal is an important product to reduce global CO₂ emissions. Making airplanes and automobiles from a lighter material makes the vehicles use less energy and release less CO₂ into the atmosphere.

1.3.2.2 Kaolinite

Kaolinite is a clay mineral that consists of an octahedral aluminium layer similar to gibbsite and a tetrahedral layer of silicon held together with van der Waals forces. It is named after the Kao-Ling area in China and is also sometimes called China-Clay. Kaolinite is a common natural clay and although the name kaolinite is not a household name, the mineral is probably one of the most common minerals used for everyday products. It is widely used as filler for cosmetics, toothpaste, paint and paper as well as being the china clay for porcelain production. The clay is common on the Earth surface and has been mined for centuries. The formation of economic kaolinite deposits can mainly be attributed to the weathering of large granite intrusions in warm and wet areas. The weathering of albite to kaolinite can be described with the formula:



Kaolinite is sometimes associated with quartz and iron hydroxides but can also be very pure and homogenous in big quarries, such as the Georgia kaolinite (Pruett and Webb, 1993). Kaolinite rich soils are sometimes referred to as kaolisols (Ganssen, 1970). The volume of kaolinite in soils generally decreases with decreasing temperature on Earth but is also found in geothermal areas such as in Krýsuvík SW-Iceland (Markússon and Stefánsson, 2011).

1.4 Methods

1.4.1 Sample preparation

Solids used in the dissolution experiments reported in this thesis were either collected from natural sites or obtained commercially from Ward's Science, with the exception of one anorthite sample, obtained from The Smithsonian Museum in Washington DC, USA.

The solids collected directly from natural locations include 1) basalts from Stapafell Mountain, SW-Iceland, and 2) bytownite from an anorthosite formation in Hrappsey Island W-Iceland (Kristmannsdottir, 1971). Samples chosen were to have no visible weathering, alteration, fungi or other visible life forms. The samples were then cleaned with DI-water and dried at 50°C for 24 hours at least.

The solids used in dissolution experiments were prepared in the same manner as in comparable dissolution studies (e.g. Oelkers and Gislason, 2001; Wolff-Boenisch et al., 2004; Stockmann et al., 2008). First any observed impurities were removed. The samples were then crushed and dry sieved to the desired size fraction. This size fraction was cleaned and gravitationally separated, then ultrasonically cleaned both with DI-water and finally with acetone, then dried at 50°C for several days before being used in experiments.

The starting material for the crystal growth experiments was purchased from commercial vendors. Kaolinite KGa-1b was acquired from the Clay Minerals Society. This kaolinite is well characterized (Pruett and Webb, 1993) and has been commercially available for over a decade. The kaolinite is well crystallized. Minor impurities were removed following the protocol of Yang and Steefel (2008).

The gibbsite used in the precipitation experiments was only washed with DI-water before being placed in the reactors. This gibbsite was previously characterized and used in precipitation experiments by Bénézeth et al. (2008).

1.4.2 Characterisation of solids

The cleaned crystalline basalt from Mt. Stapafell was analysed for whole rock chemical composition using X-ray Fluorescence (XRF) at the University of Edinburgh, UK. This analysis showed that its chemical composition was comparable to its glassy counterpart as well as MORB (Mid Ocean Ridge Basalt). The mineral abundance of the basalt was determined by point counting a thin section and by XRD peak intensity analysis resulting in plagioclase:pyroxene:olivine volume percentages of 44:39:17.

The chemical composition of the minerals in the basalt as well as the plagioclases was determined using Electron Microprobe; the basalt was analysed at The University of Copenhagen using a JEOL Superprobe JSL 8200. These analyses were performed using an acceleration voltage of 15 kV, a beam current of 15 nA and a beam diameter of 2 micrometre. Natural and synthetic minerals and glasses were used as standards to monitor potential drift. The plagioclases were analysed at GET/CNRS, Toulouse, France using the same methods. A minimum of 30 random grains were analysed per sample.

The gibbsite and kaolinite seeds both before and recovered after each precipitation experiment were analysed by X-ray Diffraction (XRD) using an INEL CPS 120 Cokα

diffractometer, with a scanning speed of 0.02° per second, at GET/CNRS, Toulouse, France. The surface composition of the kaolinite was determined using X-ray photoelectron spectroscopy (XPS). These XPS measurements were performed using a Kratos Axis Ultra^{DLD} instrument, fitted with a monochromatic Al_{Kα} X-rays source (power = 150 W). The pressure in the vacuum chamber never exceeded 5×10^{-9} Torr during a measurement. A charge neutralizer was used to avoid surface charging. Pass energies of 160 eV and 10 eV were used for wide scans and high resolution scans respectively. Analysis was carried out with the software CasaXPS using a Shirley background. Binding energy calibration was done using the carbon peak at 185 eV.

The surface areas of all solids were determined using 11 point BET analysis using a Quantachrome Gas Sorption system at the GET/CNRS in Toulouse, France. The BET theory assumes that a mono-layer of gas molecules of a non-reactive gas is absorbed on the surface of the mineral and the relative drop in pressure shows the number of molecules absorbed and therefore the surface area of the mineral (Brunauer et al., 1938). The area for small surfaces, i.e. basalt, plagioclases and gibbsite were measured using krypton while those of large surfaces i.e. kaolinite was measured using nitrogen.

1.4.3 Experimental methods

The dissolution experiments were performed in mixed flow reactor systems: either in a Ti-mixed flow reactor system from Parr Industries, with a 300 mL reactor coupled to a magnetic stirrer and furnace; or in a custom-made polypropylene reactor system with 250-300 mL reactor and a floating magnetic stirring bar. These reactor systems have been extensively used to measure dissolution rates in open system, flow-through experiments (Oelkers and Gislason, 2001; Gislason and Oelkers, 2003; Wolff-Boenisch et al., 2004; Gudbrandsson et al., 2011; Stockmann et al., 2011). These systems are rather simple in design and easy to use. A known amount of solid is placed into the reactor which is then filled with reactive fluid. The solids are kept in suspension by stirring fluid/solid mixture at a 400 rpm rotation speed, which also eliminates diffusional gradients in the fluid phase (Guy and Schott, 1989; Gislason and Oelkers, 2003). The experiments were either run in series, where the same mineral sample was kept in the reactor while the temperature or fluid composition was changed, or individually, were the solid was only used in a single experiment reacted in a single fluid. Dissolution experiments are generally run until a steady-state is reached. Steady-state is defined when the concentration of a given element *i*, is stable over ten resident times of the reactor. As such most rates in this thesis can be considered steady-state rates making them applicable to describing the behaviour of natural systems.

The crystal growth experiments on kaolinite were performed in custom-made mixed-flow reactor systems stirred using a floating stirring bar. These systems have been described by Mavromatis et al. (2012). A known amount of kaolinite seeds were placed into the reactor with a reactive fluid that is initially slightly undersaturated with respect to kaolinite. Two inlet tubes, one for injecting a Si-rich and one for injecting a Al-rich fluid, and one outlet fluid exit tube were connected to the reactor. The inlet fluid entrance positions are physically separated to prevent supersaturation from occurring before the fluids enter the reactor. The fluid flow rate was kept low and the stirring speed just high enough to keep the kaolinite seeds in suspension. The experiments were sampled daily and the reactive fluid mass in the reactor was 500 ± 20 ml during the experiment. The sampled reactive fluid was then acidified prior to analysis of Al by Flame Atomic Absorption and of Si by Colorimetry.

Gibbsite precipitation experiments were performed in a closed system reactor as commonly used in such experiments, e.g. Roncal-Herrero and Oelkers (2011). Each experiment was initiated by placing a known quantity of gibbsite seeds together with the initial reactive fluid into the reactor. The starting fluids were supersaturated with respect to gibbsite in all experiments. The initial aluminium concentrations were set to be supersaturated by a factor of 2, 5, 10, and 25 at each pH and temperature to assess the effect of fluid supersaturation on rates. The reactive fluids were regularly sampled, and rates determined from the decrease in measured fluid Al concentrations as a function of time.

1.4.4 Fluid chemistry

The inlet fluid compositions for each experiment can be found in following thesis chapters. The dissolution experiments were designed to run at far from equilibrium conditions and thus the fluids were made from distilled deionised water with a pH buffer, HCl for acid input fluid and NH₄ for basic input fluid. All input fluid ionic strengths were set at 10 mM using NH₄Cl.

The precipitation experiments were designed to measure rates as a function of fluid saturation state. The input fluids were prepared by pre-calculating the desired fluid composition using the PHREEQC computer code and either its LLNL or Phreeqc database. Prior to analyses all fluids were filtered and acidified with a suprapure HNO₃. The pH measurements were conducted on samples not used for chemical analysis.

The reactive and inlet fluids of all dissolution experiments were analysed using an Inductively Coupled Plasma-Optical Emission Spectrometer (ICP-OES) at the University of Iceland standardized with a natural water standard that was calibrated against a standard obtained from SPEXPrepTrep Ltd. The detection limits are in the order of 15 ppb for silica (SiO₂) and 5 ppb Al. The uncertainties on the ICP-OES analysis are estimated to be within 5%. However, at concentrations lower than 150 ppb SiO₂ and 50 ppb Al the uncertainties increase dramatically, and are therefore treated as being 100% at the detection limit.

The aluminium concentration of fluids obtained from precipitation experiments was analysed using Flame Atomic Absorption for concentrations as low as 1 ppm aluminium and Furnace Atomic Absorption for concentrations as low as 20 ppb. The standards were prepared prior to analysis by diluting Al standards to the desired concentration of aluminium. Fluid silica concentrations from precipitation experiments were determined by colourimetry using the Molybdate Blue method (Koroleff, 1976), calibrated to 1-10 ppm Si and standardized with Canadian Water standard (Mississippi 03). The uncertainties associated with the analysis are estimated to be within 5% for flame atomic absorption and 10% for Furnace Atomic Absorption. The colourimetry carries close to 5% uncertainties. Detailed analytical methods for each experiment can be found in the following thesis chapters.

Detailed description of experimental setup, sampling and analysing can be found in following chapters.

1.5 Thesis outline:

- Chapter 1: Introduction
- Chapter 2: Snorri Gudbrandsson, Domenik Wolff-Boenisch, Sigurdur R. Gislason, Eric H. Oelkers (2011) “*An experimental study of crystalline basalt dissolution from 2 ≤ pH ≤ 11 and temperatures from 5 to 75 °C*” Geochimica Cosmochimica Acta 75, 5496-5509.
- Chapter 3: Snorri Gudbrandsson, Domenik Wolff-Boenisch, Sigurdur R. Gislason, Eric H. Oelkers (2013) “*Experimental characterization of plagioclase dissolution rates as a function of their composition and pH at 22° C*” (Submitted to Geochimica Cosmochimica Acta).
- Chapter 4: Snorri Gudbrandsson, Vasileios Mavromatis, Eric H. Oelkers (2013) “*Precipitation of gibbsite at pH 11 at 22°C and pH 9 at 80°C*” (Draft manuscript to be submitted upon completion of work).
- Chapter 5: Snorri Gudbrandsson, Vasileios Mavromatis, Quentin Gautier, Nicolas Bovet, Jacques Schott, Eric H. Oelkers (2013) “*An experimental study of kaolinite precipitation kinetics as a function of fluid saturation state at pH 4 and 25 °C*” (Manuscript to be submitted upon completion of work).
- Chapter 6: Summary of results and remarks.

Chapters 2 and 3 were performed as a part of the CarbFix project. The aim of these studies can be divided into two parts:

- 1) To explore the dissolution behaviour of primary rocks and minerals during carbon storage in basalts and monitor the chemical release rates of divalent cations as a function of pH to the fluid during CO₂ injection into basalts.
- 2) To further improve our understanding of the dissolution rates of rocks and minerals as a function of pH.

These studies were performed using mixed flow reactors at 5, 25, 50, and 75 °C for crystalline basalt dissolution in Chapter 2 and at 22 °C for plagioclase dissolution in Chapter 3. The inlet fluid compositions, ranging from pH 2 to pH 11, were pre-calculated using the PHREEQC computer code. The results from these experiments are used to improve the kinetic databases of the dissolution of primary minerals and multi-phase rocks. Moreover, these rates provide insight into the identity and composition of the secondary mineral formed during low temperature geochemical water-rock processes. Dissolution rates of plagioclases are reported in units of moles of plagioclase/cm²/s but the dissolution rates of crystalline basalt are reported as elemental release rates based on silica (mol_{Si}/cm²/s). This is due to the fact that crystalline basalt is multi-mineralic, and more than one mineral is dissolving at any given moment. Elemental release rates of the divalent cations from the crystalline basalt were also determined.

Chapters 4 and 5 were performed as a part of the DELTA-MIN European Initial Training Network. The aim of these studies can be divided into two parts:

- 1) To quantify the precipitation rates of the aluminium rich secondary mineral gibbsite.
- 2) To quantify the precipitation rates of the aluminium rich secondary mineral kaolinite.

In Chapter 4 gibbsite precipitation rates at alkaline conditions are explored. The experiments were performed in Nalgene™ batch reactors at 25 °C and pH 11 and 80 °C and pH 9. At each condition the rates were measured as a function of fluid saturation state by preparing five batch reactors at different saturation states with respect to gibbsite. The reactors were then sealed using Teflon tape and placed on a shaking table at room temperature or in a thermostatic shaking table at 80 °C. All reactor fluids were sampled regularly and analysed for Al concentration. The fluid chemistry as well as the solid analysis indicates that precipitation took place in all experiments.

Chapter 5 focuses on kaolinite precipitation at pH 4 and at 25 °C. The experiments were carried out in mixed-flow reactors with two separate inlets of one Si-rich solution at pH 4 and another Al-rich solution at pH 4. These fluids were introduced separately into the reactor that hosted kaolinite seeds in a reactive aqueous fluid with Si and Al concentrations close to equilibrium with respect to kaolinite but undersaturated with respect to other Al and Si phases. The concentrations of the reactor fluid reached supersaturation with respect to kaolinite over time as the concentration in the reactors increased. Nevertheless, because of the slow precipitation rates of kaolinite, results based on the fluid chemistry are highly uncertain. Chemical analyses of the solids, however, indicate that the only phase present after experiments is kaolinite.

2 Chapter

An experimental study of crystalline basalt dissolution from $2 \leq \text{pH} \leq 11$ and temperatures from 5 to 75 °C

Snorri Gudbrandsson, Domenik Wolff-Boenisch, Sigurdur R. Gislason and Eric H. Oelkers

Geochimica Cosmochimica Acta 75 (2011) 5496-5509

(Reprinted with permission by Elsevier Science Ltd)

Abstract

Steady-state element release rates from crystalline basalt dissolution at far-from-equilibrium were measured at pH from 2 to 11 and temperatures from 5° to 75° C in mixed-flow reactors. Steady-state Si and Ca release rates exhibit a U-shaped variation with pH where rates decrease with increasing pH at acid condition but increase with increasing pH at alkaline conditions. Silicon release rates from crystalline basalt are comparable to Si release rates from basaltic glass of same chemical composition at low pH and temperatures $\geq 25^{\circ}\text{C}$ but slower at alkaline pH and temperatures $\geq 50^{\circ}\text{C}$. In contrast, Mg and Fe release rates decrease continuously with increasing pH at all temperatures. This behaviour is interpreted to stem from the contrasting dissolution behaviours of the three major minerals comprising the basalt: plagioclase, pyroxene, and olivine. Calcium is present in plagioclase, which exhibits a synclinal dissolution rate dependence on pH. In contrast, Mg and Fe are contained in pyroxene and olivine, minerals whose dissolution rates decrease monotonically with pH. As a result, crystalline basalt preferentially releases Mg and Fe relative to Ca at acidic conditions. The injection of acidic CO₂-charged fluids into crystalline basaltic terrain may, therefore, favour the formation of Mg and Fe carbonates rather than calcite. Element release rates estimated from the sum of the volume fraction normalized dissolution rates of plagioclase, pyroxene, and olivine are within one order of magnitude of those measured in this study.



Available online at www.sciencedirect.com



Geochimica et Cosmochimica Acta 75 (2011) 5496–5509

**Geochimica et
Cosmochimica
Acta**

www.elsevier.com/locate/gca

An experimental study of crystalline basalt dissolution from $2 \leq \text{pH} \leq 11$ and temperatures from 5 to 75 °C

Snorri Gudbrandsson^{a,b,*}, Domenik Wolff-Boenisch^a, Sigurdur R. Gislason^a,
Eric H. Oelkers^b

^a Institute of Earth Sciences, University of Iceland, Sturlugata 7, 101 Reykjavik, Iceland
^b GET, CNRS/UMR 5563-Université Paul Sabatier, 14 rue Edouard Belin, 31400 Toulouse, France

Received 2 December 2010; accepted in revised form 22 June 2011; available online 1 July 2011

Abstract

Steady-state element release rates from crystalline basalt dissolution at far-from-equilibrium were measured at pH from 2 to 11 and temperatures from 5 to 75 °C in mixed-flow reactors. Steady-state Si and Ca release rates exhibit a U-shaped variation with pH where rates decrease with increasing pH at acid condition but increase with increasing pH at alkaline conditions. Silicon release rates from crystalline basalt are comparable to Si release rates from basaltic glass of the same chemical composition at low pH and temperatures ≥ 25 °C but slower at alkaline pH and temperatures ≥ 50 °C. In contrast, Mg and Fe release rates decrease continuously with increasing pH at all temperatures. This behaviour is interpreted to stem from the contrasting dissolution behaviours of the three major minerals comprising the basalt: plagioclase, pyroxene, and olivine. Calcium is primarily present in plagioclase, which exhibits a U-shaped dissolution rate dependence on pH. In contrast, Mg and Fe are contained in pyroxene and olivine, minerals whose dissolution rates decrease monotonically with pH. As a result, crystalline basalt preferentially releases Mg and Fe relative to Ca at acidic conditions. The injection of acidic CO₂-charged fluids into crystalline basaltic terrain may, therefore, favour the formation of Mg and Fe carbonates rather than calcite. Element release rates estimated from the sum of the volume fraction normalized dissolution rates of plagioclase, pyroxene, and olivine are within one order of magnitude of those measured in this study.

© 2011 Published by Elsevier Ltd.

1. INTRODUCTION

A large number of studies have been performed to determine the dissolution rates of individual minerals in the laboratory as a function of temperature and reactive fluid composition (e.g. Lasaga et al., 1994; Brantley and Chen, 1995; Oelkers and Schott, 1995, 2001; Schott et al., 2009). Natural rocks, however, consist of a number of different minerals and glasses, each with distinct reactivities and surface areas. Geochemical modelling codes such as PHREEQC (Parkhurst and Appelo, 1999) sums together the dissolution rates of each mineral in a rock to estimate

overall rock dissolution rates. This study aims to validate this geochemical modelling approach through experimental measurement of crystalline basalt dissolution. The present communication presents the results of these experiments and uses them to assess the application of individual mineral dissolution rates to describe those of a multi-phase rock.

Crystalline basalt was chosen for this study for a number of reasons. First, the selected basalt has a simple mineralogy, consisting mostly of olivine, pyroxene, and plagioclase. The dissolution rates of these minerals have been studied extensively over the past two decades (e.g. Chou and Wollast, 1985; Blum and Lasaga, 1991; Blum and Stillings, 1995; Oelkers and Schott, 1995; Stillings and Brantley, 1995; Pokrovsky and Schott, 2000b; Hänen et al., 2006). Secondly, the composition of basalt can range from 100% glass to 100% crystalline. Experimentally measured basaltic glass

* Corresponding author at: GET, CNRS/UMR 5563-Université Paul Sabatier, 14 rue Edouard, Belin 31400 Toulouse Country, France. Tel.: +33 5 61 33 25 75; fax: +33 5 61 33 25 60.
E-mail address: snorgud@hi.is (S. Gudbrandsson).

dissolution rates have been reported in the literature (e.g. Oelkers and Gislason, 2001; Gislason and Oelkers, 2003; Wolff-Boenisch et al., 2004a,b, 2006; Flaathen et al., 2010; Stockmann et al., 2011). This study which investigates the reactivity of a basalt that contains 100% crystalline minerals allows direct assessment of the role of crystallinity on rates. Thirdly, a number of studies have considered the possibility of carbon storage in basaltic rocks (Dessert et al., 2003; McGrail et al., 2006; Marini, 2007; Matter et al., 2007; Goldberg et al., 2008; Kelemen and Matter, 2008; Oelkers et al., 2008; Prigobbe et al., 2009b; Gislason et al., 2010). This process involves dissolution of basalt releasing divalent metal cations such as Ca^{2+} , Mg^{2+} , and Fe^{2+} to solution. These ions can react with dissolved CO_2 and precipitate as carbonate minerals. The rate limiting step for this reaction is commonly assumed to be the release of divalent cations from basalts (e.g. Marini, 2007; Oelkers et al., 2008). Knowledge of basalt dissolution rates is, therefore, paramount to assessing the efficiency of this potential carbon sequestration method. Fourthly, despite the large number of past studies on basalt dissolution coupled to secondary mineral precipitation (Gislason and Eugster, 1987a,b; Gislason et al., 1993; Navarrete-Sitchler and Brantley, 2007; Wu et al., 2007; Gudbrandsson et al., 2008; Hausrath et al., 2009; Schaeff and McGrail, 2009) few studies have investigated basalt dissolution in the dilute aqueous solutions relevant to continental surface weathering processes. Fifthly, because of its high reactivity, chemical weathering of basalt plays a significant role in the global cycle of numerous elements (Gislason et al., 1996, 2006, 2009; Brady and Gislason, 1997; Louvat and Allegre, 1997; Moulton et al., 2000; Dessert et al., 2001; Stefansson and Gislason, 2001; Neaman et al., 2005; Eiriksdottir et al., 2008; Hartmann et al., 2009; Allegre et al., 2010) and may play a significant role in the weathering of the Martian surface (e.g. Hausrath et al., 2008, 2009).

2. THEORETICAL BACKGROUND

The standard state adopted in this study is that of unit activity of pure minerals and H_2O at any temperature and pressure. For aqueous species other than H_2O , the standard state is unit activity of species in a hypothetical 1 m solution referenced to infinite dilution at any temperature and pressure. All thermodynamic calculations reported in this study were performed using the PHREEQC computer code (Parkhurst and Appelo, 1999) together with its phreeqc.dat database to which thermodynamic data have been added for magnesite, siderite, thomsonite, scolecite, mesolite, laumontite, heulandite, analcime, Ca-stilbite, Ca-mordenite, Ca-clinoptilolite, Fe-celadonite, antigorite, amorphous SiO_2 , amorphous FeOOH , amorphous Al(OH)_3 , gibbsite, allophane, and imogolite taken from Gysi and Stefansson (2011).

The crystalline basalt dissolved in this study is comprised of three major mineral phases, the pyroxene augite, the plagioclase labradorite, and a forsteritic olivine in addition to minor amounts of iron oxides. Pyroxene dissolution rates and mechanisms have been reported by Knauss et al. (1993), Brantley and Chen (1995), Oelkers and Schott (2001), Golubev et al. (2005), Dixit and Carroll (2007),

and Daval et al. (2010). Pyroxene dissolution rates decrease continuously with increasing pH and are mildly inhibited by increasing divalent metal cation concentration. Oelkers (2001b) suggested that far-from-equilibrium pyroxene dissolution rates ($r_{+,py}$) can be described using

$$r_{+,py} = k_{py} (a_{\text{H}^+}^2 / a_{\text{M}^{2+}})^{n_{py}} \quad (1)$$

where k_{py} designates a rate constant, a_i corresponds to the activity of the subscripted aqueous species, M^{2+} refers to the divalent metal present in the pyroxene and n_{py} stands for a stoichiometric coefficient equal to 1/8. A large number of studies have provided forsterite dissolution rates (e.g. Grandstaff, 1977; Kuo and Kirkpatrick, 1985; de Leeuw et al., 2000; Pokrovsky and Schott, 2000a,b; Rosso and Rimstidt, 2000; Oelkers, 2001a; Morales and Herbert, 2002; Olsen and Rimstidt, 2008; Prigobbe et al., 2009a; Wimpenny et al., 2010). An equation describing far-from-equilibrium forsterite dissolution rates ($r_{+,fo}$) as a function of pH and solution composition is given by Pokrovsky and Schott (2000b)

$$r_{+,fo} = k_{\text{Si},fo} \cdot \frac{K_{\text{ads}}^* \times a_{\text{H}^+}^{0.5}}{\left(1 + K_{\text{ads}}^* \times a_{\text{H}^+}^{0.5} + \frac{a_{\text{M}^{2+}}^2}{K_{\text{ex}} + a_{\text{H}^+}^4} \right)} \\ + k_{\text{Mg},fo} \quad \{ > \text{MgOH}_2^+ \} \quad (2)$$

where $k_{\text{Si},fo}$ and $k_{\text{Mg},fo}$ correspond to rate constants, K_{ads}^* and K_{ex} refer to equilibrium constants, and $\{ > \text{MgOH}_2^+ \}$ stands for the concentration of the MgOH_2^+ surface species. Most studies of plagioclase dissolution rates have focused on the dissolution rates of the albite end member (e.g. Chou and Wollast, 1984, 1985; Blum and Lasaga, 1991; Stillings and Brantley, 1995). Fewer studies have measured the dissolution rates of more Ca/Al-rich plagioclases (Oxburgh et al., 1994) and anorthite (Oelkers and Schott, 1995). Albite dissolution rates exhibit a synclinal form, where rates decrease with increasing pH at acidic conditions but increase with increasing pH at alkaline conditions. The far-from-equilibrium dissolution rates of $\text{An} \leq 80$ plagioclases ($r_{+,plag}$) can be described using (Oelkers and Schott, 1995; Oelkers, 2001b)

$$r_{+,plag} = k_{\text{plag}} \left[\left(a_{\text{H}^+}^{3n_{\text{plag}}} / a_{\text{Al}^{3+}}^{n_{\text{plag}}} \right) K_T \right] / \left(1 + K_T \left(a_{\text{H}^+}^{3n_{\text{plag}}} / a_{\text{Al}^{3+}}^{n_{\text{plag}}} \right) \right) \quad (3)$$

where k_{plag} refers to a rate constant, n_{plag} is the stoichiometry coefficient equal to 1/3, and K_T stands for an equilibrium constant. This rate behaviour is similar to that of basaltic glass (Oelkers and Gislason, 2001) and other more acidic volcanic glasses (Wolff-Boenisch et al., 2004b). Note that a large body of experimental evidence indicates that n_{py} and n_{plag} in Eqs. (1) and (3) are temperature independent from at least $25 < T < 200$ °C (Oelkers and Schott, 2001; Oelkers, 2001b; Schott et al., 2009). The variation of the rate constants in Eqs. (1)–(3) with temperature can be estimated using the Arrhenius equation given by

$$K_i = A_A \exp(-E_A/RT) \quad (4a)$$

where E_A designates an activation energy, A_A denotes a pre-exponential factor, R stands for the gas constant, and T represents absolute temperature in K. Similarly, in the

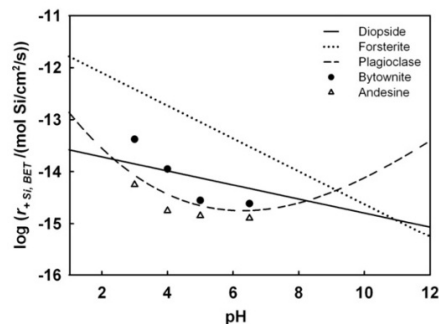


Fig. 1. Si release rates of selected minerals at 25 °C as a function of pH. The bytownite, andesine, forsterite, and diopside elemental rates illustrated in this figure were taken from Oxburgh et al. (1994), Pokrovsky and Schott (2000b), and Knauss et al. (1993), respectively. The plagioclase curve was obtained by multiplying the albite dissolution curve from Chou and Wollast (1985) by 4 to fit the bytownite and andesine rate data. This plagioclase curve was used to represent labradorite dissolution behaviour in this study.

absence of a mechanistic interpretation, apparent activation energies can be generated from measured dissolution rates using

$$r_i = A'_A \exp(-E'_A/RT) \quad (4b)$$

where E'_A designates an apparent activation energy, A'_A denotes a pre-exponential factor.

A comparison of the specific, far-from-equilibrium dissolution rates of diopside, forsterite, and plagioclase normalized to Si is shown as a function of pH at 25 °C in Fig. 1. The data sets chosen for this figure were those that covered the complete range of pH considered in this study. For example, diopside dissolution rates were chosen rather than those of augite to represent the rates of pyroxene dissolution as they are available for the full range of pH considered in this study. The plagioclase rate curve in this figure was obtained by adopting the albite dissolution curve from Chou

and Wollast (1985) and fitting it to the measured dissolution rates for andesine (An_{46}) and bytownite (An_{76}) reported by Oxburgh et al. (1994). This dissolution rate curve was used in this study rather than previously published rate curves for plagioclase (e.g. Palandri and Kharaka, 2004) because these previous curves do not provide a description of the dissolution rates of the intermediate feldspars at alkaline conditions. Plagioclase dissolution rates are slower than those of diopside at pH 4–6 and forsterite at pH < 9. This is in concert with studies of weathering susceptibility of basaltic minerals and glass in soils at mildly acid to neutral pH (Crovier et al., 1992; Gislason et al., 1996); basalt alteration was reported to proceed in the order olivine > pyroxene > plagioclase > sanidine according to Craig and Loughnan (1964), in the order glass > olivine > pyroxene > amphibole > plagioclase > pyroxene > opaque minerals according to Eggleton et al. (1987), and in the order glass, olivine > laihunite > clinopyroxene > orthopyroxene > plagioclase > K-feldspar according to Banfield et al. (1991). Similarly, the alteration of tertiary basalts in Iceland is first characterized by the hydrolysis of olivine and basaltic glass to form mixed-layer chlorite/smectite (Neuhoff, 1999). The latter stage of alteration is dominated by higher pH solutions and the replacement of plagioclase by zeolites and albite at high temperature (Neuhoff, 1999; Fridriksson et al., 2001). In contrast, Nesbitt and Wilson (1992) suggested this alteration order is olivine > glass > plagioclase > clinopyroxene > Fe-Ti-oxides. Taken together, these observations suggest that at acidic to neutral pH crystalline basalt dissolution will exhibit the preferential release of those elements that are present in olivine and pyroxene, such as Mg and Fe, whereas at basic pH crystalline basalt dissolution will release preferentially elements present in plagioclase, such as Ca and Al. The degree to which this is the case can be assessed by the experiments described below.

3. MATERIALS AND METHODS

Crystalline basalt was collected from a basaltic dyke on Stafafell Mountain, SW-Iceland. The sampled dyke had no

Table 1
Composition of crystalline and glassy basalt from the Stafafell Mountain, obtained by XRF analysis.

Sample	SiO ₂	Al ₂ O ₃	Fe ₂ O ₃ ^b	MgO	CaO	Na ₂ O	K ₂ O	TiO ₂	MnO	P ₂ O ₅	LOI	Total
Crystalline	47.9	13.4	12.3	10.0	12.2	1.5	0.3	1.6	0.2	0.2	-0.5	99.1
Glass ^a	48.1	14.6	10.9	9.1	11.8	2.0	0.3	1.6	0.2	0.2		98.8

^a From Oelkers and Gislason (2001).

^b Most iron in the +2 form (Oelkers and Gislason, 2001).

Table 2
Average composition of the major minerals present in the Stafafell crystalline basalt, determined with electron microprobe and reported as weight percentage of oxides.

Sample	#	SiO ₂	TiO ₂	Al ₂ O ₃	FeO	MnO	MgO	CaO	Na ₂ O	K ₂ O	Total
Plagioclase	46	52.10	0.00	28.36	1.68	0.00	0.71	13.57	3.74	0.13	100.28
Olivine	8	39.74	0.03	0.07	15.53	0.21	45.00	0.37	0.01	0.00	100.95
Pyroxene	44	47.74	2.13	5.64	12.10	0.26	12.94	18.85	0.32	0.00	99.97

*Number of analyses.

visible alteration features. The composition of the sampled crystalline basaltic rock is similar to that of mid-ocean ridge basalts (MORB). This basalt was also chosen because dissolution rates for basaltic glass obtained from this site have been previously reported (Oelkers and Gislason, 2001; Gislason and Oelkers, 2003).

The bulk chemical composition of the sampled crystalline basalt was analyzed using a Panalytical PW2404 wavelength-dispersive sequential X-ray fluorescence spectrometer located at the University of Edinburgh. The measured composition is reported in Table 1 and is consistent with $\text{Si}_{1.025}$ $\text{Al}_{0.329}$ $\text{Mg}_{0.310}$ $\text{Fe(III)}_{0.02}$ $\text{Fe(II)}_{0.193}$ $\text{Ca}_{0.273}$ $\text{Na}_{0.061}$ $\text{K}_{0.007}$ $\text{O}_{3.394}$. This composition is nearly identical to that of Stafafell basaltic glass (Oelkers and Gislason, 2001; Gislason and Oelkers, 2003). The mineralogical composition of the basalt was determined by point counting. Four hundred points were counted from thin sections of the basalt; this analysis shows the basalt to contain 41.3 vol.% plagioclase (plag), 34.0 vol.% pyroxene (py), 15.8 vol.% olivine (ol), 4.7 vol.% iron oxides, and 4.2 vol.% glass. Such glass is likely Na and Si-rich compared to the bulk rock (Meyer and Sigurdsson, 1978). The volcanic glass was found in the samples collected close to the edge of the dyke, so experiments were performed on samples collected from the dyke centres. No volcanic glass was observed in the samples dissolved in this study by scanning electron microscope (SEM) imaging. The mineral composition of the basalt was also determined using a Stoe Stadi P Transmission XRD. Scans were run from 5° to 109.99° with a 0.05° step. Mineral abundance was determined by XRD peak intensity. This analysis suggests that the relative volume proportion of plag:py:ol is 44:39:17.

The chemical composition of the minerals in the crystalline basalt was determined from standard wavelength dispersive techniques using a JEOL Superprobe JSL 8200 located at the University of Copenhagen. These analyses were performed using an acceleration voltage of 15 kV, a

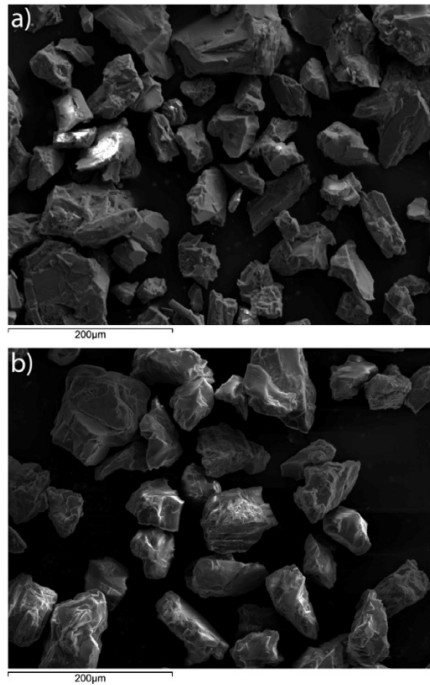


Fig. 3. SEM photomicrographs of the crystalline basalt. (a) The crystalline basalt before dissolution experiments, (b) the basalt after it was dissolved in dissolution experiments at pH 10 at 25, 50, and 75 °C for total of 623 h. No secondary phases are observed and the edges seem to be somewhat rounded by the dissolution.

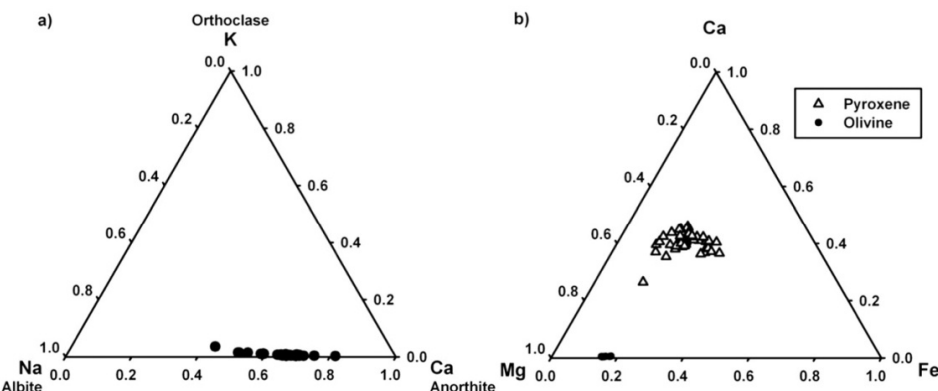


Fig. 2. Mineralogical compositions of the minerals in the basalt used in presented study plotted in ternary diagram. (a) The compositions of 46 analyzed plagioclase grains, (b) the compositions of 44 analyzed pyroxene and 8 analyzed olivine grains. Chemical analyses were performed by microprobe.

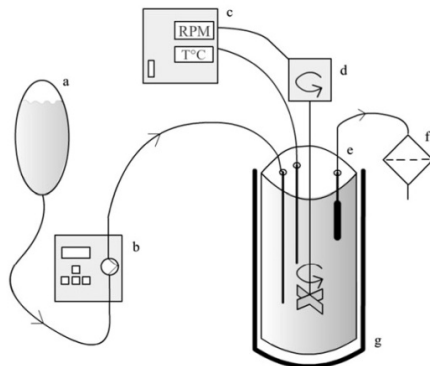


Fig. 4. Experimental design: (a) inlet solution container, (b) high pressure liquid chromatography (HPLC) pump, (c) temperature and rotation speed control, (d) stirring motor, (e) 300 mL Ti-reactor from Parr™ Instrument equipped with, from left, fluid inlet tube, thermocouple, magnetic stirrer, and fluid outlet fixed with a 2 μm Ti filter, (f) outlet solution goes through 0.2 μm cellulose acetate filter before sampling and ICP analysis, (g) thermal insulation and furnace.

beam current of 15 nA and a beam diameter of 2 μm . Natural and synthetic minerals and glasses were used as standards to check for potential drift. The resulting mineralogical composition of the basalt is given in Table 2 and is displayed graphically in Fig. 2. In total, 98 grains were

analyzed, 46 plagioclase, 8 olivine, and 44 pyroxene. The microprobe data show that the plagioclase is of labradoritic composition (An_{65}), the olivine has a forsterite component of Fo_{85} and the pyroxene is of augite composition. The measured density of the crystalline basalt is 3.03 g/cm^3 , in agreement with a calculated density of 3.11 g/cm^3 using the density of each mineral and its volume in the crystalline basalt.

The crystalline basalt was dried at room temperature for several days before it was ground using a jaw crusher. The finely grained material was dry sieved to obtain the 45–125 μm size fraction. This size fraction was subjected to gravitational settling to remove ultra-fine particles and subsequently cleaned ultrasonically five times in deionized water and then in acetone. The resulting powder was oven-dried at 50 °C for several days. An SEM image of the resulting crystalline basalt powder is shown in Fig. 3. The surfaces are free of fine particles. Most individual grains consist of single minerals, although some multi-mineral grains are evident. The specific surface area of the cleaned and dried 45–125 μm size fraction was determined to be $7030 \text{ cm}^2/\text{g}$ via 11 point krypton adsorption using a Quantachrome Gas Sorption system. The geometric surface area of the powder was calculated using $A_{\text{geo}} = 6/(\rho * d_{\text{eff}})$ (Tester et al., 1994) where ρ designates the particle density (3.03 g/cm^3) and d_{eff} represents the effective particle diameter. The number 6 is based on the assumption that grains have a smooth spherical shape. This calculation yields a geometric surface area of $246 \text{ cm}^2/\text{g}$. The ratio between BET and geometric surface area ($A_{\text{BET}}/A_{\text{geo}}$) is the roughness factor, which equals 28.6.

Table 3
Initial conditions and inlet solution compositions for all experiments.

Experiment No.	Experiments series	pH	HCl (mmol/kg)	NH_4OH (mmol/kg)	NH_4Cl (mmol/kg)	Mass of basalt (g)
02-05	A	2	33.46	0	0	4.02
03-05	A	3	3.35	0	8.97	4.02
03-25	B	3	3.35	0	8.97	2.07
03-50	C	3	3.35	0	8.97	3.30
04-05	A	4	0.33	0	9.91	4.02
04-25	D	4	0.33	0	9.91	3.99
04-50	D	4	0.33	0	9.91	3.99
04-75	D	4	0.33	0	9.91	3.99
05-05	E	5	0.03	0	9.91	5.19
05-25	E	5	0.03	0	9.91	5.19
05-50	E	5	0.03	0	9.91	5.19
05-75	E	5	0.03	0	9.91	5.19
06-25	F	6	0	0	9.91	6.00
07-50	F	7	0	0	9.91	6.00
07-75	F	7	0	0	9.91	6.00
09-05	G	9	0	5.04	9.98	4.51
09-25	G	9	0	5.04	9.98	4.51
09-50	H	9	0	5.04	9.98	5.05
09-75	H	9	0	5.04	9.98	5.05
10-25	I	10	0	50.04	9.85	4.38
10-50	I	10	0	50.04	9.85	4.38
10-75	I	10	0	50.04	9.85	4.38
11-05	J	11	0	502.04	8.96	4.50
11-25	J	11	0	502.04	8.96	4.50
11-50	K	11	0	502.04	8.96	4.50
11-75	K	11	0	502.04	8.96	4.50

Crystalline basalt dissolution experiments were performed at pH from 2 to 11 in a Parr™ mixed flow reactor system, as illustrated in Fig. 4. This system consists of a 300 mL titanium reactor with external temperature and stirring controls. Reactive fluids were injected into this reactor via a high pressure liquid chromatography (HPLC) pump allowing a constant flow rate from 0.5 to 4.5 mL/min. The inlet fluids were made of deionized water and Merck analytical grade NH₄Cl, HCl, and NH₄OH and had an ionic strength of 0.01 mol/kg. The compositions of all inlet solutions used in this study are reported in Table 3. The inlet solutions with neutral and alkaline pH were initially bubbled with N₂ and then continuously kept under a N₂ atmosphere to prevent CO₂ dissolution into this fluid. The reactor was cleaned thoroughly, assembled, and run

for at least 24 h with deionized water and then for another 24 h with the inlet solution to rinse the tubing and clean the reactor prior to each experiment. At the end of this cleaning cycle an outlet fluid sample was taken for chemical analysis.

Experiments were initiated by placing between 1 and 5 g of dry basalt powder into the reactor. The reactor was then filled with the inlet solution, sealed, and placed in a furnace jacket. Reactive fluid flow, temperature, and stirring rates were adjusted to desired settings. The fluid/basalt powder mixture was continuously stirred at approximately 400 rpm. Gislason and Oelkers (2003) observed that rotation speeds in excess of 325 rpm was sufficient to maintain surface reaction control of basaltic glass dissolution at pH 3.3. Outlet solutions were regularly sampled, filtered using 0.2 µm cellulose acetate filters, and then acidified with

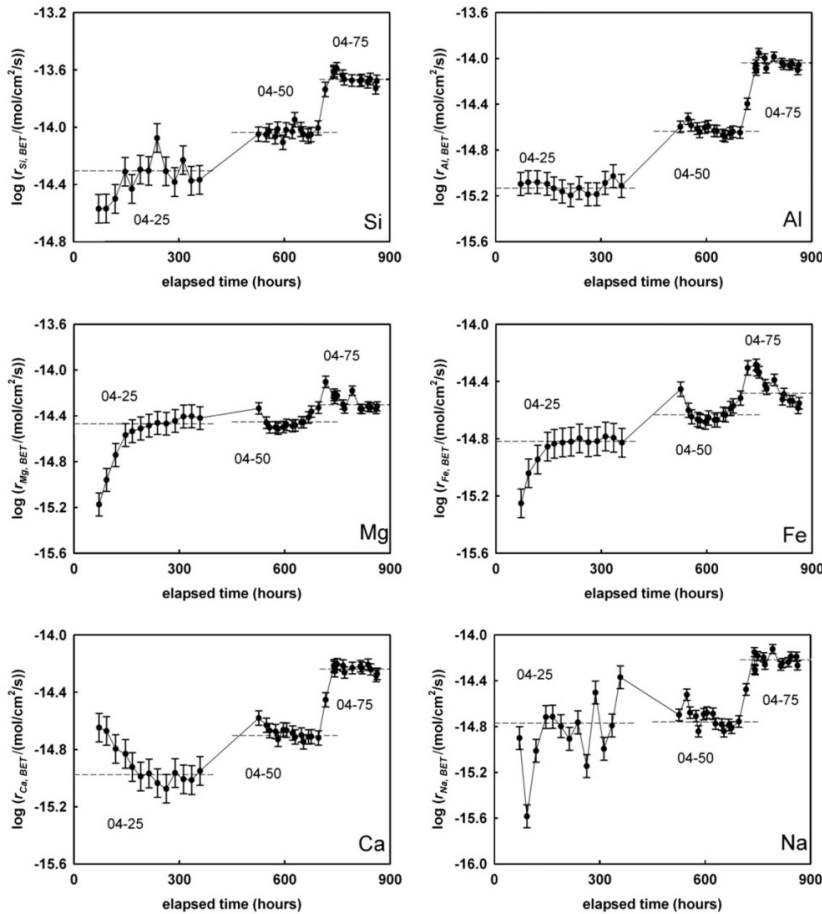


Fig. 5. Elemental release rates, $r_{i,BET}$ during experiments performed at pH 4 and 25, 50, and 75 °C as part of a single experimental series. The symbols correspond to measured $r_{i,BET}$ whereas the dashed lines correspond to their steady state values.

concentrated supra-pure HNO₃ prior to their analysis for Si, Mg, Na, Al, Fe, and Ca by ICP-OES. As was the case for a number of recent mineral dissolution rate studies (e.g. Flaathen et al., 2010; Saldi et al., 2010; Oelkers et al., 2011) experiments in this study were run in series. Each series consisted of a set of dissolution experiments performed on the same basalt powder. The experiments performed in each experimental series are listed in Table 3. Each experiment was run until a constant Si release rate was observed. Steady-state was confirmed by at least three consecutive outlet solution Si measurements performed on samples taken over a period of at least 10 residence times (the residence time is the ratio of the reactor volume to the fluid flow rate). This steady-state criterion was met for all experiments. After reaching constant Si release rates, temperature, flow rate or inlet fluid compositions were adjusted to new values and a new experiment began. Each experimental series was stopped before 5% of the initial basalt was dissolved.

4. RESULTS

Twenty six crystalline basalt dissolution experiments were performed in this study. The reactive fluid concentrations of Si, Al, Mg, Fe, Ca, and Na were regularly measured. These concentrations were used to calculate element release rates ($r_{i,j}$) using

$$r_{i,j} = \frac{C_i FR}{A_j m} \quad (5)$$

where c_i represents the concentration of the i th element in the outlet fluid, FR designates the fluid flow rate, A_j and m refer to the specific surface area and mass of the solid in the reactor, respectively. The surface area used throughout this study was obtained from BET analysis (A_{BET}). Each dissolution experiment was run until steady-state rates were attained. Steady-state Si and Al release rates were rapidly attained in all experiments as illustrated by the temporal evolution of $r_{i,BET}$ values of experimental series 04-25 to 04-75 shown in Fig. 5. This series included experiments at three distinct steady-state conditions at pH 4 and 25, 50, and 75 °C. Mg and Fe release rates appear to take longer to attain steady-state; this may be a consequence of divalent metal-proton exchange reactions occurring on the mineral surfaces (cf. Oelkers et al., 2009).

A summary of all measured steady-state $r_{i,BET}$ is given in Table 4 and are shown as a function of pH in Fig. 6. These rates exhibit the characteristic dissolution behaviour exhibited by aluminosilicate minerals; rates decrease with increasing pH at acidic conditions and increase with increasing pH at basic conditions. The dashed curves in Fig. 6 correspond to $r_{i,BET}$ from basaltic glass for a constant total dissolved Al concentration of 10⁻⁵ mol/kg as reported by Gislason and Oelkers (2003). The aqueous Al³⁺ activity is close to that of the experiments performed in this study. Rates measured in this study are compared to those for glass dissolution reported by Gislason and Oelkers (2003) because they were performed on glass samples collected from the same site, having the same chemical composition, age, and weathering history as the crystalline basalts

Table 4
Experimental results of Staphell crystalline basalt dissolution experiments.

Experiment No.	Temperature (°C)	Samples ^a #	pH ^b	Flow rate ^b (g/min)	Run time (h)	C _{Si} (mol/kg × 10 ⁻⁶)	C _{Al} (mol/kg × 10 ⁻⁶)	C _{Ca} (mol/kg × 10 ⁻⁶)	C _{Fe} (mol/kg × 10 ⁻⁶)	C _{Mg} (mol/kg × 10 ⁻⁶)	log $r_{Si,BET}$ (mol/cm ² /s)
02-05	5	8	2.04	4.39	55.0	14.23	3.21	2.69	9.29	13.35	13.44
03-05	5	8	3.05	2.71	155.0	4.11	0.85	1.49	2.71	4.03	14.12
03-25	25	11	2.94	1.34	481.5	9.92	1.02	1.72	4.07	10.85	13.77
03-50	50	9	3.16	3.13	166.0	82.30	5.40	6.87	37.75	88.63	12.76
04-05	5	11	4.06	1.61	225.0	1.01	0.55	1.62	0.59	0.70	15.02
04-25	25	13	4.13	1.26	359.0	6.15	1.02	1.70	1.86	3.96	14.31
04-50	50	15	4.09	1.67	357.5	10.02	2.57	2.23	2.64	3.93	14.03
04-75	75	13	4.04	4.46	146.5	8.43	3.40	2.21	1.42	1.99	13.67
05-05	5	6	5.00	0.53	224.0	1.33	0.88	2.16	1.18	0.42	15.50
05-25	25	5	5.03	0.53	252.5	3.02	0.38	1.47	0.90	1.13	15.13
05-50	50	6	5.14	0.54	240.0	9.00	0.25	2.46	0.51	0.95	14.76
05-75	75	5	5.65	0.52	411.5	29.05	4.05	8.17	0.25	1.68	14.16
06-25	25	10	5.86	0.54	886.0	1.95	0.38	0.59	0.29	0.37	15.45
07-50	50	6	6.89	0.54	261.0	6.09	0.69	1.41	0.10	0.31	14.95
07-75	75	5	6.59	0.54	190.0	35.22	0.66	10.13	n.g.	1.20	14.13
09-05	5	8	9.24	0.87	431.0	1.43	0.43	0.33	0.13	0.20	15.26
09-25	25	5	9.22	0.84	190.0	2.78	0.81	0.57	0.19	0.37	14.94
09-50	50	6	9.28	0.53	224.0	15.24	4.65	2.81	0.13	1.14	14.48
09-75	75	9	9.27	0.51	397.0	37.27	11.21	9.55	0.14	5.50	14.06
10-25	25	7	10.10	1.16	284.0	5.60	0.77	0.99	0.21	0.32	14.39
10-50	50	6	10.12	2.65	201.0	11.45	0.67	1.44	0.41	0.92	13.75
10-75	75	5	10.09	2.97	138.0	19.04	4.22	3.71	0.11	1.94	13.53
11-05	5	4	10.74	1.94	75.0	6.39	0.59	9.77	0.01	0.12	14.24
11-25	25	4	11.01	2.04	72.5	10.58	1.37	4.47	0.01	0.04	13.95
11-50	50	4	10.76	2.20	75.0	12.85	3.41	1.61	0.01	0.39	13.89
11-75	75	4	10.96	3.23	72.5	31.71	11.67	5.14	0.02	0.84	13.27

^a Number of measured rates.

^b Average value of all measured samples.

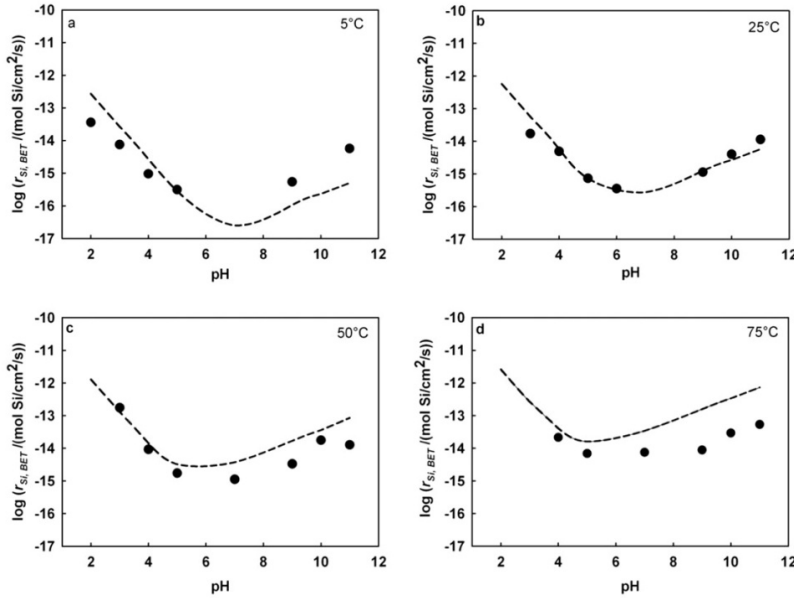


Fig. 6. Steady-state Si release rates versus pH at the indicated temperatures. The symbols correspond to measured $r_{\text{Si},\text{BET}}$ from the crystalline basalt while the dashed curves represent $r_{\text{Si},\text{BET}}$ from basaltic glass dissolution calculated using the equation reported by Gislason and Oelkers (2003) and an aqueous Al concentration of 10^{-5} mol/kg.

dissolved in this study. Measured $r_{\text{Si},\text{BET}}$ for the crystalline basalts are in general equal to or lower than those of the corresponding glass. The only exception is the 5 °C experiments at high pH where crystalline basalt dissolution appears to be slightly faster than that of basaltic glass. The observation that crystalline basalt dissolution rates are in general slower than those of basaltic glass is consistent with the conclusions of Wolff-Boenisch et al. (2006).

The ratio of the release rate of each element relative to Si normalized to the corresponding ratio in the dissolving solid is displayed as a function of pH in Fig. 7. If this ratio is equal to one, the release rate of the element is stoichiometric relative to Si, if it is greater than one the element is preferentially released relative to Si, while if it is less than one the element is preferentially retained in the solid phase relative to Si. Mg and Fe tend to be preferentially released from the basalt at acid conditions and preferentially retained at higher pH. Ca is somewhat retained by the solid phase at low pH, but exhibits close to stoichiometric release relative to Si at circum neutral pH. With few exceptions, Al is retained by the solid phase at all temperatures and pH conditions considered in this study.

Steady-state outlet fluid compositions were used to calculate the saturation state of primary and potential secondary mineral phases in all experiments. The results of these calculations are shown in Annex A. The pH 3 outlet fluids were calculated to be undersaturated with respect to all pri-

mary and potential secondary minerals while the neutral to high pH outlet fluids were calculated to be supersaturated with respect to clinopyroxene, goethite, hematite, and gibbsite. Note however that the results shown in Annex A were calculated assuming the fluids were in equilibrium with atmospheric O₂, which is likely an overestimate of the oxygen content of these fluids which were purged with N₂ prior to their injection into the reactors. As such the saturation state of oxidized iron bearing minerals (e.g. hematite and goethite) is likely overestimated in these calculations. No secondary minerals were observed in the outlet filter or on the solids recovered following the experiments by SEM analysis suggesting that these oxidized iron minerals were in fact undersaturated in the reactive fluids.

5. DISCUSSION

5.1. Elemental release rates and CO₂ storage

The results in this study illustrate the contrasting dissolution behaviour of a multi-mineral silicate rock versus its corresponding glass. Si release from both crystalline and glassy basalt exhibits a similar pH dependency, though at basic pH Si appears to be released somewhat faster from glass at 5 °C but slower at 75 °C (Fig. 6). Furthermore, the Mg and Fe release rates decrease continuously with increasing pH (see Fig. 8) while those of Si and Ca display

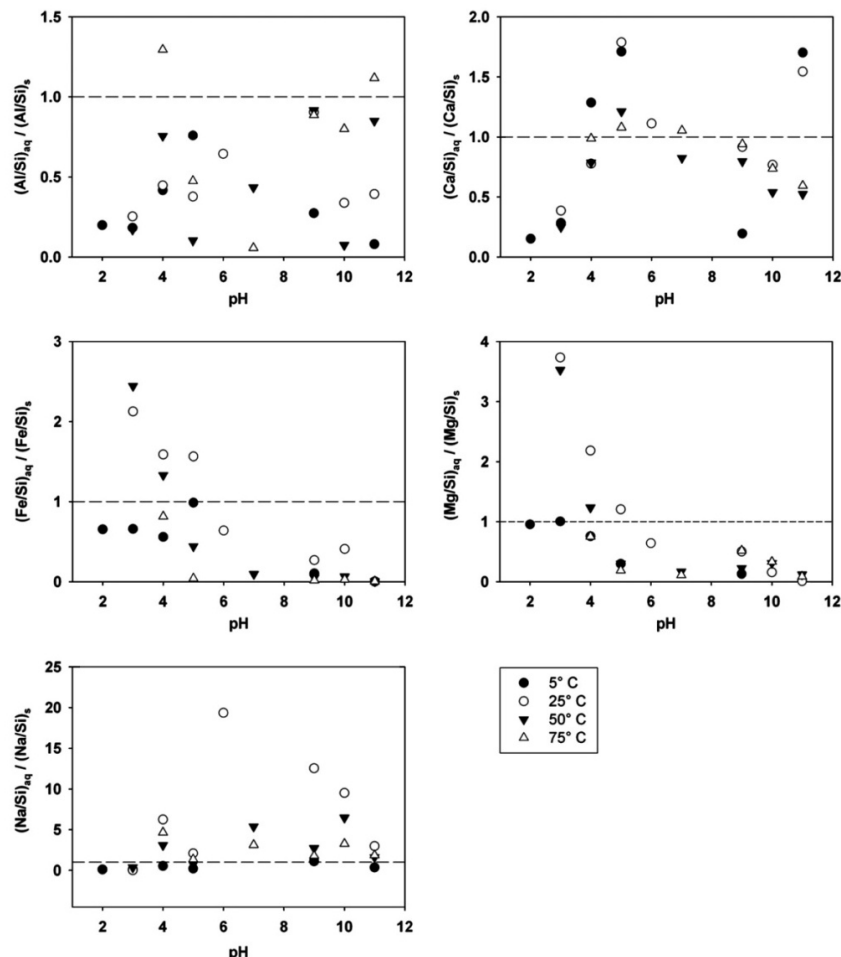


Fig. 7. The relative steady-state release of elements to aqueous solution divided by the corresponding element ratio of crystalline basalt plotted as a function of pH. Filled circles, open circles, filled triangles, and open triangles correspond to rates measured at 5, 25, 50, and 75 °C, respectively. The dashed line corresponds to stoichiometric release rates of the elements.

a synclinal shaped pH dependence. It seems likely that the distinct behaviour of crystalline basalt stems from the contrasting dissolution behaviours of its constituent minerals. The bulk of the Mg and Fe in the crystalline basalt are contained in olivine and pyroxene (see Table 2). In contrast to the dissolution behaviour of basaltic glass, the dissolution rates of olivine and pyroxene decrease monotonically with increasing pH (see Fig. 1). The effect of the distinct mineral dissolution behaviour also affects strongly the release rates of calcium. As can be deduced from Fig. 1, crystalline basalt dissolution at acid pH is dominated by the dissolution

of olivine, which has a specific dissolution rate at least one order of magnitude higher than that of diopside and Ca-rich plagioclase. Olivine is Mg and Fe rich but Ca poor. As a result Ca tends to be retained by the solid at acid conditions.

The release of divalent metals to solution from silicates is an essential and perhaps rate-limiting step for the successful carbonatization of CO₂ during carbon storage efforts (cf. Oelkers et al., 2008; Schaeff and McGarry, 2009; Gislason et al., 2010; Schaeff et al., 2010). A significant observation presented above is that the relative

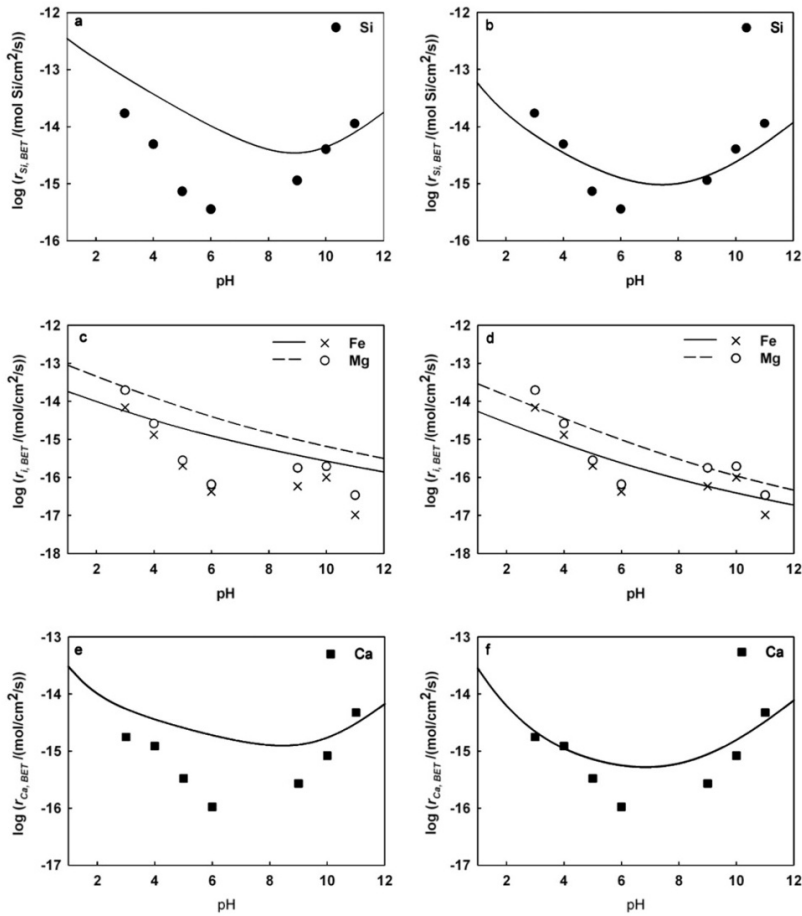


Fig. 8. Element release rates from dissolving crystalline basalts at 25 °C as a function of pH. The symbols correspond to measured release rates. The curves in plots a, c, and e represent $r_{i,\text{BET}}$ calculated assuming the reactive surface area of each mineral is proportional to its volume fraction, whereas the curves in plots (b, d, and f) stand for $r_{i,\text{BET}}$ calculated by fitting the reactive surface area of each mineral to the measured element release rates – see text for further clarification.

divalent metal release rates from crystalline basalts vary significantly with pH. The rate of Ca release from dissolving crystalline basalt as a fraction of the corresponding total divalent metal release rate at 25 °C is shown in Fig. 9. At pH 2–3 only 6–20% of the divalent metals released from basalt are calcium. At these conditions the divalent metal flux from crystalline basalt dissolution is dominated by Mg and Fe release. The fraction of Ca released increases continuously with rising pH. At pH 11, more than 80% of the divalent metal flux is Ca. Since CO₂ charged waters are acidic, crystalline basalt dissolution will release far more Mg and Fe than Ca to solution,

favouring the formation of magnesite, siderite, and mixed Fe–Mg carbonates rather than calcite. This assumption is corroborated by observations of secondary carbonate formation during the alteration of basaltic lavas by CO₂-rich fluids in West Greenland (Rogers et al., 2006). Carbonates formed in this system in the initially CO₂-rich, low pH fluids are Fe and Mg-rich. Only late stage carbonates are Ca-rich. The degree to which such Mg-rich carbonates form in other systems, however, depends on their nucleation and growth rates, which may be sluggish, compared to that of calcite (Saldi et al., 2009).

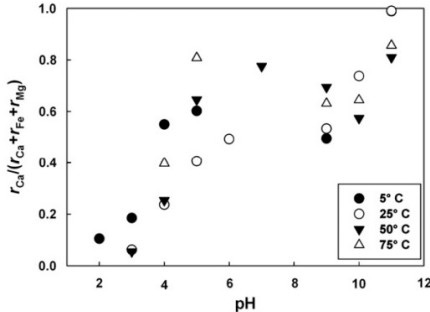


Fig. 9. Ca release rates divided by the sum of the release rates of the divalent cations from crystalline basalt at all pH and temperatures. Filled circles, open circles, filled triangle and open triangles correspond to rates measured at 5, 25, 50, and 75 °C, respectively.

5.2. Modelling element release rates from mineral dissolution rates

One of the great challenges in geochemistry is the successful prediction of chemical mass transfer rates during water-mineral interaction. Element release rates from the crystalline basalt dissolution experiments performed in this study are dominated by the dissolution of its three major minerals: olivine, pyroxene, and plagioclase. In the absence of secondary mineral precipitation and contributions from the dissolution of glass and minor minerals, the release rate of the *i*th element from crystalline basalt ($r_{i,j}$) can be approximated by

$$r_{i,j} = \sum_{k=0}^N \frac{A_{j,k}}{A_j} v_{i,k} r_{j,k} \\ = \frac{A_{j,\text{plag}}}{A_j} v_{i,\text{plag}} r_{j,\text{plag}} + \frac{A_{j,\text{ol}}}{A_j} v_{i,\text{ol}} r_{j,\text{ol}} + \frac{A_{j,\text{py}}}{A_j} v_{i,\text{py}} r_{j,\text{py}} \quad (6)$$

where $r_{j,k}$ refers to the dissolution rate of the *k*th mineral (plag, ol, py) normalized to the *j*th surface area, $v_{i,k}$ designates the stoichiometric number of the *i*th element in the *k*th mineral, $A_{j,k}$ symbolizes the *j*th specific surface area of the *k*th mineral and A_j is the overall surface area. Eq. (6) was used in the present study to model measured steady-state element release rates from crystalline basalt by adopting the 25 °C dissolution rates as a function of pH of olivine reported by Pokrovsky and Schott (2000b), those of diopside reported by Knauss et al. (1993), to correspond to that of augite, and those of plagioclase taken from Fig. 1. Stoichiometric coefficients in Eq. (6) were taken from the mineral compositions listed in Table 2. To the first approximation, it seems reasonable to assume that the relative surface area of the three minerals comprising the crystalline basalt is proportional to the relative volume percent of each mineral in the dissolving basalt (e.g. 17%, 39%, and 44% for ol, py, and plag, respectively). The results of this calculation are plotted as curves and compared with measured element release rates in Fig. 8a, c, and e. Although these calculations exhibit the correct rate trends with pH, calculated steady-state release rates are approximately one order of magnitude faster than (a) measured Si release rates at acid

Table 5
Apparent activation energies (E'_a) obtained from this study. # symbolizes the number of steady-state rates used in the regression for E'_a and R^2 stands for the correlation coefficient of a linear regression through these rates.

	E'_a (kJ/mol)	#	R^2
pH 3	54.1	3	0.93
pH 4	33.8	4	0.96
pH 5	35.2	4	0.98
pH 9	33.9	4	0.99
pH 10	35.0	3	0.95
pH 11	24.2	6	0.98

to neutral pH, (b) measured Mg and Fe release rates at all pH, and (c) measured Ca release rates at intermediate pH. It should be noted that the uncertainties in the rates adopted to perform this calculation are significant and include such factors as variable mineral compositions and the effect of reactive fluid composition other than pH on rates. Differences between measured and computed rates such that observed in Fig. 8a, c, and e, are therefore, likely within the margin of error in the calculations. It seems unlikely that the difference between the curves and data points in Fig. 8 stem from contributions from the dissolution of minor phases (e.g. interstitial glass) as measured rates are slower than those computed using Eq. (6).

An improved fit of measured element release rates was obtained by adjusting the relative surface areas of the minerals to 2.8% olivine, 13.9% pyroxene, and 83.3% plagioclase. The results of this fit are compared to measured steady-state element release rates in Fig. 8b, d, and f. This revised fit reproduces the measured element release rates within 0.5 log units at all pH. There are several reasons why the relative surface area of the minerals of the best data fit do not match the relative volume fraction of the minerals. First, pyroxene may be close to equilibrium (see the calculated saturation state of various minerals at steady-state in Annex A); rates slow as fluids approach equilibrium with respect to dissolving mineral phases (cf. Schott and Oelkers, 1995). Secondly, the grinding of the crystalline basalt may have created reactive surfaces in a heterogeneous way among the mineral phases. This may lead to a higher relative surface area for plagioclase, which is commonly comprised of fine-grained exsolution lamellae.

Apparent activation energies of Si release from crystalline basalt dissolution calculations using Eq. (4b) and the rates listed in Table 4 are near to 30 kJ/mol at pH ≥ 4 but increase to 54 kJ/mol at pH 3 (see Table 5). These values are close to the activation energies reported in the literature for basaltic glass; Gislason and Oelkers (2003) reported an activation energy for basaltic glass dissolution of 25.5 kJ/mol and Wolff-Boenisch et al. (2004a) reported activation energies of 27 kJ/mol at pH 4 and 41 kJ/mol at pH 10.6.

6. CONCLUSIONS

The results described above illustrate the contrasting behaviour of crystalline basalt versus basaltic glass. Although steady-state $r_{\text{Si,BET}}$ of crystalline basalts and basal-

tic glass exhibit similar pH dependencies the release rates of the divalent metal cations differ significantly. Because of the distinct dissolution behaviour of its constituent minerals, Mg and Fe are preferentially removed from crystalline basalt at acid conditions, whereas Ca is preferentially removed at basic conditions. These observations suggest contrasting alteration behaviours of glassy versus crystalline basalt both during carbon sequestration and natural processes.

Element release rates estimated from the sum volume fraction normalized dissolution rates of plagioclase, pyroxene, and olivine are within one order of magnitude of those measured in this study and reproduce the distinct behaviour of the major elements. The degree to which this is an acceptable approximation of the dissolution behaviour of a crystalline rock most certainly depends on the system and the required accuracy. The critical parameter of such estimates, $\frac{A_{\text{rel}}}{A}$, the relative reactive surface area of each mineral that is in contact with the reactive fluid, is impossible to predict *a priori* at present. Thus, although element release rate estimates based on the assumption that reactive surface area of individual minerals is proportional to its volume fraction in a rock can only present a crude approximation, it may provide some insight into dissolution behaviour of multi-phase rocks.

ACKNOWLEDGMENTS

The authors thank our friends and colleagues, including Helgi A. Alfredsson, Gabrielle J. Stockmann, Alexander P. Gysi, Iwona Monika Galeczka, Mahnaz Rezvani Khalilabad, Kiflom Gebrehiwot, Eyðir Salome Þirkssdóttir, Andrí Stefánsson, and Niels Óskarsson at the University of Iceland, Hólmfríður Sigurðardóttir, Einar Gunnlaugsson, Ingvi Gunnarsson, Edda Sif Aradóttir, and Bergur Sigfusson at Reykjavík Energy, Ivan Sanchez, Caroline Hem, and Susan Stipp at the NanoGeo Center at the University of Copenhagen, and Alfons Berger at the University of Copenhagen. This study was funded by The Environmental Fund of Reykjavík Energy through the CARB-FIX project, the European Community through the MIN-GRO Research and Training Network (MRTN-CT-2006-035488) and Delta-Min (Mechanisms of Mineral Replacement Reactions; Grant PITN-GA-2008-215360) and the Nordic Mineralogy Network.

APPENDIX A. SUPPLEMENTARY DATA

Supplementary data associated with this article can be found, in the online version, at doi:10.1016/j.gca.2011.06.035.

REFERENCES

- Allegre C. J., Louvat P., Gaillardet J., Maynadier L., Rad S. and Capmas F. (2010) The fundamental role of island arc weathering in the oceanic Sr isotope budget. *Earth Planet. Sci. Lett.* **292**, 51–56.
- Banfield J. F., Jones B. F. and Veblen D. R. (1991) An AEM TEM study of weathering and diagenesis, Abert Lake, Oregon. I: Weathering reactions in the volcanics. *Geochim. Cosmochim. Acta* **55**, 2781–2793.
- Blum A. E. and Lasaga A. C. (1991) The role of surface speciation in the dissolution of albite. *Geochim. Cosmochim. Acta* **55**, 2193–2201.
- Blum A. E. and Stillings L. L. (1995) Feldspar dissolution kinetics. In *Chemical Weathering Rates of Silicate Minerals* (eds. A. F. White and S. L. Brantley). Mineralogical Society of America, Washington, DC.
- Brady P. V. and Gislason S. R. (1997) Seafloor weathering controls on atmospheric CO₂ and global climate. *Geochim. Cosmochim. Acta* **61**, 965–973.
- Brantley S. L. and Chen Y. (1995) Chemical weathering rates of pyroxenes and amphiboles. *Rev. Min.* **31**, 119–172.
- Chou L. and Wollast R. (1984) Study of the weathering of albite at room-temperature and pressure with a fluidized-bed reactor. *Geochim. Cosmochim. Acta* **48**, 2205–2217.
- Chou L. and Wollast R. (1985) Steady-state kinetics and dissolution mechanisms of albite. *Am. J. Sci.* **285**, 963–993.
- Craig D. C. and Loughnan F. C. (1964) Chemical and mineralogical transformations accompanying the weathering of basic volcanic rocks from New South Wales. *Aust. J. Soil Res.* **2**, 218–234.
- Corvisier J. L., Honnorez J., Fritz B. and Petit J. C. (1992) Dissolution of subglacial volcanic glasses from Iceland: laboratory study and modelling. *Appl. Geochim.* **7**, 55–81.
- Daval D., Hellmann R., Corvisier J., Tisserand D., Martinez I. and Guyot F. (2010) Dissolution kinetics of diopside as a function of solution saturation state: macroscopic measurements and implications for modeling of geological storage of CO₂. *Geochim. Cosmochim. Acta* **74**, 2615–2633.
- de Leeuw N. H., Parker S. C., Catlow C. R. A. and Price G. D. (2000) Modelling the effect of water on the surface structure and stability of forsterite. *Phys. Chem. Miner.* **27**, 332–341.
- Dessert C., Dupré B., François L. M., Schott J., Gaillardet J., Chakrapani G. and Bajpai S. (2001) Erosion of Deccan Traps determined by river geochemistry. Impact on global climate and ⁸⁷Sr/⁸⁶Sr ratio of seawater. *Earth Planet. Sci. Lett.* **188**, 459–474.
- Dessert C., Dupré B., Gaillardet J., François L. M. and Allegre C. J. (2003) Basalt weathering laws and the impact of basalt weathering on the global carbon cycle. *Earth Planet. Sci. Lett.* **188**, 459–474.
- Dixit S. and Carroll S. A. (2007) Effect of solution saturation state and temperature on diopside dissolution. *Geochim. Trans.* **8**, 3.
- Eggerton R. A., Foudoulis C. and Varkeysser D. (1987) Weathering of basalt – changes in rock chemistry and mineralogy. *Clays Clay Miner.* **35**, 161–169.
- Eiriksdottir E. S., Louvat P., Gislason S. R., Oskarsson N. and Hardottir J. (2008) Temporal variation of chemical and mechanical weathering in NE Iceland: evaluation of a steady-state model of erosion. *Earth Planet. Sci. Lett.* **272**, 78–88.
- Flaathen T. K., Gislason S. R. and Oelkers E. H. (2010) The effect of aqueous sulphate on basaltic glass dissolution rates. *Chem. Geol.* **277**, 345–354.
- Fridriksson T., Neuhoff P. S., Arnórsson S. and Bird D. K. (2001) Geological constraints on the thermodynamic properties of the stilbite stellerite solid solution in low-grade metabasalts. *Geochim. Cosmochim. Acta* **65**, 3993–4008.
- Gislason S. R., Arnórsson S. and Armannsson H. (1996) Chemical weathering in southwest Iceland: effects of runoff, age of rocks and vegetative/glacial cover. *Am. J. Sci.* **296**, 837–970.
- Gislason S. R. and Eugster H. P. (1987a) Meteoric water basalt interactions. 2: A field-study in NE Iceland. *Geochim. Cosmochim. Acta* **51**, 2841–2855.
- Gislason S. R. and Eugster H. P. (1987b) Meteoric water basalt interactions. 2: A laboratory study. *Geochim. Cosmochim. Acta* **51**, 2827–2840.
- Gislason S. R. and Oelkers E. H. (2003) Mechanism, rates, and consequences of basaltic glass dissolution. II: An experimental

- study of the dissolution rates of basaltic glass as a function of pH and temperature. *Geochim. Cosmochim. Acta* **67**, 3817–3832.
- Gislason S. R., Oelkers E. H., Eiriksdottir E. S., Kardjilov M. I., Gisladottir G., Sigfusson G., Snorrason A., Elefsen S., Hardardottir J., Torssander P. and Oskarsson N. (2009) Direct evidence of the feedback between climate and weathering. *Earth Planet. Sci. Lett.* **277**, 213–222.
- Gislason S. R., Oelkers E. H. and Snorrason Á. (2006) The role of river suspended material in the global carbon cycle. *Geology* **34**, 49–52.
- Gislason S. R., Veblen D. R. and Livi K. J. T. (1993) Experimental meteoric water basalt interactions: characterization and interpretation of alteration products. *Geochim. Cosmochim. Acta* **57**, 1459–1471.
- Gislason S. R., Wolff-Boenisch D., Stefansson A., Oelkers E. H., Gunnlaugsson E., Sigurdardottir H., Sigfusson G., Broecker W. S., Matter J. M., Stute M., Axelsson G. and Fridriksson T. (2010) Mineral sequestration of carbon dioxide in basalt: a pre-injection overview of the carbfix project. *Int. J. Greenhouse Gas Control* **4**, 537–545.
- Goldberg D. S., Takahashi T. and Slagle A. L. (2008) Carbon dioxide sequestration in deep-sea basalt. *Proc. Natl. Acad. Sci. USA* **105**, 9920–9925.
- Golubev S. V., Pokrovsky O. S. and Schott Jaque (2005) Experimental determination of the effect of dissolved CO₂ on the dissolution kinetics of Mg and Ca silicates at 25 °C. *Chem. Geol.* **217**, 227–238.
- Grandstaff D. E. (1977) Some kinetics of forsterite olivine dissolution. *Trans. Am. Geophys. Union* **58**, 539.
- Gudbrandsson S., Wolff-Boenisch D., Gislason S. R. and Oelkers E. H. (2008) Dissolution rates of crystalline basalt at pH 4 and 10 and 25–75 °C. *Mineral. Mag.* **72**, 155–158.
- Gysi A. P. and Stefansson A. (2011) CO₂ water basalt interaction. II: Numerical simulation of low temperature CO₂ sequestration into basalts. *Geochim. Cosmochim. Acta*. doi:10.1016/j.gca.2011.05.037.
- Hänenchen M., Prigobbe V., Storti G., Seward T. M. and Mazzotti M. (2006) Dissolution kinetics of forsteritic olivine at 90–150 °C including effects of the presence of CO₂. *Geochim. Cosmochim. Acta* **70**, 4403–4416.
- Hartmann J., Jansen N., Durr H. H., Kempe S. and Kohler P. (2009) Global CO₂ consumption by chemical weathering: what is the contribution too highly active weathering regions? *Global Planet. Change* **69**, 185–194.
- Hausrath E. M., Navarre-Sitchler A. K., Sak P., Steefel C. and Brantley S. L. (2008) Basalt weathering rates on Earth and the duration of liquid water on the plains of Gusev Crater, Mars. *Geology* **36**, 67–70.
- Hausrath E. M., Neaman A. and Brantley S. L. (2009) Element release rates from dissolving basalt and granite with and without organic ligands. *Am. J. Sci.* **309**, 633–660.
- Kelemen P. B. and Matter J. (2008) In situ carbonation of peridotite for CO₂ storage. *Proc. Natl. Acad. Sci. USA* **105**, 17295–17300.
- Knauss K. G., Nguyen S. N. and Weed H. C. (1993) Diopside dissolution kinetics as a function of pH, CO₂, temperature, and time. *Geochim. Cosmochim. Acta* **57**, 285–294.
- Kuo L. C. and Kirkpatrick R. J. (1985) Kinetics of crystal dissolution in the system diopside forsterite silica. *Am. J. Sci.* **285**, 51–90.
- Lasaga A. C., Soler J. M., Ganor J., Burch T. E. and Nagy K. L. (1994) Chemical-weathering rate laws and global geochemical cycles. *Geochim. Cosmochim. Acta* **58**, 2361–2386.
- Louvat P. and Allegre C. J. (1997) Present denudation rates of the island of Reunion determined by river geochemistry: basalt weathering and mass budget between chemical and mechanical erosions. *Geochim. Cosmochim. Acta* **61**, 3645–3669.
- Marini L. (2007) Geological sequestration of carbon dioxide. In *Thermodynamics, Kinetics and Reaction Path Modeling*. Elsevier, Amsterdam, 470 pp.
- Matter J. M., Takahashi T. and Goldberg D. (2007) Experimental evaluation of in situ CO₂ water rock reactions during CO₂ injection in basaltic rocks: implications for geological CO₂ sequestration. *Geochem. Geophys. Geosyst.* **8**, 1–19.
- McGrail B. P., Schaef H. T., Ho A. M., Chien Yi-J., Dooley J. J. and Davidson C. L. (2006) Potential for carbon dioxide sequestration in flood basalts. *JGR Res.* **111**, B12201. doi:10.1029/2005JB004169.
- Meyer P. S. and Sigurdsson H. (1978) Interstitial acid glass and chlorophaeite in Iceland. *Lithos* **11**, 231–241.
- Morales T. A. and Herbert R. (2002) Surface chemistry and acidic dissolution of forsterite. *Geochim. Cosmochim. Acta* **66**, A521.
- Moulton K. L., West J. and Berner R. A. (2000) Solute flux and mineral mass balance approaches to the quantification of plant effects on silicate weathering. *Am. J. Sci.* **300**, 539–570.
- Navarre-Sitchler A. and Brantley S. (2007) Basalt weathering across scales. *Earth Planet. Sci. Lett.* **261**, 321–334.
- Neaman A., Chorover J. and Brantley S. L. (2005) Implications of the evolution of organic acid moieties for basalt weathering over geological time. *Am. J. Sci.* **305**, 147–185.
- Nesbitt H. W. and Wilson R. E. (1992) Recent chemical weathering of basalts. *Am. J. Sci.* **292**, 740–777.
- Neuhoff P. S. (1999) Thermodynamic properties and paragenesis of rock-forming zeolites. Ph.D. Dissertation, Stanford University.
- Oelkers E. H. (2001a) An experimental study of forsterite dissolution rates as a function of temperature and aqueous Mg and Si concentrations. *Chem. Geol.* **175**, 485–494.
- Oelkers E. H. (2001b) General kinetic description of multioxide silicate mineral and glass dissolution. *Geochim. Cosmochim. Acta* **65**, 3703–3719.
- Oelkers E. H. and Gislason S. R. (2001) The mechanism, rates and consequences of basaltic glass dissolution. I: An experimental study of the dissolution rates of basaltic glass as a function of aqueous Al, Si and oxalic acid concentration at 25 °C and pH = 3 and 11. *Geochim. Cosmochim. Acta* **65**, 3671–3681.
- Oelkers E. H., Gislason S. R. and Matter J. (2008) Mineral carbonation of CO₂. *Elements* **4**, 333–337.
- Oelkers E. H., Golubev S. V., Pokrovsky O. S. and Benzeeth P. (2011) Do organic ligands affect calcite dissolution rates? *Geochim. Cosmochim. Acta* **75**, 1799–1813.
- Oelkers E. H., Golubev S. V., Chaïra C., Pokrovsky O. S. and Schott J. (2009) The surface chemistry of multi-oxide silicates. *Geochim. Cosmochim. Acta* **73**, 4617–4634.
- Oelkers E. H. and Schott J. (1995) Experimental study of anorthite dissolution and the relative mechanism of feldspar hydrolysis. *Geochim. Cosmochim. Acta* **59**, 5039–5053.
- Oelkers E. H. and Schott J. (2001) An experimental study of enstatite dissolution rates as a function of pH, temperature, and aqueous Mg and Si concentration, and the mechanism of pyroxene/pyroxenoid dissolution. *Geochim. Cosmochim. Acta* **65**, 1219–1231.
- Olsen A. A. and Rimstidt J. D. (2008) Oxalate-promoted forsterite dissolution at low pH. *Geochim. Cosmochim. Acta* **72**, 1758–1766.
- Oxburgh R., Drever J. I. and Sun Y. T. (1994) Mechanism of plagioclase dissolution in acid-solution at 25 °C. *Geochim. Cosmochim. Acta* **58**, 661–669.
- Parkhurst D. L. and Appelo C. A. J. (1999) User's guide to phreeqc (version 2) – a computer program for speciation, batch-

- reaction, one-dimensional transport, and inverse geochemical calculations. U.S.G.S. Water Res. Inv. Report. 99-4259.
- Palandri J. L. and Kharaka Y. K. (2004) A compilation of rate parameters of water-mineral interaction kinetics for application to geochemical modeling. U.S.G.S. Open file report 2004-1068, 64 p.
- Pokrovsky O. S. and Schott J. (2000a) Forsterite surface composition in aqueous solutions: a combined potentiometric, electrokinetic, and spectroscopic approach. *Geochim. Cosmochim. Acta* **64**, 3299–3312.
- Pokrovsky O. S. and Schott J. (2000b) Kinetics and mechanism of forsterite dissolution at 25 °C and pH from 1 to 12. *Geochim. Cosmochim. Acta* **64**, 3313–3325.
- Prigobbe V., Costa G., Baciocchi R., Hanchen M. and Mazzotti M. (2009a) The effect of CO₂ and salinity on olivine dissolution kinetics at 120 °C. *Chem. Eng. Sci.* **64**, 3510–3515.
- Prigobbe V., Hanchen M., Werner M., Baciocchi R. and Mazzotti M. (2009b) Mineral carbonation processes for CO₂ sequestration. *Greenhouse Gas Control Technol.* **9**, 4885–4890.
- Rogers K. L., Neuhoff P. S., Pedersen A. K. and Bird D. K. (2006) CO₂ metasomatism in a basalt-hosted petroleum reservoir, Nuussuaq, West Greenland. *Lithos* **92**, 55–82.
- Rosso J. J. and Rimstidt J. D. (2000) A high resolution study of forsterite dissolution rates. *Geochim. Cosmochim. Acta* **64**, 797–811.
- Saldi G. D., Jordan G., Schott J. and Oelkers E. H. (2009) Magnesite growth rates as function of temperature and saturation state. *Geochim. Cosmochim. Acta* **73**, 5646–5657.
- Saldi G. D., Schott J., Pokrovsky O. S. and Oelkers E. H. (2010) An experimental study of magnesite dissolution rates at neutral to alkaline conditions and 150 and 200 °C as a function of pH, total dissolved carbonate concentration and chemical affinity. *Geochim. Cosmochim. Acta* **74**, 6344–6356.
- Schaeff H. T. and McGrail B. P. (2009) Dissolution of Columbia River basalt under mildly acidic conditions as a function of temperature: experimental results relevant to the geological sequestration of carbon dioxide. *Appl. Geochem.* **24**, 980–987.
- Schaeff H. T., McGrail B. P. and Owen A. T. (2010) Carbonate mineralization of volcanic province basalts. *Int. J. Greenhouse Gas Control* **4**, 249–261.
- Schott J. and Oelkers E. H. (1995) Dissolution and crystallization rates of silicate minerals as a function of chemical affinity. *Pure Appl. Chem.* **67**, 903–910.
- Schott J., Pokrovsky O. S. and Oelkers E. H. (2009) The link between mineral dissolution/precipitation kinetics and solution chemistry. *Rev. Mineral. Geochim.* **70**, 207–258.
- Stefansson A. and Gislason S. R. (2001) Chemical weathering of basalts, Southwest Iceland: effect of rock crystallinity and secondary minerals on chemical fluxes to the ocean. *Am. J. Sci.* **301**, 513–556.
- Stockmann G. J., Wolff-Boenisch D., Gislason S. R. and Oelkers E. H. (2011) Do carbonate precipitates affect dissolution kinetics? I: Basaltic glass. *Chem. Geol.* **284**, 306–316.
- Stillings L. L. and Brantley S. L. (1995) Feldspar dissolution at 25 °C and pH 3 – reaction stoichiometry and the effect of cations. *Geochim. Cosmochim. Acta* **59**, 1483–1496.
- Tester J. W., Worley W. G., Robinson B. A., Grigsby C. O. and Feerer J. L. (1994) Correlating quartz dissolution kinetics in pure water from 25 to 625 °C. *Geochim. Cosmochim. Acta* **58**, 2407–2420.
- Wimpenny J., Gislason S. R., James R. H., Gannoun A., Von Strandmann P. A. E. and Burton K. W. (2010) The behaviour of Li and Mg isotopes during primary phase dissolution and secondary mineral formation in basalt. *Geochim. Cosmochim. Acta* **74**, 5259–5279.
- Wolff-Boenisch D., Gislason S. R., Oelkers E. H. and Putnis C. V. (2004a) The dissolution rates of natural glasses as a function of their composition at pH 4 and 10.6, and temperatures from 25 to 74 °C. *Geochim. Cosmochim. Acta* **68**, 4843–4858.
- Wolff-Boenisch D., Gislason S. R. and Oelkers E. H. (2004b) The effect of fluoride on the dissolution rates of natural glasses at pH 4 and 25 °C. *Geochim. Cosmochim. Acta* **68**, 4571–4582.
- Wolff-Boenisch D., Gislason S. R. and Oelkers E. H. (2006) The effect of crystallinity on dissolution rates and CO₂ consumption capacity of silicates. *Geochim. Cosmochim. Acta* **70**, 858–870.
- Wu L. L., Jacobson A. D., Chan H. C. and Hausner M. (2007) Characterization of element release during microbe basalt interaction at 28 °C. *Geochim. Cosmochim. Acta* **71**, 2224–2239.

Associate editor: Dimitri A. Sverjensky

1
2
3
4
5
6

7 **3 Chapter**

8
9 *Experimental characterization of plagioclase*
10 *dissolution rates as a function of their composition*
11 *and pH at 22° C*

12
13 Snorri Gudbrandsson, Domenik Wolff-Boenisch, Sigurdur R. Gislason and Eric H. Oelkers
14
15
16 (Submitted to Geochimica Cosmochimica Acta)

17 **Abstract**

18 The steady-state, far-from-equilibrium dissolution rates of nine distinct plagioclases
19 ranging in composition from An2 to An89 were measured in mixed flow reactors at $22\pm2^\circ\text{ C}$
20 and pH from 2 to 11. The dissolution rates of all plagioclases based on silica release show a
21 common U-shaped behaviour as a function of pH, where rates decrease with increasing pH at
22 acid condition but increase with increasing pH at alkaline conditions. Consistent with
23 literature findings, constant pH plagioclase dissolution rates increase with increasing
24 anorthite content at acid conditions; measured anorthite dissolution rates are ~ 2.5 orders of
25 magnitude faster than those of albite at pH~2. Perhaps more significantly, rates are
26 independent of plagioclase composition at alkaline conditions. Interpretation and data fitting
27 suggests that plagioclase dissolution rates are consistent with their control by the detachment
28 of Si-rich activated complexes formed by the removal of Al from the mineral framework.
29 Taking account of this mechanism and transition state theory yields robust equations that
30 describe plagioclase dissolution rates as a function of both the mineral and fluid phase
31 compositons found in natural Earth surface systems.

32

33

34 Experimental characterization of plagioclase dissolution rates as a
35 function of their composition and pH at 22° C

36 Snorri Gudbrandsson^{1,2*}, Domenik Wolff-Boenisch^{2,3} Sigurdur R. Gislason²,
37 Eric H. Oelkers^{1,2}

38

39 ¹*Geosciences Environment Toulouse (GET), CNRS, UMR5563, Observatoire Midi-*
40 *Pyrenees, 14 Avenue Edouard Belin, 31400, Toulouse, France.*

41 ²*Institute of Earth Sciences, University of Iceland, Sturlugata 7, 101 Reykjavik, Iceland*

42 ³*Department of Applied Geology, Curtin University, GPO Box U1987, Perth, 6845, W-*
43 *Australia*

44

45 **Abstract**

46

47 The steady-state, far-from-equilibrium dissolution rates of nine distinct plagioclases
48 ranging in composition from An2 to An89 were measured in mixed flow reactors at 22±2° C
49 and pH from 2 to 11. The dissolution rates of all plagioclases based on silica release show a
50 common U-shaped behaviour as a function of pH, where rates decrease with increasing pH at
51 acid condition but increase with increasing pH at alkaline conditions. Consistent with
52 literature findings, constant pH plagioclase dissolution rates increase with increasing
53 anorthite content at acid conditions; measured anorthite dissolution rates are ~2.5 orders of
54 magnitude faster than those of albite at pH~2. Perhaps more significantly, rates are
55 independent of plagioclase composition at alkaline conditions. Interpretation and data fitting
56 suggests that plagioclase dissolution rates are consistent with their control by the detachment
57 of Si-rich activated complexes formed by the removal of Al from the mineral framework.
58 Taking account of this mechanism and transition state theory yields robust equations that
59 describe plagioclase dissolution rates as a function of both the mineral and fluid phase
60 compositons found in natural Earth surface systems.

61

62

63 3.1 Introduction

64 Plagioclase is the most abundant mineral in the Earth's crust. Plagioclase dissolution is
65 therefore a major contributor to global weathering rates, alteration and metamorphic reactions
66 in the Earth's crust, the diagenesis of sedimentary rocks, and mass transfer in hydrothermal
67 systems (e.g. Marini et al., 2000; Putnis et al., 2007; Apollaro et al., 2009; Plumer and Putnis,
68 2009; Putnis and Austrheim, 2010). The significance of plagioclase in Earth surface
69 environments has provoked a large number of laboratory studies to characterize its
70 dissolution rates and mechanisms at ambient temperatures (Chou and Wollast, 1984, 1985;
71 Casey et al., 1988; Nesbitt and Muir, 1988; Casey et al., 1989a, b, 1991; Hellmann et al.,
72 1990; Blum and Lasaga, 1991; Nesbitt et al., 1991; Amrhein and Suarez, 1992; Welch and
73 Ullman, 1993, 1996, 2000; Oxburgh et al., 1994; Blum and Stillings, 1995; Oelkers and
74 Schott, 1995; Stillings and Brantley, 1995; Gout et al., 1997; Welch et al., 1999; Hamilton et
75 al., 2000; Beig and Lüttge, 2006; Arvidson and Lüttge, 2010). Additional studies have
76 focused on the rates and mechanisms of feldspar dissolution at elevated temperatures
77 (Lagache, 1965; Hellmann et al., 1990, 2010; Rose, 1991; Brady and Walther, 1992; Hwang
78 and Longo, 1992; Gautier et al., 1994; Hellmann, 1994, 1995, 1997; Oelkers and Schott,
79 1995; Blake and Walter, 1996; Chen and Brantley, 1997; Murakami et al., 1998; Jordan et al.,
80 1999; Taylor et al., 2000; Arvidson et al., 2004; Harouya and Oelkers, 2004; Carroll and
81 Knauss, 2005; Hellmann and Tisserand, 2006; Fu et al., 2009; Hangx and Spiers, 2009; Sorai
82 and Sasaki, 2010). One challenge to interpreting these rates to illuminate the dissolution
83 behaviour of the plagioclases as a function of their composition (e.g. anorthite content) is that
84 rates measured in different laboratories and using different techniques tend to be inconsistent
85 with one another; dissolution rates of identically compositioned plagioclases at 25°C and
86 constant pH measured in different laboratories commonly range over at least one order of
87 magnitude (Blum and Stillings, 1995; Marini, 2006). Such inconsistencies make attempts to
88 deduce the effect of plagioclase composition on their dissolution rates from literature data
89 ambiguous. This study was designed to overcome these ambiguities by systematically
90 measuring the dissolution rates of plagioclase feldspars, spanning the composition range from
91 albite to anorthite, in a single laboratory using mixed-flow reactor techniques at 22 °C and pH
92 from 2 to 12. Here we report these rates and use them to deduce how they are affected by the
93 plagioclase composition.

94 Plagioclase dissolution rates have been of increasing interest due to their potential role in
95 carbon capture and storage. Plagioclase dissolution releases Ca^{2+} which can react with
96 aqueous carbonate to store carbon dioxide as calcite (Carroll and Knauss, 2005; Metz et al.,
97 2005; Oelkers et al., 2008; Kampman et al. 2009; Pham et al., 2010; Munz et al., 2012;
98 Hellevang et al., 2013). The Ca-rich plagioclases are particularly abundant in basalts making
99 these rocks attractive targets for mineral carbon storage (Marini, 2006; McGrail et al., 2006;
100 Alfredsson et al., 2008; Goldberg et al., 2008; Kelemen and Matter, 2008; Oelkers and Cole,
101 2008; Oelkers et al., 2008; Flaathen et al., 2009; Matter and Kelemen, 2009; Prigobbe et al.,
102 2009; Schaef and McGrail, 2009; Schaef et al., 2009; Gislason et al., 2010; Goldberg et al.,
103 2010; Aradottir et al., 2011; Gudbrandsson et al., 2011; Gysi and Stefánsson, 2011; Matter et
104 al., 2011; Wolff-Boenisch et al., 2011; Aradottir et al., 2012; Broecker 2012). Moreover,
105 elements released from dissolving plagioclases serve as the source for secondary minerals
106 including zeolites that play an important role in controlling the porosity of natural rocks
107 (Kristmannsdottir and Tomasson, 1978; Gislason and Eugster, 1987a; Neuhoff, 1999;
108 Fridriksson et al., 2001). Plagioclase dissolution may also be significant during the
109 weathering of Martian crust (Banfield et al., 2000; McSween et al., 2010; McGlynn et al.,
110 2012).

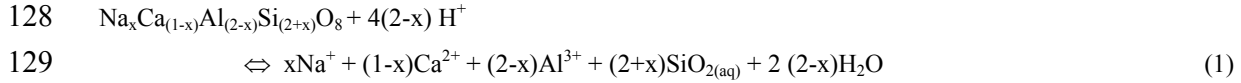
111

112 **3.2 Theoretical background**

113 The standard state adopted in this study is that of unit activity of pure minerals, the
114 plagioclases, and H_2O at any temperature and pressure; the activity of plagioclase was taken
115 as 1 regardless of its composition to estimate its saturation state in aqueous fluids (see
116 below). For aqueous species other than H_2O , the standard state is unit activity of the species
117 in a hypothetical one molal solution referenced to infinite dilution at any temperature and
118 pressure. All thermodynamic calculations reported in this study were performed using the
119 PHREEQC computer code (Parkhurst and Appelo, 1999) together with its llnl.dat database to
120 which thermodynamic data have been added for magnesite, siderite, thomsonite, scolecite,
121 mesolite, laumontite, heulandite, analcime, Ca-stilbite, Ca-mordenite, Ca-clinoptilolite, Fe-
122 celadonite, antigorite, amorphous SiO_2 , amorphous FeOOH , amorphous Al(OH)_3 , gibbsite,
123 allophane, and imogolite taken from Gysi and Stefansson (2011). Thermodynamic data from
124 Arnórsson and Stefánsson (1999) were used to calculate chemical affinities and saturation

125 indexes of the various plagioclases used in this study. All thermodynamic parameters added
126 to the PHREEQC llnl.dat database in this study are provided in Table 1.

127 Plagioclase dissolution at acid conditions can be represented by the reaction



130 where x denotes the mole fraction of Na in the plagioclase such that when $x=1$, Eq. (1)
131 corresponds to the dissolution of pure albite end and when $x=0$, Eq. (1) corresponds to the
132 dissolution of pure anorthite.

133 Taking account of the standard state, the law of mass action for Eq. (1) can be written

134 $K_{\text{Plag}} = \frac{a_{\text{Na}^+}^x a_{\text{Ca}^{2+}}^{(1-x)} a_{\text{Al}^{3+}}^{(2-x)} a_{\text{SiO}_2}^{(2+x)}}{a_{\text{H}^+}^{4(2-x)}}$ (2)

135 where K_{Plag} stands for the equilibrium constant of Eq. (1) and a_i represents the activity of the
136 subscripted aqueous species. The chemical affinity for reaction (1), A_{Plag} can be expressed as

137 $A_{\text{Plag}} = RT \ln \left(\frac{K_{\text{Plag}} a_{\text{H}^+}^{4(2-x)}}{a_{\text{Na}^+}^x a_{\text{Ca}^{2+}}^{(1-x)} a_{\text{Al}^{3+}}^{(2-x)} a_{\text{SiO}_2}^{(2+x)}} \right)$ (3)

138 where R designates the gas constant, T signifies absolute temperature.

139 Within the context of Transition State Theory, surface reaction controlled dissolution
140 rates can be considered to be the difference between the forward rate (r_+) and the reverse rate
141 (r_-) such that

142 $r = r_+ - r_- = r_+ \left(1 - \frac{r_-}{r_+} \right)$ (4)

143 Taking account of the law of detailed balancing, it can be shown that Eq. (4) is equivalent to
144 (Aagaard and Helgeson, 1977, 1982; Lasaga, 1981; Helgeson et al., 1984)

145 $r = r_+ (1 - \exp(-A/\sigma RT))$ (5)

146 where σ stands for Temkin's average stoichiometric number equal to the ratio of the rate of
147 destruction of the activated or precursor complex relative to the overall rate. Experimental

148 evidence suggests that the value of σ in Eq. (5) is 1 for quartz (Berger et al., 1994) and 3 for
149 the alkali-feldspars (Gautier et al., 1994; Oelkers and Schott, 1995). The form of Eq. (5) is
150 such that overall rates (r) equal forward rates (r_+) when $A \gg \sigma RT$. The dissolution rates in
151 the present study were measured at far-from-equilibrium conditions, such that $A \gg \sigma RT$. At
152 these conditions $r \ll r_+$ and thus $r \approx r_+$. Dissolution rates in this study are thus symbolized
153 r_+ . Such experimental results can be used to assess the effect of aqueous solution
154 composition on forward dissolution rates independently from the effects of chemical affinity.
155

156 Within the formalism of Transition State Theory, r_+ is proportional to the concentration
157 of an activated complex such that (Eyring, 1935)

158
$$r_+ = k_+[\alpha] \quad (6)$$

159 where k_+ refers to a rate constant and $[\alpha]$ designates the concentration of the activated
160 complex. The concentrations of activated complexes for mineral dissolution have been
161 demonstrated to be proportional to the concentration of rate controlling surface complexes in
162 accord with (c.f. Schott et al., 2009).

163
$$[\alpha] = K_\alpha[\Theta] \quad (7)$$

164 where K_α represents an equilibrium constant and $[\Theta]$ denotes the concentration of the rate
165 controlling surface complex. Combining Eq. (6) and (7) leads to

166
$$r_+ = k_+K_\alpha[\Theta] \quad (8)$$

167

168 A number of past studies have attempted to describe the dissolution rates of the
169 plagioclase feldspars assuming that their dissolution is controlled by two or more distinct
170 activated complexes formed by the adsorption or desorption of protons, water, or hydroxide
171 ions on the mineral surface. Such an approach yields a rate equation describing the
172 dissolution rate of each plagioclase composition that is the sum of two or more linear
173 functions of pH (Palandri and Kharaka, 2004; Marini, 2006). An alternative approach stems
174 from the observation that multi-oxide silicate mineral dissolution occurs via a series of metal-
175 proton exchange reactions (e.g. Gautier et al., 1994; Oelkers et al., 1994; Carroll and Knauss,
176 2005; Dixit and Carroll, 2007; Oelkers et al., 2009). The rate at which each metal-oxygen
177 bond breaks via these reactions depends on the relative strength of the corresponding metal-
178 oxygen bond. This mechanism leads to the rate equation given by (c.f. Oelkers, 2001):

179 $r_+ = k_+ K_\alpha [\ominus] = k_+ K_\alpha \prod_{i=1}^i \left[K_i \left(\frac{a_{H^+}^{z_i}}{a_{M_i^{z_i^+}}} \right)^{n_i} / \left(1 + K_i \left(\frac{a_{H^+}^{z_i}}{a_{M_i^{z_i^+}}} \right)^{n_i} \right) \right]$ (9)

180 where M_i designates a metal removed from the mineral to form the rate controlling surface
181 complex, n_i stands for the stoichiometric number of M_i metal atoms that need to be removed
182 to form one rate controlling surface complex, z_i denotes the valence of the metal M_i , and K_i
183 designates the equilibrium constant for the M_i /proton exchange reaction. In the case where 1)
184 only a single metal-proton exchange reaction is involved in the formation of the precursor
185 complex and 2) there are relatively few precursors at the surface, Eq. (9) reduces to:

186 $r_+ = k'_+ \left(\frac{a_{H^+}^{z_i}}{a_{M_i^{z_i^+}}} \right)^{n_i}$ (10)

187 where k'_+ denotes the product $k_+ K_\alpha K_i$. One of the advantages of this approach is that Eq. (10)
188 can be used to predict the effect of a variety of aqueous species on multi-oxide dissolution
189 rates including those of organic anions, fluoride, and sulphides. The effect of such aqueous
190 species on rates stems from a change in the aqueous activity of the metal M_i ($a_{M_i^{z_i^+}}$); the
191 formation of aqueous metal complexes lowers $a_{M_i^{z_i^+}}$ leading to higher rates as calculated
192 using Eq. (10) (e.g. Oelkers and Schott, 2001; Harouya and Oelkers, 2004; Wolff-Boenisch et
193 al., 2004; Flaathen et al., 2010).

194

195 Previous work on the feldspars (Oelkers et al., 1994; Gautier et al., 1994; Oelkers and
196 Schott, 1995) suggests that the dissolution rates of the alkali rich plagioclases (<An₆₅) are
197 proportional to the concentration of a Si-rich surface complex formed by the Al-proton
198 exchange reactions leading to the following rate equation:

199 $r_{+,b} = k'_{+,b} \left(\frac{a_{H^+}^3}{a_{Al^{3+}}} \right)^n$ (11)

200 The degree to which this equation can describe the dissolution rates as a function of pH and
201 plagioclase composition will be explored below.

202

203 Description of the dissolution behaviour of the intermediate plagioclases is confounded by
204 their structure. Exsolution on the micro scale is common in plagioclase feldspars and

205 consists of fine albite-rich and anorthite-rich intergrowths (Grove, 1977; Holdren and Speyer,
206 1987; Inskeep et al., 1991). Intergrowths are most common in three compositional ranges,
207 An2-16, An43-58, and An67-90, named persterite, Bøgghild, and Huttenlocher intergrowths,
208 respectively (Smith and Brown, 1988). These heterogeneities are commonly not detectable
209 by optical techniques, yet could influence the dissolution kinetics of the plagioclases.
210 Oxburgh et al. (1994) suggested that such heterogeneities including zoning and intergrowths,
211 may lead to significant variations in the rates of similarly compositional plagioclases. Such
212 ambiguities have led several to assume that the dissolution rates of intermediate feldspars can
213 be estimated by the sum of contributions of two distinct phases, e.g. albite and anorthite,
214 (White et al., 2005). The validity of such assumptions will be assessed below through the
215 interpretation of dissolution rates obtained over the full range of feldspar compositions.

216

217 **3.3 Sample preparation and experimental methods**

218

219 **3.3.1 Plagioclase characterisation and preparation**

220 The plagioclase feldspars used in this study were collected from various locations;
221 the sample localities are listed in Table 1. Most were purchased from Ward-Science. The
222 most anorthite rich plagioclase (An89) was acquired from the Smithsonian Institution. One
223 bytownite was collected from an anorthosite intrusion located on the Hrappsey Islands in
224 Breidafjörður, Western Iceland. The plagioclases were chosen to represent the entire
225 plagioclase compositional series from albite to anorthite. All of the plagioclases were of
226 metamorphic origin other than the anorthite and Hrappsey bytownite, which were of igneous
227 origin.

228

229 The chemical composition of the plagioclase minerals was determined from standard
230 wavelength dispersive techniques using a JEOL Superprobe JSL 8200 electron microprobe
231 located at the GET/CNRS in Toulouse, France. These analyses were performed using an
232 acceleration voltage of 15 kV, a beam current of 15 nA, and a beam diameter of 2 µm.
233 Natural and synthetic minerals and glasses were used as standards to check for potential drift.
234 The resulting chemical compositions of each plagioclase as oxide percent is given in Table 2.

235 The anorthite percentage of each plagioclase and its corresponding chemical formula are
236 given in Table 1.

237

238 All feldspars were dried at room temperature for several days before being crushed
239 with a hammer and then an agate mortar. The ground material was dry sieved to obtain the
240 45-125 μm size fraction. This size fraction was first gravitationally settled to remove fine
241 particles and subsequently cleaned ultrasonically 5 times in de-ionized water and then in
242 acetone. The resulting powder was oven-dried at 50° C for several days. SEM images of
243 some resulting powders are shown in Fig. 1. The surfaces are free of fine particles. The
244 specific surface area of the cleaned 45-125 μm size fraction was determined via 11 point
245 krypton adsorption, using a Quantachrome Gas Sorption system. These surface areas are
246 reported in Table 1. The uncertainties of these surface area measurements are estimated to be
247 $\pm 10\%$ based on repeated analysis of standard materials.

248

249 **3.3.2 Experimental methods**

250 Plagioclase dissolution experiments were performed at pH from 2 to 12 in two distinct
251 reactor systems. The first is a ParrTM mixed flow reactor system, shown in Fig. 2. This
252 system consists of a 300 mL titanium reactor with external temperature and stirring controls.
253 Reactive fluids were injected into this reactor via a High Pressure Liquid Chromatography
254 (HPLC) pump allowing a constant flow rate from 2 to 3 g/min. The fluid passed through a
255 0.2 μm titanium filter while leaving this reactor system. A detailed description of this reactor
256 system has been provided by Gudbrandsson et al. (2011). The second reactor system
257 consisted of 250 mL polyethylene reactors containing a NalgeneTM floating stirring bar and
258 placed in a temperature controlled water bath. Reactive fluids were injected into this reactor
259 using a peristaltic pump. The reactive fluid passed through a 2 μm filter while exiting this reactor
260 system. This reactor system has been described in detail by Stockmann et al. (2011).
261 All inlet fluids were comprised of deionized water and Merck analytical grade NH₄Cl, HCl,
262 and NH₄OH. The ionic strength of all inlet fluids was 0.01 mol/kg; the compositions of these
263 fluids are listed in Table 3. The alkaline inlet fluids were initially bubbled with N₂ and then
264 continuously kept under a N₂ atmosphere to prevent CO₂ dissolution into the fluid. Each

265 reactor was cleaned thoroughly, assembled, and run for at least 24 h with deionized water and
266 then for another 24 h with the inlet solution to rinse the tubing and clean the reactor prior to
267 each experiment. At the end of this cleaning cycle an outlet fluid sample was taken for
268 chemical analysis.

269

270 Experiments were initiated by placing between 3 and 4 g of dry plagioclase powder into
271 the reactor. The reactor was then filled with the initial inlet fluid and sealed. Reactive fluid
272 flow, temperature, and stirring rates were adjusted to desired settings. The fluid/plagioclase
273 powder mixture was continuously stirred at approximately 400 rpm. Gislason and Oelkers
274 (2003) observed that rotation speeds in excess of 325 rpm were sufficient to maintain surface
275 reaction control of basaltic glass dissolution at pH 3.3. Experiments performed in the
276 polyethylene reactors were run in series. An experimental series consisted of several distinct
277 steady-state rate measurements performed on a single plagioclase powder at several different
278 pH. In each series, a single inlet fluid was pumped through the reactor for 75 hours. After 75
279 hours the inlet fluid was replaced by the next inlet fluid in the series. In each experimental
280 series, the initial inlet fluid had a circum-neutral pH and subsequent inlet fluids were
281 progressively more acidic or more alkaline. Each experimental series is distinguished by the
282 prefix on the experiment number. For example, series ‘Ab-acid’ consists sequentially of
283 experiments Ab-acid-5, Ab-acid-4, Ab-acid-3, etc, where the last number denotes the
284 approximate inlet fluid pH. Each experimental series was stopped before 5% of the initial
285 mineral was dissolved. Further details on the experiments performed in each series are listed
286 in Table 4. Experiments performed in the titanium reactors were run individually. In these
287 individual experiments, a mineral powder was placed in the reactor and a reactive fluid of a
288 single composition was passed through the reactor for at least 250 hours. Once each
289 individual experiment was completed, the fluid and remaining mineral was removed and the
290 reactor cleaned in advance of initiating a new individual experiment. Further details on these
291 experiments are listed in Table 5.

292

293 Outlet fluids were regularly sampled and filtered using 0.2 µm cellulose acetate filters.
294 Part of the fluid was used to measure pH at 22° C using a Eutech Instruments© Cyberscan

pH 310 pH meter coupled to a Eutech Instruments© electrode with a 3 M KCl outer filling solution. The electrode was calibrated with NBS standards at pH 4.01, 7, and 10 with an average error less than 0.05 pH units. Part of sampled reactive fluids were then acidified with concentrated supra-pure HNO₃ prior to their analysis for Si, Mg, Na, Al, Fe, and Ca by Specro Cirios Vision Inductively Coupled Plasma Optical Emission Spectrometry (ICP-OES), with detection limits for Si and Al of 24.8 ppb and 3.2 ppb. The uncertainties on these measurements are estimated to be ±10%.

302

303 3.4 Results

304 In total, 71 distinct plagioclase dissolution rate experiments were performed. Measured
305 outlet fluid Si and Al concentrations were used to calculate dissolution rates using

$$306 r_{i,j} = \frac{c_i FR}{A_j m} \quad (12)$$

307 where c_i represents the concentration of the i th element in the outlet fluid, FR stands for the
308 fluid flow rate, A_j refers to the specific surface area of the plagioclase prior to the experiment,
309 and m denotes mass of plagioclase in the reactor. The surface area used in this calculation
310 was the measured BET surface area of the initial plagioclase prior to its dissolution.

311

312 The temporal variation of measured rates based on Si release during all experiments can
313 be seen in Annex A, corresponding rates based on Al are presented in Annex B. It can be
314 seen that measured rates based on Al and Si tend towards steady-state over the course of most
315 experiments. Steady-state is assumed if the rate calculated for three consecutive fluid
316 samples taken at least 3 residence times apart from one another are equal within experimental
317 uncertainty. The residence time is defined as the volume of the reactor divided by the reactive
318 fluid flow rate. Rates obtained from experiments that adhere to the steady-state criteria are
319 noted in bold font in Tables 4 and 5.

320

321 Outlet fluid compositions were used to calculate the saturation state of primary and
322 potential secondary mineral phases in all experiments. The results of these calculations are
323 shown in Annex C. The outlet fluids were calculated to be undersaturated with respect to all
324 primary and potential secondary minerals apart from the fluids at pH 5 to pH 9, which were

325 calculated to be supersaturated with respect to the aluminium-oxyhydroxides gibbsite,
326 boehmite, and diasporite. No secondary minerals, however, were detected by SEM-EDS
327 analysis on the recovered solids following the experiments. Nevertheless, as described below,
328 the precipitation of secondary Al-rich phases are consistent with the observed Al/Si release
329 rates of experiments performed at basic pH.

330

331 Steady-state rates based on Si release obtained from the experiments performed in series
332 and individually are shown as a function of pH in Fig. 3. In general, rates based on Si release
333 decrease with increasing pH at acid pH and increase with increasing pH at basic pH. At acid
334 conditions, rates increase substantially with the An content of the plagioclase whilst there is
335 little to no dependence of rates on An content at basic conditions. Plagioclase dissolution
336 rates based on Al release are illustrated as a function of pH in Fig. 4. These rates exhibit
337 similar pH dependence as rates based on Si release with the exception of the high pH rates
338 obtained from the individual experiments which appear not to increase with increasing pH. A
339 possible explanation for this observation is the precipitation of Al-rich secondary phases
340 during the high pH experiments. The possibility that such phases precipitate during some
341 experiments is supported by the computed saturation states listed in Annex C. Diasporite and
342 boehmite are computed to be close to equilibrium or supersaturated in many of the high pH
343 experiments.

344

345 Rates obtained from the experimental series, tend to agree within uncertainty with those
346 obtained from the individual experiments performed over at least 250 hours. Nevertheless,
347 rates obtained from the individually run experiments tend to exhibit more scatter and tend to
348 be less systematic than those obtained from the experiments run in series (see Figs. 3 and 4).
349 There are several potential reasons for this. First, as each rate was obtained from a distinct
350 plagioclase powder in the individual experiments, heterogeneities in the powders may lead to
351 less consistent rates. In addition, by running experiments in series, fine particles and/or
352 rapidly dissolving impurities would be removed during the first steady-state attainment
353 leading to more consistent rates from the subsequent steady-state experiments in series.

354

355 The stoichiometry of Al versus Si release at the end of all experiments can be assessed in
356 Fig. 5 which shows the ratio of steady-state plagioclase dissolution rates generated from Si
357 release to those generated from Al release. In general, the experiments exhibit a systematic
358 trend; the release rate of Al versus Si is close to stoichiometric at acidic pH for most
359 experiments. In contrast, Al release rates generally become slower than those of Si at basic
360 conditions. This observation is consistent with the possibility that an Al-rich secondary phase
361 precipitated during some of the experiments performed at alkaline conditions.

362

363 The variation of plagioclase dissolution rates as a function of their composition are
364 illustrated in Fig. 6. Rates appear to be independent of plagioclase composition at pH ≥ 5 .
365 At pH ~ 4 , anorthite dissolution rates are approximately one order of magnitude faster than
366 those of albite. This rate difference increases with decreasing pH; at pH ~ 2 anorthite
367 dissolution rates are approximately two and one half orders of magnitude faster than those of
368 albite. Moreover, the bulk of the increased rates with anorthite content occur in the anorthite-
369 rich plagioclases. This observation is consistent with the conclusions of Blum and Lasaga
370 (1988) who suggested that the mechanism of plagioclase dissolution changes at an An
371 content of $\sim 70\%$ due to the increase in the percentage of Al in its tetrahedral framework. At
372 this concentration, it becomes possible to break this tetrahedral structure without breaking Si-
373 O bonds (c.f. Blum and Lasaga, 1988, Oelkers and Schott, 1995).

374 **3.5 Discussion**

375 **3.5.1 Comparison with past work**

376 This study builds upon past work on the experimental characterization of plagioclase
377 dissolution rates at ambient temperatures. Most past studies on the dissolution rates of
378 plagioclases have been performed on the albite end-member (e.g. Chou and Wollast, 1984,
379 1985; Knauss and Wolery, 1986; Holdren and Speyer, 1987; Blum and Stillings, 1995;
380 Stillings and Brantley, 1995; Stillings et al., 1996). Of these studies, Chou and Wollast
381 (1985) and Knauss and Wolery (1986) published measured albite dissolution rates as a
382 function of pH from acidic to alkaline conditions. Other studies have focused on the effect
383 of the presence of alkali metals (Stilling and Brantley, 1995) and organic ligands (Franklin et
384 al., 1994; Blake and Walter, 1996; Welch and Ullman, 1996; Ullman and Welch, 2002) on
385 albite dissolution rates. A detailed summary of these rates is provided by Blum and Stillings

386 (1995), Brantley (2003, 2008), and Ganor et al. (2009). Some of these rates are illustrated in
387 Fig. 7. In the absence of complexing ligands, the pH variation of albite dissolution rates at
388 constant temperature exhibit a U-shaped dissolution behaviour, where rates decrease with
389 increasing pH at acid conditions and increase with increasing pH at alkaline conditions. Note
390 that there are significant inconsistencies among rates measured at identical conditions in
391 different laboratories. For example, rates reported by Chou and Wollast (1985) are from 0.5
392 to 1.5 orders of magnitude higher than corresponding rates reported by Knauss and Wolery
393 (1986). These inconsistencies have been attributed to differences in mineral composition,
394 mineral micro structure, the presence of exsolution boundaries, differences in sample
395 preparation, grain size, and aqueous solution saturation state (e.g. Holdren and Speyer, 1985,
396 1987; Inskeep et al., 1991). Oxburgh et al. (1994) showed that silica release rates decrease
397 with time during plagioclase dissolution experiments and suggested that several “steady-
398 states” could control the non-stoichiometric dissolution observed in experiments run over
399 shorter time spans.

400 Studies on intermediate feldspars have, as for other plagioclases, mainly focused on
401 characterising rates at acid conditions (e.g. Mast and Drever, 1987; Casey et al., 1988; 1989a;
402 1989b; Brantley and Stillings, 1994, 1996; Oxburgh et al., 1994; Stillings and Brantley, 1995;
403 Stillings et al., 1996). Some of these studies have been aimed at exploring the effects on rates
404 of organic ligands (Mast and Drever, 1987; Welch and Ullman, 1993; Stillings et al., 1996;
405 Oelkers and Schott, 1998) and alkali metals (Muir and Nesbitt, 1991; Stillings and Brantley,
406 1995). Plagioclase dissolution rates at alkaline conditions are rare in the literature; one
407 exception is Casey et al. (1988) who reported some plagioclase dissolution rates at pH 12.
408 Among the most comprehensive studies is that of Oxburgh et al. (1994) who reported the
409 dissolution rates of several plagioclases as a function of pH at acid conditions. Some of these
410 rates are illustrated in Figs. 7b and c. Similar to rates obtained in this study, plagioclase rates
411 increase with increasing An content at acidic solutions.

412 Far fewer studies have been published on the dissolution rates of anorthite-rich
413 plagioclase than on the albite end member. Anorthite dissolution rate measurements have
414 only been reported at acid to neutral pH ($\text{pH} < 7.8$). Selected published anorthite dissolution
415 rates are shown as a function of pH in Fig. 7d. Steady-state anorthite dissolution rates
416 decrease with increasing pH at acid to neutral conditions. Rates reported by Holdren and

417 Speyer (1987) are in close agreement with those from Amhrein and Suarez (1992) and
418 Oelkers and Schott (1995). Note that the rates from Oelkers and Schott (1995) shown in Fig
419 7d were extrapolated to 25°C using their reported rates at 45° C together with their reported
420 activation energies. The rates reported by Amhrein and Suarez (1992) at neutral conditions
421 scatter over approximately two orders of magnitude.

422 The rates obtained in this study are compared with some of the rates available in the
423 literature in Fig 7. Albite dissolution rates obtained in this study are 0.5 to 1 orders of
424 magnitude faster than corresponding rates reported by Chou and Wollast (1985), and 1 to 2
425 orders of magnitude faster than corresponding rates reported by Knauss and Wolery (1986).
426 Similarly, rates obtained for the intermediate plagioclases in this study are 0.5 to 1 order of
427 magnitude faster than those of Oxburgh et al. (1994). The major difference between rates
428 obtained in this study for anorthite and those obtained by Amrhein and Suarez (1992) is at
429 intermediate to basic pH. Rates in this study increase with pH at basic conditions, whereas
430 those of Amrhein and Suarez (1992) suggest these rates decrease continuously with
431 increasing pH.

432 There are several potential explanations why rates obtained in this study tend to be faster
433 than those of previous studies. First, various experimental studies have been performed over
434 different durations. Experiments in this study were performed from 75 to 600 hours, those of
435 Chou and Wollast (1985) were performed over 280 hours on average, those of Knauss and
436 Wolery (1986) were performed over ~1200 hours, those of Oxburgh et al. (1994) were
437 performed over 500-2000 hours, and those of Amrhein and Suarez (1992) were performed
438 over from 19,000-29,400 hours. Oxburgh et al. (1994) suggested that plagioclase dissolution
439 rates tend to decrease with time during laboratory experiments. Some of this effect might be
440 due to the formation of non-stoichiometric layers on the surfaces of the dissolving feldspars
441 (c.f. Chou and Wollast, 1985) or by a decrease in the reactive surface area as the mineral
442 dissolves (c.f. Köhler et al., 2005). Another explanation for differences in measured rates can
443 be the composition of the plagioclase samples. The albite used by Chou and Wollast (1985)
444 and Knauss and Wolery (1986) was collected from Amelia, Virginia, USA, and had an An
445 content of 1.5 to 3% whereas that used in the individual experiments reported in this study
446 was collected from Ontario Canada and had 9% An content. Other possible reasons for the

447 observed differences in measured rates include differences in surface area measurements,
448 mineral preparation methods, and degree of heterogeneity of the studied plagioclase.

449

450 **3.5.2 Stoichiometry of metal release during plagioclase dissolution.**

451 One noteworthy observation in this study is that Si appears to be released at slightly
452 faster rates than Al from all plagioclases at pH>9 throughout our experiments as seen in Fig.
453 5. A preferential release of Si at basic conditions suggests the formation of an Al-rich surface
454 layer or secondary phase during these experiments. Geochemical calculations performed
455 using the PHREEQC computer code suggests that gibbsite and diaspore are close to
456 equilibrium during the experiments performed in alkali conditions and supersaturated in
457 experiments performed at near to neutral conditions. No secondary phases are evident in
458 SEM images of the grains recovered after each experiment. Nevertheless, as the Si to Al
459 release ratios suggest that Al was retained in the solid phase, and Al-hydroxide phases readily
460 precipitate from supersaturated aqueous solutions (e.g. Hellmann, 1995; Hellmann and
461 Tisserand, 2006), their precipitation during the experiments at basic conditions cannot be
462 excluded. A potential reason why Si rates appear to decrease with time during some of the
463 experiments performed at basic pH is due to the blocking of plagioclase surfaces by
464 secondary Al-rich phases. The formation of Al-rich phases may be promoted in cases where
465 the bulk fluid is slightly undersaturated by secondary Al-hydroxide growth along exsolution
466 boundaries where slow transport rates may increase fluid saturation states locally (i.e.
467 Hellmann, 1995; Putnis and Putnis, 2007).

468

469 An alternative explanation for the retention of Al in the solid phase during plagioclase
470 dissolution at basic conditions is the preferential Si release during the dissolution experiment.
471 This explanation, however, is inconsistent with the results of albite surface titration
472 experiments that indicate that Al is preferentially removed from albite during its initial
473 dissolution (c.f. Oelkers et al., 2009), and the observation that the relative Si to Al release rate
474 tends to be independent of time in most of the experiments performed at basic conditions in
475 this study.

476

477 **3.5.3 Quantitative description of plagioclase dissolution rates as a function of anorthite
478 content and aqueous fluid composition**

479 The creation of a consistent set of dissolution rates spanning a wide range of plagioclase
480 compositions and pH enables retrieval of equations that can quantitatively describe these
481 rates. A critical question is determining the degree to which plagioclase dissolution occurs
482 via the dissolution of a single phase or two distinct end members, one albite and another
483 anorthite rich. The latter assumption has been adopted in a number of geochemical
484 modelling studies (e.g. Johnson et al., 1998, Gaus et al., 2005; Xu et al., 2005), and assumes
485 that the dissolution rates of intermediate plagioclase can be assumed to be a linear
486 combination of its end-members. A similar approach was used to describe the dissolution
487 behaviour of crystalline basalts (Gudbrandsson et al., 2011). Plagioclase dissolution rates at
488 acidic conditions, as shown in Fig. 6, however, exhibit a strongly non-linear dependence on
489 plagioclase composition, where rates increase dramatically with composition close to the
490 anorthite end-member. This strong non-linearity would only be consistent with the possibility
491 that plagioclase dissolved as two distinct end-member phases if the relative surface area of
492 the two distinct end-members varied hugely with plagioclase composition. As such, rates in
493 the present study were quantified assuming plagioclase dissolves as a single homogeneous
494 phase.

495

496 Logarithms of measured plagioclase dissolution rates based on Si release are depicted as
497 a function of the logarithm of the aqueous species activity ratio ($a_{\text{H}^+}^3/a_{\text{Al}^{3+}}$) in Fig 8.
498 Several observations are apparent in this figure. First, the dissolution rates of the anorthite-
499 rich feldspars plot as a single linear function of ($a_{\text{H}^+}^3/a_{\text{Al}^{3+}}$), consistent with Eq. (11) at all
500 pH. It can be seen that the rates of all the plagioclases at basic conditions are consistent with
501 those of the plagioclase An89, for which a linear regression through the data points has been
502 added to Fig. 8b. The slope of the line passing through the anorthite-rich rates yields a value
503 of n of approximately -1/3, which itself is equal to that reported for albite at 150 °C and pH 9
504 by Oelkers et al. (1994). Rates at acidic conditions depend significantly on plagioclase
505 composition, where the absolute values of the reaction order term n decreases systematically
506 with decreasing anorthite component. A similar decrease of the reaction order n at acidic

507 conditions with increasing Si content of a solid was reported for the case of natural glasses by
 508 Wolff-Boenisch et al. (2004). To a first approximation, the linear curves describing
 509 plagioclase steady-state dissolution rates at acid conditions in Fig. 8a converge at a single
 510 point of $\log(r_+/(mol/cm^2/s)) \approx -15.3$ and $\log(a_{H^+}^3/a_{Al^{3+}}) \approx -9.8$.

511

512 An equation describing plagioclase dissolution rates at 22 °C can be obtained by
 513 combining the observations summarized in Fig. 8 with Eqs. (5) and (11) to yield for $pH \geq 6$

$$514 \quad \text{Log}(r_+/(mol/cm^2/s)) = 0.35\text{Log}(a_{H^+}^3/a_{Al^{3+}}) - 11.53 \quad (12)$$

515 and for $pH < 6$

$$516 \quad \text{Log}(r_+/(mol/cm^2/s)) = n_{acid}\text{Log}(a_{H^+}^3/a_{Al^{3+}}) + 0.033An\% - 14.77 \quad (13a)$$

517 where n_{acid} refers to the value of the n generated from a linear fit of the slopes of the linear
 518 correlations shown in Fig. 8b given by

$$519 \quad n_{acid} = 0.004 An\% + 0.05 \quad (13b)$$

520 and $An\%$ represents the percent anorthite in the plagioclase solid solution. Note that Eqs. (12)
 521 and (13) account for the effects of the presence of various aqueous species on rates through
 522 their affect on the activity of the aqueous Al^{3+} species.

523 The degree to which Eqs. (12) and (13) describe the measured plagioclase steady-state
 524 dissolution rates can be assessed with the aid of Fig. 9. The average difference between
 525 calculated rates and the 40 rates measured during the experiments run in series is 0.22 log
 526 units. The corresponding difference between calculated and the 31 rates measured in the
 527 individual experiments is 0.5 log units. It is evident that rates obtained from the experiments
 528 run in series for approximately 75 hours are better described by these equations than those
 529 obtained in the longer individual experiments, due to the better consistency of the former
 530 dataset.

531

532 **3.5.4 Effects in natural waters and regional metamorphism**

533 The dissolution behaviour of primary minerals in basaltic rocks controls the availability
534 of cations for secondary mineral formation (Gislason and Eugster, 1987a; Neuhoff et al.,
535 2000; Fridriksson et al., 2001; Neuhoff and Ruhl, 2006; Rogers et al., 2006; Armorsson and
536 Neuhoff, 2007). At acid conditions plagioclase dissolution rates increase with increasing
537 An% promoting Ca-rich secondary phase formation. At basic conditions the far-from-
538 equilibrium dissolution rates of all plagioclases are identical. It follows that, during the
539 weathering of basaltic terrains which results in high pH fluids, the cation availability reflects
540 the plagioclase composition (Gudbrandsson et al., 2011). This is evident in the low
541 temperature alteration of Iceland where the availability of Na, Ca, and Al results in the zeolites
542 phillipsite, thomsonite, and chabazite, and smectite clay layers (Walker, 1960;
543 Kristmannsdottir and Tomasson, 1978; Neuhoff et al., 2000; Fridriksson et al., 2001).

544

545 **3.5.5 Consequences for subsurface carbon storage**

546 Basaltic rocks are desirable targets for mineral carbon storage due to their high divalent
547 metal cation concentration (Oelkers et al., 2008; Assayag et al., 2009; Matter and Kelemen,
548 2009; Gislason et al., 2010; Matter et al., 2011). The dissolution of basalt by acidic CO₂-rich
549 fluids both neutralizes the fluid and releases divalent metal cations. The released divalent
550 metals can promote mineral carbon storage through carbonate mineral precipitation. Much of
551 the divalent cations released by this process stems from anorthite-rich plagioclase dissolution.
552 The results presented in this study suggest that although the dissolution rates of the anorthite-
553 rich plagioclases decrease dramatically with increasing pH at acid conditions, these rates
554 minimize and increase with increasing pH at basic conditions. As such, divalent cation
555 release and basalt carbonation may be enhanced at elevated pH where Ca-release due to
556 plagioclase dissolution could promote calcite precipitation. This conclusion is consistent
557 with observations reported by Gudbrandsson et al. (2011) showing that the Ca percent of the
558 divalent metal cations released during the dissolution of crystalline basalt increases
559 continuously with increasing pH; at pH 11, >80% of the divalent metal flux stemming from
560 crystalline basalt dissolution was due to Ca release from plagioclase. Carbonation via calcite
561 precipitation at high pH conditions may be particularly favourable due to the low solubility of
562 carbonate minerals at these conditions.

563

564 **3.6 Conclusions**

565 The results described above illuminate the dissolution behaviour of the plagioclase
566 feldspars as a function of their composition and fluid pH. Rates depend strongly on
567 plagioclase composition at acid conditions, where the dissolution rates increase with the
568 increasing anorthite content of the plagioclase. In contrast, at alkaline conditions plagioclase
569 dissolution rates are independent of its composition. Regression of the experimental results
570 generated in this study enabled generation of a simple equation describing plagioclase
571 dissolution rates. The success of this equation to describe rates over wide ranges of fluid
572 composition and plagioclase compositions suggests this equation can provide useful
573 dissolution rate estimates in a variety of natural and industrial systems.

574

575

576

577

578 Acknowledgements

579 We would like to thank our friends and colleagues, including Helgi A. Alfredsson, Gabrielle
580 J. Stockmann, Alexander P. Gysi, Iwona Monika Galeczka, Kiflom Gebrehiwot, Eydís
581 Salome Eiríksdóttir, Andri Stefánsson, and Niels Óskarsson at the University of Iceland,
582 Thierry Aigouy, Sophy Gouy, Philippe de Parseval, Julien Declercq, Jacques Schott,
583 Vasileios Mavromatis, Quentin Gautier, at the GET/CNRS in Toulouse, Ingvi Gunnarsson,
584 Edda Sif Aradóttir and Bergur Sigfússon at Reykjavík Energy. We would like to thank the
585 Department of Mineral Sciences at the Smithsonian Institution for anorthite sample, NMNH
586 122261, used in this study. This study was funded by The Environmental Fund of Reykjavík
587 Energy through the CARB-FIX project, and the European Community through DELTA-MIN
588 (Mechanisms of Mineral Replacement Reactions; Grant PITN-GA-2008-215360) and CARB-
589 FIX (Collaborative Project-FP7-469 ENERGY-2011-1-283148).

590

591

592

593

594 **Figure captions.**

595

596 **Figure 1.** SEM photomicrographs of anorthite (An_{89} , left) and albite (An_2 , right) before
597 dissolution experiments (a, b), after experiments at acid conditions (c, d), and after
598 dissolution experiments at alkaline conditions (e, f). No secondary phases were observed and
599 the edges seem to be somewhat rounded by the dissolution.

600

601 **Figure 2.** Experimental design for the ParrTM Ti-reactor used in some of the individual
602 experiments performed in this study: a) inlet solution container, b) High Pressure Liquid
603 Chromatography (HPLC) pump, c) temperature and rotation speed control, d) stirring motor,
604 e) 300 mL Ti-reactor equipped with, from left, fluid inlet tube, thermocouple, magnetic
605 stirrer, and fluid outlet fixed with a 2 μm Ti filter, f) outlet solution passes through a 0.2 μm
606 cellulose acetate filter before sampling and ICP analysis, g) thermal insulation and furnace.

607

608 **Figure 3.** Steady-state plagioclase dissolution rates based on Si release for all experiments.
609 Open symbols represent rates obtained from experiments run in series for approximately 75
610 hours whereas filled symbols correspond to rates determined from individual experiments
611 that ran for more than 250 hours. The error bars correspond to 2 standard deviations of
612 steady-state rates based on Si concentrations.

613

614 **Figure 4.** Steady-state plagioclase dissolution rates based on Al release for all experiments.
615 Open symbols represent rates obtained from experiments run in series for approximately 75
616 hours whereas filled symbols correspond to rates determined from individual experiments
617 that ran for more than 250 hours. The error bars correspond to 2 standard deviations of rates
618 based on aluminium concentration at steady-state.

619

620 **Figure 5.** Ratio of plagioclase steady-state dissolution rates based on Al versus those based
621 on Si release. Open symbols represent rates obtained from experiments run in series for
622 approximately 75 hours, whereas filled symbols correspond to rates determined from
623 individual experiments that ran for minimum of 250 hours. The uncertainties on the ratios are
624 estimated to be 0.015 log units and are within the symbols in the figures.

625

626 **Figure 6.** Variation of measured plagioclase dissolution rates determined from experiments
627 run in series for approximately 75 hours as a function of plagioclase composition. Individual
628 plots groups results from within 0.3 pH units from those shown in the individual plots. The
629 error bars correspond to that of 2 standard deviations of steady-state plagioclase dissolution
630 rates based on Si concentrations.

631

632 **Figure 7.** Comparison of measured plagioclase dissolution rates determined in this study with
633 selected values of plagioclases with comparable chemical compositions reported in the
634 literature. Open symbols represent rates obtained from experiments run in series for
635 approximately 75 hours, whereas filled symbols correspond to rates determined from
636 individual experiments that ran for more than 250 hours. The error bars correspond to 2σ of
637 rates based on measured Si concentration.

638

639 **Figure 8:** Variation of the logarithm of plagioclase steady-state dissolution rates, based on Si
640 release, obtained from experiments run in series for approximately 75 hours, as a function of
641 the logarithm of the aqueous fluid activity ratio $(a_{H^+}^3/a_{Al_i^{3+}})$. Rates obtained at acidic and
642 alkaline conditions are shown in (a) and (b) respectively.

643

644 **Figure 9.** Comparison of measured steady-state plagioclase dissolution rates determined in
645 this study with corresponding rates calculated using Eqs. (12) and (13). Open symbols
646 represent rates obtained from experiments run in series for approximately 75 hours whereas
647 filled symbols correspond to rates determined from individual experiments that ran for more
648 than 250 hours.

649

650

651 **Annex Captions:**

652 **Annex A:** Temporal evolution of all plagioclase dissolution rates determined in the present
653 study based on Si release ($r_{+,Si}$) reported in (mol/cm²/s). Open symbols represent rates
654 generated from experiments performed in series running for approximately 75 hours
655 each. The filled symbols correspond to rates obtained from individual experiments run
656 for minimum of 250 hours each. Dashed lines correspond to the final steady-state
657 values in each experiment. The error bars correspond to 2 standard deviations of the
658 steady state rates.

659

660 **Annex B:** Temporal evolution of all plagioclase dissolution rates determined in the present
661 study based on Al release ($r_{+,Al}$) reported in (mol/cm²/s). Open symbols represent rates
662 generated from experiments performed in series running for approximately. 75 hours
663 each. The filled symbols correspond to rates obtained from individual experiments run
664 for minimum of 250 hours each. Dashed lines correspond to the final steady-state
665 values in each experiment. The error bars correspond to 2 standard deviations of the
666 steady state rates.

667

668 **Annex C:** Calculated saturation state of all steady-state reactive fluids with respect to the
669 indicated phases. Saturation states are negative if the mineral is undersaturated, but
670 positive if supersaturated. All saturation state values were calculated using the
671 PHREEQC computer code (Parkhurst and Appelo, 1999) using its llnl database together
672 with additions as noted in text.

673

674

675

676

677

678

679

680

681

682 REFERENCES

683

- 684 Aagaard P. and Helgeson H. C. (1977) Thermodynamic and kinetic constraints on the
685 dissolution of feldspars. *Geol. Soc. Am., Abstr. Progr.*, **9**, 873.
- 686 Aagaard P. and Helgeson, H.C. (1982) Thermodynamic and kinetic constraints on reaction-
687 rates among minerals and aqueous-Solutions .1. Theoretical Considerations. *Am. J.
688 Sci.* **282**, 237-285.
- 689 Alfredsson H.A., Hardarson B.S., Franzson H. and Gislason S.R. (2008) CO₂ sequestration in
690 basaltic rock at the Hellisheiði site in SW Iceland: stratigraphy and chemical
691 composition of the rocks at the injection site. *Min. Mag.* **72**, 1-5.
- 692 Amrhein C. and Suarez, D.L. (1992) Some factors affecting the dissolution kinetics of
693 anorthite at 25°C. *Geochim. Cosmochim. Acta* **56**, 1815-1826.
- 694 Apollaro, C., Accornero, M., Marini, L., Barca, D. and DeRosa, R. (2009) The impact of
695 dolomite and plagioclase weathering on the chemistry of shallow groundwaters
696 circulating in a granodiorite-dominated catchment of the Sila Massif (Calabria,
697 Southern Italy). *App. Geochem.* **24**, 957-979.
- 698 Aradottir E.S.P., Sigurdardottir H., Sigfusson, B. and Gunnlaugsson, E. (2011) CarbFix: a
699 CCS pilot project imitating and accelerating natural CO₂ sequestration. *Greenhouse
700 Gases-Sci. Tech.* **1**, 105-118.
- 701 Aradottir E.S.P., Sonnenthal E.L., Bjornsson G. and Jonsson H. (2012) Multidimensional
702 reactive transport modeling of CO₂ mineral sequestration in basalts at the Hellisheiði
703 geothermal field, Iceland. *Int. J. Greenhouse Gas Control* **9**, 24-40.
- 704 Arnorsson S. and Neuhoff P.S. (2007) Zeolite saturation in surface and < 100 °C ground
705 waters in a Tertiary basalt province, Iceland. In: Bullen, T.D., Wang, Y. (Eds.),
706 Water-Rock Interaction, Vols 1 and 2, Proceedings. Proceedings and Monographs in
707 Engineering, Water and Earth Sciences, pp. 935-938.
- 708 Arnorsson S. and Stefansson A. (1999) Assessment of feldspar solubility constants in water
709 in the range 0 to 350 °C at vapor saturation pressures. *Am. J. Sci.* **299**, 173-209.
- 710 Arvidson R.S., Beig M.S. and Luttge A. (2004) Single-crystal plagioclase feldspar
711 dissolution rates measured by vertical scanning interferometry. *Am. Min.* **89**, 51-56.
- 712 Arvidson R.S. and Luttge A. (2010) Mineral dissolution kinetics as a function of distance
713 from equilibrium - New experimental results. *Chem. Geol.* **269**, 79-88.
- 714 Assayag N., Matter J., Ader M. Goldberg D. and Agrinier, P. (2009) Water-rock interactions
715 during a CO₂ injection field-test: Implications on host rock dissolution and alteration
716 effects. *Chem. Geol.* **265**, 227-235.
- 717 Banfield J.L., Hamilton V.E. and Christensen, P.R. (2000) A global view of Martian surface
718 compositions from MGS-TES. *Science* **287**, 1626-1630.
- 719 Beig M.S. and Lütte A. (2006) Albite dissolution kinetics as a function of distance from
720 equilibrium: Implications for natural feldspar weathering. *Geochim. Cosmochim. Acta*
721 **70**, 1402-1420.
- 722 Berger G., Cadore E., Schott J. and Dove P.M. (1994) Dissolution rate of quartz in lead and
723 sodium electrolyte solutions between 25 and 300 °C: Effect of the nature of surface
724 complexes and reaction affinity. *Geochim. Cosmochim. Acta* **58**, 541-551.
- 725 Blake R.E. and Walter L.M. (1996) Effects of organic acids on the dissolution of orthoclase
726 at 80 °C and pH 6. *Chem. Geol.* **132**, 91-102.
- 727 Blum A. and Lasaga A. (1988) Role of surface speciation in the low-temperature dissolution
728 of minerals. *Nature* **331**, 431-433.

- 729 Blum A.E. and Lasaga A.C. (1991) The role of surface speciation in the dissolution of albite.
730 *Geochim. Cosmochim. Acta* **55**, 2193-2201.
- 731 Blum A.E. and Stillings L.L. (1995) Feldspar dissolution kinetics. *Rev. Min.*, **31**, 291-331.
- 732 Brady P.V. and Walther J.V. (1992) Surface chemistry and silicate dissolution at elevated
733 temperatures. *Am. J. Sci.* **292**, 639-639.
- 734 Brantley S.L. (2003) 5.03 - Reaction Kinetics of Primary Rock-forming Minerals under
735 Ambient Conditions. In: Editors-in-Chief: Heinrich, D.H., Karl, K.T. (Eds.), *Treatise*
736 on *Geochemistry*. Pergamon, Oxford, pp. 73-117.
- 737 Brantley S.L. (2008) Kinetics of mineral dissolution, Kinetics of water-rock interaction.
738 Springer, pp. 151-210.
- 739 Brantley S.L. and Stillings L. (1994) An integrated model for feldspar dissolution under acid
740 conditions. *Min. Mag. A*, **58**, 117-118.
- 741 Brantley S.L. and Stillings L.L. (1996) Feldspar dissolution at 25 °C and low pH. *Am. J. Sci.*
742 **296**, 101-127.
- 743 Broecker, W. (2012) The carbon cycle and climate change: Memoirs of my 60 years in
744 science. *Geochem. Perspectives*, **1**, 221-340.
- 745 Carroll S.A. and Knauss K.G. (2005) Dependence of labradorite dissolution kinetics on CO₂
746 _(aq), Al_(aq), and temperature. *Chem. Geol.* **217**, 213-225.
- 747 Casey W.H., Westrich H.R. and Arnold G.W. (1988) Surface chemistry of labradorite
748 feldspar reacted with aqueous solutions at pH = 2, 3, and 12. *Geochim. Cosmochim. Acta*
749 **52**, 2795-2807.
- 750 Casey W.H., Westrich H.R., Arnold G.W. and Banfield J.F. (1989a) The surface chemistry of
751 dissolving labradorite feldspar. *Geochim. Cosmochim. Acta* **53**, 821-832.
- 752 Casey W.H., Westrich H.R. and Holdren G.R. (1991) Dissolution rates of plagioclase at pH=
753 2 and 3. *Am. Min.* **76**, 211-217.
- 754 Casey W.H., Westrich H.R., Massis T., Banfield J.F. and Arnold, G.W. (1989b) The surface
755 of labradorite feldspar after acid hydrolysis. *Chem. Geol.* **78**, 205-218.
- 756 Chen, Y. and Brantley S.L. (1997) Temperature-and pH-dependence of albite dissolution rate
757 at acid pH. *Chem. Geol.* **135**, 275-290.
- 758 Chou L. and Wollast R. (1984) Study of the weathering of albite at room-temperature and
759 pressure with a fluidized-bed reactor. *Geochim. Cosmochim. Acta* **48**, 2205-2217.
- 760 Chou L. and Wollast R. (1985) Steady-state kinetics and dissolution mechanisms of albite.
761 *Am. J. Sci.* **285**, 963-993.
- 762 Dixit S. and Carroll S.A. (2007) Effect of solution saturation state and temperature on
763 diopside dissolution. *Geochem. Trans.* **8**.
- 764 Eyring H. (1935) The activated complex in chemical reactions. *J. Chem. Phys.* **3**, 107.
- 765 Flaathen T.K., Gislason S.R. and Oelkers E.H. (2010) The effect of aqueous sulphate on
766 basaltic glass dissolution rates. *Chem. Geol.* **277**, 345-354.
- 767 Flaathen T.K., Gislason S.R., Oelkers E.H. and Sveinbjornsdottir A.E. (2009) Chemical
768 evolution of the Mt. Hekla, Iceland, groundwaters: A natural analogue for CO₂
769 sequestration in basaltic rocks. *App. Geochem.* **24**, 463-474.
- 770 Franklin S.P., Hajash A., Dewers T.A. and Tieh, T.T. (1994) The role of carboxylic acids in
771 albite and quartz dissolution: An experimental study under diagenetic conditions.
772 *Geochim. Cosmochim. Acta* **58**, 4259-4279.
- 773 Fridriksson T., Neuhoff P.S., Arnórrsson S. and Bird D.K. (2001) Geological constraints on
774 the thermodynamic properties of the stilbite--stellerite solid solution in low-grade
775 metabasalts. *Geochim. Cosmochim. Acta* **65**, 3993-4008.

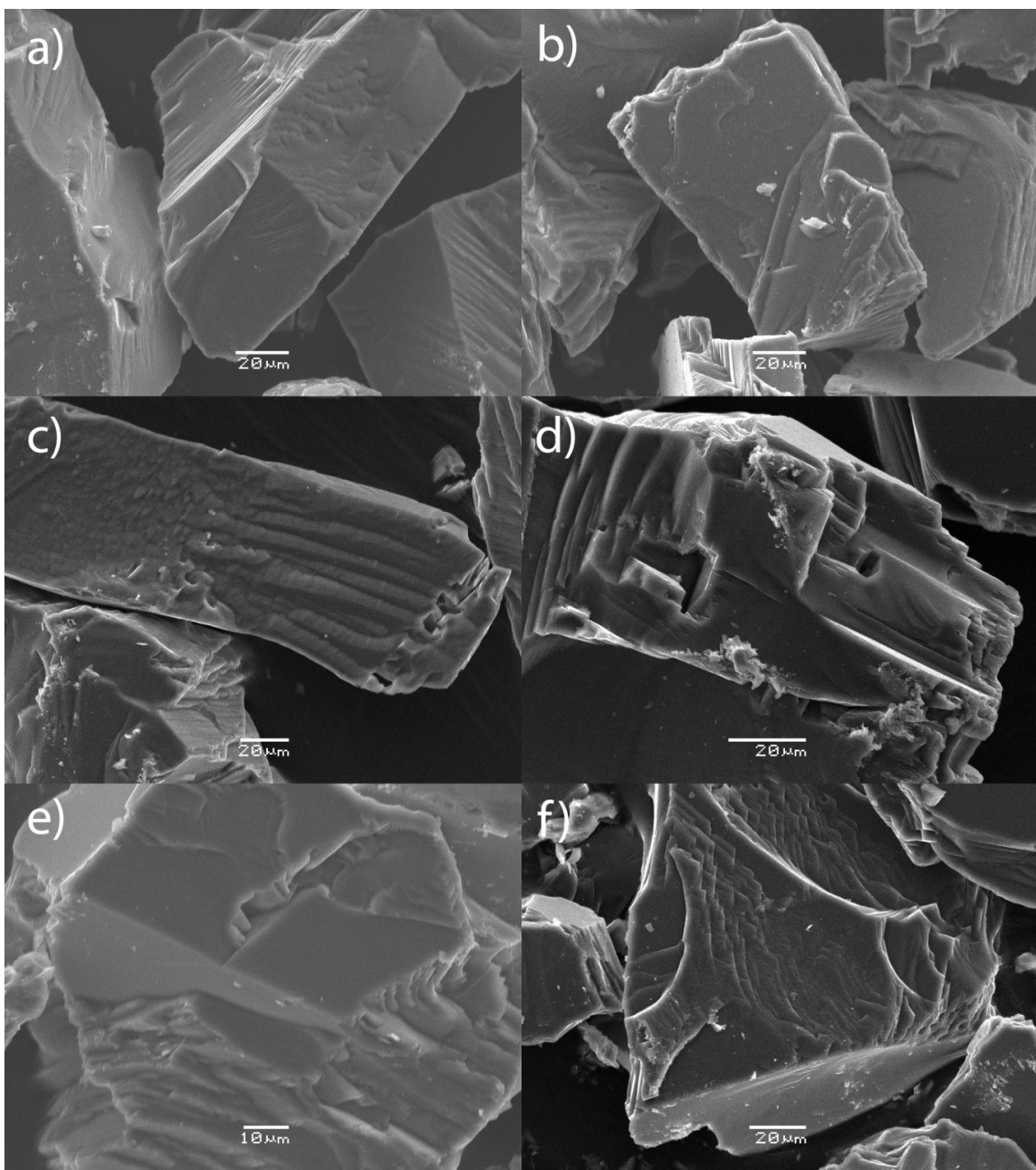
- 776 Fu Q., Lu P., Konishi H., Dilmore R., Xu H., Seyfried W. and Zhu, C. (2009) Coupled alkali-
777 feldspar dissolution and secondary mineral precipitation in batch systems: 1. New
778 experiments at 200 °C and 300 bars. *Chem. Geol.* **258**, 125-135.
- 779 Ganor J., Reznik I.J. and Rosenberg Y.O. (2009) Organics in water-rock interactions. *Rev.*
780 *Min. Geochem.* **70**, 259-369.
- 781 Gaus I., Azaroual M. and Czernichowski-Lauriol I. (2005) Reactive transport modelling of
782 the impact of CO₂ injection on the clayey cap rock at Sleipner (North Sea). *Chem.*
783 *Geol.* **217**, 319-337.
- 784 Gautier J.M., Oelkers E.H. and Schott J. (1994) Experimental study of K-feldspar dissolution
785 rates as a function of chemical affinity at 150 °C and pH 9. *Geochim. Cosmochim. Acta*
786 **58**, 4549-4560.
- 787 Gislason S.R. and Eugster H.P. (1987a) Meteoric water-basalt interactions 2. A Field-Study
788 in Ne Iceland. *Geochim. Cosmochim. Acta* **51**, 2841-2855.
- 789 Gislason S.R. and Oelkers E.H. (2003) Mechanism, rates, and consequences of basaltic glass
790 dissolution: II. An experimental study of the dissolution rates of basaltic glass as a
791 function of pH and temperature. *Geochim. Cosmochim. Acta* **67**, 3817-3832.
- 792 Gislason S.R., Wolff-Boenisch D., Stefansson A., Oelkers E. H., Gunnlaugsson E.,
793 Sigurdardottir H., Sigfusson B., Broecker W. S., Matter J. M., Stute M., Axelsson G.
794 and Fridriksson T. (2010) Mineral sequestration of carbon dioxide in basalt: A pre-
795 injection overview of the CarbFix project. *Int. J. Greenhouse Gas Control* **4**, 537-545.
- 796 Goldberg D.S., Kent D.V. and Olsen P.E. (2010) Potential on-shore and off-shore reservoirs
797 for CO₂ sequestration in Central Atlantic magmatic province basalts. *Proc. Nat. Acad.*
798 *Sci.* **107**, 1327-1332.
- 799 Goldberg D.S., Takahashi T. and Slagle A.L. (2008) Carbon dioxide sequestration in deep-
800 sea basalt. *Proc. Nat. Acad. Sci.* **105**, 9920-9925.
- 801 Gout R., Oelkers E.H., Schott J. and Wick A. (1997) The surface chemistry and structure of
802 acid-leached albite: New insights on the dissolution mechanism of the alkali feldspars.
803 *Geochim. Cosmochim. Acta* **61**, 3013-3018.
- 804 Grove T. (1977) Structural characterization of labradorite-bytownite plagioclase from
805 volcanic, plutonic and metamorphic environments. *Cont. Min. Pet.* **64**, 273-302.
- 806 Gudbrandsson S., Wolff-Boenisch D., Gislason S.R. and Oelkers E.H. (2011) An
807 experimental study of crystalline basalt dissolution from 2 <= pH <= 11 and
808 temperatures from 5 to 75 °C. *Geochim. Cosmochim. Acta*, **75**, 5496-5509.
- 809 Gysi A.P. and Stefánsson A. (2011) CO₂-water-basalt interaction. Numerical simulation of
810 low temperature CO₂ sequestration into basalts. *Geochim. Cosmochim. Acta* **75**, 4728-
811 4751.
- 812 Hamilton J.P., Pantano C.G. and Brantley S.L. (2000) Dissolution of albite glass and crystal.
813 *Geochim. Cosmochim. Acta*, **64**, 2603-2615.
- 814 Hangx S.J. and Spiers C.J. (2009) Reaction of plagioclase feldspars with CO₂ under
815 hydrothermal conditions. *Chem. Geol.* **265**, 88-98.
- 816 Harouiya N. and Oelkers E.H. (2004) An experimental study of the effect of aqueous fluoride
817 on quartz and alkali-feldspar dissolution rates. *Chem. Geol.* **205**, 155-167.
- 818 Helgeson H.C., Murphy W.M. and Aagaard P. (1984) Thermodynamic and kinetic
819 constraints on reaction rates among minerals and aqueous solutions .2. Rate constants,
820 effective surface area, and the hydrolysis of feldspar. *Geochim. Cosmochim. Acta* **48**,
821 2405-2432.
- 822 Hellevang, H., Pham, V.T.H. and Aagaard, P. (2013) Kinetic modelling of CO₂-water-rock
823 interactions. *Int. J. Greenhouse Gas Cont.*, **15**, 3-15.

- 824 Hellmann R. (1994) The albite-water system: Part I. The kinetics of dissolution as a function
825 of pH at 100, 200 and 300 °C. *Geochim. Cosmochim. Acta* **58**, 595-611.
- 826 Hellmann R. (1995) The albite-water system: Part II. The time-evolution of the stoichiometry
827 of dissolution as a function of pH at 100, 200, and 300 C. *Geochim. Cosmochim. Acta*
828 **59**, 1669-1697.
- 829 Hellmann R. (1997). The albite-water system: Part IV. Diffusion modeling of leached and
830 hydrogen-enriched layers. *Geochim. Cosmochim. Acta* **61**, 1595-1611.
- 831 Hellmann R., Daval D. and Tisserand D. (2010) The dependence of albite feldspar
832 dissolution kinetics on fluid saturation state at acid and basic pH: Progress towards a
833 universal relation. *Comptes Rendus Geosci.* **342**, 676-684.
- 834 Hellmann R., Eggleston C.M., Hochella M.F. and Crerar D.A. (1990) The formation of
835 leached layers on albite surfaces during dissolution under hydrothermal conditions.
836 *Geochim. Cosmochim. Acta* **54**, 1267-1281.
- 837 Hellmann R. and Tisserand D. (2006) Dissolution kinetics as a function of the Gibbs free
838 energy of reaction: An experimental study based on albite feldspar. *Geochim. Cosmochim. Acta*
839 **70**, 364-383.
- 840 Holdren G.R. and Speyer P.M. (1985) Reaction rate-surface area relationships during the
841 early stages of weathering—I. Initial observations. *Geochim. Cosmochim. Acta* **49**,
842 675-681.
- 843 Holdren G.R. and Speyer P.M. (1987) Reaction rate-surface area relationships during the
844 early stages of weathering. II. Data on eight additional feldspars. *Geochim. Cosmochim. Acta* **51**, 2311-2318.
- 845 Hwang W. and Longo J. (1992) The effects of organics on feldspar dissolution under
846 hydrothermal conditions. *Chem. Geol.* **98**, 271-292.
- 847 Inskeep W.P., Nater E.A., Bloom P.R., Vandervoort D.S. and Erich M.S. (1991)
848 Characterization of laboratory weathered labradorite surfaces using X-ray
849 photoelectron spectroscopy and transmission electron microscopy. *Geochim. Cosmochim. Acta*
850 **55**, 787-800.
- 851 Johnson J.W., Knauss K.G., Glassley W.E., DeLoach L.D. and Tompson A.F. (1998)
852 Reactive transport modeling of plug-flow reactor experiments: quartz and tuff
853 dissolution at 240 °C. *J. Hydrol.* **209**, 81-111.
- 854 Jordan G., Higgins S.R., Eggleston C.M., Swapp S.M., Janney D.E. and Knauss K.G. (1999)
855 Acidic dissolution of plagioclase: In-situ observations by hydrothermal atomic force
856 microscopy. *Geochim. Cosmochim. Acta* **63**, 3183-3191.
- 857 Kampman, N., Bickle, K., Becker, J. Assayag, N., Chapman H. (2009) Feldspar dissolution
858 kinetics and gibbs free energy dependence in a CO₂-enriched groundwater system,
859 Green River Utah. *Earth. Planet. Sci. Let.* **284**, 473-488.
- 860 Kelemen P.B. and Matter J. (2008) In situ carbonation of peridotite for CO₂ storage. *Proc.
861 Nat. Acad. Sci.* **105**, 17295-17300.
- 862 Knauss K.G. and Wolery T.J. (1986) Dependence of albite dissolution kinetics on pH and
863 time at 25 °C and 70 °C. *Geochim. Cosmochim. Acta* **50**, 2481-2497.
- 864 Köhler S.J., Bosbach D. and Oelkers E.H. (2005) Do clay mineral dissolution rates reach
865 steady state? *Geochim. Cosmochim. Acta* **69**, 1997-2006.
- 866 Kristmannsdottir H. and Tomasson J. (1978) Zeolite zones in geothermal areas in Iceland,
867 Natural Zeolites, Occurrence, Properties, Use LB Sand, FA Mumpton, 277–284.
- 868 Lagache M. (1965) Contribution à l'étude de l'altération des feldspaths dans l'eau, entre 100 et
869 200 °C sous diverses pressions de CO₂, et application à la synthèse des minéraux
870 argileux. Université, Faculté des Sciences.
- 871 Lasaga A.C. (1981) Transition state theory. *Rev. Min.* **8**, 135-169.

- 873 Marini L. (2006) Geological Sequestration of Carbon Dioxide: Thermodynamics, Kinetics,
 874 and Reaction Path Modeling. Elsevier, Amsterdam, 470 pp.
- 875 Marini, L., Ottonello, G., Canepa, M., Cipilli, F. (2000) Water-rock chemistry in the Bisagno
 876 valley (Genoa, Italy): application of an inverse approach to model spring water
 877 chemistry. *Geochim. Cosmochim. Acta* **64**, 2617-2635.
- 878 Mast A.M. and Drever J.I. (1987) The effect of oxalate on the dissolution rates of oligoclase
 879 and tremolite. *Geochim. Cosmochim. Acta* **51**, 2559-2568.
- 880 Matter J.M., Broecker W.S., Gislason S.R., Gunnlaugsson E., Oelkers E.H., Stute M.,
 881 Sigurdardóttir H., Stefansson A., Alfreðsson H.A., Aradóttir E.S., Axelsson G.,
 882 Sigfússon B. and Wolff-Boenisch D. (2011) The CarbFix Pilot Project—Storing carbon
 883 dioxide in basalt. *Energy Procedia* **4**, 5579-5585.
- 884 Matter J.M. and Kelemen P.B. (2009) Enhanced in situ carbonation of peridotite for
 885 permanent CO₂ storage. *Geochim. Cosmochim. Acta*, **73**, A848-A848.
- 886 McGlynn I.O., Fedo C.M. and McSween H.Y. (2012) Soil mineralogy at the Mars
 887 Exploration Rover landing sites: An assessment of the competing roles of physical
 888 sorting and chemical weathering. *J. Geophys. Res.* **117**(E1): E01006.
- 889 McGrail B.P., Schaef H.T., Ho A.M., Chien Y.J., Dooley J.J. and Davidson C.L. (2006)
 890 Potential for carbon dioxide sequestration in flood basalts. *JGR Research* **111**, B12.
- 891 McSween H.Y., McGlynn I.O. and Rogers A.D. (2010) Determining the modal mineralogy
 892 of Martian soils. *JGR Research* **115**, E7.
- 893 Metz B., Davidson O., De Coninck H. C., Loos M., and Meyer L. A. (2005). IPCC, 2005:
 894 IPCC special report on carbon dioxide capture and storage. Prepared by Working
 895 Group III of the Intergovernmental Panel on Climate Change. Cambridge, United
 896 Kingdom and New York, NY, USA, 442 pp.
- 897 Muir I. and Nesbitt H. (1991) Effects of aqueous cations on the dissolution of labradorite
 898 feldspar. *Geochim. Cosmochim. Acta* **55**, 3181-3189.
- 899 Munz I.A., Brandvoll Ø., Haug T.A., Iden K., Smeets R., Kihle J. and Johansen H. (2012).
 900 Mechanisms and rates of plagioclase carbonation reactions. *Geochimica et
 901 Cosmochimica Acta*, **77**, 27-51.
- 902 Murakami T., Kogure T., Kadohara H. and Ohnuki T. (1998) Formation of secondary
 903 minerals and its effect on anorthite dissolution. *Am. Min.* **83**, 1209-1219.
- 904 Nesbitt H., Macrae N. and Shotyk W. (1991) Congruent and incongruent dissolution of
 905 labradorite in dilute, acidic, salt solutions. *J. Geol.* **99**, 429-442.
- 906 Nesbitt H.W. and Muir I.J. (1988) SIMS depth profiles of weathered plagioclase and
 907 processes affecting dissolved Al and Si in some acidic soil solutions. *Nature* **334**,
 908 336-338.
- 909 Neuhoff P.S. (1999) Thermodynamic properties and paragenesis of rock-forming zeolites.
 910 Dissertation Thesis, Standford University, 240 pp.
- 911 Neuhoff P.S., Fridriksson T. and Bird D.K. (2000) Zeolite parageneses in the north Atlantic
 912 igneous province: Implications for geotectonics and groundwater quality of basaltic
 913 crust. *Int. Geol. Rev.* **42**, 15-44.
- 914 Neuhoff P.S. and Ruhl L.S. (2006) Mechanisms and geochemical significance of Si-Al
 915 substitution in zeolite solid solutions. *Chem. Geol.* **225**, 373-387.
- 916 Oelkers E.H. (2001) General kinetic description of multioxide silicate mineral and glass
 917 dissolution. *Geochim. Cosmochim. Acta* **65**, 3703-3719.
- 918 Oelkers E.H. and Cole D.R. (2008) Carbon dioxide sequestration a solution to a global
 919 problem. *Elements*, **4**, 305-310.
- 920 Oelkers E.H., Gislason S.R. and Matter J. (2008) Mineral Carbonation of CO₂. *Elements* **4**,
 921 333-337.

- 922 Oelkers E.H., Golubev S.V., Chairat C., Pokrovsky O.S. and Schott J. (2009) The surface
923 chemistry of multi-oxide silicates. *Geochim. Cosmochim. Acta* **73**, 4617-4634.
- 924 Oelkers E.H. and Schott J. (1995) Experimental study of anorthite dissolution and the relative
925 mechanism of feldspar hydrolysis. *Geochim. Cosmochim. Acta* **59**, 5039-5053.
- 926 Oelkers E.H. and Schott J. (1998) Does organic acid adsorption affect alkali-feldspar
927 dissolution rates? *Chem. Geol.* **151**, 235-245.
- 928 Oelkers E.H. and Schott J. (2001) An experimental study of enstatite dissolution rates as a
929 function of pH, temperature, and aqueous Mg and Si concentration, and the
930 mechanism of pyroxene/pyroxenoid dissolution. *Geochim. Cosmochim. Acta* **65**,
931 1219-1231.
- 932 Oelkers E.H., Schott J. and Devidal J.L. (1994) The effect of aluminum, pH and chemical
933 affinity on the rates of aluminosilicate dissolution reactions. *Geochim. Cosmochim.
Acta* **58**, 2011-2024.
- 935 Oxburgh R., Drever J.I. and Sun Y.T. (1994) Mechanism of plagioclase dissolution in acid-
936 solution at 25 °C. *Geochim. Cosmochim. Acta* **58**, 661-669.
- 937 Palandri J.L. and Kharaka Y.K. (2004) A compilation of rate parameters of water-mineral
938 interaction kinetics for application to geochemical modeling, U.S.G.S Open file report
939 2004-1068, 64 p.
- 940 Parkhurst D.L. and Appelo C.A.J. (1999) User's guide to PHREEQC (Version 2)—A
941 computer program for speciation, batch-reaction, one-dimensional transport, and
942 inverse geochemical calculations. U. S. G. S. Water Resour. Inv. Report. 99-4259.
- 943 Pham, V.T.H., Lu, P., Aagaard, P., Zhu, C., and Hellevang, H. (2010) On the potential of
944 CO₂-water-rock interactions for CO₂ storage using a modified kinetic model. *Int. J.
Greenhouse Gas Cont.*, **5**, 1002-1015.
- 945 Plumper, O. and Putnis, A. (2009) The complex hydrothermal history of granitic rocks:
946 Multiple feldspar replacement reactions under subsolidus conditions. *J. Petrology*, **50**,
947 967-987.
- 948 Prigobbe V., Costa G., Baciocchi R., Hanchen M. and Mazzotti M. (2009) The effect of CO₂
949 and salinity on olivine dissolution kinetics at 120 °C. *Chem. Eng. Sci.* **64**, 3510-3515.
- 950 Putnis, A., and Austrheim, H. (2010) Fluid-induced processes: Metasomatism and
951 metamorphism. *Geofluids*, **10**, 254-269.
- 952 Putnis, A., Hinrichs, R., Putnis, C.V., Golla-Schindler, U. and Collins, L. G. (2007) Hematite
953 in porous red-clouded feldspars: Evidence of large-scale crustal fluid-rock interaction.
954 *Lithos* **95**, 10-18.
- 955 Putnis A. and Putnis C.V. (2007) The mechanism of reequilibration of solids in the presence
956 of a fluid phase. *J. Solid State Chem.* **180**, 1783-1786.
- 957 Rogers K.L., Neuhoff P.S., Pedersen A.K. and Bird D.K. (2006) CO₂ metasomatism in a
958 basalt-hosted petroleum reservoir, Nuussuaq, West Greenland. *Lithos* **92**, 55-82.
- 959 Rose N. (1991) Dissolution rates of prehnite, epidote, and albite. *Geochim. Cosmochim. Acta*,
960 **55** 3273-3286.
- 961 Schaeaf H.T. and McGrail B.P. (2009) Dissolution of Columbia River Basalt under mildly
962 acidic conditions as a function of temperature: Experimental results relevant to the
963 geological sequestration of carbon dioxide. *App. Geochem.* **24**, 980-987.
- 964 Schaeaf H.T., McGrail B.P. and Owen A.T. (2009) Basalt-CO₂-H₂O interactions and
965 variability in carbonate mineralization rates. *Energy Procedia*, **1** 4899-4906.
- 966 Schott J., Pokrovsky O.S. and Oelkers E.H. (2009) The link between mineral
967 dissolution/precipitation kinetics and solution chemistry. *Rev. Mineral. Geochem.* **70**,
968 207-258.
- 969 Smith J.V. and Brown W.L. (1988) Feldspar minerals. Springer-Verlag. p. 828.

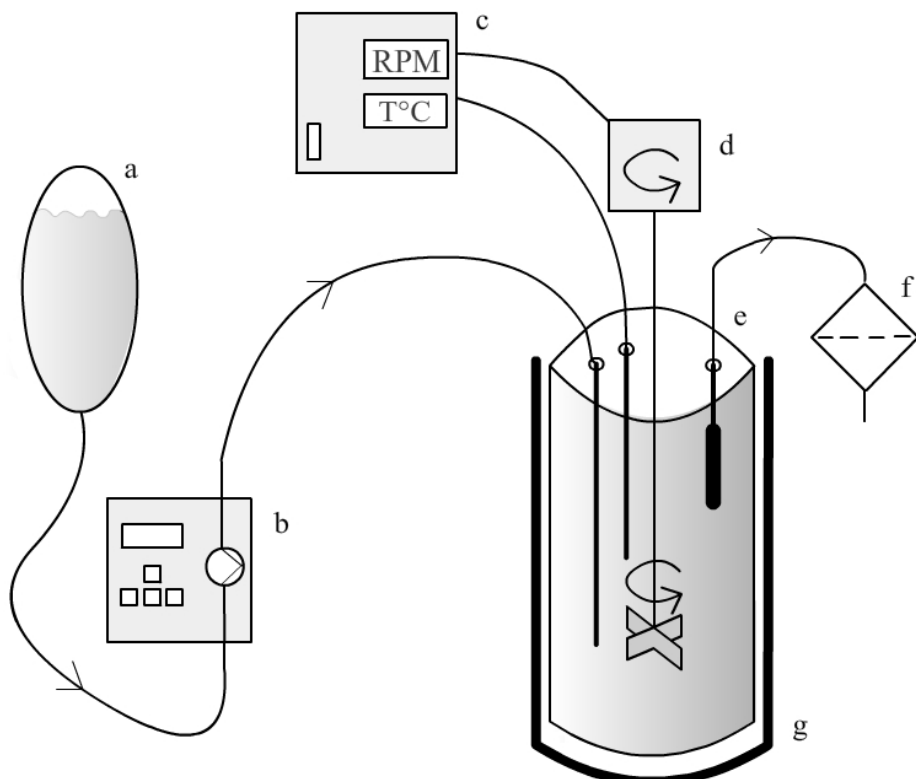
- 971 Sorai M. and Sasaki M. (2010) Dissolution kinetics of anorthite in a supercritical CO₂-water
972 system. *Am. Mineral.* **95**, 853-862.
- 973 Stillings L.L. and Brantley S.L. (1995) Feldspar dissolution at 25 °C and pH 3: Reaction
974 stoichiometry and the effect of cations. *Geochim. Cosmochim. Acta* **59**, 1483-1496.
- 975 Stillings L.L., Drever J.I., Brantley S.L., Sun, Y. and Oxburgh R. (1996) Rates of feldspar
976 dissolution at pH 3–7 with 0–8 mM oxalic acid. *Chem. Geol.* **132**, 79-89.
- 977 Stockmann G.J., Wolff-Boenisch D., Gislason S.R. and Oelkers E.H. (2011) Do carbonate
978 precipitates affect dissolution kinetics? 1: Basaltic glass. *Chem. Geol.*, **284**, 306-316.
- 979 Taylor A.S., Blum J.D. and Lasaga A.C. (2000) The dependence of labradorite dissolution
980 and Sr isotope release rates on solution saturation state. *Geochim. Cosmochim. Acta*
981 **64**, 2389-2400.
- 982 Ullman W.J. and Welch S.A. (2002) Organic ligands and feldspar dissolution. Water–rock
983 interactions, ore deposits, and environmental geochemistry: A tribute to David Crerar.
984 Special publication, **7**, 3-35.
- 985 Walker G.P. (1960) Zeolite zones and dike distribution in relation to the structure of the
986 basalts of eastern Iceland. *J. Geol.* **51**, 515-528.
- 987 Welch S., Barker W. and Banfield J. (1999) Microbial extracellular polysaccharides and
988 plagioclase dissolution. *Geochim. Cosmochim. Acta* **63**, 1405-1419.
- 989 Welch S.A. and Ullman W.J. (1993) The effect of organic acids on plagioclase dissolution
990 rates and stoichiometry. *Geochim. Cosmochim. Acta* **57**, 2725-2736.
- 991 Welch S. and Ullman W. (1996) Feldspar dissolution in acidic and organic solutions:
992 Compositional and pH dependence of dissolution rate. *Geochim. Cosmochim. Acta*
993 **60**, 2939-2948.
- 994 Welch S.A. and Ullman W.J. (2000) The temperature dependence of bytownite feldspar
995 dissolution in neutral aqueous solutions of inorganic and organic ligands at low
996 temperature (5–35 C). *Chem. Geol.*, **167**, 337-354.
- 997 White S., Allis R., Moore J., Chidsey T., Morgan C., Gwynn W. and Adams M. (2005)
998 Simulation of reactive transport of injected CO₂ on the Colorado Plateau, Utah, USA.
999 *Chem. Geol.*, **217**, 387-405.
- 1000 Wolff-Boenisch D., Gislason S.R. and Oelkers E.H. (2004) The effect of fluoride on the
1001 dissolution rates of natural glasses at pH 4 and 25 °C. *Geochim. Cosmochim. Acta* **68**,
1002 4571-4582.
- 1003 Wolff-Boenisch D., Wenau S., Gislason S.R. and Oelkers E.H. (2011) Dissolution of basalts
1004 and peridotite in seawater, in the presence of ligands, and CO₂: Implications for
1005 mineral sequestration of carbon dioxide. *Geochim. Cosmochim. Acta*, **75**, 5510-5525.
- 1006 Xu T., Apps J.A. and Pruess K. (2005) Mineral sequestration of carbon dioxide in a
1007 sandstone–shale system. *Chem. Geol.* **217**, 295-318.



1008

1009

1010 **Figure 1.**



1011

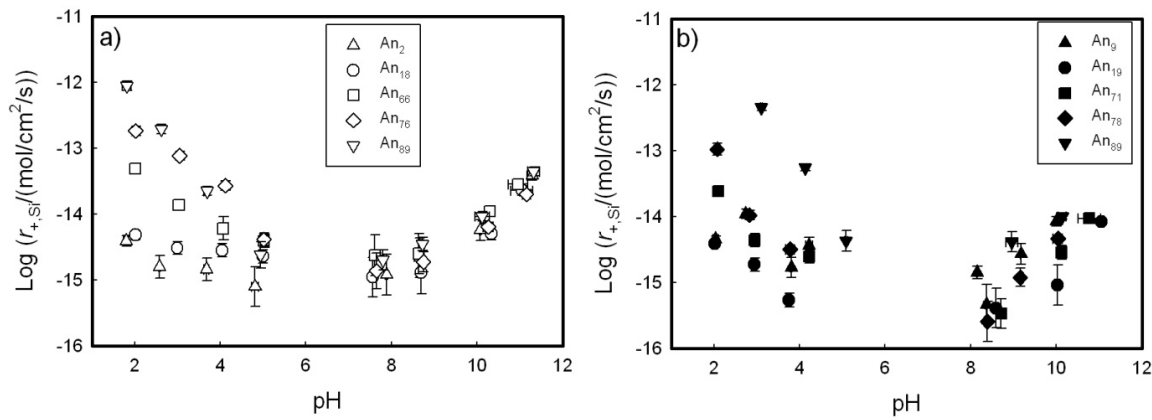
1012

1013

1014 **Figure 2.**

1015

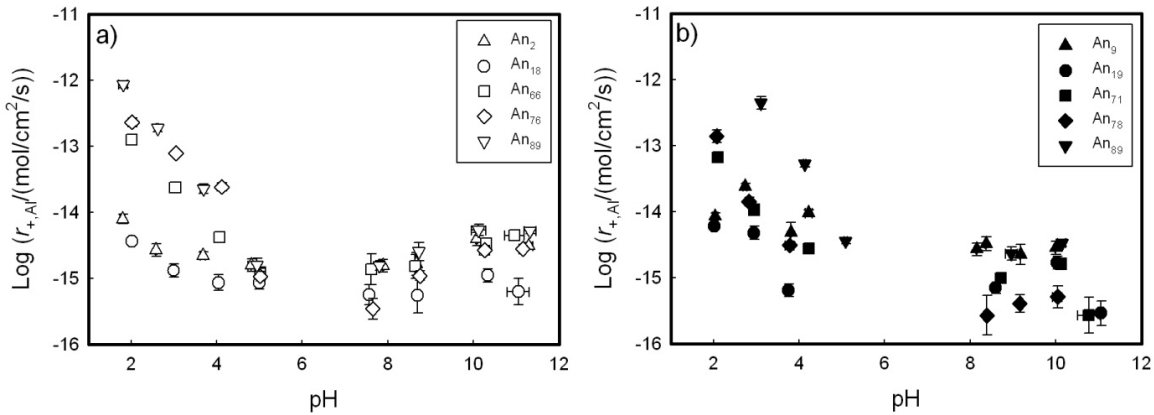
1016



1017

1018 **Figure 3.**

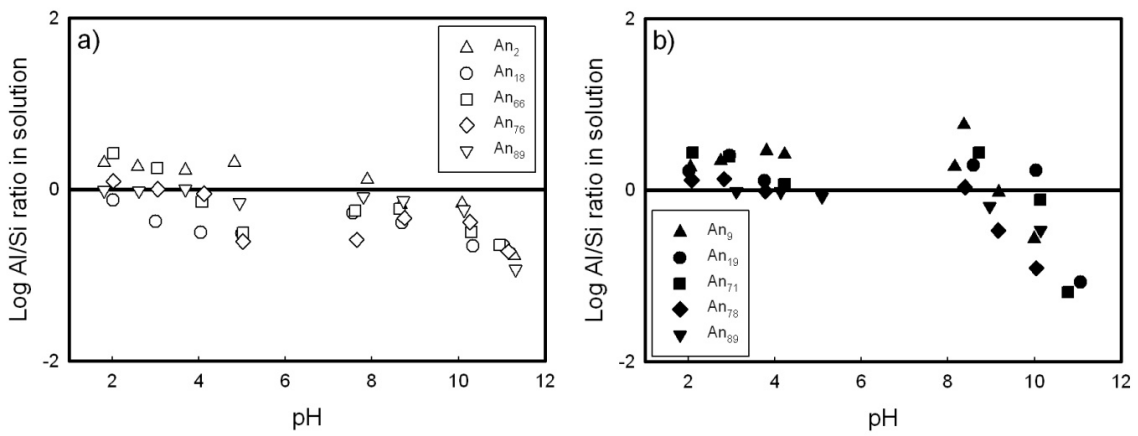
1019



1020

1021 **Figure 4.**

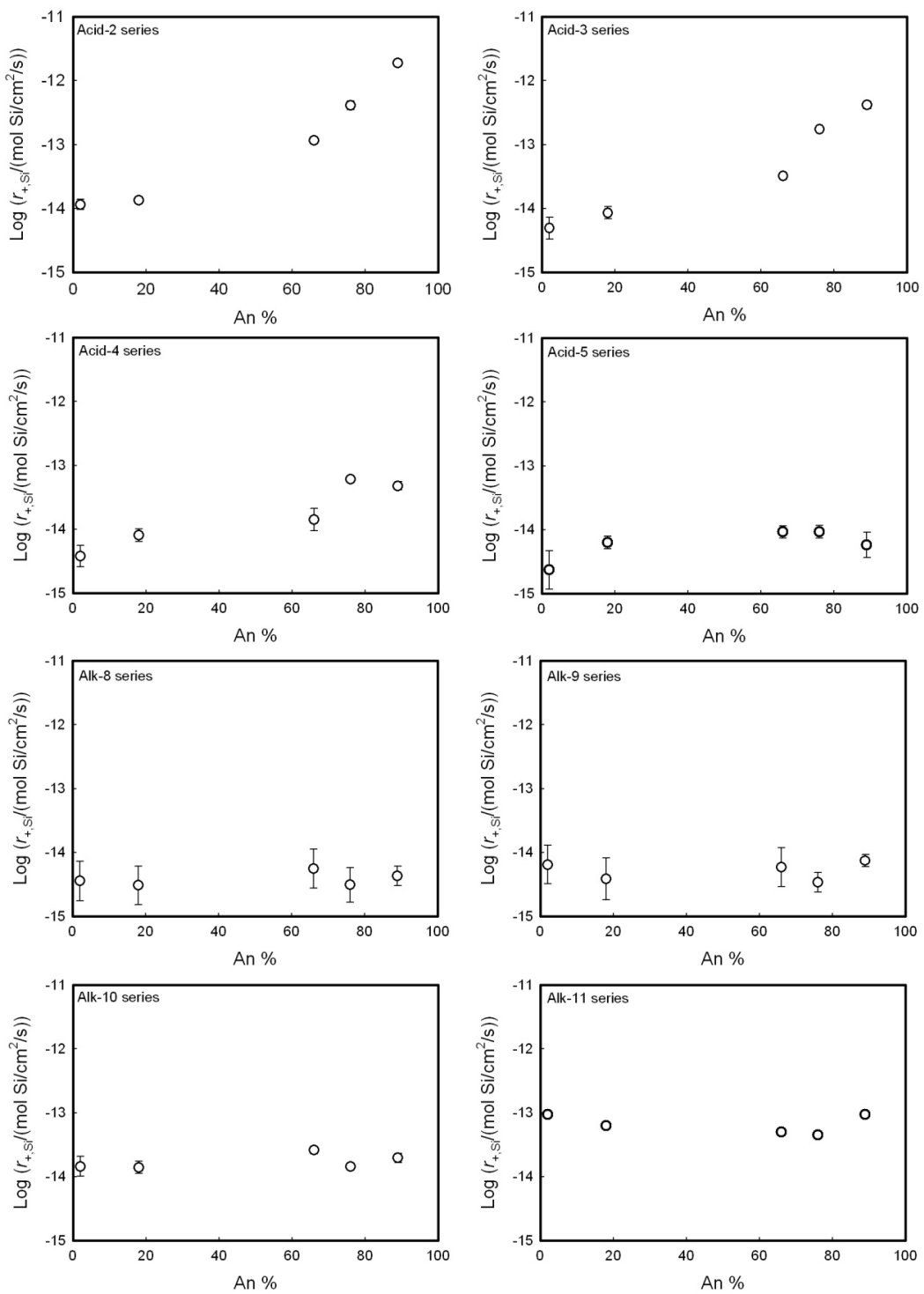
1022



1023

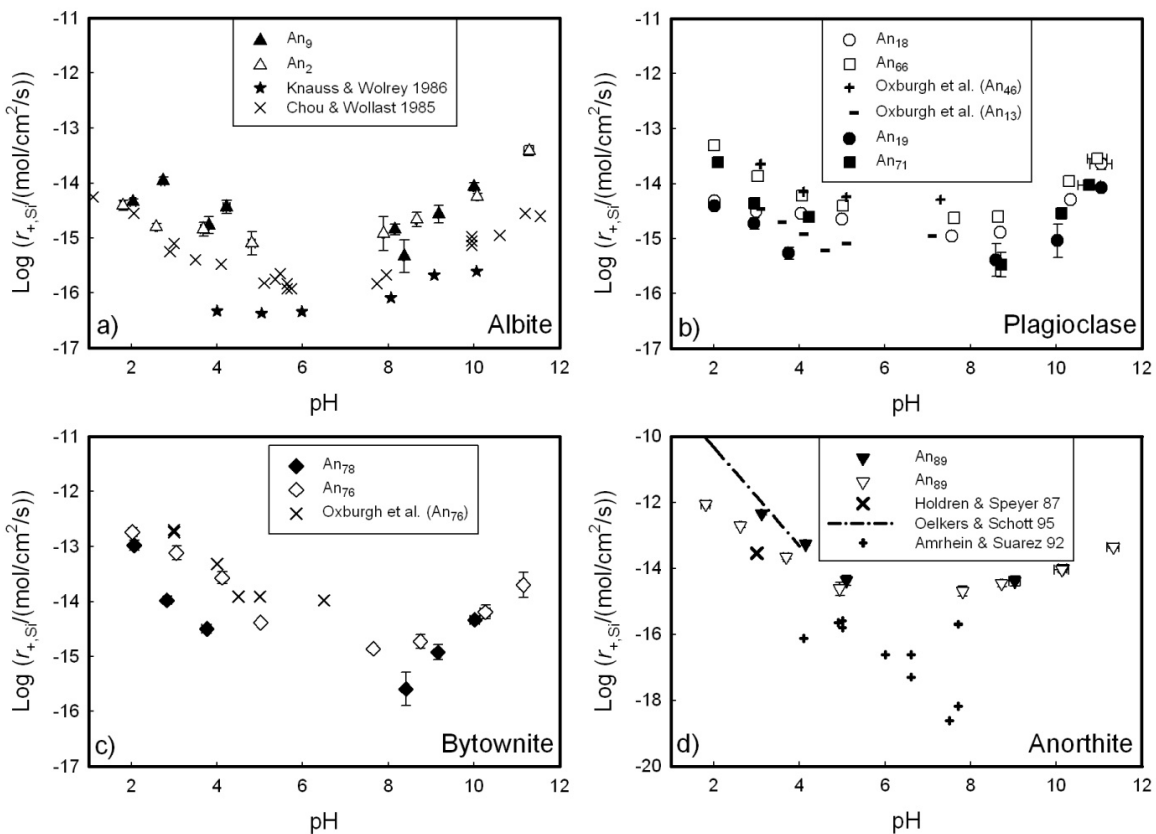
1024 **Figure 5.**

1025



1026

1027 **Figure 6.**



1028

1029 **Figure 7.**

1030

1031

1032

1033

1034

1035

1036

1037

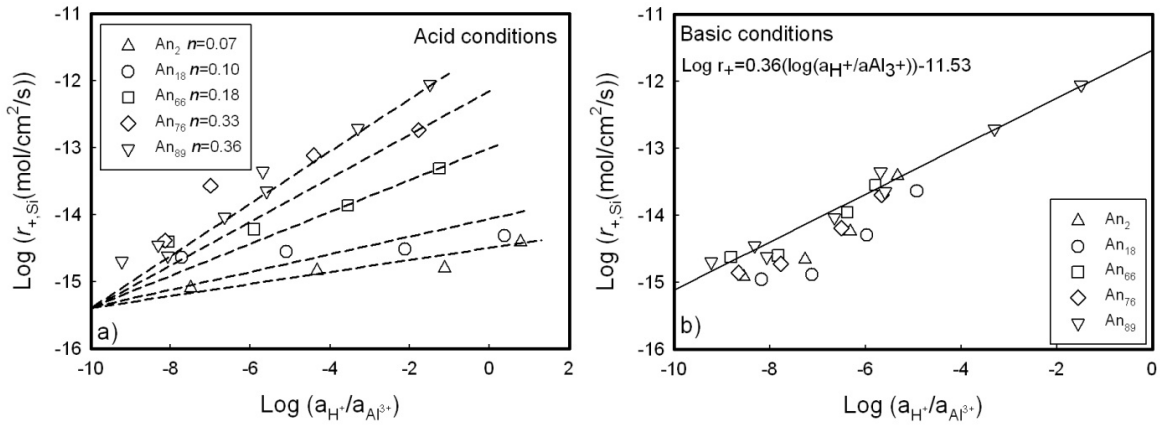
1038

1039

1040

1041

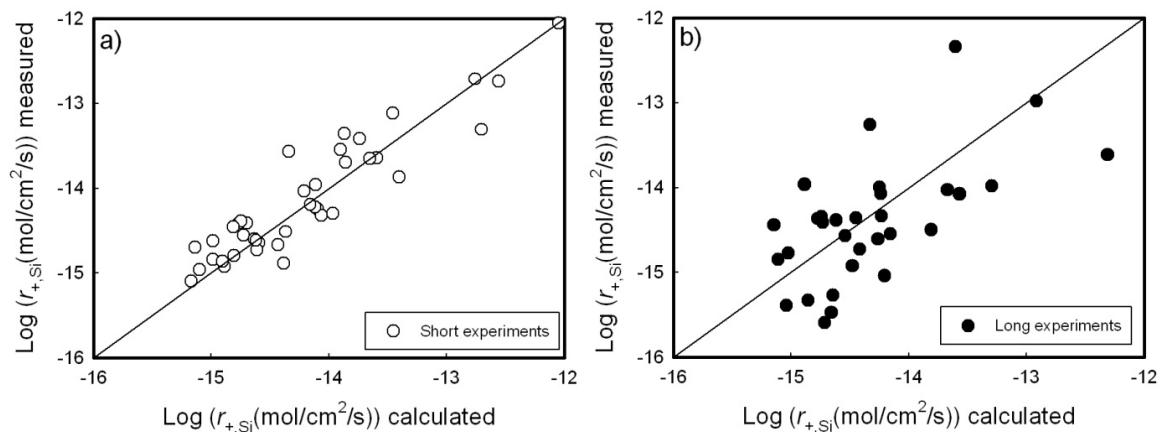
1042



1043

1044 **Figure 8.**

1045



1046

1047 **Figure 9.**

1048

1049

1050

1051

1052

1053

1054

1055

1056 Table 1. Origin, chemical composition, and specific surface area of the plagioclases used in
 1057 this study.

Mineral	Origin	Ref.	Chemical analysis			BET (cm ² /g)	General formula	Log K _{25°C}
			# of analysis	An%	σ*			
Albite ^a	Virginia, USA	49-5851	35	1.6	0.6	911	Na _{0.99} Ca _{0.01} Al _{1.04} Si _{2.97} O ₈	-20.15
Albite ^b	Ontario, Canada	46 E 0233	41	8.9	4.1	1638	Na _{0.91} Ca _{0.09} Al _{1.11} Si _{2.89} O ₈	-20.10
Oligoclase ^a	Ontario, Canada	49-5915	37	18.2	1.5	1124	Na _{0.79} Ca _{0.21} Al _{1.21} Si _{2.78} O ₈	-20.05
Oligoclase ^b	Ontario, Canada	46 E 5803	40	18.9	1.0	1159	Na _{0.79} Ca _{0.19} Al _{1.19} Si _{2.81} O ₈	-20.05
Labradorite ^a	Oregon, USA	Andesine	63	65.5	1.1	856	Na _{0.34} Ca _{0.66} Al _{1.63} Si _{2.35} O ₈	-19.96
Labradorite ^b	Oregon, USA	49 E 5877	30	70.5	1.3	811	Na _{0.30} Ca _{0.72} Al _{1.69} Si _{2.29} O ₉	-19.97
Bytownite ^a	Minnesota, USA	49 E 5859	35	75.5	3.2	1611	Na _{0.24} Ca _{0.77} Al _{1.73} Si _{2.25} O ₈	-19.98
Bytownite ^b	Hrapsey, Iceland	Anorthosite	161	77.6	2.1	5310	Na _{0.23} Ca _{0.79} Al _{1.71} Si _{2.25} O ₈	-19.17
Anorthite ^{a,b,c}	Pacaya, Guatemala	NMNH#122261	28	88.8	3.2	944	Na _{0.13} Ca _{0.87} Al _{1.83} Si _{2.14} O ₈	-19.70

^a Used in experiments that were run in series

^b Used in individual experiments

^c Sample from The Smithsonian

* Standard deviation

1058
1059

1060

1061 Table 2. Chemical composition of the plagioclases used in this study as determined by
 1062 microprobe analysis.

	Albite ¹	Albite ²	Oligoclase ¹	Oligoclase ²	Labradorite ¹	Labradorite ²	Bytownite ¹	Bytownite ²	Anorthite
Wt % oxide									
SiO ₂	67.5	65.1	62.7	63.1	51.0	49.7	48.5	48.5	46.4
Al ₂ O ₃	20.0	21.2	23.1	22.8	30.1	31.0	31.6	31.3	33.6
Fe ₂ O ₃	0.0	0.0	0.07	0.0	0.5	0.4	0.47	0.67	0.63
CaO	0.3	1.9	4.44	4.0	13.4	14.5	15.4	15.9	17.6
Na ₂ O	11.6	10.5	9.23	9.1	3.9	3.3	2.72	2.51	1.47
K ₂ O	0.14	0.10	0.37	0.4	0.1	0.1	0.08	0.05	0.03

¹ Used in experiments run in series

² Used in experiments run individually

1063

1064

1065

1066

1067

1068

1069

1070

1071

1072

1073

1074

1075

1076

1077

1078

1079

1080

1081

1082

1083

1084 Table 3. Compositions of inlet fluids used in this study.

pH	HCl mmol/kg	NH ₄ OH mmol/kg	NH ₄ Cl mmol/kg
2	11.0	0	0
3	1.05	0	8.90
4	0.10	0	9.89
5	0.01	0	9.97
8	0	0.51	10.0
9	0	5.11	9.99
10	0	50.9	9.85
11	0	510	8.88

1085

1086

1087 Table 4. Experimental results of all dissolution experiments run as series in polyethylene
 1088 reactors for approximately 75 hours. Rates obtained from experiments that adhere to the
 1089 steady-state criteria are noted in bold font.

Exp. number	pH	Flow rate g/min	Surface area cm ²	C _{Si} mol/kg *10 ⁻⁶	C _{Ca} mol/kg *10 ⁻⁶	C _{Na} mol/kg *10 ⁻⁶	C _{Al} mol/kg *10 ⁻⁶	Al/Si	log r _{Plag,Si,BET} mol/cm ² /s	log r _{Plag,Al,BET} mol/cm ² /s
Ab-acid-5	4.8	2.48	3107	0.18	0.13	D.L.	0.12	1.97	-15.10	-14.80
Ab-acid-4	3.7	2.44	3107	0.33	0.05	D.L.	0.18	1.53	-14.84	-14.66
Ab-acid-3	2.6	2.43	3107	0.36	0.06	D.L.	0.21	1.69	-14.80	-14.57
Ab-acid-2	1.8	2.38	3107	0.91	0.25	D.L.	0.64	2.02	-14.41	-14.10
Ab-alk-8	7.9	2.45	3107	0.27	3.30	0.07	0.12	1.29	-14.92	-14.81
Ab-alk-9	8.7	2.41	3107	0.50	0.53	0.06	0.13	0.76	-14.66	-14.78
Ab-alk-10	10.1	2.45	3107	1.29	0.24	0.78	0.31	0.69	-14.24	-14.41
Ab-alk-11	11.3	2.40	3107	8.86	0.68	2.11	0.25	0.08	-13.42	-14.51
OI-acid-5	5.0	2.07	3990	0.73	1.60	D.L.	0.12	0.38	-14.64	-15.06
OI-acid-4	4.0	2.70	3990	0.70	0.27	D.L.	0.09	0.31	-14.55	-15.06
OI-acid-3	3.0	2.69	3990	0.76	1.01	D.L.	0.14	0.43	-14.51	-14.88
OI-acid-2	2.0	2.68	3990	1.20	0.78	D.L.	0.39	0.75	-14.32	-14.44
OI-alk-8	7.6	2.42	3923	0.30	0.66	1.04	0.07	0.51	-14.96	-15.25
OI-alk-9	8.7	2.55	3923	0.34	0.32	0.47	0.06	0.42	-14.88	-15.26
OI-alk-10	10.3	2.54	3923	1.31	0.66	0.65	0.12	0.22	-14.30	-14.96
OI-alk-11	11.1	2.52	3923	5.92	1.71	1.75	0.07	0.03	-13.64	-15.20
La-acid-5	5.0	2.34	3030	0.72	0.56	0.07	0.15	0.30	-14.41	-14.93
La-acid-4	4.1	2.42	3030	1.07	0.60	D.L.	0.53	0.70	-14.22	-14.38
La-acid-3	3.0	2.45	3030	2.37	2.02	0.11	2.97	1.75	-13.87	-13.62
La-acid-2	2.0	2.44	3030	8.65	8.27	2.27	15.9	2.58	-13.31	-12.90
La-alk-8	7.6	2.52	3099	0.41	1.22	0.68	0.17	0.57	-14.62	-14.86
La-alk-9	8.6	2.60	3099	0.42	0.82	0.57	0.18	0.61	-14.60	-14.82
La-alk-10	10.3	2.62	3099	1.84	2.35	0.72	0.41	0.31	-13.96	-14.47
La-alk-11	11.0	2.55	3099	4.88	0.99	1.43	0.56	0.16	-13.55	-14.35
By-acid-5	5.0	2.64	5655	1.19	0.75	0.48	0.24	0.26	-14.38	-14.97
By-acid-4	4.1	2.78	5655	7.41	2.07	1.47	5.13	0.90	-13.57	-13.61
By-acid-3	3.0	2.76	5655	21.3	9.84	4.83	16.8	1.02	-13.11	-13.10
By-acid-2	2.0	2.70	5655	51.7	22.1	8.88	50.1	1.26	-12.74	-12.64
By-alk-8	7.6	2.33	5558	0.44	51.5	1.05	0.09	0.25	-14.86	-15.46
By-alk-9	8.7	2.37	5558	0.60	9.44	0.71	0.27	0.58	-14.73	-14.96
By-alk-10	10.3	2.18	5558	2.20	4.30	1.14	0.71	0.42	-14.19	-14.57
By-alk-11	11.2	2.54	5558	5.93	2.70	1.67	0.64	0.14	-13.70	-14.55
An-acid-5	4.9	2.35	3313	0.44	0.22	D.L.	0.25	0.66	-14.62	-14.80
An-acid-4	3.7	2.35	3313	4.06	1.76	0.03	3.53	1.01	-13.65	-13.64
An-acid-3	2.6	2.40	3313	34.5	14.1	0.68	28.6	0.97	-12.71	-12.72
An-acid-2	1.8	2.36	3313	160	64.8	6.20	133	0.97	-12.05	-12.06
An-alk-8	7.8	2.41	3191	0.34	0.03	0.02	0.23	0.78	-14.70	-14.80
An-alk-9	8.7	2.38	3191	0.61	0.09	1.00	0.38	0.72	-14.45	-14.59
An-alk-10	10.1	2.36	3191	1.60	0.44	0.62	0.80	0.58	-14.04	-14.27
An-alk-11	11.3	2.34	3191	7.75	1.25	2.20	0.78	0.12	-13.35	-14.28

1091

1092

1093

1094

1095

1096 Table 5. Experimental results of all dissolution experiments run individually for more than
 1097 250 hours in titanium mixed flow reactors. Rates obtained from experiments that adhere to
 1098 the steady-state criteria are noted in bold font.

Exp. number	pH	Flow rate g/min	Surface area cm ²	C _{Si} mol/kg *10 ⁻⁶	C _{Ca} mol/kg *10 ⁻⁶	C _{Na} mol/kg *10 ⁻⁶	C _{Al} mol/kg *10 ⁻⁶	Al/Si	log r _{Plag,Si,BET} mol/cm ² /s	log r _{Plag,Al,BET} mol/cm ² /s
Ab-2	2.04	2.04	6044	2.35	1.13	D.L.	1.69	1.87	-14.34	-14.07
Ab-3	2.74	1.94	5635	5.52	0.92	7.38	4.66	2.20	-13.96	-13.62
Ab-4	3.80	2.09	5799	0.82	0.26	0.33	0.90	2.87	-14.77	-14.31
Ab-4r	4.22	0.77	8206	6.77	3.03	4.39	6.80	2.62	-14.44	-14.02
Ab-8	8.37	2.38	5717	0.19	0.68	1.13	0.52	7.01	-15.33	-14.48
Ab-8r	8.15	0.93	7781	2.07	0.67	D.L.	1.51	1.90	-14.85	-14.57
Ab-9	9.17	2.45	6044	1.16	1.07	1.03	0.37	0.82	-14.57	-14.65
Ab-10	10.00	2.34	5733	3.61	1.28	1.80	0.46	0.33	-14.07	-14.55
OI-2	2.01	1.68	5123	2.00	0.79	D.L.	1.32	1.56	-14.41	-14.22
OI-3	2.95	1.77	5795	1.04	0.76	D.L.	1.11	2.54	-14.73	-14.32
OI-4	3.76	0.80	5795	0.66	0.21	D.L.	0.33	1.20	-15.27	-15.19
OI-9	8.60	1.02	5818	0.39	0.94	D.L.	0.28	1.70	-15.39	-15.16
OI-10	10.03	1.75	4949	0.43	0.76	D.L.	0.34	1.86	-15.04	-14.77
OI-11	11.06	1.79	5007	3.96	0.59	D.L.	0.06	0.03	-14.08	-15.54
La-2	2.10	1.74	3236	6.22	5.73	2.35	12.5	2.72	-13.61	-13.18
La-3	2.95	1.69	3236	1.16	1.59	D.L.	2.07	2.43	-14.36	-13.97
La-4	4.22	0.84	4063	1.64	0.94	D.L.	1.37	1.13	-14.61	-14.55
La-9	8.71	1.26	3714	0.14	1.42	D.L.	0.30	2.93	-15.47	-15.00
La-10	10.13	1.75	3349	0.75	0.72	D.L.	0.31	0.57	-14.54	-14.79
La-11	10.77	1.67	3536	2.75	1.45	D.L.	0.06	0.03	-14.02	-15.57
By-2	2.06	2.05	19544	136	60.4	16.4	136	1.31	-12.98	-12.86
By-3	2.83	2.20	18744	12.1	5.49	0.74	12.4	1.35	-13.98	-13.85
By-4	3.76	2.11	19010	3.87	1.63	D.L.	2.86	0.97	-14.50	-14.51
By-8	8.41	2.36	18691	0.27	1.01	1.26	0.22	1.05	-15.59	-15.57
By-9	9.16	2.51	19859	1.27	1.77	1.15	0.33	0.34	-14.92	-15.39
By-10	10.02	2.46	18638	4.73	1.96	1.91	0.40	0.11	-14.34	-15.29
An-3	3.12	2.48	3616	85.1	34.7	4.88	70.7	0.97	-12.34	-12.35
An-4	4.14	2.59	3861	10.5	4.48	0.87	8.66	0.97	-13.26	-13.28
An-5	5.09	2.62	3493	0.74	0.51	2.33	0.53	0.84	-14.37	-14.44
An-9	9.03	2.53	3776	0.79	0.10	0.49	0.38	0.56	-14.38	-14.63
1099 An-10	10.15	2.53	3776	1.93	0.81	D.L.	0.55	0.33	-14.00	-14.48

1100

1101

1102

4 Chapter

Precipitation of gibbsite at pH 11 at 22°C and pH 9 at 80 °C as a function of saturation degree

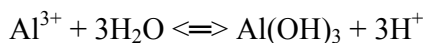
Snorri Gudbrandsson, Vasileios Mavromatis, Eric H. Oelkers

(To be submitted upon completion of work)

Abstract

Gibbsite growth rates were measured in closed system reactors at pH 11 and 25 °C, and pH 9 at 80 °C and 0.01M ionic strength. The experiments were carried out at close-to-equilibrium conditions and reported as a function of fluid saturation state. Initial reactive fluids were made of an AlCl₃ stock solution, using NaOH to adjust pH and NaCl to fix ionic strength. Gibbsite seeds were placed in the reactors to initiate precipitation.

The rates of gibbsite growth, in accord with the reaction



at pH 11 and 25 °C are consistent with

$$r_{22\text{ }^\circ\text{C}} = 2.06 \times 10^{-10} (\text{mol}/\text{m}^2/\text{s}) (\Omega - 1)$$

and those at pH ~9 and 80 °C are consistent with

$$r_{80\text{ }^\circ\text{C}} = 1.24 \times 10^{-7} (\text{mol}/\text{m}^2/\text{s})(m_{\text{OH}^-}) (\Omega - 1)$$

These results are coherent with previous studies reporting that gibbsite growth is proportional to the reactive fluid saturation state, consistent with growth being controlled by the addition of material to step sites on existing gibbsite seeds. Compared to the far from equilibrium dissolution rates of plagioclases at basic pH suggests that sluggish gibbsite precipitation rates could influence weathering processes at the close to neutral conditions typical of many natural Earth surface environments.

1

2

3 Precipitation of gibbsite at pH 11 at 22°C and pH 9 at 80°C.

4

5 Snorri Gudbrandsson^{1,2*}, Vasileios Mavromatis¹ and Eric H. Oelkers^{1,2}6 ¹*Geosciences Environment Toulouse (GET), CNRS, UMR5563, Observatoire Midi-*
7 *Pyrenees, 14 Avenue Edouard Belin, 31400, Toulouse, France.*8 ²*Institute of Earth Sciences, University of Iceland, Sturlugata 7, 101 Reykjavik, Iceland*

9

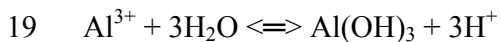
10 Abstract

11

12

13 Gibbsite growth rates were measured in closed system reactors at pH 11 and 25 °C, and pH 9
14 at 80 °C and 0.01M ionic strength. The experiments were carried out at close-to-equilibrium
15 conditions and reported as a function of fluid saturation state. Initial reactive fluids were
16 made of an AlCl₃ stock solution, using NaOH to adjust pH and NaCl to fix ionic strength.
17 Gibbsite seeds were placed in the reactors to initiate precipitation.

18 The rates of gibbsite growth, in accord with the reaction



20 at pH 11 and 25 °C are consistent with

21 $r_{22^\circ\text{C}} = 2.06 \times 10^{-10} (\text{mol}/\text{m}^2/\text{s}) (\Omega - 1)$

22 and those at pH ~9 and 80 °C are consistent with

23 $r_{80^\circ\text{C}} = 1.24 \times 10^{-7} (\text{mol}/\text{m}^2/\text{s})(m_{\text{OH}^-}) (\Omega - 1)$

24 These results are coherent with previous studies reporting that gibbsite growth is proportional
25 to the reactive fluid saturation state, consistent with growth being controlled by the addition
26 of material to step sites on existing gibbsite seeds. Compared to the far from equilibrium
27 dissolution rates of plagioclases at basic pH suggests that sluggish gibbsite precipitation rates
28 could influence weathering processes at the close to neutral conditions typical of many
29 natural Earth surface environments.30 *Keywords:* Gibbsite, Precipitation kinetics, chemical weathering, crystal growth, clay

31 minerals, aluminohydroxide

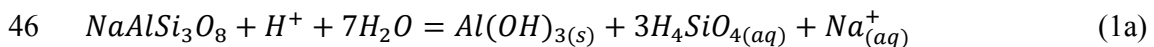
32

33

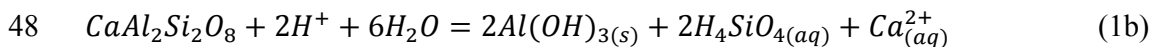
34 **4.1 Introduction**

35 During the weathering of rocks and/or minerals, dissolution/precipitation reactions
36 proceed slowly, normally at close to equilibrium conditions. In laboratory experiments
37 however, the rates are usually measured at far from equilibrium conditions because at such
38 conditions the rates are faster and thus easier to measure. This study was designed to measure
39 gibbsite growth rates as a function of distance from equilibrium in an attempt to bridge this
40 knowledge gap.

41 Gibbsite is an aluminium hydroxide (Al(OH)_3) that is a common secondary mineral in
42 soils (Chadwick et al., 2003). It is also present in large bauxite deposits, the main source of
43 aluminium ore. Its formation in nature is attributed to the weathering of feldspars in warm
44 and humid areas, so that the Si from the feldspars is leached out of the system and gibbsite
45 remains. The weathering of plagioclase feldspars to gibbsite can be described by:



47 and



49 for the albite and anorthite endmembers, respectively.

50 The mineralogy of the secondary aluminium phases is controlled by external factors
51 including humidity and temperature, as seen in Hawaiian weathering products, where the
52 weight percentage of secondary aluminium phases are smectite > kaolinite > gibbsite with

53 increasing rainfall, suggesting that the rainfall controls Si leaching from soils (Sherman,
54 1952; Sherman and Uehara, 1956; Hay and Jones, 1972).

55 Numerous studies of the weathering of plagioclases into aluminium rich secondary
56 phases such as gibbsite are available in the literature (e.g. Bricker and Garrels, 1967;
57 Helgeson et al., 1969; Berner and Holdren Jr, 1979; Helgeson et al., 1984; Berner et al.,
58 1985; Berner and Berner, 1996, Chadwick et al., 2003). Additional efforts have been made to
59 understand the behaviour of gibbsite precipitation in the laboratory, both directly and as it co-
60 precipitates with kaolinite, boehmite or diaspore (Nagy and Lasaga, 1990; 1992; Verdes et
61 al., 1992; Nagy and Lasaga, 1993; Nagy et al., 1999; Bénézeth et al., 2008; Wang et al.,
62 2010).

63 Annually, more than 160 million tons of bauxite is mined for aluminium production
64 globally, making it one of the most important industrial metals. Aluminium production has
65 increased rapidly since 1950. This increase can be attributed to the metal's light weight,
66 relative toughness, recyclability, and durability. Over the last decade, the emission of
67 greenhouse gases (i.e. CO₂, NO₂, CH₄) has become of increasing concern due to their effect
68 on Earth's climate. It is thus a scientific challenge to find ways to reduce the emission of
69 these gases into the atmosphere. Making airplanes and automobile from a lighter material
70 makes the vehicles more energy efficient and releases less CO₂ into atmosphere. Aluminium
71 is extracted from bauxite industrially by the Bayer and the Hall-Heroult process (Hind et al.,
72 1999) wherein one of the steps is gibbsite precipitation. As such a considerable effort has
73 been made to understand gibbsite's reactivity during the Bayer process (e.g. Hind et al., 1999;
74 Verdes et al., 1992).

75 In this study, closed system experiments were performed at alkaline pH as a function of
76 reactive fluid saturation state to quantify gibbsite growth rates. One motivation for this work

77 is the improved understanding of the plagioclase weathering process; in particular to
78 determine the rate limiting processes controlling gibbsite formation from plagioclase during
79 natural Earth surface processes.

80

81 **4.2 Theoretical background**

82 The standard state adopted in this study is that of unit activity of pure minerals and H₂O
83 at any temperature and pressure. For aqueous species other than H₂O, the standard state is
84 unit activity of species in a hypothetical one molal solution referenced to infinite dilution at
85 any temperature and pressure. All thermodynamic calculations reported in this study were
86 performed using the PHREEQC computer code (Parkhurst and Appelo, 1999). Several
87 available databases were used in these calculations, as explained below.

88 The gibbsite structure consists of octahedrally co-ordinated Al³⁺ ions with every third
89 spot in the octahedral structure left vacant (Drever, 1997). The dissolution/precipitation of
90 gibbsite can be described by the reaction:



92 For which the law of mass action is given by

$$93 K_{eq} = \frac{a_{\text{Al}^{3+}}}{a_{\text{H}^+}^3} \quad (3)$$

94 where K_{eq} represents the equilibrium constant for gibbsite and a_i refers to the activity of i th
95 aqueous species. The chemical affinity for reaction (2), A_{Gibbsite} can be expressed as

$$96 A_{\text{Gibbsite}} = RT \ln \left(\frac{K_{eq} a_{\text{Al}^{3+}}}{a_{\text{H}^+}^3} \right) = RT \ln \Omega \quad (4)$$

97 where R designates the gas constant, T signifies absolute temperature, and Ω refers to the
98 saturation degree of the fluid with respect to gibbsite ($\Omega = K_{eq}/Q$, where Q symbolizes the
99 reaction quotient).

100 Experiments were performed in this study using closed-system reactors. Gibbsite growth
 101 rates (r) are calculated from these experiments using

$$102 \quad r = \frac{\partial C_{Al}}{\partial t_{sec}} \left(\frac{V_{reactor}}{A_{BET} m_g} \right) \quad (5)$$

103 where $\frac{\Delta C_{Al}}{\Delta t_{sec}}$ represents the rate change in reactive fluid aluminium concentration with time,
 104 $V_{reactor}$ refers to the reactor fluid volume at the time of sampling, A_{BET} denotes the specific
 105 surface area in m^2/g , and m_g designates the mass of gibbsite seeds placed into the reactor. The
 106 value of $\frac{\partial C_{Al}}{\partial t}$ in Eqn. 5 is calculated directly from a fit of measured reactive fluid
 107 concentrations (see below).

108 The variation of mineral growth rates with the saturation state of its co-existing fluid
 109 phase is commonly described using

$$110 \quad r = r_+ (\Omega - 1)^n \quad (6)$$

111 r_+ represents the forward reaction rate constant, which may itself depend on the fluid
 112 composition (e.g. Saldi et al., 2009; Saldi et al., 2012). The parameter n in Eqn. (8) is often
 113 related to the precipitation mechanism. It has been argued that, for elementary reactions, $n =$
 114 1 is consistent with transport or adsorption controlled growth on existing mineral surfaces
 115 and $n = 2$ is consistent with a spiral growth mechanism. If growth is controlled by surface
 116 nucleation, rates tend to vary as an exponential function of saturation state, i.e. $n > 2$ (Gratz et
 117 al., 1993; Nielsen, 1964; Nielsen, 1984; Shiraki and Brantley, 1995; Teng et al., 2000). As
 118 emphasized by Temkin (1963), however, the chemical affinity of an overall reaction needs to
 119 be normalized to that of the elementary reaction to accurately use reaction orders based on
 120 these elementary reaction mechanisms. As can be observed from Eqn. 2, each mole of
 121 gibbsite contains one mole of Al. It seems likely, therefore, that the elementary reaction for
 122 gibbsite precipitation contains one mole of aluminium.

123 4.3 Methods and materials

124 Gibbsite powder was acquired commercially from Riedel-De Haen AG in Seelze,
 125 Hannover (Benezeth, 2008). The gibbsite powder was washed in ultra pure H_2O (18.2 MΩ

126 cm) prior to the experiments and dried for 48 hours at 50 °C. The gibbsite powder was
127 analyzed by X-ray Diffraction (XRD) using an INEL CPS 120 Cokα diffractometer, with a
128 scanning speed of 0.02° per second, both prior to and after experiments. The resulting
129 diffraction patters are shown in Fig. 1, and compared to well crystallize gibbsite powder.

130 A photomicrograph obtained using a JEOL JSM-6360LV Scanning Electron Microscope
131 (SEM) of the gibbsite powder is shown in Fig. 2a and Fig 3a. The gibbsite grains are
132 relatively clean and the trenches between the octahedral structures are free of particles. The
133 surface area of the cleaned gibbsite was determined to be $0.1254 \text{ m}^2/\text{g} \pm 10\%$ using an 11
134 point Krypton adsorption using a Quantachrome Gas Sorption system and the BET method
135 (Brunauer et al., 1938).

136 Experiments were performed in closed system reactors, using acid-washed
137 polypropylene Nalgene© vessels, as described by Roncal-Herrero and Oelkers (2011).
138 Experiments were initiated by placing from 2.57 to 4.55 g of gibbsite powder into the reactor
139 and then adding ~500 mL of the initial reactive fluid. The reactors were then closed and
140 sealed with Teflon tape to avoid evaporation.

141 Two distinct experimental series were carried out. R-series was performed at 22 °C and
142 pH 11 and H-series was performed at 80 °C and pH 9. The initial reactive fluids were
143 prepared by adding Merck aluminium chloride to $18 \Omega \text{ cm}^{-1}$ Milli-Q water. NaOH was
144 added to this solution to fix pH and NaCl was added to fix the ionic strength at 10 mM. For
145 each experiment, the initial reactive fluid was supersaturated with respect to gibbsite. The
146 saturation states of the inlet fluids were set to be 2x, 5x, 10x and 25x higher than gibbsite
147 solubility. The compositions of these fluids were calculated using PHREQC 2.17.4799
148 (Parkhurst and Appelo, 1990). The fluid compositions are provided in Table 1.

149 The reactors were placed on a shaking table at 22 °C or into a custom made temperature
150 controlled shaking bath with an automatic water level control at 80 °C. The reactors were

151 sampled regularly through a 0.22 μm cellulose acetate filter using syringes. Prior to sampling,
152 the reactors were removed from the shaking equipment and solids allowed to settle. Part of
153 the reactive fluid sample was used to measure pH at 25°C using a 713 Metrohm pH meter
154 coupled to a Mettler Toledo Inlab® 422. The remaining fluid sample was acidified
155 immediately with 30 μl of 16 M bi-distilled HNO₃ prior to Al analysis. Reactive fluids were
156 analyzed for aluminium via flame Atomic Absorption Spectroscopy (AAS) using a Perkin
157 Elmer AAnalyst 400. The reproducibility was 4 percent for Al concentrations greater than
158 4 $\times 10^{-4}$ mmol/L, but on the order of ± 10 percent for lower concentrations.

159

160 4.4 Results

161 Figure 1 displays the XRD results for all experiments, displayed together with the
162 corresponding initial gibbsite seed XRD pattern. As can be seen, there are no changes in the
163 XRD-pattern during the experiments, indicating that gibbsite is the only mineral phase
164 present in all experiments, or that if alternative minerals have precipitated they comprise less
165 than ~3% volume percent of the total solid.

166 Photomicrographs of the gibbsite prior to and after the 22 °C experiments can be seen in
167 Fig. 2. The initial gibbsite is shown in Fig. 2a and Fig. 2b – 2f display the SEM
168 photomicrographs from experiments R1 – R5 respectively. Precipitation is apparent on solids
169 recovered from all experiments. Most growth appears to have been located in the “trenches”
170 between the octahedral crystals of the initial powder. The same can be seen in Fig. 3 where
171 photomicrographs of the gibbsite prior to and after the 80 °C experiments are displayed. The
172 SEM photomicrographs show clear evidence of a precipitated phase in all experiments.

173 The temporal evolution of reactive fluid Al concentrations during all the experiments
174 performed in this study is presented in Fig. 4 and Annex A. Reactive fluid Al concentrations
175 decrease continuously in each experiment. Experiments R1, H6, and H7 had the lowest initial

176 Al concentrations, and were just barely supersaturated with respect to gibbsite. Experiments
177 H6 and H7 had not attained a steady-state Al concentration (Fig. 4) nor did they have
178 constant pH prior to stopping the experiment (see below and Fig 5). All other experiments
179 had attained a steady state Al and pH prior to the end of the experiment.

180 The fluid concentrations shown in Fig. 4 were used to calculate gibbsite growth rates as a
181 function of fluid composition using Eqn. (5). To overcome ambiguities associated with the
182 minor analytical scatter apparent in Fig. 4 measured Al concentrations were fit to

183 $C_{Al} = C_{Al,0} - \alpha \exp(-bt)$ (7)

184 where $C_{Al,0}$ refers to the concentration of Al at the beginning of the experiment, respectively,
185 and α and b represent fit parameters and t is time in hours. The measured values of Al
186 concentration and pH as a function of time are provided in Annex A; corresponding
187 calculated values are provided in Annex B. Resulting fit parameters are listed in Table 2. A
188 comparison of fit and measured Al concentrations for all experiments is provided in Fig. 4.

189 The temporal evolution of pH in all experiments is shown in Fig 5. During experimental
190 series R- at 22 °C, the pH is stable during all experiments with the possible exception of the
191 last 1000 hours of R1 (see Figure 5a). The fluctuations in the pH observed in all experiments
192 are comparable and are likely within the uncertainties of the measurements. The pH in H-
193 series is not as stable as for R-series, and the pH in the two experiments with the lowest
194 initial Al concentration dropped significantly after 3000 hours. It is worth mentioning that
195 after 4000 hours some of the reactor lids opened slightly, but there was no evidence of
196 evaporation from the reactors. The observed stability in pH could be due to the influence of
197 atmospheric CO₂ on reactive fluid compositions.

198 The time derivative of Eqn. (7) was determined analytically and used generate $\frac{\partial C_{Al}}{\partial t}$.
199 These values were then used together with Eqn. (5) to generate rates. Resulting rates are

200 shown as a function of saturation state (Ω -1) in Fig. 6. In both the R-series and the H-series,
 201 growth rates increase linearly with increasing saturation state and are thus consistent with
 202 previous gibbsite precipitation studies (Nagy and Lasaga, 1992; Nagy et al., 1999; Bénézeth
 203 et al., 2008).

204 The symbols in Fig. 6 display measured gibbsite growth rates at as a function of (Ω -1),
 205 the degree of fluid supersaturation at pH 11 and 22 °C and pH 9 at 80 °C. The line passing
 206 through the results from 22 °experiments in Fig 6a is consistent with

$$207 r_{22\text{ }^{\circ}\text{C}} = 2.06 \times 10^{-10} (\text{mol}/\text{m}^2/\text{s}) (\Omega - 1) \quad (8a)$$

208 As the pH differed somewhat among the experiments performed at 80 °C, it is possible to
 209 assess the effects of pH on these rates. The lines drawn through the measured rates in Fig 6b
 210 are consistent with

$$211 r_{80\text{ }^{\circ}\text{C}} = 1.24 \times 10^{-7} (\text{mol}/\text{m}^2/\text{s})(m_{OH^-}) (\Omega - 1) \quad (8b)$$

212

213

214 4.5 Discussion

215 The results from this study, shown in figure 6, indicate that measured Al concentrations
 216 are consistent with the linear rate equation presented above (Eqn. 6) where $n=1$. Such
 217 behaviour is consistent with gibbsite growth occurring via the attachment of material on steps
 218 present on existing gibbsite surfaces. These results are in agreement with Bénézeth et al.
 219 (2008) who suggested that the precipitation of gibbsite, measured using surface relaxation
 220 techniques at pH 10.3 – 8.4, can be described using Eqn. (6) at 50°C and pH between 8.2-9.7
 221 and ΔG_r 0.7-3.7 kJ mol⁻¹.

222 Various thermodynamic databases report different equilibrium constants for the gibbsite
 223 solubility reaction. Some of these constants are illustrated as a function of pH in figures 7a
 224 and 7b. It can be seen that the various databases yield equilibrium constants for the Reaction

225 2 that range over approximately an order of magnitude at both 22 and 80 °C. Gibbsite
226 solubilities generated in this study appear to be most consistent with the minteq database for
227 experiments at 22 °C and wateq4f database at 80 °C.

228

229 **4.5.1 What controls feldspar dissolution rates during weathering?**

230 As mentioned above, the feldspars are thought to be the primary source for Al^{3+} in the
231 weathering process because their abundance in the Earth's crust (Nesbitt and Young, 1984) as
232 well as for their relatively high weathering rates (Gudbrandsson et al., 2011). A number of
233 past studies suggested that the relatively slow rates of clay mineral precipitation could limit
234 the overall rates of this reaction (Emmanuel and Ague, 2011; Ganor et al., 2007; Maher et al.,
235 2009; Zhu, 2005; Zhu and Lu, 2009). At steady-state, reaction (1a) requires that the rate of
236 gibbsite precipitation three times more rapid than the rate of albite dissolution. Gibbsite
237 precipitation rates from this study and measured plagioclase dissolution rates, at far from
238 equilibrium as reported by Gudbrandsson et al. (submitted 2013) are compared in Fig. 8.
239 Note the precipitation rates of gibbsite are measured at mildly supersaturated conditions
240 ($\Omega \leq 3$) while the dissolution rates of plagioclases are at far from equilibrium ($\Omega < 1*10^{-20}$). It
241 can be seen in this figure that gibbsite precipitation rates are similar to those of plagioclase at
242 pH 11. Gibbsite precipitation rates, however, decrease faster with decreasing pH than those
243 of plagioclase. As such gibbsite precipitation rates are likely far slower than those of
244 plagioclase at the closer to neutral conditions, typical of Earth surface weathering. It seems
245 likely therefore that the slow rates of gibbsite precipitation, at least influences plagioclase
246 weathering rates at near to neutral conditions. This slowing, may, however be mitigates
247 somewhat if the surface area of the secondary gibbsite is far greater than that of the
248 dissolving plagioclase, as rates are proportional to these surface areas.

249 During plagioclase and crystalline basalt dissolution experiments (Gudbrandsson et al
250 2011, submitted) the reactive fluids are supersaturated, or close to equilibrium with respect to
251 gibbsite at intermediate pH and up to pH 9. Although the reactive fluids in these dissolution
252 experiments are supersaturated with respect to gibbsite, no aluminium rich phases were
253 detected on the surface of the solids from those experiments using SEM and SEM-EDS. This
254 indicates that although gibbsite appears to readily grow at the near to equilibrium conditions
255 considered in this study, its nucleation may be sluggish preventing its precipitation, at least
256 over the short term in some systems.

257

258 **4.6 Summary**

259 Measured gibbsite growth rates in seeded experiments at 25 °C and pH 11, and 80 °C
260 and pH ~9 are found to vary linearly with the saturation state of the reactive aqueous fluid.
261 This observation suggests that gibbsite growth in these experiments proceeded by the direct
262 incorporation of Al to step sites available on the seeds. This suggestion, consistent with the
263 results of some previously reported studies, was confirmed by SEM analysis of post
264 experiment solids. Measured gibbsite growth rate constants are similar to those of
265 plagioclase dissolution at pH 11 and 25°C, but decrease more rapidly with decreasing pH.
266 These observations suggest that sluggish gibbsite precipitation rates could influence
267 weathering processes at the close to neutral conditions typical of many natural Earth surface
268 environments.

269

270 Acknowledgements

271 We would like to thank our friends and colleagues, including Jacques Schott, Quentin
272 Gautier, Carole Causserand, Stephanie Mounic, Alain Castillo, Pasquale Gisquet, Sophy
273 Gouy, Thierry Aigouy, Philippe de Parseval, Olivier Bosc, and Julien Declercq at the
274 GET/CNRS in Toulouse, France Sigurður R. Gislason, Andri Stefánsson, Niels Oskarsson
275 and the Carb-Fix Group at the University of Iceland, Bergur Sigfusson and Ingvi Gunnarsson

276 at Reykjavík Energy. This study was funded by the European Community through the Delta-
277 Min (Mechanisms of Mineral Replacement Reactions; Grant PITN-GA-2008-215360).

278

279 **References**

280

- 281 Bénézeth, P., Palmer, D.A., Wesolowski, D.J., 2008. Dissolution/precipitation kinetics of
282 boehmite and gibbsite: Application of a pH-relaxation technique to study near-
283 equilibrium rates. *Geochimica Et Cosmochimica Acta*, 72(10): 2429-2453.
- 284 Berner, E., Berner, R., 1996. Global environment: Water, air and geochemical cycles.
- 285 Berner, R.A., Holdren Jr, G.R., 1979. Mechanism of feldspar weathering—II. Observations
286 of feldspars from soils. *Geochimica Et Cosmochimica Acta*, 43(8): 1173-1186.
- 287 Berner, R.A., Holdren Jr, G.R., Schott, J., 1985. Surface layers on dissolving silicates:
288 (Comments on “Study of the weathering of albite at room temperature and pressure
289 with a fluidized bed reactor” by L. Chou and R. Wollast). *Geochimica Et
290 Cosmochimica Acta*, 49(7): 1657-1658.
- 291 Bricker, O.P., Garrels, R., 1967. Mineralogic factors in natural water equilibria. Principles
292 and applications of water chemistry. Wiley, New York: 449-469.
- 293 Brunauer, S., Emmett, P., Teller, E., 1938. Adsorption of gases in multimolecular layers,
294 *Journal of the American Chemical Society*, pp. 309-319.
- 295 Chadwick, O.A. et al., 2003. The impact of climate on the biogeochemical functioning of
296 volcanic soils. *Chemical Geology*, 202(3–4): 195-223.
- 297 Drever, J.I., 1997. The Geochemistry of Natural Waters. Surface and Groundwater
298 Environments. Prentice Hall, 71 pp.
- 299 Emmanuel, S., Ague, J.J., 2011. Impact of nano-size weathering products on the dissolution
300 rates of primary minerals. *Chemical Geology*, 282(1–2): 11-18.
- 301 Ganor, J., Lu, P., Zheng, Z.P., Zhu, C., 2007. Bridging the gap between laboratory
302 measurements and field estimations of silicate weathering using simple calculations.
303 *Environmental Geology*, 53(3): 599-610.
- 304 Gratz, A.J., Hillner, P.E., Hansma, P.K., 1993. Step dynamics and spiral growth on calcite.
305 *Geochimica Et Cosmochimica Acta*, 57(2): 491-495.
- 306 Gudbrandsson, S., Wolff-Boenisch, D., Gislason, S.R., Oelkers, E.H., 2011. An experimental
307 study of crystalline basalt dissolution from $2 \leq \text{pH} \leq 11$ and temperatures from 5 to
308 75 degrees C. *Geochimica Et Cosmochimica Acta*, 75(19): 5496-5509.
- 309 Hay, R.L., Jones, B.F., 1972. Weathering of basaltic tephra on the island of Hawaii.
310 *Geological Society of America Bulletin*, 83(2): 317-332.
- 311 Helgeson, H.C., Garrels, R.M., MacKenzie, F.T., 1969. Evaluation of irreversible reactions in
312 geochemical processes involving minerals and aqueous solutions—II. Applications.
313 *Geochimica Et Cosmochimica Acta*, 33(4): 455-481.
- 314 Helgeson, H.C., Murphy, W.M., 1983. Calculations of mass-transfer among minerals and
315 aqueous-solutions as a function of time and surface-area in geochemical processes. 1.
316 Comutational approach *Journal of the International Association for Mathematical
317 Geology*, 15(1): 109-130.
- 318 Helgeson, H.C., Murphy, W.M., Aagaard, P., 1984. Thermodynamic and Kinetic Constraints
319 on Reaction-Rates among Minerals and Aqueous-Solutions .2. Rate Constants,
320 Effective Surface-Area, and the Hydrolysis of Feldspar. *Geochimica Et
321 Cosmochimica Acta*, 48(12): 2405-2432.
- 322 Hind, A.R., Bhargava, S.K., Grocott, S.C., 1999. The surface chemistry of Bayer process
323 solids: a review. *Colloids and Surfaces A: Physicochemical and Engineering Aspects*,
324 146(1–3): 359-374.

- 325 Maher, K., Steefel, C.I., White, A.F., Stonestrom, D.A., 2009. The role of reaction affinity
326 and secondary minerals in regulating chemical weathering rates at the Santa Cruz Soil
327 Chronosequence, California. *Geochimica Et Cosmochimica Acta*, 73(10): 2804-2831.
- 328 Markússon, S.H., Stefánsson, A., 2011. Geothermal surface alteration of basalts, Krýsuvík
329 Iceland—Alteration mineralogy, water chemistry and the effects of acid supply on the
330 alteration process. *Journal of Volcanology and Geothermal Research*, 206(1–2): 46-
331 59.
- 332 Nagy, K.L., Cygan, R.T., Hanchar, J.M., Sturchio, N.C., 1999. Gibbsite growth kinetics on
333 gibbsite, kaolinite, and muscovite substrates: Atomic force microscopy evidence for
334 epitaxy and an assessment of reactive surface area. *Geochimica Et Cosmochimica
335 Acta*, 63(16): 2337-2351.
- 336 Nagy, K.L., Lasaga, A.C., 1990. The effect of deviation from equilibrium on the kinetics of
337 dissolution and precipitation of kaolinite and gibbsite. *Chemical Geology*, 84(1–4):
338 283-285.
- 339 Nagy, K.L., Lasaga, A.C., 1992. Dissolution and precipitation of gibbsite at 80 °C and pH 3.
340 The dependence on solution saturation state. *Geochimica Et Cosmochimica Acta*,
341 56(8): 3093-3111.
- 342 Nagy, K.L., Lasaga, A.C., 1993. Simultaneous precipitation kinetics of kaolinite and gibbsite
343 at 80 °C and pH 3. *Geochimica Et Cosmochimica Acta*, 57(17): 4329-4335.
- 344 Nesbitt, H.W., Young, G.M., 1984. Prediction of some weathering trends of plutonic and
345 volcanic rocks based on thermodynamic and kinetic considerations. *Geochimica Et
346 Cosmochimica Acta*, 48(7): 1523-1534.
- 347 Nielsen, A.E., 1964. Kinetics of precipitation, Pergamon Press, pp. 151.
- 348 Nielsen, A.E., 1984. Electrolyte crystal-growth mechanisms. *Journal of Crystal Growth*,
349 67(2): 289-310.
- 350 Parkhurst, D.L., Appelo, C.A.J., 1999. User's guide to PHREEQC (Version 2)—A computer
351 program for speciation, batch-reaction, one-dimensional transport, and inverse
352 geochemical calculations. U. S. G. S. Water Resour. Inv. Report.: 99-4259.
- 353 Roncal-Herrero, T., Oelkers, E.H., 2011. Experimental determination of struvite dissolution
354 and precipitation rates as a function of pH. *Applied Geochemistry*, 26(5): 921-928.
- 355 Saldi, G.D., Jordan, G., Schott, J., Oelkers, E.H., 2009. Magnesite growth rates as a function
356 of temperature and saturation state. *Geochimica Et Cosmochimica Acta*, 73(19):
357 5646-5657.
- 358 Saldi, G.D., Schott, J., Pokrovsky, O.S., Gautier, Q., Oelkers, E.H., 2012. An experimental
359 study of magnesite precipitation rates at neutral to alkaline conditions and 100–200
360 °C as a function of pH, aqueous solution composition and chemical affinity.
361 *Geochimica Et Cosmochimica Acta*, 83(0): 93-109.
- 362 Sherman, G.D., 1952. The titanium content of Hawaiian soils and its significance. *Soil
363 Science Society of America Journal*, 16(1): 15-18.
- 364 Sherman, G.D., Uehara, G., 1956. The weathering of olivine basalt in Hawaii and its
365 pedogenic significance. *Soil Science Society of America Journal*, 20(3): 337-340.
- 366 Shiraki, R., Brantley, S.L., 1995. Kinetics of near-equilibrium calcite precipitation at 100 °C -
367 an evaluation of elementary reaction-based rate laws. *Geochimica Et Cosmochimica
368 Acta*, 59(8): 1457-1471.
- 369 Temkin, M.I., 1963. Kinetics of stationary reactions. *Doklady Akademii Nauk SSSR*, 152:
370 156-157.
- 371 Teng, H.H., Dove, P.M., De Yoreo, J.J., 2000. Kinetics of calcite growth: Surface processes
372 and relationships to macroscopic rate laws. *Geochimica Et Cosmochimica Acta*,
373 64(13): 2255-2266.

- 374 Verdes, G., Gout, R., Castet, S., 1992. Thermodynamic Properties of the Aluminate Ion and
 375 of Bayerite, Boehmite, Diaspore and Gibbsite. European Journal of Mineralogy, 4(4):
 376 767-792.
- 377 Wang, Z., Yang, L., Zhang, J., Guo, Z.-c., Zhang, Y., 2010. Adjustment on gibbsite and
 378 boehmite co-precipitation from supersaturated sodium aluminate solutions.
 379 Transactions of Nonferrous Metals Society of China, 20(3): 521-527.
- 380 Wesolowski, D.J., Palmer, D.A., 1994. Aluminum speciation and equilibria in aqueous
 381 solution: V. Gibbsite solubility at 50 C and pH 3-9 in 0.1 molal NaCl solutions (a
 382 general model for aluminum speciation; analytical methods). Geochimica Et
 383 Cosmochimica Acta, 58(14): 2947-2969.
- 384 Zhu, C., 2005. In situ feldspar dissolution rates in an aquifer. Geochimica Et Cosmochimica
 385 Acta, 69(6): 1435-1453.
- 386 Zhu, C., Lu, P., 2009. Alkali feldspar dissolution and secondary mineral precipitation in batch
 387 systems: 3. Saturation states of product minerals and reaction paths. Geochimica Et
 388 Cosmochimica Acta, 73(11): 3171-3200.
- 389

390 **Figure captions:**

- 391 Figure 1 X-Ray powder diffraction pattern of the gibbsite used in this study, prior to and
 392 after each experiment compared the gibbsite reference powder diffraction pattern.
- 393 Figure 2 SEM images of the gibbsite powder before and after experiments at 25 °C. Figure
 394 1a, displays the gibbsite prior to experiments. Figures 1b-1f show the gibbsite
 395 after experiments at 25 °C (R-series) from low supersaturation (b) increasing to
 396 high supersaturation (f). In figure a, small particles can be seen on big gibbsite
 397 crystals, with the “trenches” clean and no precipitation or dissolution features. At
 398 low supersaturation (b) there are likely some dissolution forms on the edges but
 399 also gibbsite has accumulated in the trenches. With increasing supersaturation,
 400 figures c-f, the dissolution features are not found but the grains found on the
 401 gibbsite crystals increase in size with increasing supersaturation.
- 402 Figure 3 Gibbsite powder before and after experiments at 80 °C. Figure 2a displays the
 403 gibbsite prior to experiments. Figures 1b-1f show the gibbsite after experiments at
 404 80 °C (series H) from low supersaturation (b) increasing to high supersaturation
 405 (f). In Fig a, small particles on big gibbsite crystals, with the “trenches” clean and
 406 no precipitation or dissolution features. At low supersaturation (b) there are no
 407 visible precipitation nor dissolution features. With increasing supersaturation,
 408 figures c-f, the precipitation increases and the grain size as well as in experiments
 409 at 25°C.
- 410 Figure 4 The reactive fluid Al concentrations of all experiments plotted against elapsed
 411 over time. Plots on the left display Al concentrations of R-series and plots on the
 412 left from H-series. The filled circles represent measured Al concentrations and the
 413 solid lines represent the fit of these results to Eqn. (7). Aluminium concentration
 414 decrease with time in all experiments. All attain a steady state, with the exception
 415 of experiments R1, H6, and H7.
- 416 Figure 5 The temporal reactive fluid pH evolution during all experiments. The left figure
 417 shows results of the R-series and the right figure the H-series. The filled circles,
 418 open circles, filled triangles, open triangles and filled squares represent

419 experiments from low saturation to high, respectively. In R-series experiments at
420 22 °C, the pH variation is within analytical uncertainty. In H-series experiments
421 at 80 °C, experiments at low saturation show a pH that systematically decreases
422 with time.

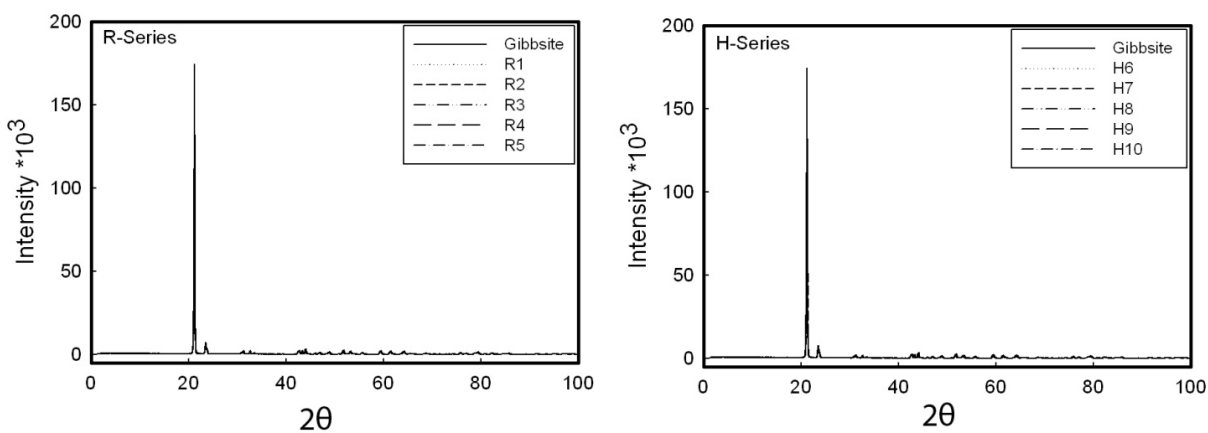
423 Figure 6 The precipitation rates from gibbsite experiments as a function of reactive fluid
424 saturation state. Figure 6a displays the rates from R-series and figure 6b displays
425 the rates from H-series experiments. The symbols represent measured rates,
426 whereas the lines correspond to a fit of these data consistent with Eqns. (8a) and
427 (8b).

428 Figure 7 Solubility of gibbsite at 25 and 80 °C and 0.01M ionic strength, as a function of
429 pH figure a and b respectively. The curves display the saturation curve calculated
430 using the denoted databases. The disagreement between the databases is constant
431 between temperatures as the Llnl database and the Minteq, with the Phreeqc
432 database between. The symbols represent the final steady state Al concentrations
433 of the reactive fluids in this study. At 22°C these steady states are consistent
434 with the Minteq database but at 80 °C these steady-states are consistent with the
435 Phreeqc database.

436 Figure 8 Rates of plagioclase dissolution and gibbsite precipitation as a function of pH at
437 alkaline conditions and at 22 °C. The dissolution rates of plagioclases dissolution
438 are shown as open circles, but the precipitation rates of gibbsite are shown as
439 filled circles.

440

441

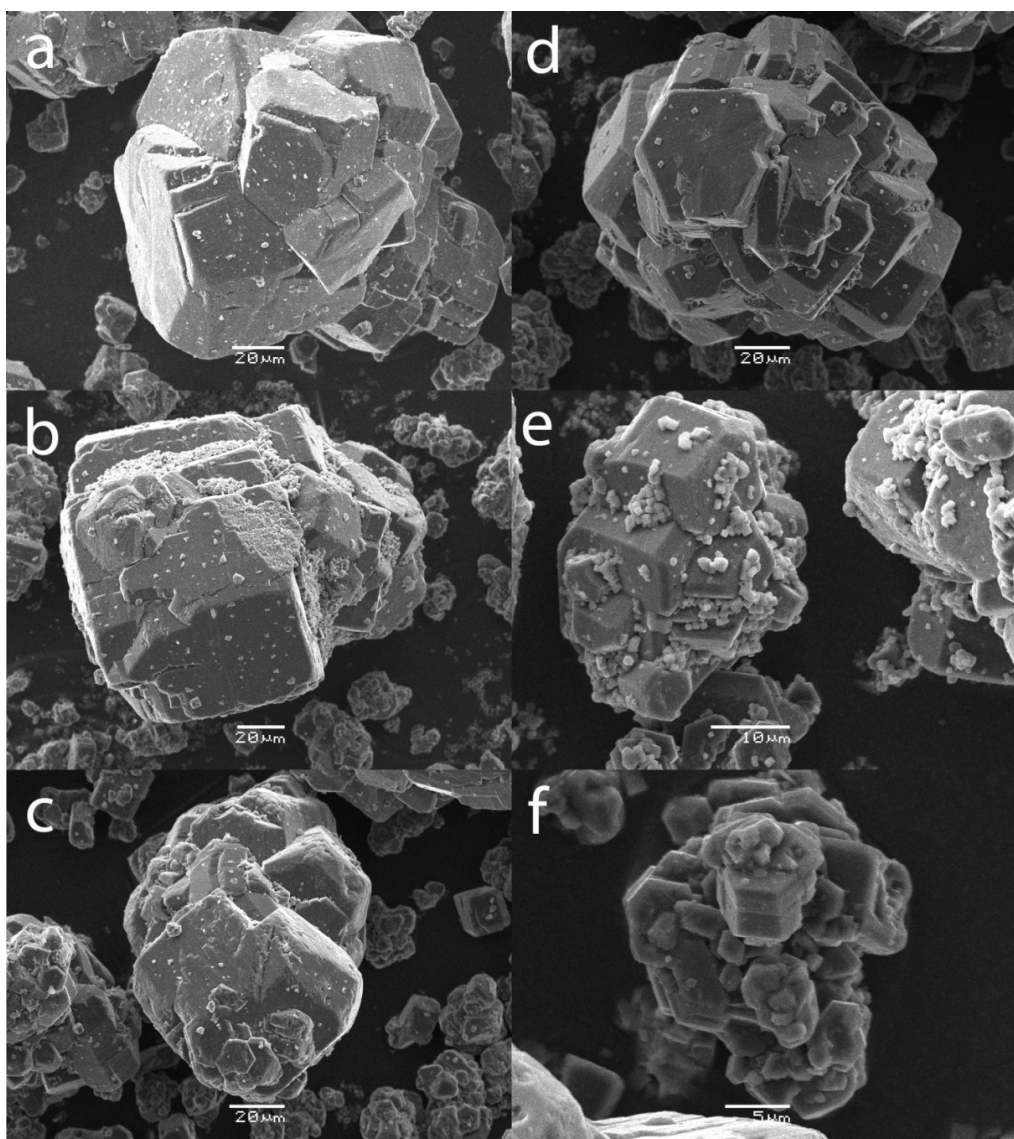


442

443 Figure 1

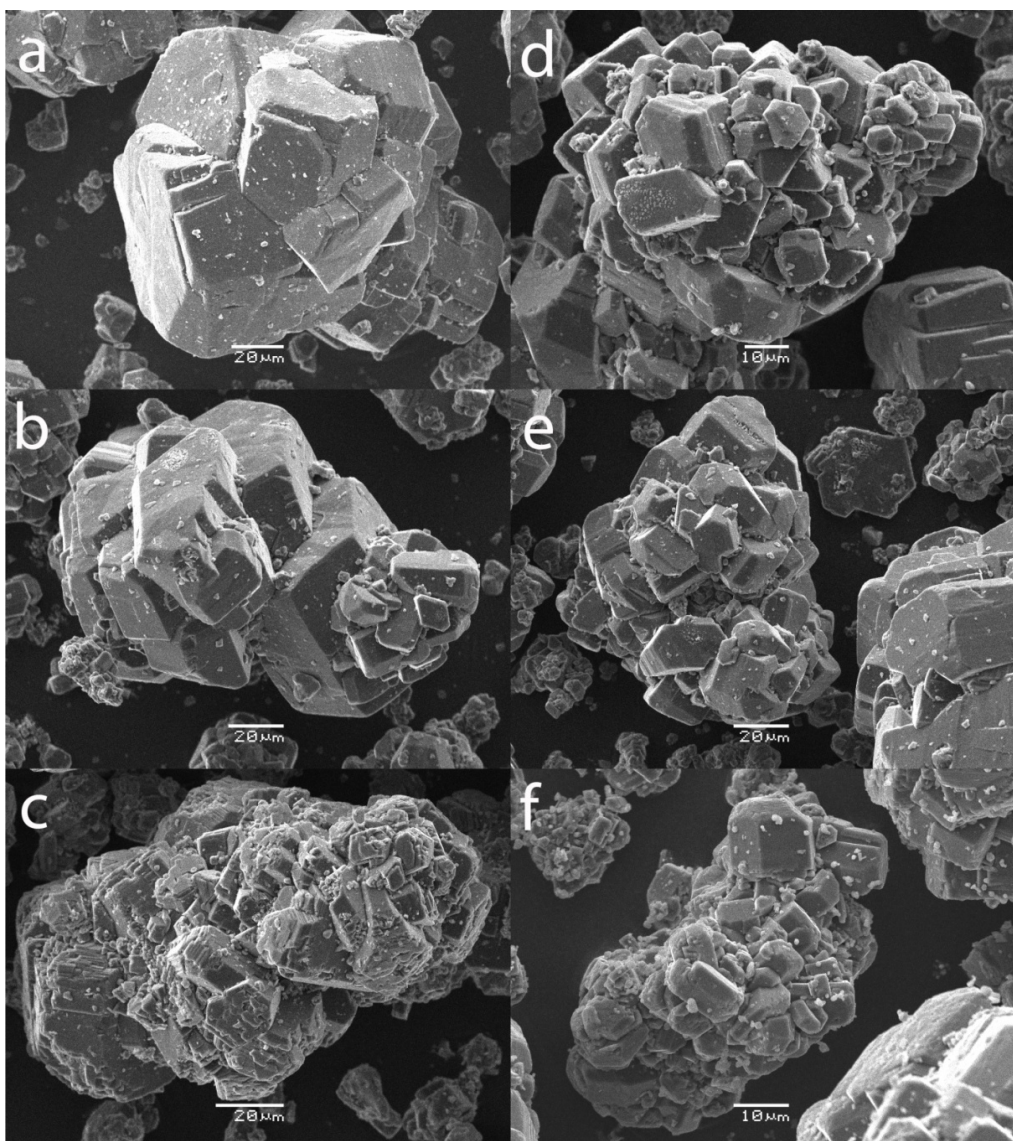
444

445



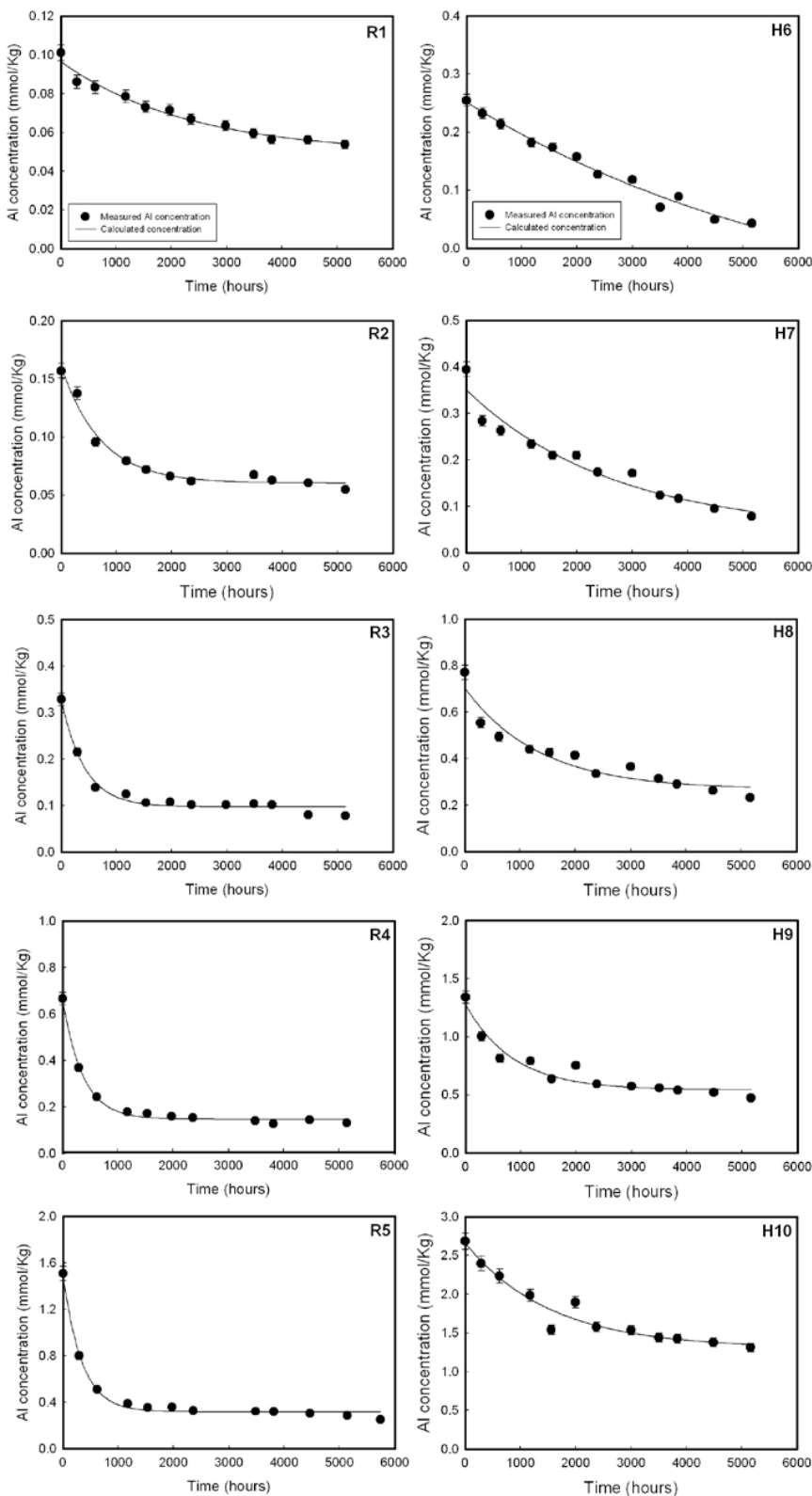
446

447 Figure 2



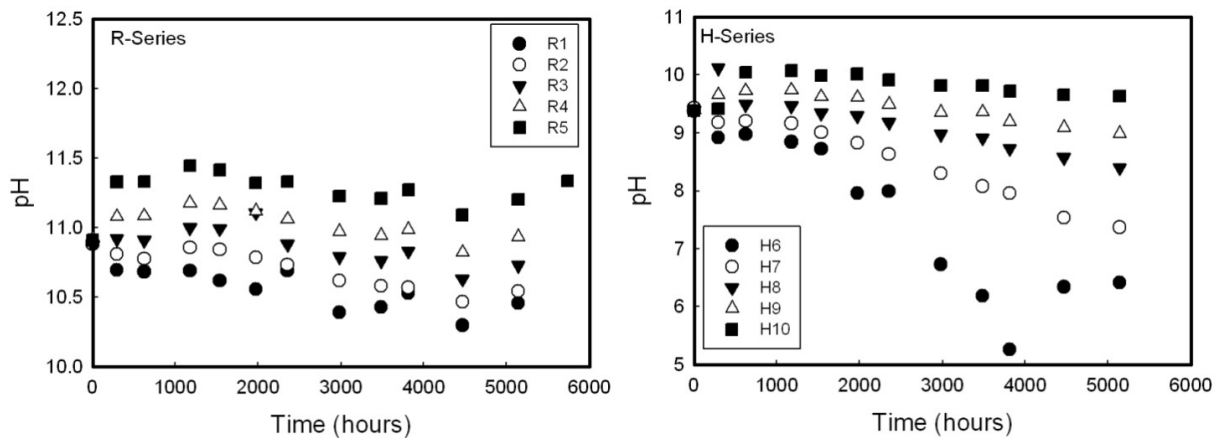
448

449 Figure 3



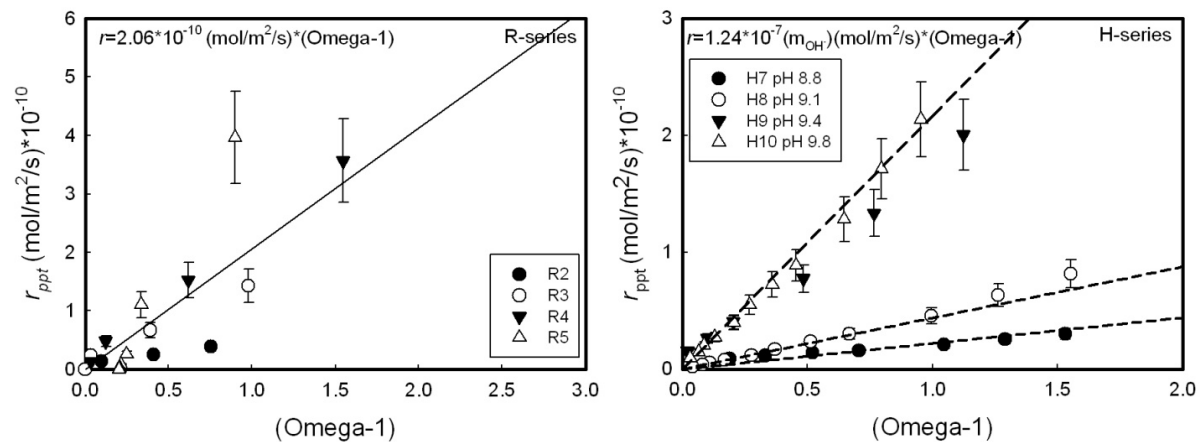
450

451 Figure 4



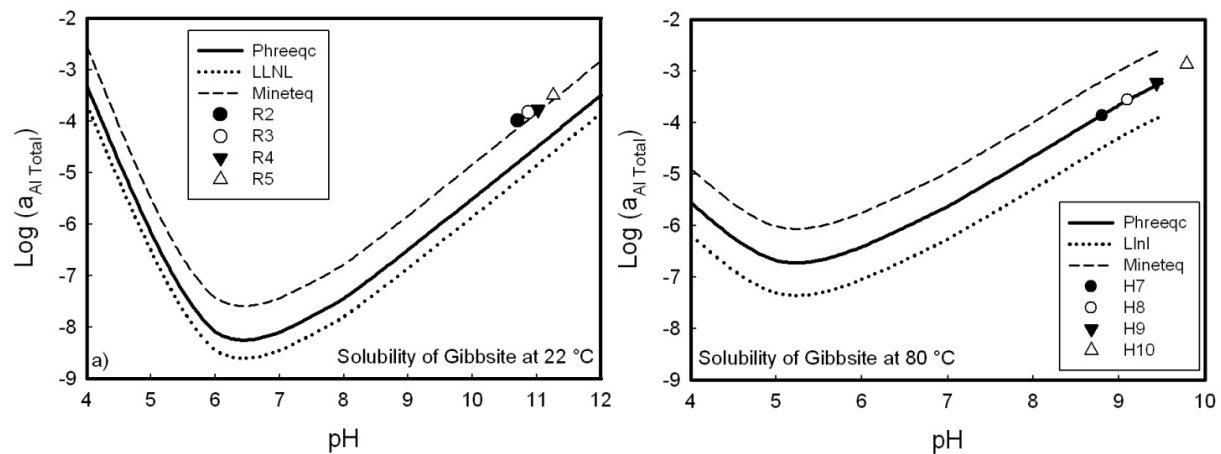
452

453 Figure 5



454

455 Figure 6

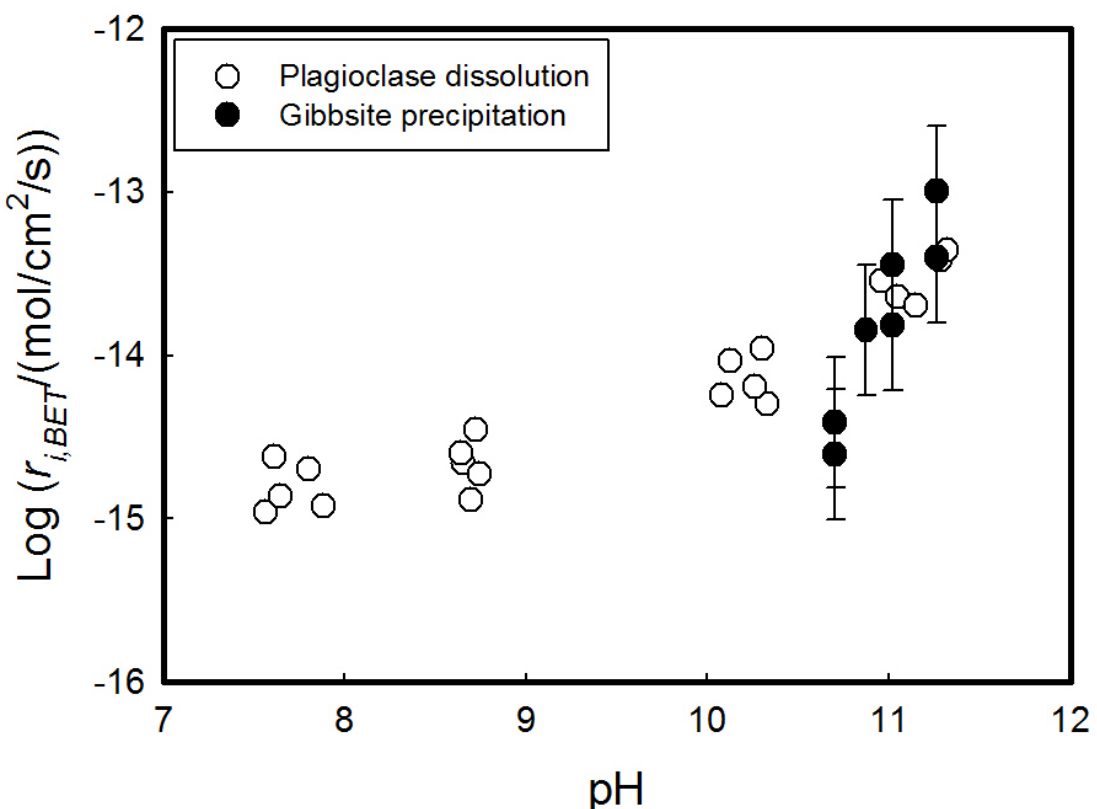


456

457 Figure 7

458

459



460

461 Figure 8

462

463

464

465

466

467

468

469

470

471

472

473

474

475 Table 1. Experimental values at $t=0$ in each of the experiments, temperature (T), reactive
 476 surface area of gibbsite seeds (m^2), saturation degree (Ω) and pH.

Exp #	Initial values			
	T °C	m^2	Ω	pH
R1	22	0.41	2.19	10.90
R2	22	0.41	3.55	10.88
R3	22	0.38	7.59	10.87
R4	22	0.37	13.8	10.92
R5	22	0.32	31.6	10.91
H6	80	0.57	1.23	9.38
H7	80	0.43	1.70	9.43
H8	80	0.38	3.63	9.39
H9	80	0.42	6.31	9.39
H10	80	0.40	12.9	9.38

477

478

479

480 Table 2. Fit parameters of concentration evolution as a function of time. The $C_{Al,0}$ stands for
 481 the initial concentration at the beginning of experiments (mmol/kg), a and b represent fit
 482 parameters and R and R^2 stands for the quality of the fit.

Exp #	$C_{Al,0}$ mmol/kg	a mmol/kg	b $t^{-1} \cdot 10^4$	R	R^2
R1	0.05	0.05	4	0.99	0.97
R2	0.06	0.10	14	0.99	0.98
R3	0.10	0.23	24	0.99	0.98
R4	0.15	0.52	27	1.00	0.99
R5	0.32	1.19	30	1.00	0.99
H6	-0.14	0.40	2	0.99	0.98
H7	0.05	0.31	4	0.97	0.94
H8	0.27	0.44	7	0.96	0.92
H9	0.54	0.74	12	0.97	0.93
H10	1.30	1.36	6	0.97	0.95

483

484

1

2

3

4

5

6

5 Chapter

7

8

An experimental study of kaolinite precipitation kinetics as a function of fluid saturation state at pH 4 and 25 °C

10

11

Snorri Gudbrandsson, Vasileios Mavromatis, Quentin Gautier, Nicolas Bovet, Jacques
Schott, Eric H. Oelkers

14

15

16

(To be submitted upon completion of work)

1 **Abstract**

2 Kaolinite precipitation rates were measured in mixed flow reactors as a function of
3 fluid saturation state at pH=4 and 25 °C. In total 8 long-term precipitation experiments were
4 performed in fluids mildly supersaturated with respect to kaolinite, together with a known
5 quantity of cleaned low defect Georgia Kaolinite, KGa-1b, as seeds. The inlet fluids, one
6 aluminium and one silica rich, were added separately into the reactor at constant flow rates.
7 The kaolinite precipitation rates (r_{kaol}) from this study can be described using

8 $r_{\text{kaol}} = 7.632 \times 10^{-14} \text{ mol/m}^2/\text{s} * (\Omega - 1)^{0.25}$

9 where Ω refers to the fluid saturation state with respect to the precipitating kaolinite.

10 Elemental and mineralogic analyses of the solids suggest that the only phase present after
11 experiments is kaolinite, with two exceptions. In two cases, the post-experiment solids are Al
12 rich, suggesting precipitation of a gibbsite composition phase. Measured kaolinite
13 precipitation rates are relatively slow compared with plagioclase dissolution rates reported in
14 the literature. This observation suggests that kaolinite formation during weathering is limited
15 by its precipitation rates rather than by the availability of aqueous species sourced from
16 plagioclase dissolution.

17 An experimental study of kaolinite precipitation kinetics as a function
18 of fluid saturation state at pH 4 and 25 °C

19

20 Snorri Gudbrandsson^{1,2*}, Vasileios Mayromatis¹, Quentin Gautier¹, Nicolas
21 Bovet³, Jacques Schott¹, Eric H. Oelkers^{1,2}

22 ¹*Geosciences Environment Toulouse (GET), CNRS, UMR5563, Observatoire Midi-Pyrénées,
23 14 Avenue Edouard Belin, 31400, Toulouse, France.*

24 ²*Institute of Earth Sciences, University of Iceland, Sturlugata 7, 101 Reykjavik, Iceland*

25 ³*Nano-Science Center, Department of Chemistry, University of Copenhagen, Denmark.*

26

27 ABSTRACT

28 Kaolinite precipitation rates were measured in mixed flow reactors as a function of fluid
29 saturation state at pH=4 and 25 °C. In total 8 long-term precipitation experiments were
30 performed in fluids mildly supersaturated with respect to kaolinite, together with a known
31 quantity of cleaned low defect Georgia Kaolinite, KGa-1b, as seeds. The inlet fluids, one
32 aluminium and one silica rich, were added separately into the reactor at constant flow rates.
33 The kaolinite precipitation rates (r_{kaol}) from this study can be described using

34 $r_{\text{kaol}} = 7.632 \times 10^{-14} \text{ mol/m}^2/\text{s} * (\Omega - 1)^{0.25}$

35 where Ω refers to the fluid saturation state with respect to the precipitating kaolinite.

36 Elemental and mineralogic analyses of the solids suggest that the only phase present after
37 experiments is kaolinite, with two exceptions. In two cases, the post-experiment solids are Al
38 rich, suggesting precipitation of a gibbsite composition phase. Measured kaolinite
39 precipitation rates are relatively slow compared with plagioclase dissolution rates reported in
40 the literature. This observation suggests that kaolinite formation during weathering is limited
41 by its precipitation rates rather than by the availability of aqueous species sourced from
42 plagioclase dissolution.

43

44 *Keywords:* Kaolinite, Precipitation kinetics, chemical weathering, crystal growth, clay
45 minerals, aluminosilicates

46

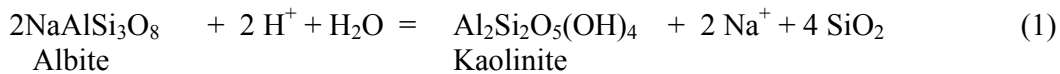
47 5.1 Introduction

48 This study focuses on the precipitation rates of kaolinite, a common silicate weathering
49 product; with a chemical formula that can be represented by $\text{Al}_2\text{Si}_2\text{O}_5(\text{OH})_4$. The rates and
50 mechanism of kaolinite dissolution have been studied for almost 50 years (Polzer, 1965;
51 Carroll and Walther, 1990; Nagy and Lasaga, 1990; Nagy et al., 1991; Oelkers et al., 1994;
52 Ganor et al., 1995; Devidal et al., 1997; Huertas et al., 1999; Cama et al., 2002; Yang and
53 Steefel, 2008) while far fewer kaolinite precipitation rate measurements have been reported
54 (Nagy et al., 1991; Soong, 1992; Nagy and Lasaga, 1993; Devidal et al., 1997; Yang and
55 Steefel, 2008; Yang et al., 2009). Building upon these past studies, we have measured
56 kaolinite precipitation rates as a function of fluid saturation state at 25 °C and pH 4.

57

58 Kaolinite is among the most important minerals produced by weathering at the Earth's
59 surface both due to its importance in soil and subsurface interaction with water (Yang and
60 Steefel, 2008) as well as for its commercial values and the wide range of products kaolinite is
61 used for. Its formation is commonly associated to the weathering of primary feldspar minerals
62 according for example (Helgeson et al., 1984), by substituting K-feldspar for albite

63



64

65 where the resulting aqueous sodium and silica can be removed from the system by fluid flow.
66 The overall rate of this weathering reaction is controlled by the coupling of the rates of
67 feldspar dissolution and kaolinite precipitation. A large number of feldspar dissolution rates
68 have been measured as a function of pH, aqueous fluid composition, and the saturation state
69 of the fluid phase (Chou and Wollast, 1984; Chou and Wollast, 1985; Blum and Lasaga,
70 1991; Oxburgh et al., 1994; Blum and Stillings, 1995; Oelkers and Schott, 1995; Stillings and

71 Brantley, 1995; Brantley and Stillings, 1996, Gudbrandsson et al., 2013). Comparison of the
72 results from reactive transport calculations performed using these feldspar dissolution rates
73 with field weathering rates suggest that rates measured in the laboratory are faster than those
74 found in natural systems (White and Brantley, 2003). A number of studies suggested that this
75 difference stems from the effect of slow clay mineral precipitation, on the overall rate of the
76 natural weathering reactions (Zhu, 2005; Ganor et al., 2007; Maher et al., 2009; Zhu and Lu,
77 2009; Emmanuel and Ague, 2011). This study has been motivated in part to assess this
78 possibility quantitatively, through the measurement of kaolinite precipitation rates as a
79 function of fluid saturation state at conditions typical of natural weathering environments and
80 to use them to assess the role of kaolinite precipitation kinetics in controlling weathering rates
81 at the Earth's surface.

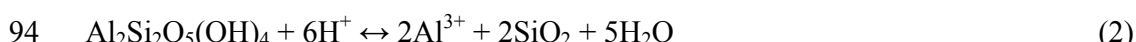
82

83 **5.2 Theoretical background**

84 The standard state adopted in this study is that of unit activity of pure minerals and H₂O
85 at any temperature and pressure. For aqueous species other than H₂O, the standard state is unit
86 activity of species in a hypothetical one molal solution referenced to infinite dilution at any
87 temperature and pressure. All thermodynamic calculations reported in this study were
88 performed using the PHREEQC computer code (Parkhurst and Appelo, 1999) together with
89 its phreeqc.dat database.

90

91 Kaolinite is a sheet mineral consisting of tetrahedral silicon layer and an octahedral
92 aluminium layer that is similar to gibbsite (Drever, 1997). The dissolution/precipitation of
93 kaolinite can be described using the reaction



95 Taking account of the standard state, the law of mass action for Eqn. (2) can be expressed

96
$$K_{eq} = \frac{a_{Al^{3+}}^2 a_{H_4SiO_4}^2}{a_{H^+}^6} \quad (3)$$

97 where K_{eq} represents the equilibrium constant for kaolinite and a_i refers to the activity of i th
98 aqueous species. The chemical affinity, A_{Kaol} , for reaction (2), can be expressed as

99

100
$$A_{Kaol} = RT \ln \left(\frac{K_{eq} a_{H^+}^6}{a_{Al^{3+}}^2 a_{SiO_2}^2} \right) = RT \ln \Omega \quad (4)$$

101

102 where R designates the gas constant, T signifies absolute temperature, Ω refers to the
103 saturation degree of the fluid with respect to kaolinite ($\Omega = K_{eq}/Q$, where Q symbolizes the
104 reaction quotient).

105 Kaolinite precipitation rates are measured in this study with the aid of flow through
106 reactors and are calculated based on mass balance considerations. Mass balance requires that

107
$$\frac{\partial m_{i,in}}{\partial t} - \frac{\partial m_{i,out}}{\partial t} = \frac{\partial m_{i,fluid}}{\partial t} + \frac{\partial m_{i,precip}}{\partial t} \quad (5)$$

108 where $m_{i,in}$, $m_{i,out}$, $m_{i,fluid}$, and $m_{i,precip}$ designate the mass of the i th metal injected into the
109 reactor, flowing out of the reactor, being added to the reactor fluid, and precipitating as a solid
110 phase, and t refers to time. The fluxes in Eqn. (5) are given by

111
$$\frac{\partial m_{i,in}}{\partial t} = c_{i,in} \cdot FR \quad (6a)$$

112
$$\frac{\partial m_{i,out}}{\partial t} = c_{i,out} \cdot FR \quad (6b)$$

113
$$\frac{\partial m_{i,fluid}}{\partial t} = \frac{\partial c_{i,fluid}}{\partial t} \cdot V \quad (6c)$$

114 and

115
$$\frac{\partial m_{i,precip}}{\partial t} = \frac{\partial m_{kaol}}{\partial t} \cdot v_{i,kaol} = r_{kaol,i} \cdot \bar{s}_{kaol} m_{kaol} v_{i,kaol} \quad (6d)$$

116 where $c_{i,in}$, $c_{i,out}$, and $c_{i,fluid}$, represent the concentration of the i th metal in the fluid injected
 117 into the reactor, flowing out of the reactor, present in the reactor, FR refers to the fluid flow
 118 rate, V denotes the volume of fluid in the reactor, $\frac{\partial m_{kaol}}{\partial t}$ signifies the change in the mass of
 119 kaolinite in the reactor with time, $v_{i,kaol}$ symbolizes the stoichiometric number of moles of
 120 the i th metal in one mole of kaolinite, $r_{kaol,i}$ corresponds to the surface area normalized
 121 precipitation rate of kaolinite based on the consumption of the i th metal, and A_{kaol} and m_{kaol}
 122 represent the specific surface area and mass of kaolinite present in the reactor. Combining
 123 Eqns. (5) and (6) and rearranging leads to

$$124 \quad r_{kaol,i} = \frac{(c_{i,in} - c_{i,out}) \cdot FR - \frac{\partial c_{i,fluid}}{\partial t} \cdot V}{A_{kaol} m_{kaol} v_{i,kaol}} \quad (7)$$

125 which allows calculation of kaolinite precipitation rates as a function of time from mixed flow
 126 experiments from the knowledge of the temporal evolution of the fluid concentration of the
 127 i th metal.

128 The variation of mineral precipitation rates with the saturation state of its co-existing
 129 fluid phase is commonly expressed by the relation

$$130 \quad r = r_+ (\Omega - 1)^n \quad (8)$$

131 where r_+ represents the forward reaction rate which may itself depend on the fluid
 132 composition (e.g. Saldi et al., 2009; Saldi et al., 2012) and Ω refers to the saturation degree of
 133 the fluid with respect to kaolinite. The parameter n in Eqn. (8) is often related to the
 134 precipitation mechanism. It has been argued that, for elementary reactions, $n = 1$ is consistent
 135 with transport or adsorption controlled growth on existing mineral surfaces and $n = 2$ is
 136 consistent with spiral growth (Nielsen, 1964; Nielsen, 1984; Gratz et al., 1993; Shiraki and
 137 Brantley, 1995; Teng et al., 2000). If growth is controlled by surface nucleation, rates are
 138 quantified via an exponential function of saturation state, i.e. $n > 2$. As emphasized by
 139 Temkin (1963), however, the chemical affinity of an overall reaction needs to be normalized

140 to that of the elementary reaction to accurately use reaction orders based on these elementary
141 reaction mechanisms. In the case of kaolinite which has a chemical formula containing 2 Al
142 and 2 Si, it seems likely that the elementary reaction for kaolinite precipitation contains less
143 than a mole of kaolinite.

144

145 **5.3 Materials and Methods**

146 Low defect Georgia Kaolinite, KGa-1b, supplied from The Clay Mineral Society (Pruett
147 and Webb, 1993) was used as seed material in the experiments. This kaolinite was cleaned
148 according to (Yang and Steefel, 2008). To remove any possible iron oxy-hydroxide phases the
149 kaolinite was placed in an aqueous pH 3 HCl solution until the supernatant reattained a pH of
150 3. The kaolinite seeds were subsequently washed in ultra pure H₂O (18.2 MΩ cm) until the
151 fluid attained a pH ≥ 5 and the recovered kaolinite was dried for 48 hours at 50 °C. A
152 photomicrograph obtained with scanning electron microscope (SEM) of the resulting cleaned
153 kaolinite powder is shown in Fig. 2a. The kaolinite seeds appear as agglomerated clusters.
154 The surface area for the cleaned kaolinite was 13.2 m²/g ±10% as determined using a via 11
155 point nitrogen adsorption using a Quantachrome Gas Sorption system and the BET method
156 (Brunauer et al., 1938). These kaolinite seeds as well as the kaolinite recovered after each
157 experiment were analyzed by X-ray Diffraction (XRD) using an INEL CPS 120 Cokα
158 diffractometer, with a scanning speed of 0.02° per second; resulting diffraction patters are
159 shown in Fig. 3. The surface composition of the kaolinite was determined using X-ray
160 photoelectron spectroscopy (XPS). These XPS measurements were performed in a Kratos
161 Axis Ultra^{DLD} instrument, fitted with a monochromatic Al_{Kα} X-rays source (power = 150 W).
162 The pressure in the vacuum chamber never exceeded 5x10⁻⁹ Torr during a measurement. A
163 charge neutralizer was used to avoid surface charging. Pass energies of 160 eV and 10 eV

164 were used for wide scans and high resolution scans respectively. Analysis was carried out
165 with the software CasaXPS using a Shirley background. Binding energy calibration was done
166 using the adventitious carbon peak at 185 eV. The results show that the surface atomic ratio
167 Si/Al is 1.15 for the cleaned kaolinite.

168 Precipitation experiments were performed at 25 °C and pH~4 at atmospheric pressure.
169 The reactor system used has been previously described in by Mavromatis et al., (2013) and
170 can be seen in Fig. 1. The reactors consist of 1000 ml polypropylene containers placed in a
171 thermostated water bath. These reactors were equipped with floating magnetic stirring bars,
172 which rotated at approximately 100 rpm to maintain kaolinite seeds in suspension.

173 At the beginning of each experiment, 500 ml of an initial fluid of initial pH of 4 was
174 placed in the reactor together with a known quantity of cleaned kaolinite seeds. Initial reactor
175 fluids contained Al and Si at various concentrations, close to kaolinite saturation.

176 Two distinct inlet fluids were injected into the reactors, using Gilson Minipuls 3
177 peristaltic pumps, to provoke kaolinite precipitation. One of these inlet fluids was Al-rich,
178 prepared by adding the selected quantity of AlCl_3 to H_2O . The second was Si-rich, prepared
179 by adding Baker (experiment FKB) or Maerk (all other experiments) silicic acid to pure
180 water. The pH of the initial and inlet fluids were adjusted to 4 by adding HCl and the ionic
181 strength of these fluids was adjusted to 0.01 by adding NaCl. The concentrations of the inlet
182 fluids were chosen such that most would remain undersaturated after mixing with respect to
183 gibbsite and amorphous Si, respectively. Mixing of these fluids creates a supersaturated
184 aqueous solution with respect to kaolinite in the reactor and precipitation occurs. The
185 experiments were sampled daily and the mass of fluid sampled each day was equal to that
186 added to the reactors since the previous sampling, such that the volume of the reactive fluid in
187 the reactor remained 500ml ($\pm 4\%$) throughout each experiment. The flow rate for both inlet
188 solutions was monitored every fortnight and adjusted if needed, no major changes where

189 observed in the fluid flow rate during the experiments. The kaolinite was allowed to settle for
190 30 to 60 minutes prior to sampling; each fluid sample was taken with a syringe through a
191 0.22 μ m cellulose acetate filter. If any kaolinite particles were found in the filter, they were
192 replaced back into the reactor. This sampling procedure aims to minimize the possibility of
193 removing kaolinite seeds from the reactor, maintaining a constant kaolinite surface area in the
194 reactor throughout the duration of the experiments.

195 The compositions of these initial fluids and the initial surface areas of kaolinite are listed
196 in Table 1. The saturation state of the reactor fluids with respect to kaolinite varied during
197 each experiment as Si and Al were added to the reactor and kaolinite precipitated. Reactor
198 fluids were sampled daily. Part of this sample was used to measure pH at 25 °C using a 713
199 Metrohm pH meter coupled to a Mettler Toledo Inlab® 422. The remaining fluid sample was
200 acidified immediately with 30 μ l bi-distilled HNO₃ 16 M prior to Al and Si analysis. Both inlet
201 and outlet fluids were analyzed for aluminium via flame Atomic Absorption Spectroscopy
202 (AAS) using a Perkin Elmer AAnalyst 400. Fluid silica concentrations were determined by
203 colorimetry using the Molybdate Blue method (Koroleff, 1976), calibrated to 0,036-0,36
204 mmol/L Si, quality checked with Canadian Water standard analytical reference material
205 (Mississippi 03). The reproducibility of pH was \pm 0.02 pH units. The corresponding
206 reproducibility of Si and Al concentrations was \pm 4 % for Si concentrations greater than 0,018
207 mmol/L and Al concentrations greater than 4x10⁻⁴ mmol/L, but on the order of \pm 10 percent
208 for lower concentrations. Selected fluid samples were also analyzed for Si and Al using ICP-
209 OES. These analyses were consistent within uncertainty to those measured by colorimetry and
210 AAS.

211

212 **5.4 Results**

213 The temporal evolution of reactive fluid Al and Si concentrations during all experiments
214 performed in this study is presented in Fig. 4 and Annex A. Reactive fluid Al and Si
215 concentrations increase continuously in each experiment. Experiments FKB and KFC were
216 performed at the highest kaolinite saturation state. Some of the reactive fluids in these
217 experiments were supersaturated with respect to gibbsite. In addition, the Al/Si of the reactive
218 fluids in these experiments is less than 1 suggesting precipitation of an Al-rich phase. The
219 precipitation of an Al-hydroxide phase during these two experiments is also suggested by the
220 results of XRD and XPS analysis of the solids recovered following the experiments (see
221 below).

222 A SEM photomicrograph of the kaolinite after precipitation experiment FKC is shown in
223 Fig. 2b. No distinct surface features are evident on these grains, suggesting that growth
224 occurred by adding material to kaolinite edges rather than growing new kaolinite sheets. The
225 XRD patterns of the solids recovered after each experiment are presented in Fig. 3. The
226 diffraction pattern for all solids apart from those recovered from experiments FKB and FKC
227 are consistent with the presence of only pure kaolinite. An additional peak at around 21° (2θ),
228 consistent with the presence of an aluminium hydroxide phase, is apparent in the solids
229 recovered after experiments FKB and FKC. The Si/Al surface ratios of the solids recovered
230 after each experiment and measured by XPS are listed in Table 2. The Si/Al surface ratios of
231 all solids other than that of FKB were, within uncertainty, the same as that of the initial solid.
232 The Si/Al ratio of FKB was relatively low consistent with the precipitation of some Al-rich
233 phase. The measured specific surface areas, of the solids recovered after each experiment, are
234 presented in Table 2. These surface areas are 10 to 15% lower than that of the initial kaolinite,
235 other than that recovered after experiment FKB, which was ~20% lower.

236 The fluid concentrations shown in Fig. 4 were used to calculate kaolinite precipitation
237 rates as a function of fluid composition using Eqn. (7). To overcome ambiguities associated
238 with the analytical scatter apparent in Fig. 4 measured Si and Al concentrations were fit to

239 $[i] = [i]_0 - a \exp(-t/b)$ (9)

240 where $[i]$ and $[i]_0$ refer to the concentration of the i th element at time t and time 0, where time
241 zero refers to the time the experiments began, and a and b represent fit parameters, as
242 discussed in detail in 5.4. The measured values of Al and Si concentration, pH and time are
243 provided in Annex A. A comparison of the fit and measured concentration values for all
244 experiments is provided in Fig. 4.

245 The fitted Al and Si concentration with time were used to generate kaolinite precipitation
246 rates using Eqn. (7) and the resulting rates are shown as a function of saturation state ($\sqrt{\Omega}-1$)
247 in Fig. 5a. The rates based on Al precipitation in experiment FKB and FKC are substantially
248 higher than other measured rates and substantially higher than those based on Si release. This
249 behaviour may be due to the precipitation of an Al-rich phase as suggested by the XRD
250 pattern of solids recovered after this experiment and the saturation index of some of the
251 reactive fluids with respect to gibbsite. In Fig. 5b we have removed precipitation rates from
252 fluids that were calculated to have been undersaturated with respect to kaolinite and those
253 which did not exhibit dependence with fluid saturation state. Rates based on Si consumption
254 from FKB and those based on Al consumption from experiments FKD and FKJ vary
255 systematically with increasing saturation state (Figure 5b). By considering only these results,
256 kaolinite precipitation rates vary systematically as a function of saturation state as illustrated
257 in Fig. 6. The symbols in this figure plot linearly consistent with

258 $r_{kaol} = 7.632 \times 10^{-14} mol/m^2/s (\Omega_{kaol} - 1)^{0.25}$ (10)

259 The error bars in Fig. 6 correspond to a $\pm 1.5 \times 10^{-13}$ mol/m²/s uncertainty of measured rates.
260 These uncertainties are described in detail below. It can be seen in Fig. 6 that most of the

261 experiments performed at near to equilibrium conditions ($\Omega < 10$) have rates that are equal to
262 zero with experimental uncertainty.

263

264 **5.5 Discussion**

265 **5.5.1 Comparison with previous studies**

266 Kaolinite precipitation rates have been previously reported by Yang and Steefel (2008)
267 and Nagy et al. (1991). A comparison of these values with those of the present study can be
268 made with the aid of Fig. 6. The experiments from Yang and Steefel (2008) were performed
269 at the same pH and temperature as this study as well as the same kaolinite seeds where used.
270 Three of the four kaolinite precipitation rates reported by Yang and Steefel (2008) are equal
271 or within uncertainty to those generated in the present study, whereas the fourth rate that they
272 report is considerably lower than those obtained in this study. Nagy et al. (1991) reported
273 kaolinite precipitation rates at pH 3 and 80 °C. As can be seen in Fig. 6 these 80 °C rates, in
274 general plot above those measured at 25 °C and pH 4 in the present study.

275

276 **5.5.2 Significance of the kaolinite reaction order**

277 The variation of measured kaolinite precipitation rates as a function of saturation state
278 suggests that the reaction order for the kaolinite precipitation reaction is $\frac{1}{4}$. A reaction order
279 of $\frac{1}{4}$ would be consistent with kaolinite growth controlled by the adsorption of material to
280 steps present at kaolinite edges, if 4 elementary adsorption steps were required to form each
281 kaolinite atom. As the chemical kaolinite formula contains 2 Al and 2 Si, this elementary
282 reaction could consist of the attachment of either Al or Si to steps located at kaolinite edges.

283

284 **5.5.3 The role of clay mineral precipitation in controlling weathering rates.**

285 Kaolinite formation is widely attributed to the weathering of primary rocks, such as
286 feldspars (Veizer and Mackenzie, 2003; Markússon and Stefánsson, 2011) as described in Eq.
287 (1) for K-feldspars weathering into kaolinite (Helgeson and Murphy, 1984). As mentioned
288 above, the feldspars are thought to be the primary source for Al^{3+} during terrestrial weathering
289 because their abundance in the Earth's crust (Nesbitt and Young, 1984). A number of past
290 studies suggested that the relatively slow rates of clay mineral precipitation could limit the
291 overall rates of this reaction (Zhu, 2005; Ganor et al., 2007; Maher et al., 2009; Zhu and Lu,
292 2009; Emmanuel and Ague, 2011). At steady-state reaction (1) requires that the rate of
293 kaolinite precipitation equals twice the rate of albite dissolution. Taking account of the
294 kaolinite precipitation rates generated above, Eqn. (9), and those for albite dissolution
295 reported by Gudbrandsson et al. (submitted 2013) one can write

$$\begin{aligned} r_{kaol} = r_{ab} &= 7.632 \times 10^{-14} A_{kaol} (\Omega_{kaol} - 1)^{0.25} \\ &= 6.0 \times 10^{-11} A_{ab} \left(\frac{a_{H^+}^3}{a_{Al^{3+}}} \right)^{0.1} (1 - \Omega_{ab})^{0.33} \end{aligned}$$

296 where r_i represents the rates of denoted mineral in $\text{mol}/\text{m}^2/\text{s}$ and A_i the specific surface area of
297 the denoted mineral, in m^2 . Figure 7 displays $r_{diss, ab}$ and $r_{ppt, kaol}$ as a function of aluminium
298 concentration at pH 4 and 25 °C and assuming an equal surface area of kaolinite and K-
299 feldspar. At conditions just supersaturated with respect to kaolinite, the dissolution rates of
300 albite are fast but rapidly decrease with increasing Al concentration until reaching equilibrium
301 at concentration close to 0.126 mol/kg. On the other hand, kaolinite precipitation rates
302 increase steadily with increasing aluminium concentration and show a behaviour that is likely
303 to reach a plateau in precipitation rates at close to $5 \times 10^{-12} \text{ mol}_{kaol}/\text{m}^2/\text{s}$. The albite dissolution
304 rates and kaolinite precipitation rates are equal when aluminium concentrations are approx
305 0.04 mol/kg. At these conditions, the albite dissolution rate is approximately 7 times lower

306 than it's far from equilibrium dissolution rate, confirming, at least in part the possibility that
307 slow clay mineral precipitation rates limit weathering in natural Earth surface systems. At
308 lower concentrations gibbsite is supersaturated and likely to form at much lower aluminium
309 concentrations. This is in agreement with Helgeson and Murphy (1983) where the evolution
310 of secondary minerals forming during K-feldspar weathering is shown to enter first the
311 stability of gibbsite and with time and increasing Al^{3+} and SiO_2 activity, kaolinite becomes
312 supersaturated.

313

314 **5.5.4 Error and uncertainties**

315 A large amount of scatter was observed in the kaolinite precipitation experiments
316 described above. Much of this scatter derives from the large experimental uncertainties
317 associated with these measurements. The reactor design used in this study was a reactor
318 originally designed to measure the precipitation rates of carbonate minerals (Mavromatis et
319 al., 2013). The precipitation rates of carbonate minerals are, however, on average several
320 orders of magnitude faster than those of kaolinite.

321 Uncertainties in laboratory rate experiments are commonly attributed to several sources.
322 The measurement of the fluid-mineral surface area surface by the BET method is typically on
323 the order of 10%, and this surface area can vary somewhat during fluid-mineral interaction
324 experiments. The uncertainties associated with the measurement of fluid concentrations are
325 ~4%, the measurement of sampling volume are ~2% and the measurement of fluid flow-rate
326 is estimated ~5%. Of these individual uncertainties, the most significant to the results of this
327 study is the uncertainties in measured fluid concentrations. The significance of this
328 uncertainty is due to the fact that the rates in this study are calculated from 1) the difference
329 the inlet and outlet fluid concentrations ($c_{i,in} - c_{i,out}$) and 2) the temporal variation in the
330 reactor fluid as determined from the outlet fluid concentration. The concentration of the

331 outlet fluids ($c_{i,out}$) varied from 0 to \sim 90% of $c_{i,in}$ during the experiments performed in the
332 present study. As such the uncertainties in the ($c_{i,in} - c_{i,out}$) term in Eqn. (7) due to a 4%
333 uncertainty in measured concentrations increased from \sim 10% to 80% as each flow experiment
334 progressed. Uncertainties in the temporal variation in reactive fluid concentrations may be
335 even larger. As can be seen in Annex A, the concentrations of consecutively sampled outlet
336 fluids in general vary by less than a few percent, which is less than the uncertainties in the
337 measured concentrations themselves. It is for this reason that rates in the present study were
338 estimated by first fitting the temporal reactor fluid concentrations to a power function.

339 Although this limits somewhat the uncertainties associated with the estimation of the $\frac{\partial c_{i,fluid}}{\partial t}$
340 term in Eqn. (7) these uncertainties are nevertheless large. An additional source of
341 uncertainty in measured rates may stem from the pH stability of the reactive fluid; the pH
342 during the experiments performed in this study varies within ± 0.1 pH units over the course of
343 the experiments (see Annex A). The variation of kaolinite precipitation rates with fluid pH is
344 currently unknown. ***Taking account of the important uncertainties described above suggests***
345 ***that the overall uncertainties on the kaolinite dissolution rates generated in this study are***
346 ***large and likely exceeds 100%.*** This conclusion could explain why some of the experiments
347 performed in this study yielded negative kaolinite precipitation rates (suggesting kaolinite
348 dissolution) in experiments performed in fluids calculated to be supersaturated with respect to
349 kaolinite, and the large scatter in the rates illustrated in Fig. 5. It should also be noted that the
350 uncertainties of kaolinite precipitation rates reported in the literature are also high. Nagy et al.
351 (1991) reported that the kaolinite precipitation rates generated in their study had an
352 uncertainty of $\pm 30\%$. Similarly, Yang and Steefel (2008) that the kaolinite precipitation rates
353 generated in their study based on Al release had an uncertainty of $\pm 30\%$.

354

355 **5.6 Conclusions**

356 In this study kaolinite precipitation rates are reported as a function of fluid saturation
357 state. Although the precipitation rates of kaolinite from this study are in good agreement with
358 corresponding precipitation rates reported by Yang and Steefel (2008) and Nagy et al. (1991)
359 all rates have high uncertainties so these rates should be viewed as provisional estimated until
360 more precise values are available.

361 The precipitation rates of kaolinite are also considerably slower than the dissolution rates
362 of the plagioclase, the main aluminium source during weathering for kaolinite formation. It is
363 therefore likely that the slow rates of kaolinite precipitation rather than the dissolution rates of
364 the aluminium bearing primary rock, is the limiting factor in kaolinite formation in many
365 natural systems.

366

367 Acknowledgements

368 We would like to thank our friends and colleagues, including Sigurður R. Gislason, Andri Stefánsson,
369 Niels Oskarsson and the Carb-Fix Group at the University of Iceland, Carole Causserand, Stephanie
370 Mounic, Alain Castillo, Pasquale Gisquet, Sophy Gouy, Thierry Aigouy, Philippe de Parseval, and
371 Julien Declercq at the GET/CNRS in Toulouse, France and Ingvi Gunnarsson at Reykjavík Energy.
372 This study was funded by the European Community through the Delta-Min (Mechanisms of Mineral
373 Replacement Reactions; Grant PITN-GA-2008-215360) and SPI-2011 Cooperation Grant #283148.

374 **References**

- 375 Blum, A.E., Lasaga, A.C., 1991. The Role of Surface Speciation in the Dissolution of Albite.
376 *Geochimica Et Cosmochimica Acta*, 55(8): 2193-2201.
- 377 Blum, A.E., Stillings, L.L., 1995. Feldspar dissolution kinetics. In: White, A.F., Brantley, S.L.
378 (Eds.), *Chemical Weathering Rates of Silicate Minerals*. Mineralogical Society of
379 America, Washington, DC, pp. 291-351.
- 380 Brantley, S.L., Stillings, L., 1996. Feldspar dissolution at 25 degrees C and low pH. *American
381 Journal of Science*, 296(2): 101-127.
- 382 Brunauer, S., Emmett, P., Teller, E., 1938. Adsorption of gases in multimolecular layers,
383 *Journal of the American Chemical Society*, pp. 309-319.
- 384 Cama, J., Metz, V., Ganor, J., 2002. The effect of pH and temperature on kaolinite dissolution
385 rate under acidic conditions. *Geochimica Et Cosmochimica Acta*, 66(22): 3913-3926.
- 386 Carroll, S.A., Walther, J.V., 1990. Kaolinite dissolution at 25 °C, 60 °C, and 80 °C. *American
387 Journal of Science*, 290(7): 797-810.
- 388 Chou, L., Wollast, R., 1984. Study of the Weathering of Albite at Room-Temperature and
389 Pressure with a Fluidized-Bed Reactor. *Geochimica Et Cosmochimica Acta*, 48(11):
390 2205-2217.
- 391 Chou, L., Wollast, R., 1985. Steady-State Kinetics and Dissolution Mechanisms of Albite.
392 *American Journal of Science*, 285(10): 963-993.
- 393 Devidal, J.L., Schott, J., Dandurand, J.L., 1997. An experimental study of kaolinite
394 dissolution and precipitation kinetics as a function of chemical affinity and solution
395 composition at 150 degrees C, 40 bars, and pH 2, 6.8, and 7.8. *Geochimica Et
396 Cosmochimica Acta*, 61(24): 5165-5186.
- 397 Drever, J.I., 1997. *The Geochemistry of Natural Waters. Surface and Groundwater
398 Environments*. Prentice Hall, 71 pp.
- 399 Emmanuel, S., Ague, J.J., 2011. Impact of nano-size weathering products on the dissolution
400 rates of primary minerals. *Chemical Geology*, 282(1-2): 11-18.
- 401 Ganor, J., Lu, P., Zheng, Z.P., Zhu, C., 2007. Bridging the gap between laboratory
402 measurements and field estimations of silicate weathering using simple calculations.
403 *Environmental Geology*, 53(3): 599-610.
- 404 Ganor, J., Mogollón, J.L., Lasaga, A.C., 1995. The effect of pH on kaolinite dissolution rates
405 and on activation energy. *Geochimica Et Cosmochimica Acta*, 59(6): 1037-1052.
- 406 Gratz, A.J., Hillner, P.E., Hansma, P.K., 1993. Step dynamics and spiral growth on calcite.
407 *Geochimica Et Cosmochimica Acta*, 57(2): 491-495.
- 408 Gudbrandsson S., Wolff-Boenisch D., Gislason S.R. and Oelkers E.H. (2013) Experimental
409 characterization of plagioclase dissolution rates as a function of their composition and
410 pH at 22° C. Submitted to *Geochim. Cosmochim. Acta*.
- 411 Helgeson, H.C., Murphy, W.M., 1983. Calculations of mass-transfer among minerals and
412 aqueous-solutions as a function of time and surface-area in geochemical processes. 1.
413 Comutational approach *Journal of the International Association for Mathematical
414 Geology*, 15(1): 109-130.
- 415 Helgeson, H.C., Murphy, W.M., Aagaard, P., 1984. Thermodynamic and Kinetic Constraints
416 on Reaction-Rates among Minerals and Aqueous-Solutions .2. Rate Constants,
417 Effective Surface-Area, and the Hydrolysis of Feldspar. *Geochimica Et Cosmochimica
418 Acta*, 48(12): 2405-2432.
- 419 Huertas, F.J., Fiore, S., Huertas, F., Linares, J., 1999. Experimental study of the hydrothermal
420 formation of kaolinite. *Chemical Geology*, 156(1-4): 171-190.

- 421 Koroleff, F., 1976. Determination of silicon. In: Grasshoff, K. (Ed.), *Methods of Seawater*
422 Analysis. Springer-Verlag, Berlin, Germany.
- 423 Maher, K., Steefel, C.I., White, A.F., Stonestrom, D.A., 2009. The role of reaction affinity
424 and secondary minerals in regulating chemical weathering rates at the Santa Cruz Soil
425 Chronosequence, California. *Geochimica Et Cosmochimica Acta*, 73(10): 2804-2831.
- 426 Markússon, S.H., Stefánsson, A., 2011. Geothermal surface alteration of basalts, Krýsuvík
427 Iceland—Alteration mineralogy, water chemistry and the effects of acid supply on the
428 alteration process. *Journal of Volcanology and Geothermal Research*, 206(1–2): 46-
429 59.
- 430 Mavromatis, V., Gautier, Q., Bosc, O., Schott, J., 2013. Kinetics of Mg partition and Mg
431 stable isotope fractionation during its incorporation in calcite. *Geochimica Et*
432 *Cosmochimica Acta*(0).
- 433 Nagy, K.L., Blum, A.E., Lasaga, A.C., 1991. Dissolution and precipitation of kaolinite at 80
434 °C and pH 3 - The dependence on solution saturation state. *American Journal of*
435 *Science*, 291(7): 649-686.
- 436 Nagy, K.L., Lasaga, A.C., 1990. The effect of deviation from equilibrium on the kinetics of
437 dissolution and precipitation of kaolinite and gibbsite. *Chemical Geology*, 84(1–4):
438 283-285.
- 439 Nagy, K.L., Lasaga, A.C., 1993. Simultaneous precipitation kinetics of kaolinite and gibbsite
440 at 80 °C and pH 3. *Geochimica Et Cosmochimica Acta*, 57(17): 4329-4335.
- 441 Nesbitt, H.W., Young, G.M., 1984. Prediction of some weathering trends of plutonic and
442 volcanic rocks based on thermodynamic and kinetic considerations. *Geochimica Et*
443 *Cosmochimica Acta*, 48(7): 1523-1534.
- 444 Nielsen, A.E., 1964. Kinetics of precipitation, Pergamon Press, pp. 151.
- 445 Nielsen, A.E., 1984. Electrolyte crystal-growth mechanisms. *Journal of Crystal Growth*,
446 67(2): 289-310.
- 447 Oelkers, E.H., Schott, J., 1995. Experimental study of anorthite dissolution and the relative
448 mechanism of feldspar hydrolysis. *Geochimica Et Cosmochimica Acta*, 59(24): 5039-
449 5053.
- 450 Oelkers, E.H., Schott, J., Devidal, J.L., 1994. The effect of aluminum, pH and chemical
451 affinity on the rates of aluminosilicate dissolution reactions. *Geochimica Et*
452 *Cosmochimica Acta*, 58(9): 2011-2024.
- 453 Oxburgh, R., Drever, J.I., Sun, Y.T., 1994. Mechanism of Plagioclase Dissolution in Acid-
454 Solution at 25-Degrees-C. *Geochimica Et Cosmochimica Acta*, 58(2): 661-669.
- 455 Parkhurst, D.L., Appelo, C.A.J., 1999. User's guide to PHREEQC (Version 2)—A computer
456 program for speciation, batch-reaction, one-dimensional transport, and inverse
457 geochemical calculations. U. S. G. S. Water Resour. Inv. Report.: 99-4259.
- 458 Polzer, W.L.H., J. D., 1965. The Dissolution of Kaolinite. *Journal of Geophysical Research*,
459 70: 6233-6240.
- 460 Pruett, R.J., Webb, H.L., 1993. Sampling and analysis of KGa-1b well-crystallized kaolin
461 source clay. *Clays and Clay Minerals*, 41(4): 514-519.
- 462 Saldi, G.D., Jordan, G., Schott, J., Oelkers, E.H., 2009. Magnesite growth rates as a function
463 of temperature and saturation state. *Geochimica Et Cosmochimica Acta*, 73(19): 5646-
464 5657.
- 465 Saldi, G.D., Schott, J., Pokrovsky, O.S., Gautier, Q., Oelkers, E.H., 2012. An experimental
466 study of magnesite precipitation rates at neutral to alkaline conditions and 100–200 °C
467 as a function of pH, aqueous solution composition and chemical affinity. *Geochimica*
468 *Et Cosmochimica Acta*, 83(0): 93-109.

- 469 Shiraki, R., Brantley, S.L., 1995. Kinetics of near-equilibrium calcite precipitation at 100 °C -
470 an evaluation of elementary reaction-based rate laws. *Geochimica Et Cosmochimica
471 Acta*, 59(8): 1457-1471.
- 472 Soong, C.B., H. L., 1992. Precipitation and dissolution kinetics of kaolinite under
473 hydrothermal conditions. *Geol. Soc. Am., Abstr. Programs*, 24: 7.
- 474 Stillings, L.L., Brantley, S.L., 1995. Feldspar dissolution at 25 °C and pH 3: Reaction
475 stoichiometry and the effect of cations. *Geochimica Et Cosmochimica Acta*, 59(8):
476 1483-1496.
- 477 Temkin, M.I., 1963. Kinetics of stationary reactions. *Doklady Akademii Nauk SSSR*, 152:
478 156-157.
- 479 Teng, H.H., Dove, P.M., De Yoreo, J.J., 2000. Kinetics of calcite growth: Surface processes
480 and relationships to macroscopic rate laws. *Geochimica Et Cosmochimica Acta*,
481 64(13): 2255-2266.
- 482 Veizer, J., Mackenzie, F., 2003. Evolution of sedimentary rocks. *Treatise on geochemistry*, 7:
483 369-407.
- 484 White, A.F., Brantley, S.L., 2003. The effect of time on the weathering of silicate minerals:
485 why do weathering rates differ in the laboratory and field? *Chemical Geology*, 202(3-
486 4): 479-506.
- 487 Yang, L., Steefel, C.I., 2008. Kaolinite dissolution and precipitation kinetics at 22 °C and pH
488 4. *Geochimica Et Cosmochimica Acta*, 72(1): 99-116.
- 489 Yang, L., Steefel, C.I., Maher, K., White, A., 2009. Kinetics of kaolinite precipitation at the
490 laboratory and field scale. *Geochimica Et Cosmochimica Acta*, 73(13): A1476-A1476.
- 491 Zhu, C., 2005. In situ feldspar dissolution rates in an aquifer. *Geochimica Et Cosmochimica
492 Acta*, 69(6): 1435-1453.
- 493 Zhu, C., Lu, P., 2009. Alkali feldspar dissolution and secondary mineral precipitation in batch
494 systems: 3. Saturation states of product minerals and reaction paths. *Geochimica Et
495 Cosmochimica Acta*, 73(11): 3171-3200.
- 496
- 497
- 498

499 **Figure Captions**

500

501 Figure 1 Design of the reactor system used in this study: a) Peristaltic pump for inlet
 502 solutions, b) 1000 mL constant temperature vessel , with 500 mL of reactive fluid,
 503 equipped with, from left, fluid inlet tubes, floating stirring bar, and fluid outlet, c)
 504 Outlet sampled with a syringe and filtered through a 0.22 μm cellulose acetate
 505 filter.

506 Figure 2 SEM photomicrographs of the kaolinite used in this study. Image a) depicts the
 507 pristine kaolinite before precipitation experiments, whereas image b shows the
 508 kaolinite after precipitation experiment FKC.

509 Figure 3 XRD patterns of the initial seed kaolinite and the kaolinite recovered after all
 510 experiments, noted by the last name of the experiment. All patterns indicate that
 511 the solid is pure kaolinite, apart from KFB (B) and FKC (C). In these samples a
 512 peak at $\sim 20^\circ$ is present likely due to the presence of an aluminium-rich phase.

513 Figure 4 Temporal evolution of reactive fluid composition in all experiments. During
 514 experiments FKB and FKC, the aluminium concentration is lower than that of the
 515 Si suggesting the precipitation of an Al-rich phase.

516 Figure 5 Measured instantaneous kaolinite precipitation rates versus $(\sqrt{\Omega}-1)^{0.5}$ are shown
 517 in figure a). Filled and open circles represent precipitation rates based on fluid
 518 aluminium and silica concentrations, respectively. The rates based on aluminium
 519 precipitations from experiments FKB and FKC are higher than those based on
 520 silica in the same experiments, likely because of and aluminium-rich phase is also
 521 forming in these experiments. Figure 5b displays selected rates from the
 522 experiments, specifically Si rates from FKB, open squares, and aluminium rates
 523 from FKJ, filled triangles and aluminium rates from FKJ, filled hexagons.

524 Figure 6 Precipitation rates of kaolinite from selected experiments versus $(\Omega^{1/2}-1)$. The
 525 open circles represent the selected precipitation rates from this study. Red filled
 526 circles represent measured precipitation rates from Yang and Steefel (2008) and
 527 yellow filled circles represent measured precipitation rates from Nagy and Lasaga
 528 (1988).

529 Figure 7 Rates of albite plagioclase dissolution and kaolinite precipitation as a function of
 530 aluminium concentration at pH 4 and Si concentration set to be in equilibrium
 531 with quartz. The dissolution rate of albite decreases with increasing aluminium
 532 concentration in solution whereas the precipitation rate of kaolinite is likely to
 533 increase.

534

535

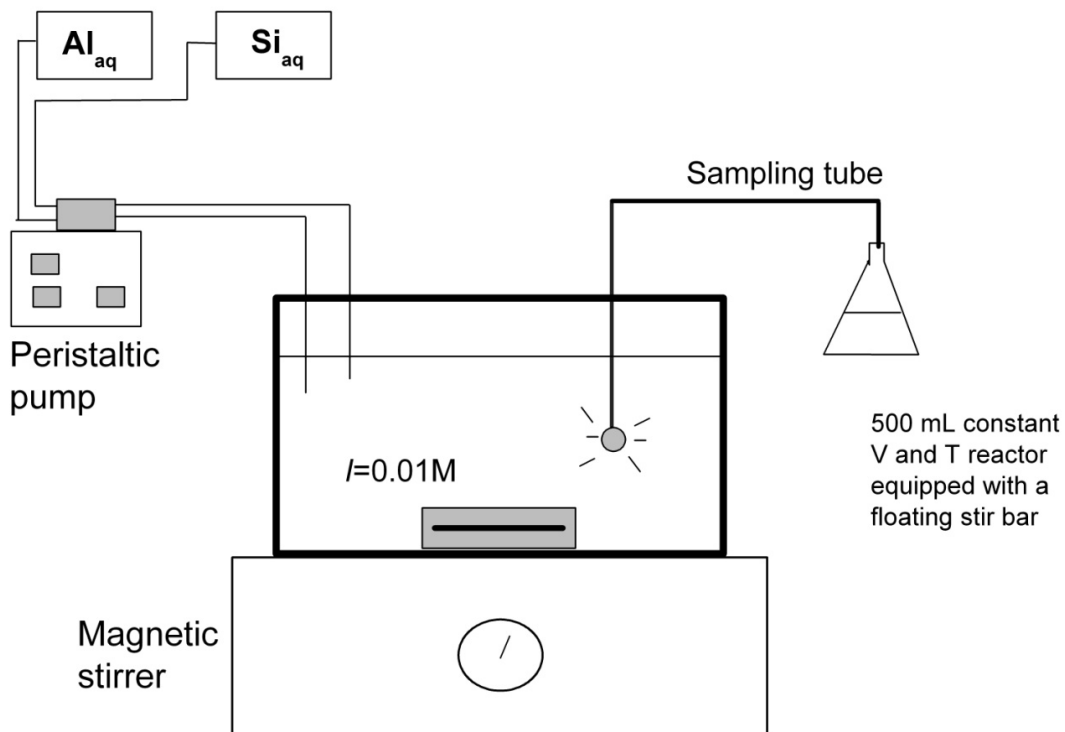
536

537

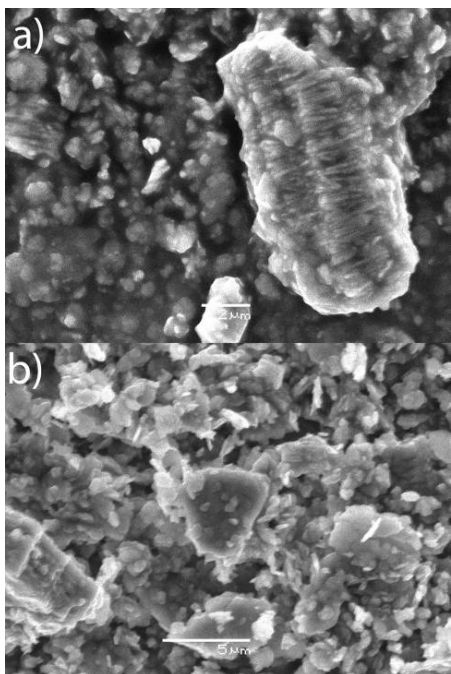
538

539

540 **Figure Captions**
541



542
543 Figure 1 Design of the reactor system used in this study: a) Peristaltic pump for inlet
544 solutions, b) 1000 mL constant T vessel , with 500 mL of reactive fluid, equipped
545 with, from left, fluid inlet tubes, floating stirring bar, and fluid outlet, c) Outlet
546 sampled with a syringe and filtered through a $0.22 \mu\text{m}$ cellulose acetate filter.
547
548
549

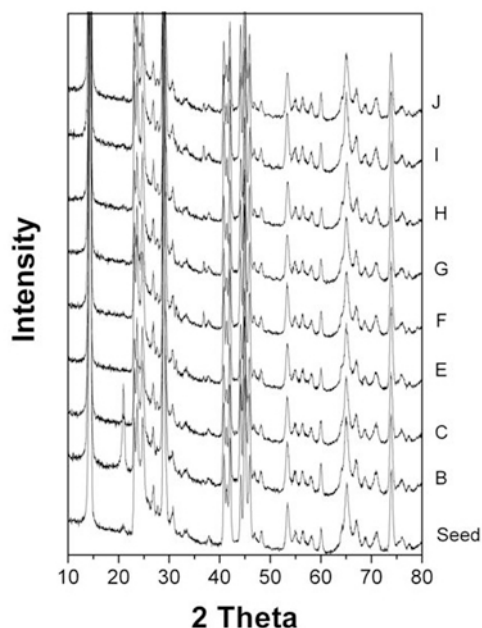


550

551

552 Figure 2 SEM photomicrographs of the kaolinite used in this study. Image a) depicts the
553 pristine kaolinite before precipitation experiments, whereas image b shows the
554 kaolinite after precipitation experiment FKC.

555



556

557

558 Figure 3 XRD patterns of the initial seed kaolinite and the kaolinite recovered after all
559 experiments, noted by the last name of the experiment. All patterns indicate that
560 the solid is pure kaolinite, apart from KFB (B) and FKC (C). In these samples a
561 peak at $\sim 20^\circ$ is present likely due to the presence of an aluminium-rich phase.
562

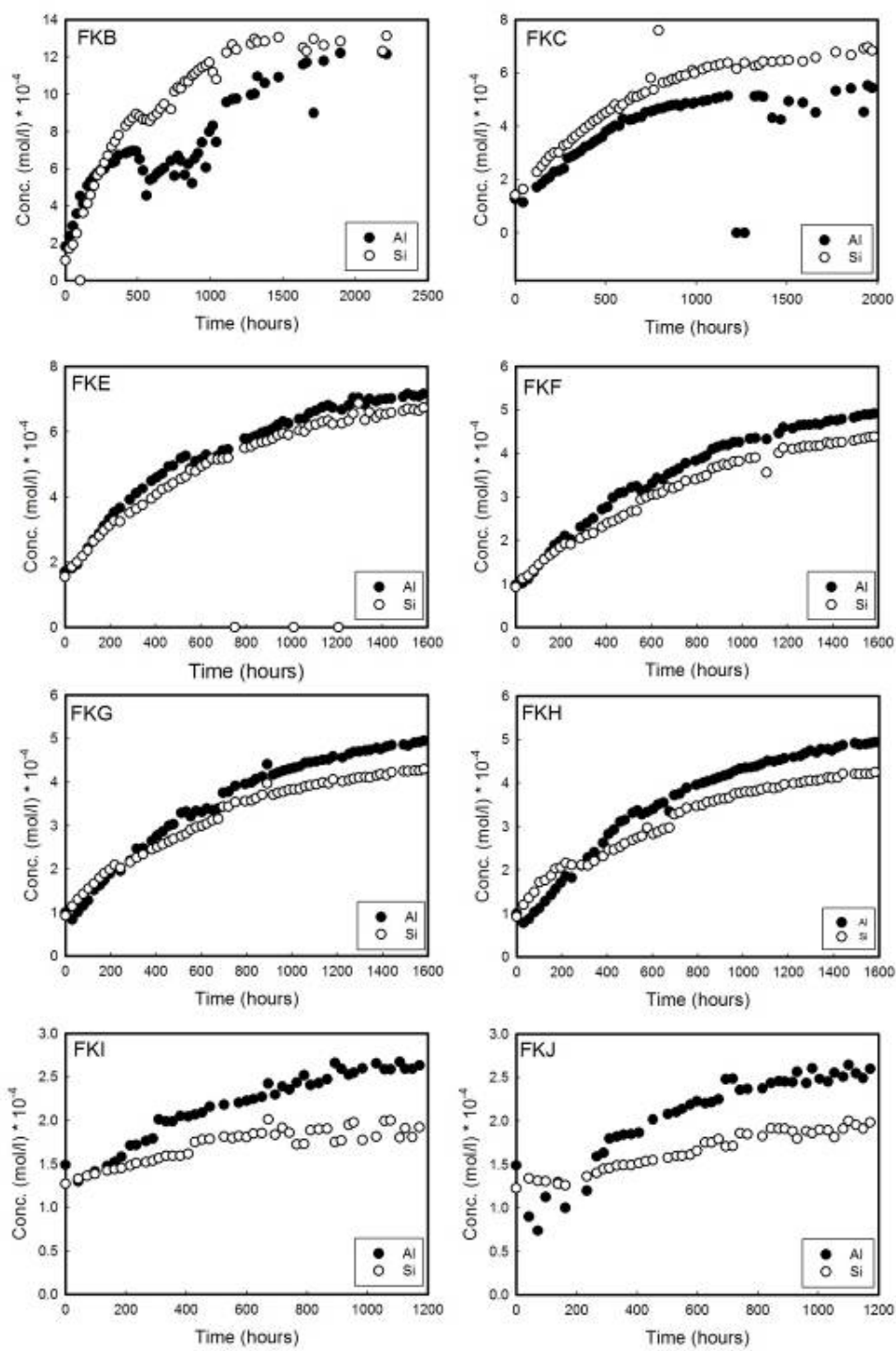
563

564

565

566

567

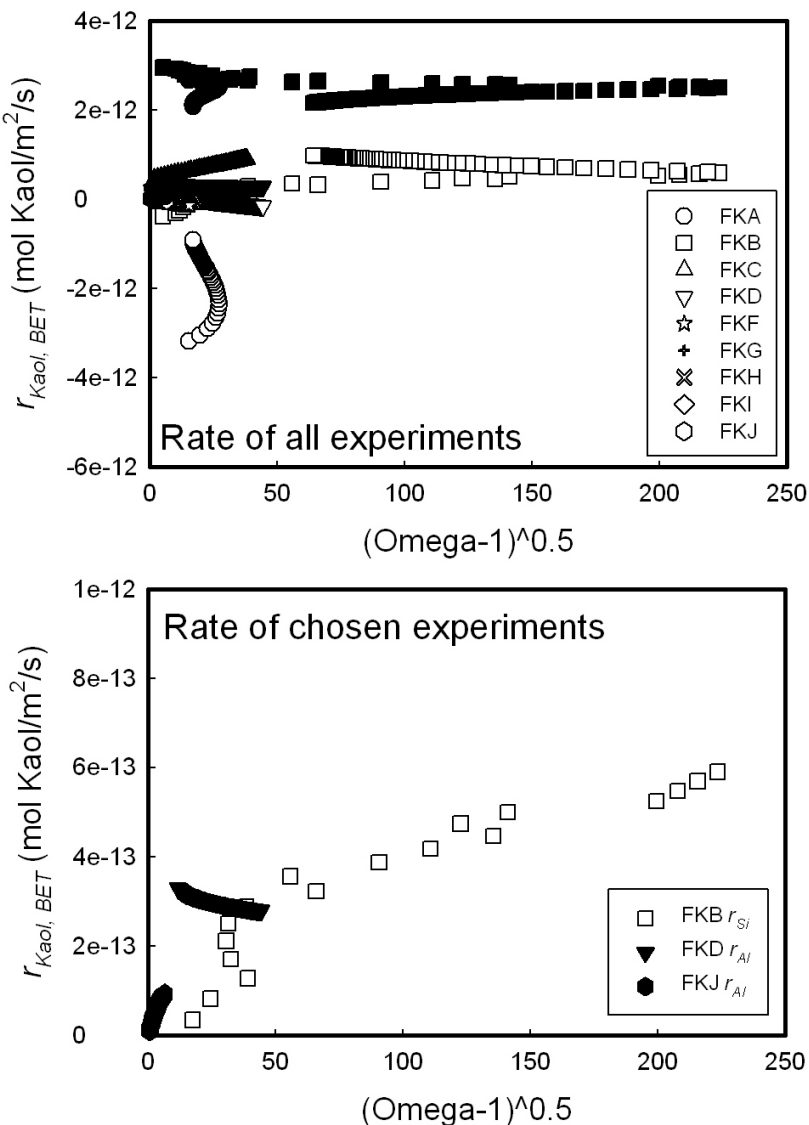


568

569

570 Figure 4 Temporal evolution of reactive fluid composition in all experiments. During
 571 experiments FKB and FKC, the aluminium concentration is lower than that of the
 572 Si suggesting the precipitation of an Al-rich phase.

573

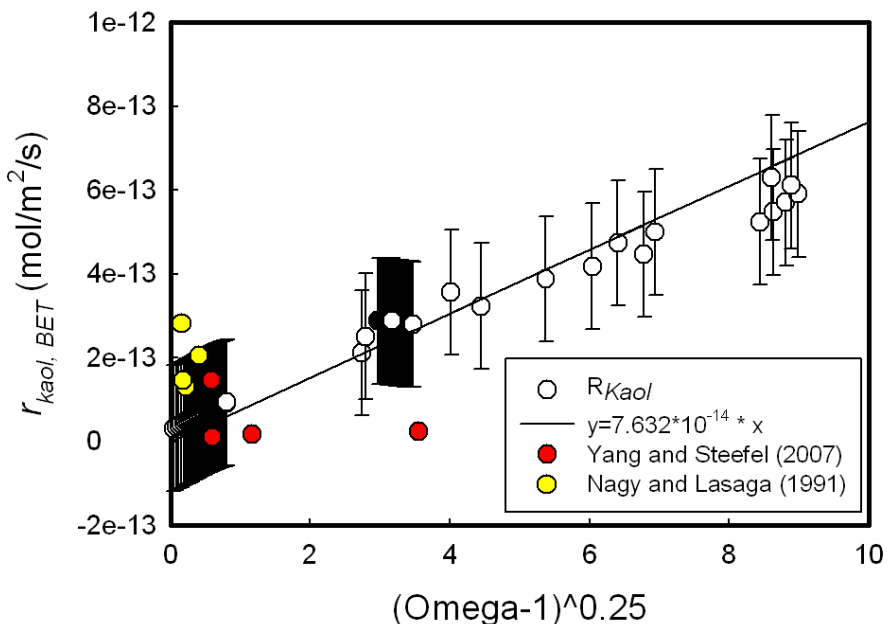


574

575

576 Figure 5 Measured instantaneous kaolinite precipitation rates versus $(\Omega-1)^{0.5}$ are shown
 577 in figure a). Filled and open circles represent precipitation rates based on fluid
 578 aluminium and silica concentrations, respectively. The rates based on aluminium
 579 precipitations from experiments FKB and FKC are higher than those based on
 580 silica in the same experiments, likely because of an aluminium-rich phase is also
 581 forming in these experiments. Figure 5b displays selected rates from the
 582 experiments, specifically Si rates from FKB, open squares, and aluminium rates
 583 from FKD, filled triangles and aluminium rates from FKJ, filled hexagons.

584



585

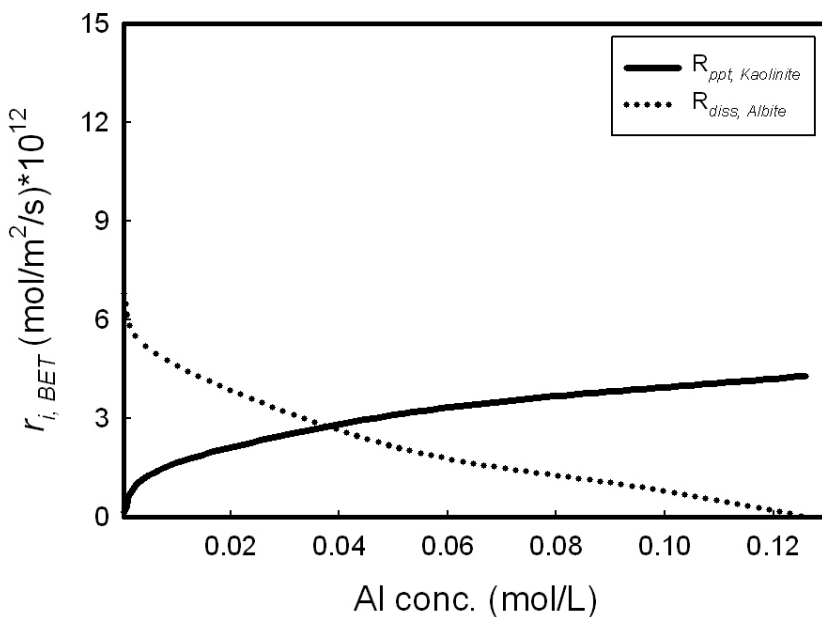
586 Figure 6 Precipitation rates of kaolinite from selected experiments versus $(\Omega^{1/2}-1)$. The
 587 open circles represent the selected precipitation rates from this study.
 588 Red filled circles represent measured precipitation rates from Yang and Steefel (2008)
 589 and yellow filled circles represent measured precipitation rates from Nagy and Lasaga
 590 (1988).

591

592

593

594



595

596 Figure 7 Rates of albite plagioclase dissolution and kaolinite precipitation as a function of
597 aluminium concentration at pH 4 and Si concentration set to be in equilibrium
598 with quartz. The dissolution rate of albite decreases with increasing aluminium
599 concentration in solution whereas the precipitation rate of kaolinite is likely to
600 increase.

601

602

603

604

605

606

607

608

609

610

611

612

613

614 Table 1. Initial concentrations and surface area for kaolinite flow-through experiments.

Experiment Name	Initial (mmol/l)		Inlet (mmol/l)		Kaolinite	
	Al	Si	Al	Si	gr	m ²
FKB	0.19	0.06	3.45	3.14	2.06	27.1
FKC	0.13	0.14	1.56	1.39	2.01	26.6
FKE	0.17	0.16	1.78	1.49	2.66	35.1
FKF	0.10	0.09	1.11	0.87	2.58	34.0
FKG	0.10	0.09	1.11	0.87	5.13	67.7
FKH	0.10	0.09	1.11	0.87	7.78	103
FKI	0.15	0.13	0.54	0.37	2.99	39.5
FKJ	0.15	0.12	0.57	0.37	8.07	107

615

616

617

618

619

620

621

622

623

624

625

626

627

628

629

630

631

632

633 Table 2. Experimental runtime and surface measurements and Si/Al ratios from the solids,
 634 prior to and after experiments.

Experiment Name	Experiment Runtime	Surface change			
		Si/Al	Δ%	BET	Δ%
Initial		1.15		13.20	
FKB	2215	0.97	84%	10.64	81%
FKC	1971	1.13	98%	11.96	91%
FKE	1584	1.19	103%	11.81	89%
FKF	1584	1.14	99%	11.34	86%
FKG	1584	1.14	99%	11.12	84%
FKH	1584	1.16	101%	11.43	87%
FKI	1288	1.13	98%	12.86	97%
FKJ	1288	1.15	100%	11.84	90%

635

636

637

638

6 Conclusions and implications

In this thesis I combined experimental studies on the dissolution behaviour of primary silicate rocks and minerals with measured precipitation rates of common aluminium rich secondary clay minerals. Each study has major implications, both for experimental and natural systems. Below I list the main conclusions of this study in the same order as the chapters presented in this thesis:

- The dissolution of crystalline basalt is temperature dependent, with dissolution rates increasing with increasing temperature.
- The dissolution of crystalline basalt at acid conditions is dominated by olivine and pyroxene dissolution but at alkaline conditions, it is dominated by plagioclase dissolution. This results in the preferential release of Fe^{+2} and Mg^{+2} cations at acid condition but Ca^{+2} at alkaline conditions.
- The dissolution of all plagioclases shows the same pH dependence as observed by Chou and Wollast (1985) and Knauss and Wolery (1986) for albite and also for basaltic glass (Gislason and Oelkers , 2003) where the rates decrease with increasing pH at acid conditions and increase with increasing pH at alkaline conditions for rates based on Si release.
- At acid conditions plagioclase dissolution rates increase with increasing An content i.e. the anorthite dissolves fastest and the albite slowest.
- There is no effect of plagioclase An content on dissolution rates at alkaline conditions.
- A simple equation describing plagioclase dissolution rates as a function of temperature and the composition of the fluid and the solid phase was proposed.
- Gibbsite precipitates readily at supersaturated conditions in the reactor at both 25 and 80 °C.
- At pH 11 and 22 °C the precipitation rates of gibbsite at measured saturation are equal to the far from equilibrium dissolution rates of plagioclases.
- Precipitation rates of gibbsite decrease faster with decreasing pH than the plagioclase dissolution rates. That implies that at pH close to natural environments slow gibbsite precipitation rates are the limiting factor to clay mineral formation, rather than slow aluminium release rates from plagioclase.
- Fluid chemistry as well as solid analysis suggests that kaolinite precipitation took place during most experiments performed at 22 °C. This was, however, not confirmed by SEM analysis as the precipitation features are hard to detect due to the agglomeration of the kaolinite sheets.
- Reported kaolinite precipitation rates are in agreement with previously published rates.
- Kaolinite precipitation rates are significantly slower than the dissolution rates of Al-bearing primary minerals such as plagioclase.

6.1 Implications

The CarbFix project in Iceland where the aim is to inject CO₂ from a geothermal power plant into basalts for carbon mineral storage started in the year 2007 (Loose et al., 2009; Gislason et al., 2009; Gislason et al., 2010; Matter et al., 2009, 2011). The behaviour of crystalline basalt elemental release vs. that of basaltic glass observed in this thesis suggests differing behaviour depending on crystallinity.

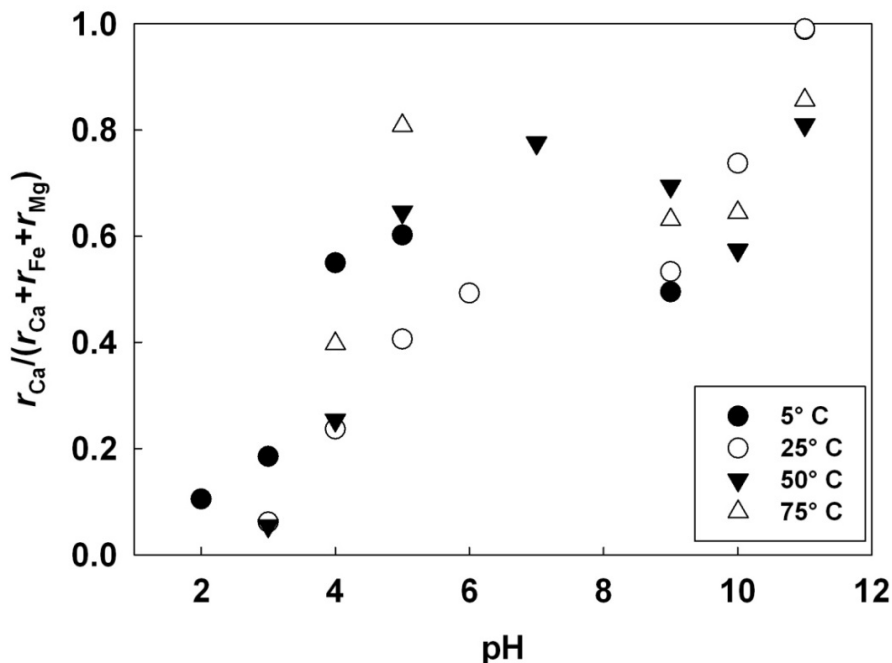
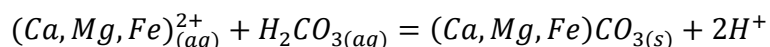


Figure 7 The fraction of Ca versus total divalent metal cation release as a function of pH. At acid conditions the dissolution of Fe and Mg bearing minerals dominate the dissolution while as the pH increases the role of Ca bearing minerals in dissolution increases. Source: Gudbrandsson et al. (2011)

During the CO₂ injection the divalent cations, Ca, Mg, and Fe are released from the basalt to the fluid phase and are available to form carbonates according to:



were the supply of divalent cations when injecting into crystalline basalts varies with pH because of the distinct dissolution rates of the constituent minerals (Fig 7). At alkaline conditions, plagioclase is the main dissolving mineral in crystalline basalt. This is consistent with observation in nature, where in basaltic terrains such as Iceland the pH of the groundwater is alkaline and the dominant secondary minerals are Fe and Ca rich clays, calcium carbonates and zeolites that are usually Na, Ca, and Al rich (Fig 8) (Walker, 1960; Kristmannsdottir and Tomasson, 1978; Johnson et al., 1983; Neuhoff et al., 1997; Neuhoff,

1999; Neuhoff et al., 2000; Gustavson, 2006; Neuhoff et al., 2006; Rogers et al., 2006; Arnorsson and Neuhoff, 2007; Stockmann et al., 2008).

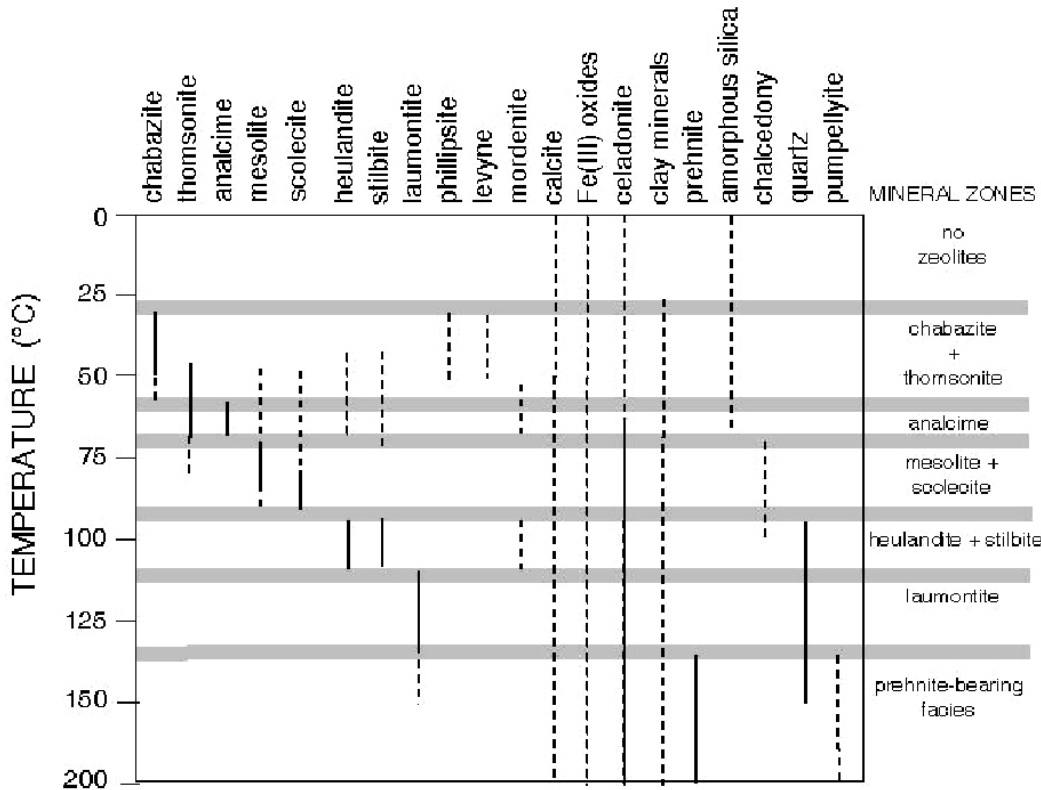


Figure 8. Diagram showing the secondary minerals found in low grade metamorphism of igneous provinces. The solid line indicates the temperatures where each mineral is commonly observed, whereas the dashed lines show where each mineral is only occasionally observed. The grey horizontal bars note the zeolite zones as listed on the right of the figure. Source: Gustavson (2006).

In geothermal areas the secondary minerals can be used as a thermometer to identify the rock alteration temperature (Kristmannsdottir and Tomasson, 1978) and the zeolites zones described by Walker (1960). The thermometer indicates that basalts alter to zeolites > chabazite > thomsonite > analcime > scolecite > heulandite > laumontite > prehnite > epidote with increasing temperature (Figure 8). In the acid surface alteration on top of the high temperature geothermal system located at Krýsuvík, SW-Iceland, the secondary phases found include kaolinite, montmorillonite, and goethite. This suggests that kaolinite can also be found as a secondary phase in basaltic formations where the pH is acidic (Markússon and Stefánsson, 2011).

6.2 The future

As is the case with all scientific research, each study provokes further work. In the case of carbon storage, it remains to be determined where carbonate minerals precipitate and how this

affects reservoir properties. In steam from geothermal fields sulphur is commonly a major component of the gas phase. In the next few years there will be legislation to limit the sulphur released into atmosphere from geothermal power plants. Sulphur is found in several common secondary phases formed during basalt alteration, i.e. pyrite (FeS) as well as in some zeolites. It is therefore interesting to investigate if and what effects sulphur has on the dissolution/precipitation behaviour of basalts. Similar to the work done on carbon coating effect on basaltic glass and diopside by Stockmann et al. (2011), as well as work done by Gysi and Stefánsson (2011) where the CO_2 effect on basaltic glass dissolution was investigated. Some previous work on the effect of SO_4 on basaltic glass reactivity has been published (Flaathen et al., 2010) suggesting sulphur has minimum effects. The effect of temperature on crystalline basalt dissolution rates suggests that there is a smaller effect of temperature on rates at alkaline condition than at acidic conditions. Does this stem from plagioclase dissolution behaviour? This question remains unanswered.

Still there are only few published precipitation rates of secondary aluminium phases available despite this thesis. Although the indication is that gibbsite readily precipitates at low temperature and alkaline pH, many conditions are experimentally challenging i.e. at intermediate pH where the aqueous solution Al concentration is low or at conditions where rates are extremely slow. Such is also the case for kaolinite where the precipitation rates are so slow that the uncertainties in measured rates are high. These uncertainties can possibly be decreased by increasing the reaction temperature where the rates are faster.

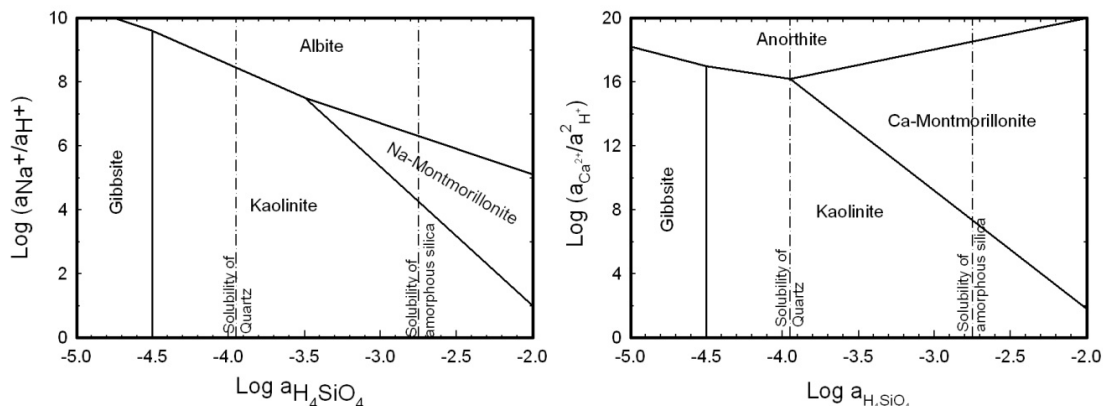


Figure 9. The stability diagrams of $\text{Na}_2\text{O}-\text{Al}_2\text{O}_3-\text{SiO}_2-\text{H}_2\text{O}$ in figure a) and $\text{CaO}-\text{Al}_2\text{O}_3-\text{SiO}_2-\text{H}_2\text{O}$ in figure b). In both cases when the Si activity is low the likely phase to precipitate due to plagioclase dissolution is gibbsite. But with increasing aqueous Si activity the fluid becomes supersaturated with respect to kaolinite. (Figure remade from Drever 1997)

In this thesis I focused on the solution chemistry and the saturation states of the reactive fluids with respect to the minerals dissolving and that were likely to precipitate and those commonly found in nature. Analysis of the solids, by SEM and EDS were used prior to and after experiments have been to determine if there are any evidence of secondary phases present after experiments. Such techniques are somewhat limited and cannot detect small quantities of surface alteration. Future studies can better emphasize more novel surface techniques such as X-ray Photoelectron spectroscopy (XPS) where the ratios of elements can be analysed in the surface layer of a mineral prior and after experiments, and Atomic Force Microscopy (AFM). The XPS and AFM have been widely used in dissolution and precipitation experiments on single phase systems such as basaltic glass and calcite (e.g. Ruiz-Agudo et al., 2009; Stockmann et al., 2012; Klasa et al., 2013; Renard et al., 2013). Such techniques have the

potential to provide a more realistic view of natural processes such as those suggested by i.e. Bricker and Garrels (1967) and Helgeson et al (1969) and is shown in Figure 9.

It is still fresh in my memory when just couple of months after I started my PhD-work, at my first international meeting in La Palma in the Canary Islands, Professor Jacques Schott and Professor Andrew Putnis had a heated debate about what chemical weathering is and the terms dissolution and precipitation. I was unfortunate enough to sit right between them and I did not understand a single word. I think that they were debating about the question: *Do things dissolve and then move places and precipitate as something else or is the dominating mechanism mineral replacement?* I am still not sure if I understand the arguments and I have not solved it in this thesis nor have they solved it yet. I would still like to believe that I have contributed a little bit towards the answer, but my feeling is that the truth is somewhere between and we are getting closer.

7 References

- Aagaard, P., Helgeson, H.C., 1982. Thermodynamic and Kinetic Constraints on Reaction-Rates among Minerals and Aqueous-Solutions .1. Theoretical Considerations. *American Journal of Science*, 282(3): 237-285.
- Albarède, F., 2005. The survival of mantle geochemical heterogeneities. In *Earth's Deep Mantle: Structure, Composition, and Evolution*. Geophys. Monogr. R. D. van der Hilst, J. Bass, J. Matas and J. Trampert. Washington D.C., Amer. Geophys. Union. 160, pp 27-46.
- Alfredsson, H.A., Oelkers, E.H., Hardarsson, B.S., Franzson, H., Gunnlaugsson, E., Gislason, S.R., 2013. The geology and water chemistry of the Hellisheiði, SW-Iceland carbon storage site. *International Journal of Greenhouse Gas Control*, 12(0): 399-418.
- Arnorsson, S., Neuhoff, P.S., 2007. Zeolite saturation in surface and < 100 °C ground waters in a Tertiary basalt province, Iceland. In: Bullen, T.D., Wang, Y. (Eds.), *Water-Rock Interaction*, Vols 1 and 2, Proceedings. Proceedings and Monographs in Engineering, Water and Earth Sciences, pp. 935-938.
- Arnorsson, S.N., Gunnarsson, I., Stefansson, A., Andresdottir, A., Sveinbjornsdottir, A.E., 2002. Major element chemistry of surface- and ground waters in basaltic terrain, N-Iceland. I. Primary mineral saturation. *Geochimica Et Cosmochimica Acta*, 66(23): 4015-4046.
- Benezeth, P., Palmer, D.A., Wesolowski, D.J., 2001. Aqueous high-temperature solubility studies. II. The solubility of boehmite at 0.03 m ionic strength as a function of temperature and pH as determined by in situ measurements. *Geochimica Et Cosmochimica Acta*, 65(13): 2097-2111.
- Bénézeth, P., Palmer, D.A., Wesolowski, D.J., 2008. Dissolution/precipitation kinetics of boehmite and gibbsite: Application of a pH-relaxation technique to study near-equilibrium rates. *Geochimica Et Cosmochimica Acta*, 72(10): 2429-2453.
- Benning, L.G., Waychunas, G.A., 2008. Nucleation, growth, and aggregation of mineral phases: Mechanisms and kinetic controls, *Kinetics of Water-Rock Interaction*. Springer, pp. 259-333.
- Berner, E., Berner, R., 2012. Global environment: Water, air and geochemical cycles. Princeton University Press.
- Blum, A.E., Lasaga, A.C., 1991. The Role of Surface Speciation in the Dissolution of Albite. *Geochimica Et Cosmochimica Acta*, 55(8): 2193-2201.
- Blum, A.E., Stillings, L.L., 1995. Feldspar dissolution kinetics. In: White, A.F., Brantley, S.L. (Eds.), *Chemical Weathering Rates of Silicate Minerals*. Mineralogical Society of America, Washington, DC, pp. 291-351.

- Brantley, S.L., 2003. 5.03 - Reaction Kinetics of Primary Rock-forming Minerals under Ambient Conditions. In: Editors-in-Chief: Heinrich, D.H., Karl, K.T. (Eds.), Treatise on Geochemistry. Pergamon, Oxford, pp. 73-117.
- Brantley, S.L., Chen, Y., 1995. Chemical weathering rates of pyroxenes and amphiboles, Chemical Weathering Rates of Silicate Minerals. Reviews in Mineralogy, pp. 119-172.
- Brantley, S.L., Stillings, L., 1996. Feldspar dissolution at 25 °C and low pH. American Journal of Science, 296(2): 101-127.
- Bricker, O.P., Garrels, R., 1967. Mineralogic factors in natural water equilibria. Principles and applications of water chemistry. Wiley, New York: 449-469.
- Brunauer, S., Emmett, P., Teller, E., 1938. Adsorption of gases in multimolecular layers, Journal of the American Chemical Society, pp. 309-319.
- Brynhildur Davíðsdóttir, Ágústa Loftsdóttir, Birna Hallsdóttir, Bryndís Skúladóttir, Daði Már Kristófersson, Guðbergur Rúnarsson, Hreinn Haraldsson, Pétur Reimarsdóttir, Stefán Einarsson, Þorsteinn Ingi Sigfusson, 2009, Möguleikar til að draga úr nettóútstreymi gróðurhúsalofttegunda á Íslandi, Skýrsla Sérfræðinganeftnar, Umhverfisráðuneytið.
- Cama, J., Metz, V., Ganor, J., 2002. The effect of pH and temperature on kaolinite dissolution rate under acidic conditions. Geochimica Et Cosmochimica Acta, 66(22): 3913-3926.
- Chen, Y., Brantley, S.L., 1998. Diopside and anthophyllite dissolution at 25° and 90° C and acid pH. Chemical Geology, 147(3-4): 233-248.
- Chen, Y., Brantley, S.L., 2000. Dissolution of forsteritic olivine at 65 °C and $2 < \text{pH} < 5$. Chemical Geology, 165(3-4): 267-281.
- Chou, L., Wollast, R., 1984. Study of the Weathering of Albite at Room-Temperature and Pressure with a Fluidized-Bed Reactor. Geochimica Et Cosmochimica Acta, 48(11): 2205-2217.
- Chou, L., Wollast, R., 1985. Steady-State Kinetics and Dissolution Mechanisms of Albite. American Journal of Science, 285(10): 963-993.
- Daux, V., Guy, C., Advocat, T., Crovisier, J.L., Stille, P., 1997. Kinetic aspects of basaltic glass dissolution at 90 °C: role of aqueous silicon and aluminium. Chemical Geology, 142(1-2): 109-126.
- Daval, D., Sissmann, O., Menguy, N., Saldi, G.D., Guyot, F., Martinez, I., Corvisier, J., Garcia, B., Machouk, I., Knauss, K.G., Hellmann, R., 2011. Influence of amorphous silica layer formation on the dissolution rate of olivine at 90 °C and elevated pCO₂. Chemical Geology, 284(1-2): 193-209.
- Devidal, J.L., Schott, J., Dandurand, J.L., 1997. An experimental study of kaolinite dissolution and precipitation kinetics as a function of chemical affinity and solution composition at 150 °C, 40 bars, and pH 2, 6.8, and 7.8. Geochimica Et Cosmochimica Acta, 61(24): 5165-5186.

- Drever, J.I., 1997. The Geochemistry of Natural Waters. Surface and Groundwater Environments. Prentice Hall, 71 pp.
- Eggleton, R.A., Foudoulis, C., Varkevisser, D., 1987. Weathering of basalt changes in rock chemistry and mineralogy. *Clays and Clay Minerals*, 35(3): 161-169.
- Eiriksdottir, E.S., Louvat, P., Gislason, S.R., Oskarsson, N., Hardarottir, J., 2008. Temporal variation of chemical and mechanical weathering in NE Iceland: Evaluation of a steady-state model of erosion. *Earth and Planetary Science Letters*, 272(1-2): 78-88.
- Flaathen, T.K., Gislason, S.R., Oelkers, E.H., 2010. The effect of aqueous sulphate on basaltic glass dissolution rates. *Chemical Geology*, 277(3–4): 345-354.
- Flaathen, T.K., Oelkers, E.H., Gislason, S., 2008. The effect of aqueous sulphate on basaltic glass dissolution rates. *Mineralogical Magazine*, 72(1): 39-41.
- Fridriksson, T., Neuhoff, P.S., Arnórsson, S., Bird, D.K., 2001. Geological constraints on the thermodynamic properties of the stiltite--stellerite solid solution in low-grade metabasalts. *Geochimica Et Cosmochimica Acta*, 65(21): 3993-4008.
- Galeczka, I., Wolff-Boenisch, D., Gislason, S., 2013. Experimental Studies of Basalt-H₂O-CO₂ Interaction with a High Pressure Column Flow Reactor: the Mobility of Metals. *Energy Procedia*, 37: 5823-5833.
- Ganor, J., Mogollón, J.L., Lasaga, A.C., 1995. The effect of pH on kaolinite dissolution rates and on activation energy. *Geochimica Et Cosmochimica Acta*, 59(6): 1037-1052.
- Ganor, J., Roueff, E., Erel, Y., Blum, J.D., 2005. The dissolution kinetics of a granite and its minerals - Implications for comparison between laboratory and field dissolution rates. *Geochimica Et Cosmochimica Acta*, 69(3): 607-621.
- Ganssen, R., 1970. The nature and tasks of soil geography and its place within the geosciences. *Geoforum*, 1(1): 77-93.
- Garrels, R.M., Mackenzie, F.T., 1971. Evolution of sedimentary rocks. Norton New York.
- Giammar, D.E., Bruant, R.G., Peters, C.A., 2005. Forsterite dissolution and magnesite precipitation at conditions relevant for deep saline aquifer storage and sequestration of carbon dioxide. *Chemical Geology*, 217(3-4): 257-276.
- Gislason, S.R., Eugster, H.P., 1987a. Meteoric Water-Basalt Interactions .2. A Field-Study in Ne Iceland. *Geochimica Et Cosmochimica Acta*, 51(10): 2841-2855.
- Gislason, S.R., Eugster, H.P., 1987b. Meteoric Water-Basalt Interactions .2. A Laboratory Study. *Geochimica Et Cosmochimica Acta*, 51(10): 2827-2840.
- Gislason, S.R., Arnorsson, S., 1993. Dissolution of primary basaltic minerals in natural waters - saturation state and kinetics. *Chemical Geology*, 105(1-3): 117-135.

- Gislason, S.R., Veblen, D.R., Livi, K.J.T., 1993. Experimental meteoric water-basalt interactions - characterization and interpretation of alteration products. *Geochimica Et Cosmochimica Acta*, 57(7): 1459-1471.
- Gislason, S.R., Arnorsson, S., Armannsson, H., 1996. Chemical weathering of basalt in southwest Iceland: Effects of runoff, age of rocks and vegetative/glacial cover. *American Journal of Science*, 296(8): 837-907.
- Gislason, S.R., Broecker, W., S.Oelkers, E., H.Gunnlaugsson, E., Sigurdardottir, H., Stefansson, A., Wolff-Boenisch, D., Matter, J., Stute, M., Axelsson, G., 2009. The Carbfix project: Mineral CO₂ sequestration into basalt. *Geochimica Et Cosmochimica Acta*, 73(13): A440-A440.
- Gislason, S.R., Oelkers, E.H., 2003. Mechanism, rates, and consequences of basaltic glass dissolution: II. An experimental study of the dissolution rates of basaltic glass as a function of pH and temperature. *Geochimica Et Cosmochimica Acta*, 67(20): 3817-3832.
- Gislason, S.R. Wolff-Boenisch, D., Stefansson, A., Oelkers, E.H., Gunnlaugsson, E., Sigurdardottir, H., Sigfusson, B., Broecker, W.S., Matter, J.M., Stute, M., 2010. Mineral sequestration of carbon dioxide in basalt: A pre-injection overview of the CarbFix project. *International Journal of Greenhouse Gas Control*, 4(3): 537-545.
- Grandstaff, D.E., 1977. Some kinetics of forsterite olivine dissolution. *Transactions-American Geophysical Union*, 58(6): 539-539.
- Gratz, A.J., Hillner, P.E., Hansma, P.K., 1993. Step dynamics and spiral growth on calcite. *Geochimica Et Cosmochimica Acta*, 57(2): 491-495.
- Gudbrandsson, S., Wolff-Boenisch, D., Gislason, S.R., Oelkers, E.H., 2011. An experimental study of crystalline basalt dissolution from $2 \leq \text{pH} \leq 11$ and temperatures from 5 to 75 °C. *Geochimica Et Cosmochimica Acta*, 75(19): 5496-5509.
- Gustavson, J.E., 2006. Analysis of Porosity Evolution During Low Temperature Metamorphism of Basaltic Lavas and Implications for Fluid Flow, University of Florida.
- Guy, C., Schott, J., 1989. Multisite surface reaction versus transport control during the hydrolysis of a complex oxide. *Chemical Geology*, 78(3-4): 181-204.
- Gysi, A.P., Stefánsson, A., 2011. CO₂-water-basalt interaction. Numerical simulation of low temperature CO₂ sequestration into basalts. *Geochimica Et Cosmochimica Acta*, 75(17): 4728-4751.
- Gysi, A.P., Stefánsson, A., 2012. Experiments and geochemical modeling of CO₂ sequestration during hydrothermal basalt alteration. *Chemical Geology*, 306-307(0): 10-28.
- Hamilton, J.P., Pantano, C.G., Brantley, S.L., 2000. Dissolution of albite glass and crystal. *Geochimica Et Cosmochimica Acta*, 64(15): 2603-2615.
- Hanchen, M., Krevor, S., Mazzotti, M., Lackner, K.S., 2007. Validation of a population balance model for olivine dissolution. *Chemical Engineering Science*, 62(22): 6412-6422.

- Hanchen, M., Prigobbe, V., Storti, G., Seward, T.M., Mazzotti, M., 2006. Dissolution kinetics of fosteritic olivine at 90-150 °C including effects of the presence of CO₂. *Geochimica Et Cosmochimica Acta*, 70(17): 4403-4416.
- Hay, R.L., Jones, B.F., 1972. Weathering of basaltic tephra on the island of Hawaii. *Geological Society of America Bulletin*, 83(2): 317-332.
- Helgeson, H.C., Garrels, R.M., MacKenzie, F.T., 1969. Evaluation of irreversible reactions in geochemical processes involving minerals and aqueous solutions—II. Applications. *Geochimica Et Cosmochimica Acta*, 33(4): 455-481.
- Helgeson, H.C., Murphy, W.M., Aagaard, P., 1984. Thermodynamic and Kinetic Constraints on Reaction-Rates among Minerals and Aqueous-Solutions. 2. Rate Constants, Effective Surface-Area, and the Hydrolysis of Feldspar. *Geochimica Et Cosmochimica Acta*, 48(12): 2405-2432.
- Hellmann, R., Daval, D., Tisserand, D., 2010. The dependence of albite feldspar dissolution kinetics on fluid saturation state at acid and basic pH: Progress towards a universal relation. *Comptes Rendus Geoscience*, 342(7): 676-684.
- Hellmann, R., Tisserand, D., 2006. Dissolution kinetics as a function of the Gibbs free energy of reaction: An experimental study based on albite feldspar. *Geochimica Et Cosmochimica Acta*, 70(2): 364-383.
- Hind, A.R., Bhargava, S.K., Grocott, S.C., 1999. The surface chemistry of Bayer process solids: a review. *Colloids and Surfaces A: Physicochemical and Engineering Aspects*, 146(1-3): 359-374.
- Johnson, G.K., Flotow, H.E., Ohare, P.A.G., Wise, W.S., 1983. Thermodynamic Studies of Zeolites - Natrolite, Mesolite and Scolecite. *American Mineralogist*, 68(11-1): 1134-1145.
- King, H.E., Plumper, O., Putnis, A., 2010. Effect of Secondary Phase Formation on the Carbonation of Olivine. *Environmental Science & Technology*, 44(16): 6503-6509.
- Klasa, J., Ruiz-Agudo, E., Wang, L. J., Putnis, C. V., Valsami-Jones, E., Menneken, M., Putnis, A., 2013. An atomic force microscopy study of the dissolution of calcite in the presence of phosphate ions. *Geochimica Et Cosmochimica Acta*, 117(0): 115-128.
- Knauss, K.G., Nguyen, S.N., Weed, H.C., 1993. Diopside Dissolution Kinetics as a Function of pH, CO₂, Temperature, and Time. *Geochimica Et Cosmochimica Acta*, 57(2): 285-294.
- Knauss, K.G., Wolery, T.J., 1986. Dependence of Albite Dissolution Kinetics on pH and Time at 25 °C and 70 °C. *Geochimica Et Cosmochimica Acta*, 50(11): 2481-2497.
- Kobayashi, M., Sawada, A., Tani, Y., Soma, M., Tanaka, A., Honma, T., Seyama, H., Theng, B.K.G., 2001. Acid dissolution of olivines, feldspars and dunite. *Water Air and Soil Pollution*, 130(1-4): 757-762.
- Koroleff, F., 1976. Determination of silicon. In: Grasshoff, K. (Ed.), *Methods of Seawater Analysis*. Springer-Verlag, Berlin, Germany.

- Kristmannsdottir, H., 1971. Anorthosite inclusions in tertiary dolerite from island groups Hrappsey and Purkey, West-Iceland. *Journal of Geology*, 79(6): 741-748.
- Kristmannsdottir, H., Tomasson, J., 1978. Zeolite zones in geothermal areas in Iceland, Natural Zeolites, Occurrence, Properties, Use LB Sand, FA Mumpton, 277–284. Pergamon, New York.
- Li, X., Wang, D., Zhou, Q., Liu, G., Peng, Z., 2011. Concentration variation of aluminate ions during the seeded precipitation process of gibbsite from sodium aluminate solution. *Hydrometallurgy*, 106(1–2): 93-98.
- Liu, Y., Olsen, A.A., Rimstidt, J.D., 2006. Mechanism for the dissolution of olivine series minerals in acidic solutions. *American Mineralogist*, 91(2-3): 455-458.
- Loose, B., Stute, M., Matter, J., Schlosser, P., 2009. A characterization of the aquifer system near the Hellisheiði geothermal plant in south-eastern Iceland, using noble and other gas tracers. *Geochimica Et Cosmochimica Acta*, 73(13): A790-A790.
- Markússon, S.H., Stefánsson, A., 2011. Geothermal surface alteration of basalts, Krýsuvík Iceland—Alteration mineralogy, water chemistry and the effects of acid supply on the alteration process. *Journal of Volcanology and Geothermal Research*, 206(1–2): 46-59.
- Marshak, S. and Prothero, D.R., 2008. Earth: portrait of a planet. WW Norton.
- Matter, J.M., Broecker, W., S.Gislason, S.R., Gunnlaugsson, E., Oelkers, E.H., Stute, M., Sigurdardóttir, H., Stefansson, A., Alfreðsson, H.A., Aradóttir, E.S., Axelsson, G., Sigfusson, B., Wolff-Boenisch, D., 2011. The CarbFix Pilot Project—Storing carbon dioxide in basalt. *Energy Procedia*, 4(0): 5579-5585.
- Matter, J.M., Broecker, W.S., Stute, M., Gislason, S.R., Oelkers, E.H., Stefansson, A., Wolff-Boenisch, D., Gunnlaugsson, E., Axelsson, G., Bjornsson, G., 2009. Permanent Carbon Dioxide Storage into Basalt: The CarbFix Pilot Project, Iceland. In: Gale, J., Herzog, H., Braitsch, J. (Eds.), *Greenhouse Gas Control Technologies 9*. Energy Procedia, pp. 3641-3646.
- Maurice, P.A., Vierkorn, M.A., Hersman, L.E., Fulghum, J.E., 2001. Dissolution of well and poorly ordered kaolinites by an aerobic bacterium. *Chemical Geology*, 180(1–4): 81-97.
- Mavromatis, V., Schmidt, M., Botz, R., Comas-Bru, L., Oelkers, E.H., 2012. Experimental quantification of the effect of Mg on calcite–aqueous fluid oxygen isotope fractionation. *Chemical Geology*, 310–311(0): 97-105.
- McBirney, A.R., 1993. Igneous petrology. Jones & Bartlett Learning.
- Nagy, K.L., Blum, A.E., Lasaga, A.C., 1991. Dissolution and precipitation of kaolinite at 80 °C and pH 3 - The dependence on solution saturation state. *American Journal of Science*, 291(7): 649-686.
- Nagy, K.L., Cygan, R.T., Hanchar, J.M., Sturchio, N.C., 1999. Gibbsite growth kinetics on gibbsite, kaolinite, and muscovite substrates: Atomic force microscopy evidence for epitaxy and an assessment of reactive surface area. *Geochimica Et Cosmochimica Acta*, 63(16): 2337-2351.

- Nagy, K.L., Lasaga, A.C., 1990. The effect of deviation from equilibrium on the kinetics of dissolution and precipitation of kaolinite and gibbsite. *Chemical Geology*, 84(1–4): 283-285.
- Nagy, K.L., Lasaga, A.C., 1992. Dissolution and precipitation of gibbsite at 80 °C and pH 3. The dependence on solution saturation state. *Geochimica Et Cosmochimica Acta*, 56(8): 3093-3111.
- Nagy, K.L., Lasaga, A.C., 1993. Simultaneous precipitation kinetics of kaolinite and gibbsite at 80 °C and pH 3. *Geochimica Et Cosmochimica Acta*, 57(17): 4329-4335.
- Nesbitt, H.W., Wilson, R.E., 1992. Recent chemical weathering of basalts. *American Journal of Science*, 292(10): 740-777.
- Nesbitt, H.W., Young, G.M., 1984. Prediction of some weathering trends of plutonic and volcanic rocks based on thermodynamic and kinetic considerations. *Geochimica Et Cosmochimica Acta*, 48(7): 1523-1534.
- Neuhoff, P.S., 1999. Thermodynamic properties and paragenesis of rock-forming zeolites. Dissertation Thesis, Standford University, 240 pp.
- Neuhoff, P.S., Fridriksson, T., Bird, D.K., 2000. Zeolite parageneses in the north Atlantic igneous province: Implications for geotectonics and groundwater quality of basaltic crust. *International Geology Review*, 42(1): 15-44.
- Neuhoff, P.S., Rogers, K.L., Stannius, L.S., Bird, D.K., Pedersen, A.K., 2006. Regional very low-grade metamorphism of basaltic lavas, Disko-Nuussuaq region, West Greenland. *Lithos*, 92(1-2): 33-54.
- Neuhoff, P.S., Watt, W.S., Bird, D.K., Pedersen, A.K., 1997. Timing and structural relations of regional zeolite zones in basalts of the East Greenland continental margin. *Geology*, 25(9): 803-806.
- Nielsen, A.E., 1964. Kinetics of precipitation, Pergamon Press, pp. 151.
- Nielsen, A.E., 1984. Electrolyte crystal-growth mechanisms. *Journal of Crystal Growth*, 67(2): 289-310.
- Oelkers, E.H., 2001a. An experimental study of forsterite dissolution rates as a function of temperature and aqueous Mg and Si concentrations. *Chemical Geology*, 175(3-4): 485-494.
- Oelkers, E.H., 2001b. General kinetic description of multioxide silicate mineral and glass dissolution. *Geochimica Et Cosmochimica Acta*, 65(21): 3703-3719.
- Oelkers, E.H., Gislason, S.R., 2001. The mechanism, rates and consequences of basaltic glass dissolution: I. An experimental study of the dissolution rates of basaltic glass as a function of aqueous Al, Si and oxalic acid concentration at 25 °C and pH=3 and 11. *Geochimica Et Cosmochimica Acta*, 65(21): 3671-3681.
- Oelkers, E.H., Schott, J., Devidal, J.L., 1994. The effect of aluminum, pH and chemical affinity on the rates of aluminosilicate dissolution reactions. *Geochimica Et Cosmochimica Acta*, 58(9): 2011-2024.

- Oxburgh, R., Drever, J.I., Sun, Y.T., 1994. Mechanism of Plagioclase Dissolution in Acid-Solution at 25 °C. *Geochimica Et Cosmochimica Acta*, 58(2): 661-669.
- Palmer, D.A., Benezeth, P., Wesolowski, D.J., 2001. Aqueous high-temperature solubility studies. I. The solubility of boehmite as functions of ionic strength (to 5 molal, NaCl), temperature (100-290 °C), and pH as determined by in situ measurements. *Geochimica Et Cosmochimica Acta*, 65(13): 2081-2095.
- Pokrovsky, O.S., Schott, J., 2000a. Forsterite surface composition in aqueous solutions: A combined potentiometric, electrokinetic, and spectroscopic approach. *Geochimica Et Cosmochimica Acta*, 64(19): 3299-3312.
- Pokrovsky, O.S., Schott, J., 2000b. Kinetics and mechanism of forsterite dissolution at 25 °C and pH from 1 to 12. *Geochimica Et Cosmochimica Acta*, 64(19): 3313-3325.
- Pruett, R.J., Webb, H.L., 1993. Sampling and analysis of KGa-1b well-crystallized kaolin source clay. *Clays and Clay Minerals*, 41(4): 514-519.
- Putnis, A., 2009. Mineral Replacement Reactions. In: Oelkers, E.H., Schott, J. (Eds.), *Thermodynamics and Kinetics of Water-Rock Interaction. Reviews in Mineralogy & Geochemistry*. Mineralogical Soc Amer, Chantilly, pp. 87-124.
- Ramseyer, K., Boles, J.R., Lichtner, P.C., 1992. Mechanism of plagioclase albitization. *Journal of Sedimentary Research*, 62(3).
- Renard, F., Montes-Hernandez, G., Ruiz-Agudo, E., Putnis, C.V., 2013. Selenium incorporation into calcite and its effect on crystal growth: An atomic force microscopy study. *Chemical Geology*, 340(0): 151-161.
- Rogers, K.L., Neuhoff, P.S., Pedersen, A.K., Bird, D.K., 2006. CO₂ metasomatism in a basalt-hosted petroleum reservoir, Nuussuaq, West Greenland. *Lithos*, 92(1-2): 55-82.
- Roncal-Herrero, T., Oelkers, E.H., 2011. Experimental determination of struvite dissolution and precipitation rates as a function of pH. *Applied Geochemistry*, 26(5): 921-928.
- Rosso, J.J., Rimstidt, J.D., 2000. A high resolution study of forsterite dissolution rates. *Geochimica Et Cosmochimica Acta*, 64(5): 797-811.
- Ruiz-Agudo, E., Putnis, C.V., Jiménez-López, C., Rodriguez-Navarro, C., 2009. An atomic force microscopy study of calcite dissolution in saline solutions: The role of magnesium ions. *Geochimica Et Cosmochimica Acta*, 73(11): 3201-3217.
- Saldi, G.D., Jordan, G., Schott, J., Oelkers, E.H., 2009. Magnesite growth rates as a function of temperature and saturation state. *Geochimica Et Cosmochimica Acta*, 73(19): 5646-5657.
- Saldi, G.D., Schott, J., Pokrovsky, O.S., Gautier, Q., Oelkers, E.H., 2012. An experimental study of magnesite precipitation rates at neutral to alkaline conditions and 100–200 °C as a function of pH, aqueous solution composition and chemical affinity. *Geochimica Et Cosmochimica Acta*, 83(0): 93-109.

- Schaef, H.T., McGrail, B.P., 2009. Dissolution of Columbia River Basalt under mildly acidic conditions as a function of temperature: Experimental results relevant to the geological sequestration of carbon dioxide. *Applied Geochemistry*, 24(5): 980-987.
- Schott, J., Berner, R.A., 1985. Dissolution mechanisms of pyroxenes and olivines during weathering. In: *The chemistry of weathering*. Springer, pp. 35-53.
- Schott, J., Pokrovsky, O.S., Oelkers, E.H., 2009. The link between mineral dissolution/precipitation kinetics and solution chemistry. *Reviews in mineralogy and geochemistry*, 70(1): 207-258.
- Sherman, G.D., Uehara, G., 1956. The weathering of olivine basalt in Hawaii and its pedogenic significance. *Soil Science Society of America Journal*, 20(3): 337-340.
- Shiraki, R., Brantley, S.L., 1995. Kinetics of near-equilibrium calcite precipitation at 100 °C - an evaluation of elementary reaction-based rate laws. *Geochimica Et Cosmochimica Acta*, 59(8): 1457-1471.
- Smith, J.V., Brown, W.L., 1988. *Feldspar minerals*. Springer-Verlag.
- Stillings, L.L., Brantley, S.L., 1995. Feldspar dissolution at 25 °C and pH 3: Reaction stoichiometry and the effect of cations. *Geochimica Et Cosmochimica Acta*, 59(8): 1483-1496.
- Stockmann, G.J., 2012. Experimental study of basalt carbonatization, Université de Toulouse, Université Toulouse III-Paul Sabatier.
- Stockmann, G., Wolff-Boenisch, D., Gislason, S.R., Oelkers, E.H., 2008. Dissolution of diopside and basaltic glass: the effect of carbonate coating. *Mineralogical Magazine*, 72(1): 135-139.
- Stockmann, G.J., Wolff-Boenisch, D., Gislason, S.R., Oelkers, E.H., 2011. Do carbonate precipitates affect dissolution kinetics? 1: Basaltic glass. *Chemical Geology*, 284(3-4): 306-316.
- Stockmann, G.J. et al., 2012. Does the presence of heterotrophic bacterium *Pseudomonas reactans* affect basaltic glass dissolution rates? *Chemical Geology*, 296-297(0): 1-18.
- Stopar, J.D., Taylor, G.J., Hamilton, V.E., Browning, L., 2006. Kinetic model of olivine dissolution and extent of aqueous alteration on Mars. *Geochimica Et Cosmochimica Acta*, 70(24): 6136-6152.
- Temkin, M.I., 1963. Kinetics of stationary reactions. *Doklady Akademii Nauk SSSR*, 152: 156-157.
- Teng, H.H., Dove, P.M., De Yoreo, J.J., 2000. Kinetics of calcite growth: Surface processes and relationships to macroscopic rate laws. *Geochimica Et Cosmochimica Acta*, 64(13): 2255-2266.
- Upper, D., 1974. Unsuccessful self-treatment of a case of writers block. *Journal of Applied Behavior Analysis*, 7(3): 497-497.

Velbel, M.A., 2009. Dissolution of olivine during natural weathering. *Geochimica Et Cosmochimica Acta*, 73(20): 6098-6113.

Walker, G.P., 1960. Zeolite zones and dike distribution in relation to the structure of the basalts of eastern Iceland. *The Journal of Geology*: 515-528.

Wang, Z., Yang, L., Zhang, J., Guo, Z.-c., Zhang, Y., 2010. Adjustment on gibbsite and boehmite co-precipitation from supersaturated sodium aluminate solutions. *Transactions of Nonferrous Metals Society of China*, 20(3): 521-527.

Wasklewicz, T., Dorn, R.I., Clark, S., Hetrick, J., Pope, G., Liu, T., Krinsley, D.H., Dixon, J., Moore, R.B., Clark, J. 1993. Olivine does not necessarily weather 1st. *Singapore Journal of Tropical Geography*, 14(1): 72-80.

Wogelius, R.A., Walther, J.V., 1992. Olivine Dissolution Kinetics at near-Surface Conditions. *Chemical Geology*, 97(1-2): 101-112.

Wolff-Boenisch, D., Gislason, S.R., Oelkers, E.H., Putnis, C.V., 2004. The dissolution rates of natural glasses as a function of their composition at pH 4 and 10.6, and temperatures from 25 to 74 °C. *Geochimica Et Cosmochimica Acta*, 68(23): 4843-4858.

Yang, L., Steefel, C.I., 2008. Kaolinite dissolution and precipitation kinetics at 22 °C and pH 4. *Geochimica Et Cosmochimica Acta*, 72(1): 99-116.

Zakaznova-Herzog, V.P., Nesbitt, H.W., Bancroft, G.M., Tse, J.S., 2008. Characterization of leached layers on olivine and pyroxenes using high-resolution XPS and density functional calculations. *Geochimica Et Cosmochimica Acta*, 72(1): 69-86.

Webpage

European Aluminium Association (2013) Data from webpage.
<http://www.alueurope.eu/about-aluminium/facts-and-figures/> September 2013.

8 Appendices

Appendix 1

Snorri Gudbrandsson, Domenik Wolff-Boenisch, Sigurdur R. Gislason, Eric H. Oelkers (2008) “*Dissolution rates of crystalline basalt at pH 4 and 10 and 25-75°C*” Min-Mag 72(1), 159-162.

Mineralogical Magazine, February 2008, Vol. 72(1), pp. 159–162

Dissolution rates of crystalline basalt at pH 4 and 10 and 25–75°C

S. GUDBRANDSSON^{1,*}, D. WOLFF-BOENISCH¹, S. R. GISLASON¹ AND E. H. OELKERS²

¹ Institute of Earth Science, University of Iceland, Sturlugata 7, 101 Reykjavik, Iceland

² Géochimie et Biogéochimie Experimentale – LMTG/Université Paul Sabatier, 14 rue Edouard Belin, 31400 Toulouse, France

ABSTRACT

Far-from-equilibrium dissolution rates of crystalline basalt were measured in a mixed-flow reactor at pH 4 and 10, and at temperatures from 25 to 75°C. The material used was obtained from a dyke on Stólfell Mountain on Reykjanes peninsula in Iceland because of its similarity with previous experiments on dissolution rates on basaltic glass by Oelkers and Gislason (2001) and Gislason and Oelkers (2003). Comparison of dissolution rates of basaltic glass and of crystalline basalt of similar chemical composition (from Gislason and Oelkers, 2003) indicates lower rates for crystalline material.

Introduction

REDUCING CO₂ emission into the atmosphere is one of the most important environmental challenges of the 21st century. The search for a permanent solution for large-scale CO₂ storage, with low risk of leakage, has become an important geochemical issue. Injecting CO₂-charged waters into basaltic rock formations may be a viable solution given the large amount of Ca, Mg and Fe in basalt and the relatively fast dissolution of the host rock compared to silicic rocks (e.g. Wolff-Boenisch *et al.*, 2004). In the process, the dissolved CO₂ will react with the basalt to form Ca-, Mg-, and Fe-carbonates. The dissolution rate of basaltic glass has been extensively studied under controlled conditions in the laboratory (Oelkers and Gislason, 2001; Gislason and Oelkers, 2003). These rates can be used in reactive transport modelling of the reaction of dissolved CO₂ with basaltic glass at various temperatures and solution compositions. No such general dissolution rate is available for crystalline basalt dissolution. The overall purpose of this study is to fill this gap. Here we present the dissolution rates of crystalline basalt at varying pH and temperatures.

Methods and material

Crystalline basalt was collected from a basaltic dyke on Stólfell Mountain, SW-Iceland. Stólfell is the first mountain on the Reykjanes peninsula where the Mid-Atlantic Ridge appears onshore in Iceland. The composition of the rocks in Stólfell is similar to that of mid-ocean ridge basalts (MORB; e.g. Oelkers and Gislason, 2001). This location was also chosen because the dissolution rates for basaltic glass were determined with material from the same location (Oelkers and Gislason, 2001; Gislason and Oelkers, 2003). Stólfell is a hyaloclastite (broken glass) formation, consisting mostly of basaltic glass, crystalline rock fragments and pillow lavas. The hyaloclastite formation at Stólfell is crossed by various dykes. The sampled dyke had no visible alteration features on the surface.

The material was dried at room temperature for several days before it was crushed with a jaw crusher. The fine-grained material was dry sieved to yield the 45–125 µm size fraction. This size fraction was cleaned ultrasonically five times in de-ionized water and then in acetone. Subsequently, the sample was dried at ~50°C for several days. The chemical composition of the dyke was analysed by XRF and is shown in Table 1. Its composition is comparable to basaltic glass used to determine glass-dissolution rates.

* E-mail: snorgud@hi.is
DOI: 10.1180/minmag.2008.072.1.159

S. GUDBRANDSSON ET AL.

TABLE 1. Chemical analyses of the basaltic rocks of this comparative study.

Major elements Sample	SiO ₂	Al ₂ O ₃	Fe ₂ O ₃ ^c	MgO	CaO	Na ₂ O	K ₂ O	TiO ₂	MnO	P ₂ O ₅	LOI	Total
Stapafell dyke	47.9	13.4	12.3	10.0	12.2	1.5	0.3	1.6	0.2	0.2	-0.5	99.1
Stapafell glass ^a	48.1	14.6	10.9	9.1	11.8	2.0	0.3	1.6	0.2	0.2	-0.5	98.8
Krafla glass ^b	49.8	13.4	14.6	5.7	10.2	2.4	0.3	2.0	0.2	0.2	-0.9	98.9

^a Oelkers and Gislason (2001)^b Wolff-Boenisch *et al.* (2004)^c most Fe is in the form Fe²⁺ (Oelkers and Gislason, 2001)

These glasses will serve as points of reference in the discussion section and therefore their chemical composition was added to Table 1.

Based on CIPW norm calculations, the crystalline basalt is composed of the following minerals (mol. %): hypersthene 28.15%, diopside 22.20%, anorthite 21%, olivine 13.53%, albite 9.82%, ilmenite 4.04%, orthoclase 1.09% and apatite 0.15%. The specific surface area of the cleaned and dried 45–125 µm size fraction was determined via 11 point krypton adsorption using a Quantachrome Gas Sorption system. The measured BET surface of the crystalline basalt was 7030 cm²/g. The dissolution experiments were performed in a ParrTM mixed-flow reactor shown in Fig. 1, consisting of a 300 mL titanium container with temperature and stirring controller (e.g. Wolff-Boenisch *et al.*, 2004).

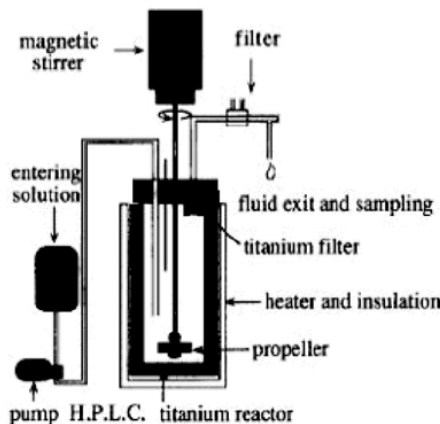


FIG. 1. Mixed-flow reactor for dissolution experiments.

The solution was delivered using an HPLC pump at a constant flow rate between 1 and 4.5 ml/min. The reactor was vigorously and continuously stirred at ~400 rpm and the outlet solution was filtered with 0.2 µm cellulose acetate filter, acidified with HNO₃ and subsequently analysed by means of ICP-OES.

These experiments were performed at pH 4 and 10 with an ionic strength of 10 mM. The acid inlet solution was made of de-ionized water and Merck analytical grade NH₄Cl and HCl, whereas ammonia replaced HCl at pH 10. The compositions of the solutions were pre-defined using PHREQC 2.14 (Parkhurst and Appelo, 1990) to yield the desired ionic strength and pH. The inlet solution with alkaline pH was purged with N₂ during the experiment to prevent dissolved carbonate precipitation due to CO₂ entering the reactor. At the beginning of each experiment the reactor was cleaned thoroughly, assembled and run for at least 24 h with de-ionized water and another 24 hour with solution to rinse the tubing and clean the reactor.

Results and discussion

For experiments conducted far-from-equilibrium, the dissolution rate ($r_{+,BET}$) is calculated using the formula:

$$r_{+,BET} = \frac{C_{Si} \cdot fr}{A_{BET} \times m}$$

where C_{Si} is the silica content in the outlet solution, fr is the flow rate, A_{BET} is the specific surface area and m is the mass of sample in the solution.

Figure 2 shows the pH-dependent dissolution of basaltic glass, reported by Gislason and

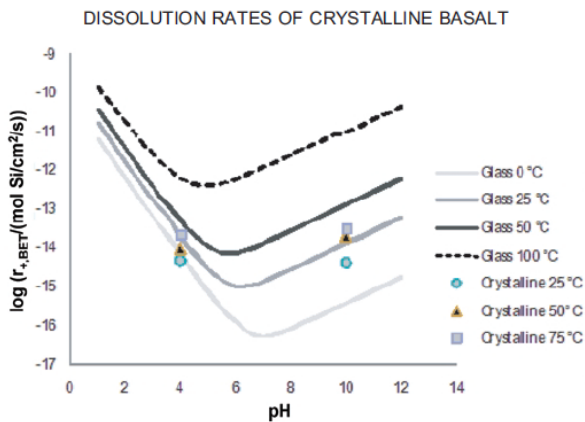


FIG. 2. Dissolution rates of crystalline basalt (symbols) are compared to modelled dissolution rates (curves) of basaltic glass from the same location (Gislason and Oelkers, 2003).

Oelkers (2003). Our own data have been added to these modelled curves to illustrate that the dissolution rate of crystalline basalt is considerably slower than its glassy counterpart, in acid and alkaline conditions. For example, the dissolution rate for crystalline basalt at pH 4 and 75°C falls on the 25°C isothermal line for basaltic glass dissolution. From the experimental results we can obtain apparent activation energies (E_a):

$$E_a = \frac{\delta \ln r_{+,BET}}{\delta(1/T)} \times R$$

where R is the gas constant, T is the temperature in Kelvin and $r_{+,BET}$ is the forward rate. At pH 4 we find an E_a of 26 kJ/mol, in very good agreement with the $E_a = 27$ kJ/mol that Wolff-Boenisch *et al.* (2004) reported for a basaltic glass of similar composition (Krafla, cf. Table 1). At pH 10, the calculated E_a is 35 kJ/mol compared to 41 kJ/mol for Krafla at pH 10.6 (Wolff-Boenisch *et al.*, 2004). Overall, the temperature dependence of the dissolution mechanisms seems slightly greater at pH 10 than at pH 4. This observation is consistent with the curves in Fig. 1 which lie more closely together at acidic pH and start to spread when the conditions become more alkaline.

Summary

We have started to map the dissolution rates of crystalline basalt as a function of pH, solution composition and temperature. These rates can

eventually be used in reactive-transport modelling of the reaction of dissolved CO₂ with crystalline MORB basaltic at various temperatures and solution compositions. Dissolution rates have been obtained by similar methods for basaltic glass from the same volcanic formation. The preliminary results indicate lower rates for crystalline basalt than for basaltic glass of comparable chemical composition under same experimental conditions. This is in concert with previous studies on the effect of crystallinity on dissolution rates (Gislason and Eugster, 1987; Wolff-Boenisch *et al.*, 2006). Further investigations are required to probe the reasons for this phenomenon.

Acknowledgements

We thank Reykjavík Energy, Nordural and Hitaveita Sudurnesja for their financial support. This study is part of the Carb-Fix project. We would like thank several colleagues for their help, in particular Helgi Alfredsson for the XRF analysis, Eydís Salome Eiríksdóttir, Gabrielle Stockman and Ingvi Gunnarsson at the University of Iceland, and Hólmfridur Sigurdardóttir at Reykjavík Energy.

References

- Gislason, S.R. and Eugster, H.P. (1987) Meteoric water-basalt interactions. I: A laboratory study. *Geochimica et Cosmochimica Acta*, **51**, 2827–2840.
- Gislason, S.R. and Oelkers, E.H. (2003) Mechanism, rates, and consequences of basaltic glass dissolution:

S. GUDBRANDSSON ET AL.

- II. An experimental study of the dissolution rates of basaltic glass as a function of pH and temperature. *Geochimica et Cosmochimica Acta*, **67**, 3817–3832.
- Oelkers, E.H. and Gislason, S.R. (2001) The mechanism, rates, and consequences of basaltic glass dissolution: I. An experimental study of the dissolution rates of basaltic glass as a function of aqueous Al, Si and oxalic acid concentration at 25°C and pH = 3 and 11. *Geochimica et Cosmochimica Acta*, **65**, 3671–3681.
- Parkhurst, D.L. and Appelo, C.A.J. (1999) *User's guide to PHREEQC (Version 2) - A computer program for speciation, batch-reaction, one-dimensional transport and inverse geochemical calculations*. US Geological Survey Water Resources Investigations Report 99-4259. U. S. Geological Survey, Denver, 312 pp.
- Wolff-Boenisch, D., Gislason, S.R., Oelkers, E.H. and Putnis, C.V. (2004) The dissolution rates of natural glasses as a function of their composition at pH 4 and 10.6, and temperatures from 25 to 74°C. *Geochimica et Cosmochimica Acta*, **68**, 4843–4858.
- Wolff-Boenisch, D., Gislason, S.R. and Oelkers, E.H. (2006) The effect of crystallinity on dissolution rates and CO₂ consumption capacity of silicates. *Geochimica et Cosmochimica Acta*, **70**, 858–870.

8.1 Appendix 2

Snorri Gudbrandsson, Domenik Wolff-Boenisch, Sigurdur R. Gislason, Eric H. Oelkers (2011) “*An experimental study of crystalline basalt dissolution from $2 \leq pH \leq 11$ and temperatures from 5 to 75 °C*” Geochimica Cosmochimica Acta 75, 5496-5509.

Supporting information, four pages, containing four tables.

Saturation indexes of various minerals at dissolving temperatures.

5° C	02-05	03-05	04-05	05-05	09-05	11-05
Albite	-23.74	-22.19	-20.71	-17.69	-10.36	-11.18
An70	-37.13	-32.72	-28.10	-22.23	-11.64	-11.18
Anorthite	-44.97	-39.36	-33.40	-24.36	-14.33	-13.31
Diopside	-24.97	-22.72	-20.91	-16.89	0.53	6.95
Enstatite	-18.73	-17.73	-17.20	-15.47	-6.49	-4.18
Fayalite	-28.82	-26.33	-24.52	-19.45	-13.97	-23.30
Fo80Fa20	-36.11	-33.59	-31.84	-28.17	-12.59	-11.10
Forsterite	-32.12	-29.59	-27.85	-24.46	-6.41	-1.31
Ferrosilite	-14.73	-13.75	-13.17	-10.74	-7.94	-12.86
Stapafell	-6.11	-5.74	-5.45	-4.21	-3.97	-4.79
Al(OH)3_amorph	-11.80	-9.36	-6.70	-3.40	-2.50	-3.86
Analcime	-21.91	-19.89	-17.70	-14.70	-7.37	-7.82
Allophane_Al/Si=1.26	-21.62	-17.54	-13.29	-6.48	-4.89	-8.20
Allophane_Al/Si=1.64	-21.68	-17.42	-12.91	-6.13	-4.52	-7.68
Allophane_Al/Si=2.02	-21.94	-17.57	-12.92	-6.15	-4.52	-7.61
Ca-Montmorillonite	-29.28	-25.11	-21.08	-12.61	-9.50	-13.32
Ca-stilbite	-41.24	-38.01	-35.52	-26.12	-16.33	-17.28
Chalcedony	-1.00	-1.52	-2.18	-2.12	-2.22	-2.55
Chabacite-Ca	-9.43	-4.78	-0.20	8.98	18.91	19.15
Clinopyroxene	-25.88	-23.70	-22.10	-17.92	-3.17	-1.06
Gibbsite	-9.56	-7.12	-4.47	-1.17	-0.27	-1.62
Goethite	-8.29	-5.81	-3.57	-0.14	7.36	4.27
analcime_0.96	-21.41	-19.52	-17.50	-14.65	-7.59	-8.06
Hematite	-14.66	-9.69	-5.21	1.96	16.69	10.69
Heulandite	-41.33	-38.10	-35.60	-26.20	-16.42	-17.36
Kaolinite	-18.26	-14.38	-10.41	-3.57	-2.01	-5.47
Laumondite	-39.03	-34.38	-29.80	-20.62	-10.69	-10.45
mic-gibbsite	-10.32	-7.88	-5.23	-1.93	-1.03	-2.38
Pyrite	-15.34	NA	NA	NA	NA	-175.12
Thomsonite	-93.80	-80.07	-65.00	-47.13	-16.64	-14.81
Sulfur	-9.09	NA	NA	NA	NA	-81.15
Scolecite	-36.21	-31.08	-25.81	-16.70	-6.72	-6.09
Quartz	-1.09	-1.61	-2.27	-2.21	-2.31	NA

NA: Data not available

25° C	03-25	04-25	05-25	06-25	09-25	10-25	11-25
Albite	-20.34	-15.62	NA	-11.65	-10.16	-10.44	-11.08
An70	-29.04	-21.32	NA	-13.39	-10.83	-11.07	-10.66
Anorthite	-31.05	-22.13	-17.81	-12.56	-9.53	-9.77	-8.90
Diopside	-20.14	-16.08	-14.22	-10.89	1.15	5.26	7.29
Enstatite	-15.99	-14.24	-13.60	-12.05	-5.94	-4.13	-3.86
Fayalite	-24.05	-20.07	-17.96	-14.85	-14.05	-17.10	-23.67
Fo80Fa20	-30.20	-26.42	-24.70	-21.23	-11.55	-9.39	-9.80
Forsterite	-31.96	-28.23	-26.61	-23.02	-11.13	-7.40	-6.53
Ferrosilite	-12.58	-10.71	-9.82	-8.44	-7.94	-9.75	-12.97
Stapafell	-5.02	-4.05	-3.76	-3.32	-3.75	-4.31	-4.70
Al(OH)3_amorph	-7.83	-4.47	-2.70	-0.83	-2.31	-3.50	-3.82
Analcime	-18.25	-13.26	NA	-8.81	-7.30	-7.45	-7.82
Allophane_Al/Si=1.26	-14.19	-7.81	-4.82	-1.35	-4.32	-6.90	-7.98
Allophane_Al/Si=1.64	-14.10	-7.62	-4.50	-0.98	-3.96	-6.49	-7.47
Allophane_Al/Si=2.02	-14.23	-7.69	-4.50	-0.94	-3.93	-6.43	-7.35
Ca-Montmorillonite	-21.40	-14.02	-10.92	-6.78	-9.32	-12.18	-13.57
Ca-stilbite	-33.29	-25.86	-23.36	-18.56	-15.77	-16.65	-17.17
Chalcedony	-1.39	-1.61	-1.97	-2.21	-2.11	-2.24	-2.52
Chabacite-Ca	1.14	9.48	13.12	18.16	21.12	20.62	20.93
Clinopyroxene	-19.61	-15.68	-13.88	-10.62	-1.18	0.93	1.08
Gibbsite	-5.60	-2.23	-0.47	1.41	-0.07	-1.26	-1.58
Goethite	-4.74	-1.39	0.62	3.31	6.77	6.20	3.91
analcime_0.96	-17.91	-13.15	NA	-8.94	-7.48	-7.64	-8.03
Hematite	-7.44	-0.67	3.27	8.81	15.55	14.83	9.87
Heulandite	-33.47	-26.04	-23.54	-18.74	-15.95	-16.83	-17.35
Kaolinite	-11.82	-5.54	-2.69	0.72	-2.25	-4.89	-6.07
Laumondite	-30.29	-21.95	-18.30	-13.26	-10.31	-10.80	-10.49
mic-gibbsite	-6.37	-3.00	-1.24	0.63	-0.84	-2.03	-2.35
Pyrite	NA	-55.00	NA	NA	-139.21	-161.84	-176.09
Thomsonite	-70.91	-47.32	NA	-23.00	-16.30	-16.84	-15.22
Sulfur	NA	-28.12	NA	NA	-66.90	-76.16	-81.16
Scolecite	-27.17	-18.53	-14.55	-9.40	-6.41	-6.77	-6.19
Quartz	-1.52	-1.74	-2.11	-2.35	-2.25	-2.38	NA

NA: Data not available

50° C	03-50	04-50	05-50	07-50	09-50	10-50	11-50
Albite	-13.24	-13.92	-13.18	-11.41	-8.36	-11.52	-10.50
An70	-18.76	-17.42	-14.73	-12.45	-8.17	-11.87	-9.95
Anorthite	-15.55	-13.35	-9.67	-7.33	-2.53	-6.46	-4.14
Diopside	-13.24	-13.88	-11.09	-10.11	3.09	8.51	7.05
Enstatite	-12.31	-13.03	-12.08	-11.59	-4.92	-2.14	-3.03
Fayalite	-17.58	-17.80	-15.48	-15.21	-13.81	-21.48	-22.61
Fo80Fa20	-23.18	-23.68	-21.49	-20.62	-9.99	-6.37	-8.35
Forsterite	-31.31	-31.88	-29.72	-28.70	-15.73	-9.31	-11.34
Ferrosilite	-9.11	-9.64	-8.59	-8.49	-7.64	-11.91	-12.53
Stapafell	-3.09	-3.42	-3.23	-3.00	-3.01	-4.85	-4.14
Al(OH)3_amorph	-4.46	-2.68	-1.67	-0.69	-1.73	-4.63	-3.27
Analcime	-11.99	-11.58	-10.85	-8.77	-6.09	-8.44	-7.65
Allophane_Al/Si=1.26	-6.06	-4.44	-2.64	-0.92	-2.43	-9.47	-6.43
Allophane_Al/Si=1.64	-6.25	-4.22	-2.36	-0.59	-2.24	-8.98	-6.02
Allophane_Al/Si=2.02	-6.50	-4.22	-2.33	-0.53	-2.26	-8.83	-5.91
Ca-Montmorillonite	-10.62	-10.70	-8.56	-6.69	-6.77	-15.85	-12.05
Ca-stilbite	-18.94	-22.38	-19.47	-17.82	-11.18	-19.12	-15.74
Chalcedony	-0.73	-1.70	-1.86	-1.99	-1.63	-2.43	-2.21
Chabacite-Ca	15.31	15.25	18.63	20.70	26.23	20.70	23.44
Clinopyroxene	-11.00	-11.87	-9.27	-8.50	2.05	4.31	2.80
Gibbsite	-2.22	-0.44	0.56	1.55	0.50	-2.40	-1.04
Goethite	-1.52	-0.19	1.97	2.69	6.09	4.39	3.19
analcime_0.96	-11.81	-11.53	-10.86	-8.87	-6.26	-8.61	-7.82
Hematite	-0.74	1.74	6.22	7.51	14.36	11.03	8.97
Heulandite	-18.98	-22.43	-19.51	-17.86	-11.23	-19.16	-15.78
Kaolinite	-4.40	-3.23	-1.50	0.17	-1.20	-8.56	-5.43
Laumondite	-18.12	-18.18	-14.80	-12.73	-7.20	-12.73	-9.98
mic-gibbsite	-3.14	-1.36	-0.35	0.63	-0.41	-3.31	-1.95
Pyrite	NA	NA	NA	NA	-138.12	-173.14	-168.37
Thomsonite	-42.90	-38.31	-29.96	-23.14	-11.23	-20.38	-15.47
Sulfur	NA	NA	NA	NA	-65.56	-79.38	-76.91
Scolecite	-15.79	-14.71	-11.18	-8.98	-3.81	-8.54	-6.01
Quartz	-0.92	-1.89	-2.05	-2.18	-1.82	-2.62	NA

NA: Data not available

75° C	04-75	05-75	07-75	09-75	10-75	11-75
Albite	-13.35	-9.92	-8.94	-7.35	-11.31	-9.05
An70	-15.10	-10.61	-9.59	-6.61	-10.19	-8.05
Anorthite	-6.86	-1.92	-0.89	2.70	-0.73	1.36
Diopside	-12.84	-6.92	-5.21	4.68	10.15	9.37
Enstatite	-12.49	-9.86	-9.09	-3.79	-1.30	-1.83
Fayalite	-16.82	-13.55	-12.53	-13.67	-24.11	-22.50
Fo80Fa20	-22.10	-17.71	-16.34	-8.10	-5.23	-6.30
Forsterite	-35.72	-31.04	-29.59	-18.99	-12.81	-14.49
Ferrosilite	-9.36	-7.44	-6.89	-7.47	-13.27	-12.17
Stapafell	-3.25	-2.49	-2.42	-2.58	-4.72	-3.76
Al(OH)3_amorph	-1.39	-0.90	-0.85	-1.33	-3.94	-3.05
Analcime	-10.77	-7.96	-7.00	-5.41	-8.16	-6.54
Allophane_Al/Si=1.26	-2.50	-0.52	-0.40	-1.37	-8.50	-5.71
Allophane_Al/Si=1.64	-2.14	-0.40	-0.28	-1.25	-7.93	-5.38
Allophane_Al/Si=2.02	-2.03	-0.42	-0.31	-1.28	-7.70	-5.29
Ca-Montmorillonite	-9.40	-5.50	-5.21	-5.60	-15.39	-11.14
Ca-stilbite	-21.72	-13.66	-12.65	-9.06	-18.48	-13.23
Chalcedony	-2.04	-1.45	-1.40	-1.39	-2.59	-1.96
Chabacite-Ca	18.64	24.83	25.86	29.45	23.62	26.97
Clinopyroxene	-9.54	-4.14	-2.60	4.78	6.31	6.14
Gibbsite	0.85	1.34	1.39	0.91	-1.70	-0.82
Goethite	0.51	2.87	3.82	5.52	3.21	3.13
analcime_0.96	-10.81	-8.04	-7.11	-5.59	-8.38	-6.74
Hematite	3.25	7.98	9.85	13.30	8.63	8.49
Heulandite	-21.41	-13.35	-12.34	-8.76	-18.18	-12.92
Kaolinite	-2.39	-0.16	-0.03	-1.00	-8.62	-5.56
Laumondite	-16.53	-10.33	-9.30	-5.71	-11.54	-8.19
mic-gibbsite	-0.28	0.21	0.26	-0.22	-2.83	-1.95
Pyrite	-68.99	NA	-92.16	-135.02	-179.95	-169.94
Thomsonite	-32.20	-19.80	-17.03	-8.62	-17.03	-11.86
Sulfur	-33.96	NA	-44.58	-63.71	-81.28	-77.12
Scolecite	-12.74	-7.17	-6.14	-2.55	-7.18	-4.46
Quartz	-2.27	-1.69	-1.63	-1.62	-2.82	NA

NA: Data not available

8.2 Appendix 3

Snorri Gudbrandsson, Domenik Wolff-Boenisch, Sigurdur R. Gislason, Eric H. Oelkers (2013) “*Experimental characterization of plagioclase dissolution rates as a function of their composition and pH at 22° C*” (submitted to Geochimica Cosmochimica Acta).

Supporting information, eighteen pages, containing fourteen figures and five tables.

Annex A

Rates vs. time based on Si concentrations

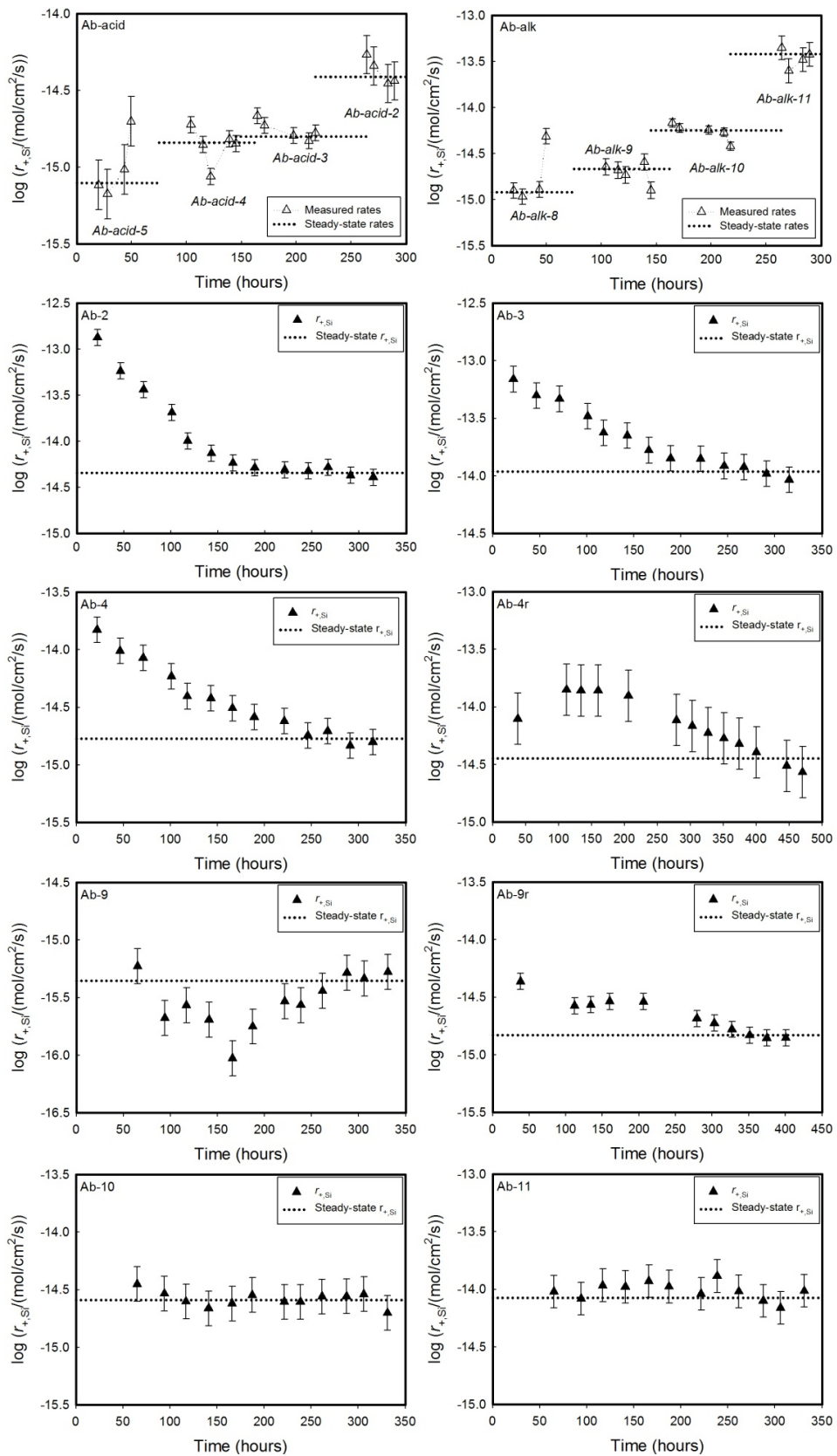
Annex B

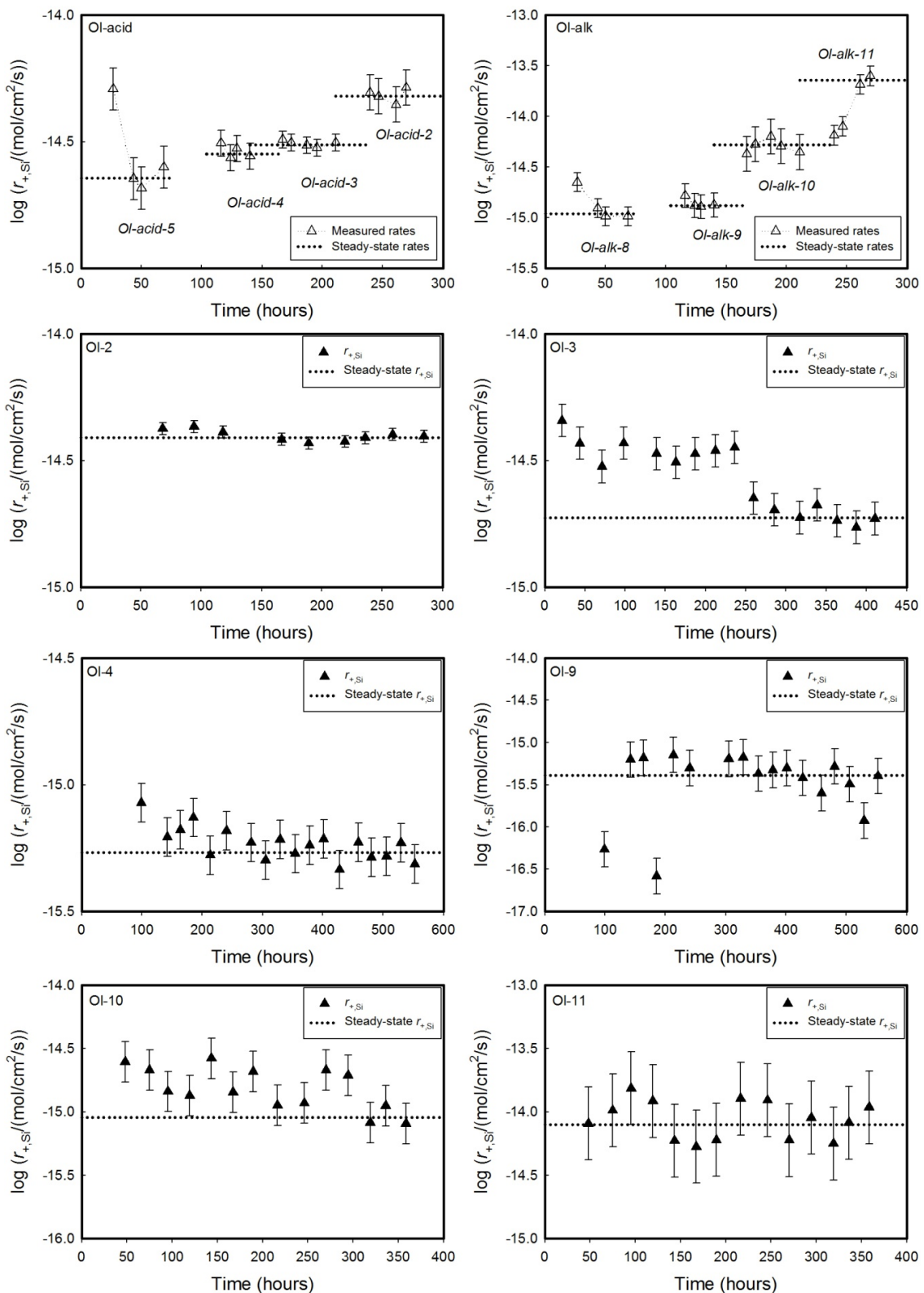
Rates vs. time based on Al concentrations

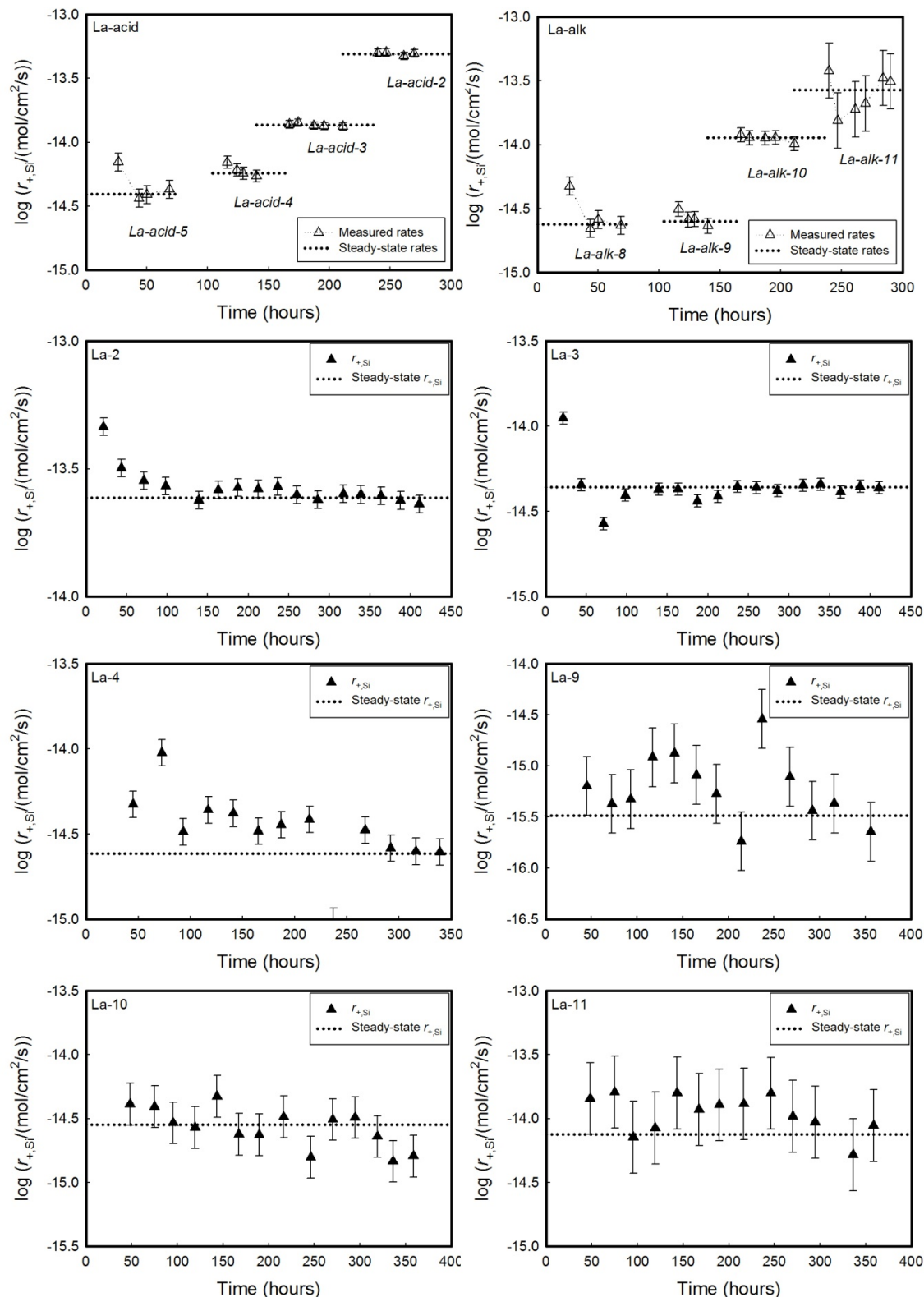
Annex C

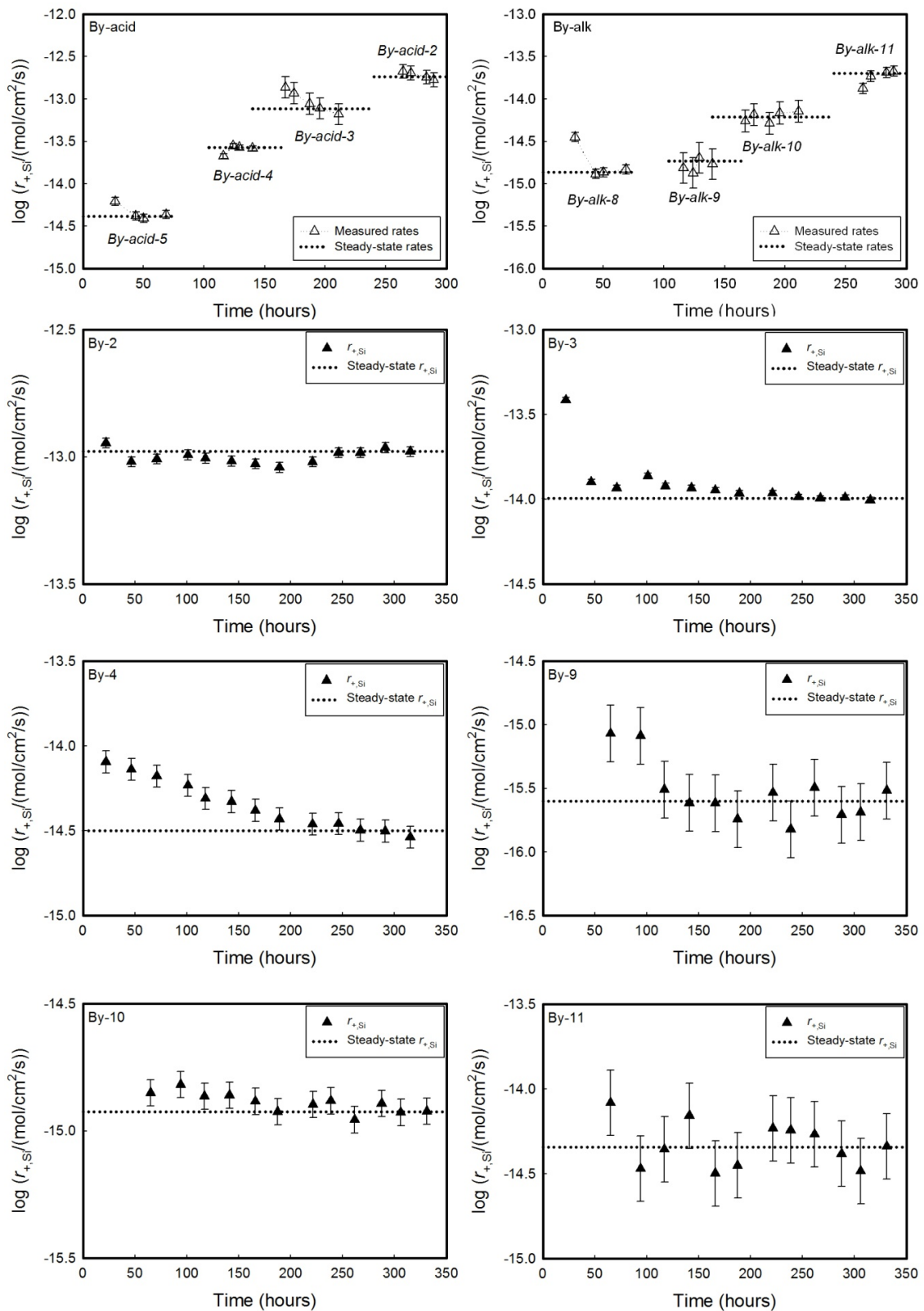
Saturation indexes of noted minerals in fluids from all experiments

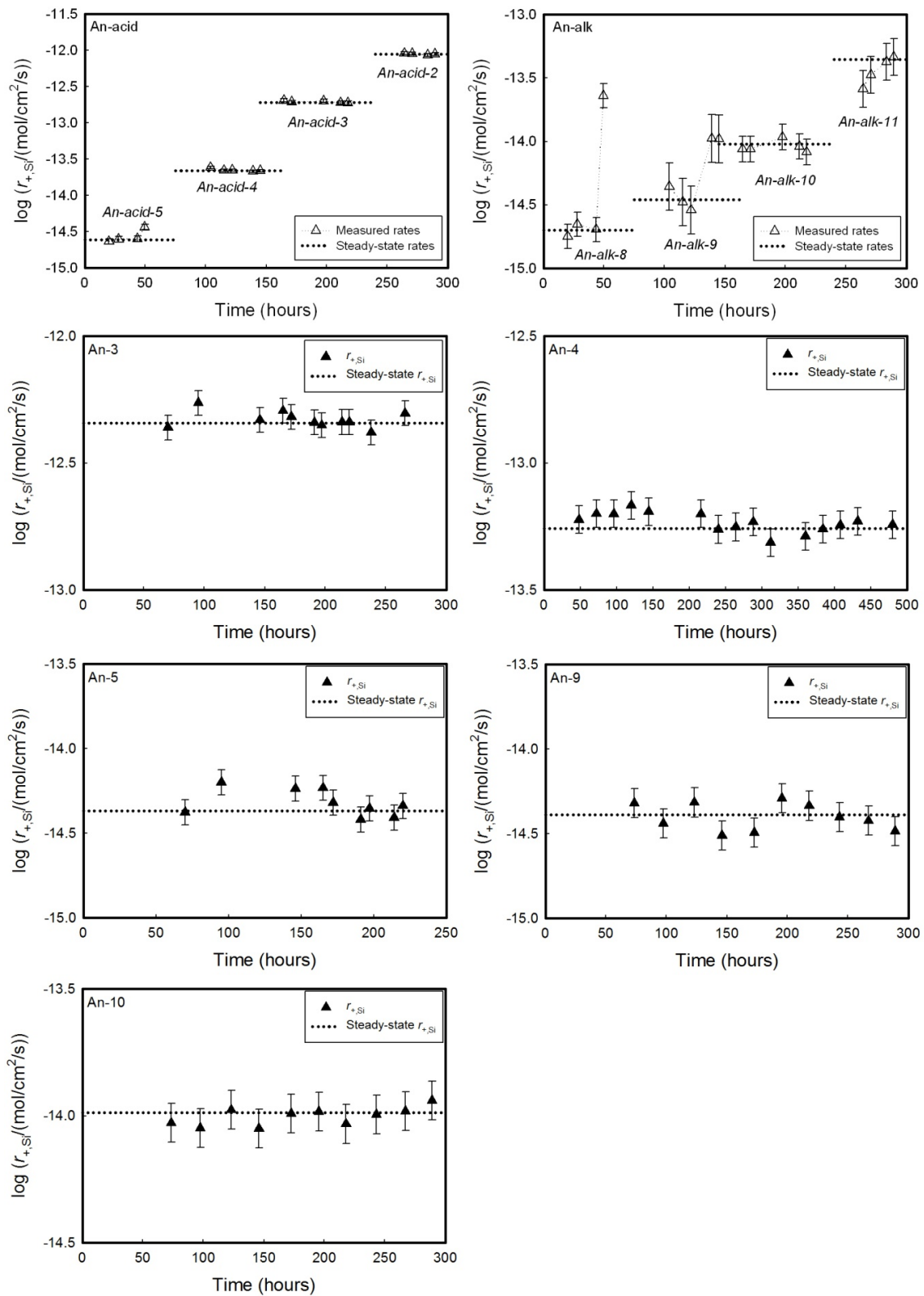
Annex A: Temporal evolution of all plagioclase dissolution rates determined in the present study based on Si release ($r_{+,Si}$) reported in (mol/cm²/s). Open symbols represent rates generated from experiments performed in series running for approximately 75 hours each. The filled symbols correspond to rates obtained from individual experiments run for minimum of 250 hours each. Dashed lines correspond to the final steady-state values in each experiment. The error bars correspond to the standard deviation of measured rates at steady-state multiplied by two.



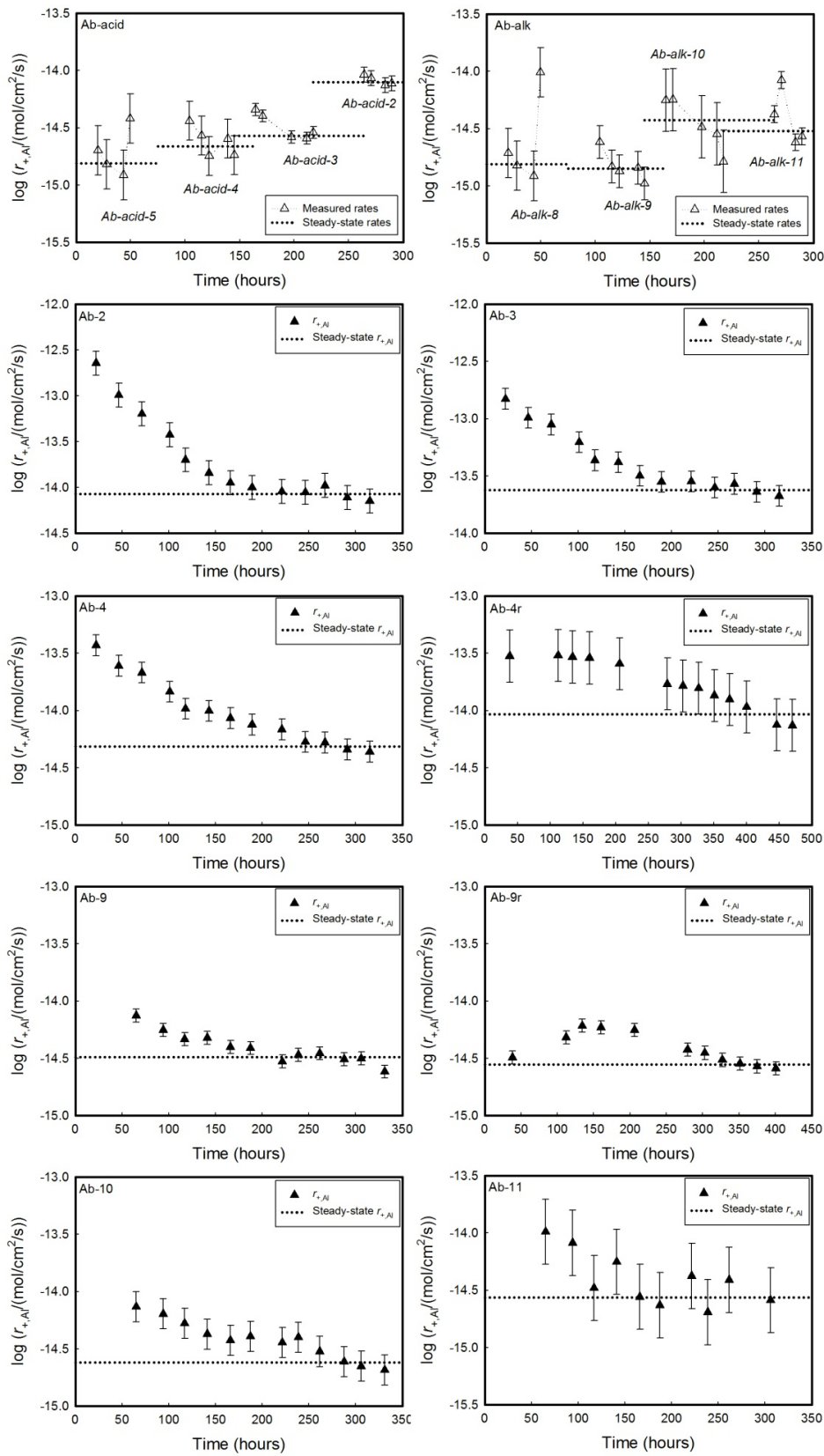


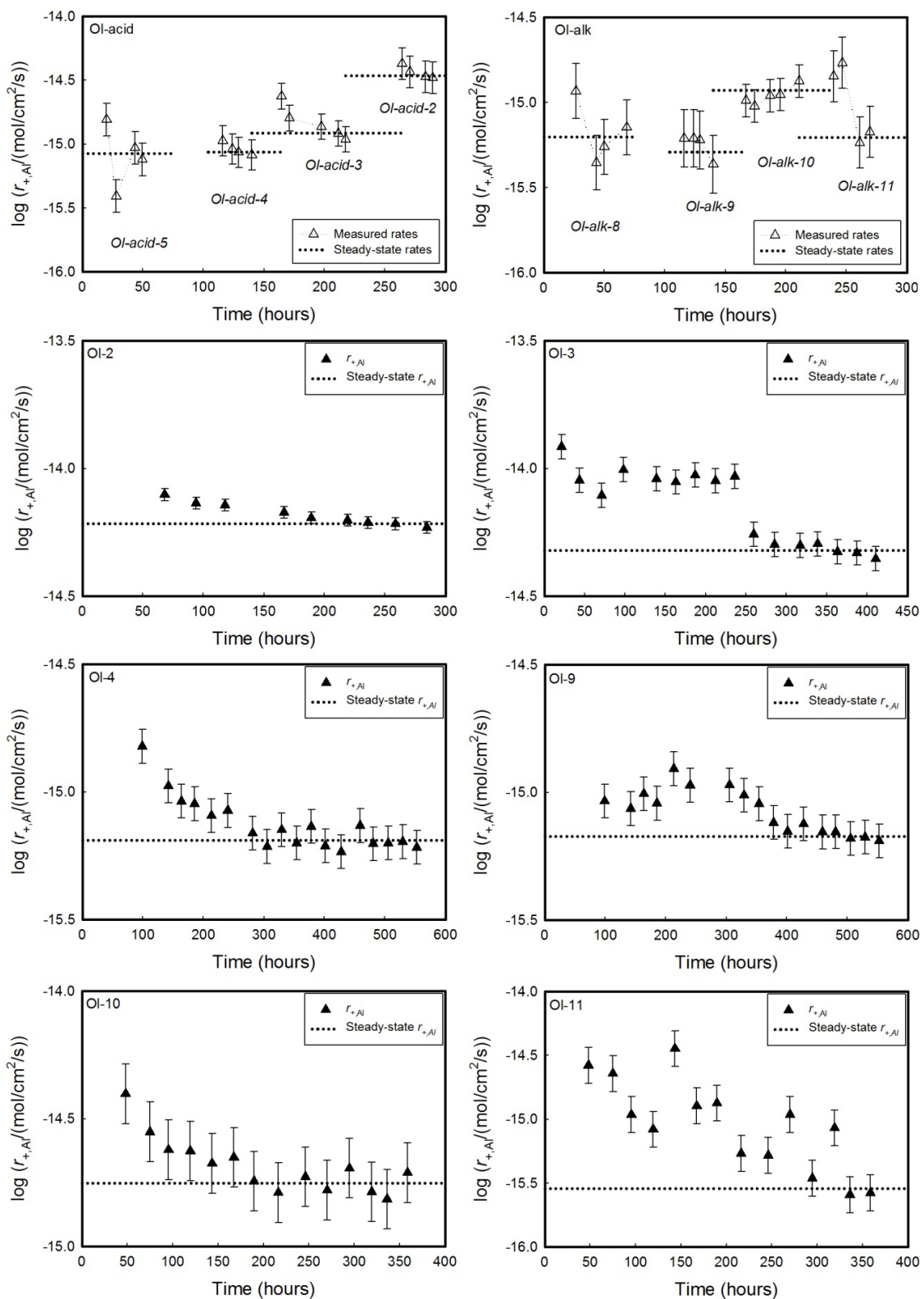


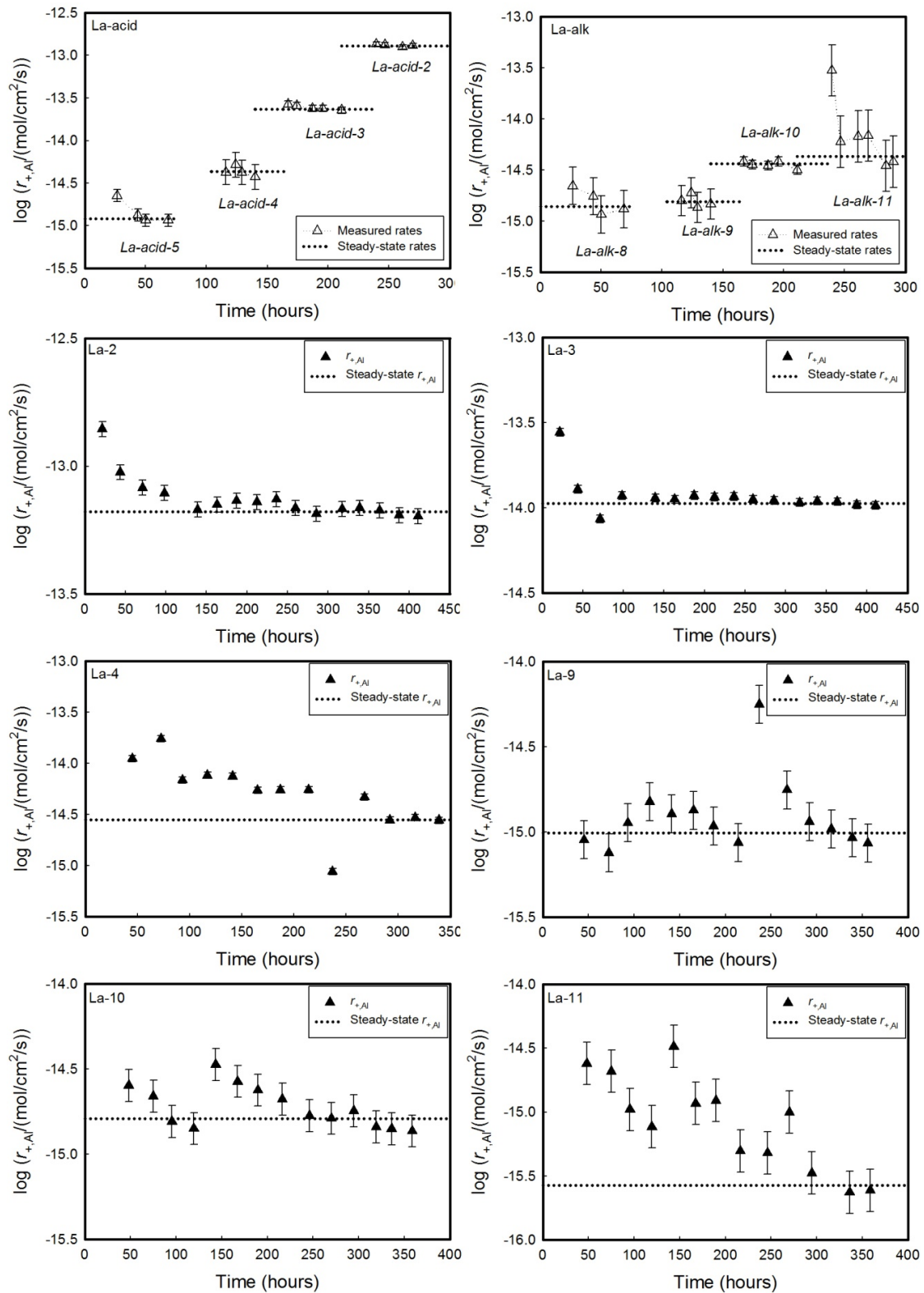


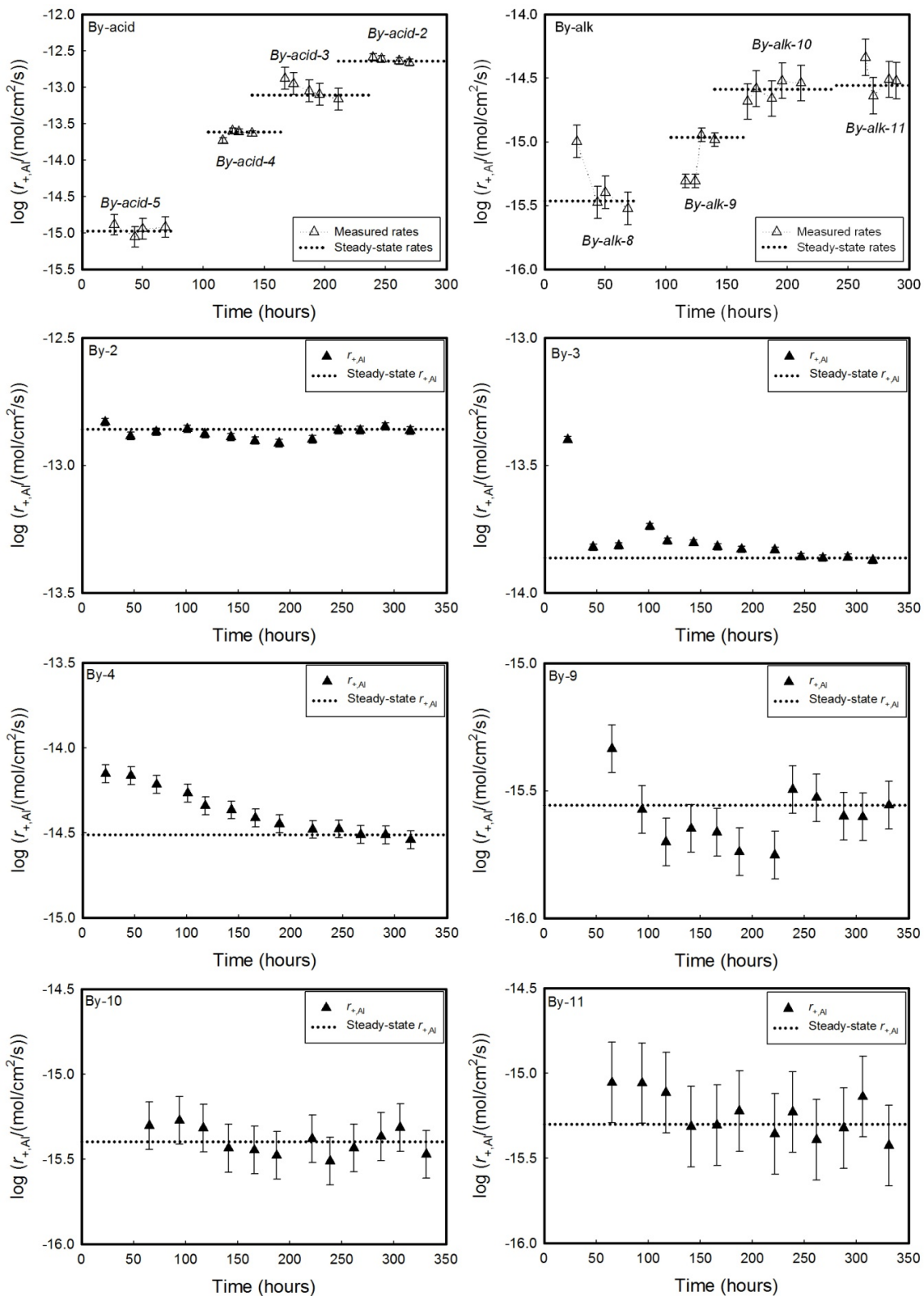


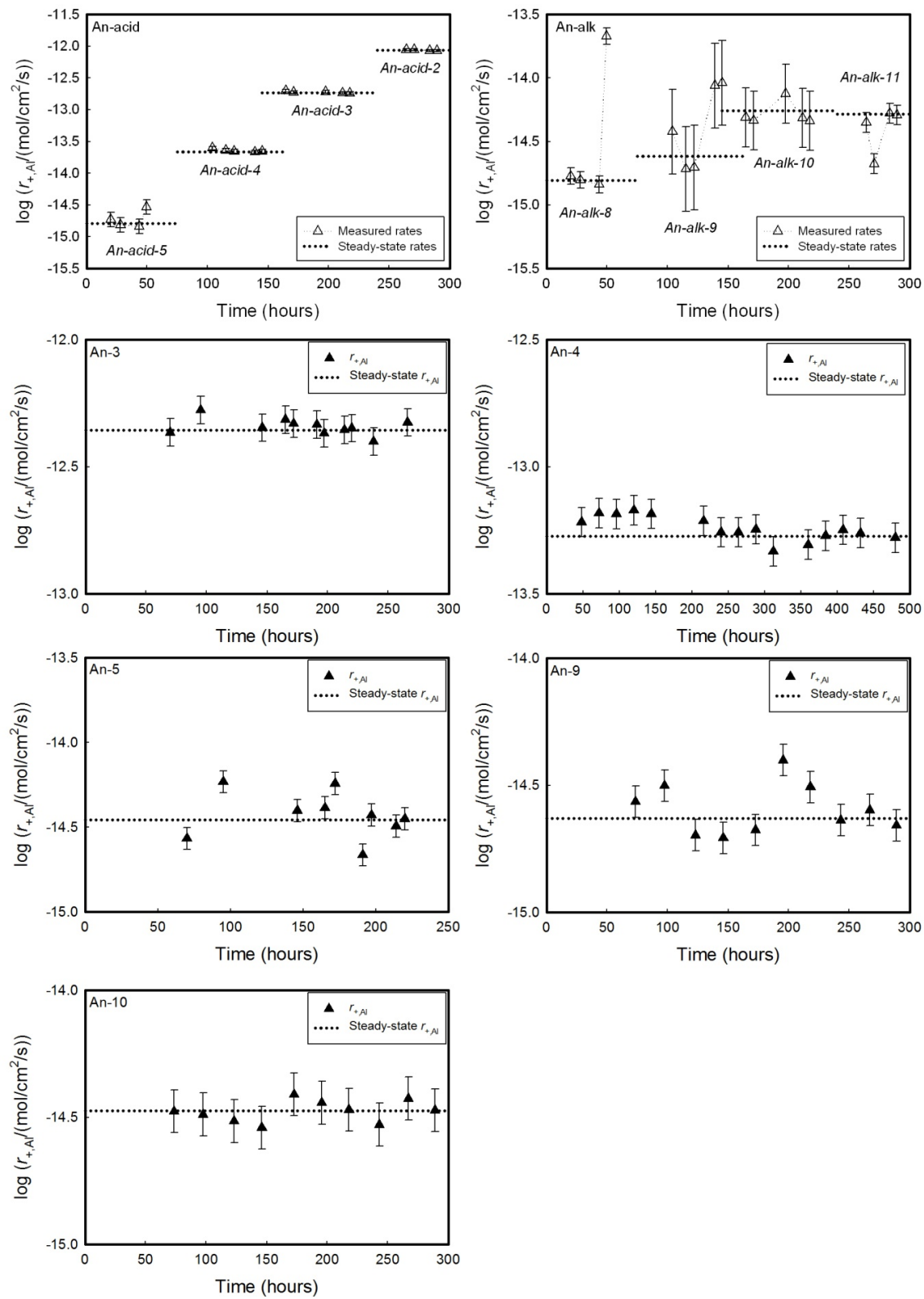
Annex B: Temporal evolution of all plagioclase dissolution rates determined in the present study based on Al release ($r_{+,Al}$) reported in (mol/cm²/s). Open symbols represent rates generated from experiments performed in series running for approximately 75 hours each. The filled symbols correspond to rates obtained from individual experiments run for minimum of 250 hours each. Dashed lines correspond to the final steady-state values in each experiment. The error bars correspond to the standard deviation of measured rates at steady-state multiplied by two.











Annex C: Saturation state of all steady state reactive fluids with respect to the indicated phases. Saturation states are negative if the mineral is undersaturated, but positive if supersaturated. All saturation state values were calculated using the PHREEQC computer code (Parkhurst and Appelo, 1999) – with additions as noted in text.

Albite	Experiments run in series										Experiments run individually					
	Ab-acid-2	Ab-acid-3	Ab-acid-4	Ab-acid-5	Ab-alk-8	Ab-alk-9	Ab-alk-10	Ab-alk-11	Ab-2	Ab-3	Ab-4	Ab-4r	Ab-9	Ab-9r	Ab-10	Ab-11
Albite	-36.8	-35.4	-31.5	-27.6	-23.5	-23.4	-21.7	-21.9	-32.8	-27.6	-27.4	-21.0	-23.1	-22.2	-20.3	-19.1
Anorthite	-51.6	-47.2	-39.6	-30.5	-19.4	-20.6	-20.3	-19.7	-45.8	-38.2	-33.4	-24.9	-20.1	-18.4	-18.1	-17.5
Albite_high	-27.6	-26.2	-22.3	-18.4	-14.3	-12.4	-12.6	-12.6	-23.6	-18.4	-18.2	-11.8	-13.9	-11.1	-9.9	
Albite_low	-26.2	-24.9	-20.9	-17.1	-12.9	-12.8	-11.1	-11.3	-22.2	-17.1	-16.9	-10.4	-12.5	-11.6	-9.8	-8.6
Gibbsite	-9.9	-7.9	-4.8	-1.5	0.0	-1.0	-2.3	-3.0	-8.4	-5.7	-3.3	-0.9	0.0	0.6	-0.8	-1.7
Diaspore	-8.7	-6.7	-3.5	-0.3	1.2	0.2	-1.1	-1.8	-7.2	-4.5	-2.1	0.3	1.2	1.8	0.4	-0.5
Boehmite	-9.1	-7.1	-4.0	-0.7	0.8	-0.2	-1.5	-2.2	-7.6	-4.9	-2.5	-0.1	0.8	1.4	0.0	-0.9
Kaolinite	-21.6	-18.4	-12.3	-6.1	-2.7	-4.4	-6.3	-8.8	-17.1	-11.2	-8.0	-1.4	-3.7	-2.6	-3.5	-4.5
SiO ₂ (am)	-3.2	-3.6	-3.7	-3.9	-3.6	-3.6	-3.2	-3.7	-2.5	-2.2	-3.0	-2.1	-4.1	-4.2	-3.2	-2.9
Al(OH) ₃ (am)	-12.2	-10.1	-7.0	-3.7	-2.3	-3.2	-4.5	-5.3	-10.6	-7.9	-5.5	-3.1	-2.3	-1.7	-3.1	-3.9
Allophane_Al/Si=1.26	-28.9	-25.5	-19.4	-13.1	-9.8	-11.6	-13.6	-16.0	-24.7	-18.9	-15.3	-9.1	-10.6	-9.5	-10.8	-12.0
Allophane_Al/Si=1.64	-27.4	-23.9	-17.7	-11.4	-8.2	-10.0	-12.1	-14.3	-23.5	-17.7	-13.9	-8.1	-8.8	-7.6	-9.3	-10.6
Allophane_Al/Si=2.02	-26.8	-23.1	-16.9	-10.6	-7.4	-9.2	-11.5	-13.5	-23.0	-17.3	-13.3	-7.6	-7.9	-6.7	-8.6	-10.0
Analcime_0.96	-30.5	-28.8	-25.0	-21.1	-17.3	-17.3	-16.0	-15.7	-27.2	-22.5	-21.6	-16.2	-15.6	-14.6	-13.8	
Analcime	-30.8	-29.1	-25.0	-21.0	-17.1	-17.1	-15.7	-15.4	-27.6	-22.7	-21.7	-16.1	-16.2	-15.3	-14.4	-13.5
Ca-stilbite	-72.1	-69.8	-62.5	-54.4	-42.0	-42.9	-40.7	-42.7	-62.7	-53.8	-52.8	-40.0	-45.4	-43.9	-38.8	-36.5
Chaledony	-2.1	-2.6	-2.6	-2.8	-2.6	-2.5	-2.1	-2.7	-1.4	-1.1	-1.9	-1.1	-3.1	-2.2	-1.9	
Heulandite	-72.3	-70.0	-62.7	-54.6	-42.1	-43.1	-40.8	-42.9	-62.9	-54.0	-53.0	-40.2	-45.5	-44.0	-38.9	-36.7
Laumontite	-43.7	-40.2	-32.6	-24.1	-12.3	-13.4	-12.4	-12.7	-36.6	-28.5	-25.2	-15.0	-14.2	-12.7	-10.3	-9.1
mic-gibbsite	-10.7	-8.7	-5.5	-2.3	-0.8	-1.7	-3.1	-3.8	-9.2	-6.5	-4.1	-1.7	-0.8	-0.2	-1.6	-2.4
Quartz	-5.3	-5.7	-5.8	-6.0	-5.7	-5.7	-5.3	-5.8	-4.6	-4.3	-5.1	-4.2	-6.2	-6.3	-5.3	-5.0
Scolecite	-50.4	-46.5	-38.8	-30.2	-18.6	-19.8	-19.2	-19.0	-44.0	-36.2	-32.1	-22.8	-20.0	-18.4	-17.0	-16.1
Thomsonite	-118.7	-108.0	-88.3	-66.4	-40.2	-42.6	-41.3	-38.9	-105.0	-85.2	-73.7	-52.0	-40.6	-36.3	-35.4	-33.7
An1_low	-36.5	-34.9	-30.9	-26.8	-22.5	-22.5	-20.7	-20.9	-32.4	-27.1	-26.7	-20.2	-22.0	-21.1	-19.3	-18.1
An9_low	-37.5	-35.8	-31.5	-27.0	-22.2	-22.2	-20.6	-20.7	-33.3	-27.9	-27.1	-20.4	-21.8	-20.8	-19.2	-18.0

Oligoclase	Experiments run in series											Experiments run individually				
	OI-acid-2	OI-acid-3	OI-acid-4	OI-acid-5	OI-acid-8	OI-alk-9	OI-alk-10	OI-alk-11	OI-2	OI-3	OI-4	OI-9	OI-10	OI-11		
Albite	-35.9	-33.3	-29.8	-26.3	-23.0	-22.4	-22.9	-34.7	-32.8	-22.6	-22.8	-22.8	-22.7			
Anorthite	-49.6	-43.0	-35.4	-27.1	-20.1	-21.3	-20.5	-46.8	-40.1	-39.6	-19.2	-19.1	-19.9			
Albite_high	-26.7	-24.1	-20.5	-17.1	-13.1	-13.8	-13.6	-25.6	-23.7	-23.2	-13.5	-13.7	-13.5			
Albite_low	-25.3	-22.7	-19.2	-15.8	-11.8	-12.5	-12.3	-24.3	-22.3	-21.8	-12.1	-12.4	-12.2			
Gibbsite	-9.4	-6.9	-4.0	-1.2	-0.1	-1.3	-2.6	-3.4	-8.6	-5.9	-3.8	-0.6	-2.0	-3.2		
Diaspore	-8.2	-5.7	-2.7	0.0	1.1	-0.1	-1.4	-2.2	-7.4	-4.7	-2.6	0.6	-0.8	-2.0		
Boehmite	-8.6	-6.1	-3.2	-0.4	0.7	-0.5	-1.8	-2.6	-7.8	-5.1	-3.0	0.2	-1.2	-2.5		
Kaolinite	-20.4	-15.8	-10.0	-4.4	-2.8	-5.4	-7.8	-9.7	-18.4	-13.7	-11.1	-4.1	-6.8	-9.4		
SiO ₂ (am)	-3.1	-3.3	-3.3	-3.3	-3.6	-3.7	-3.6	-3.8	-2.9	-3.2	-4.0	-3.7	-3.7	-3.7		
Al(OH) ₃ (am)	-11.6	-9.2	-6.2	-3.4	-2.3	-3.6	-4.9	-5.6	-10.8	-8.1	-6.0	-2.8	-4.2	-5.5		
Allophane_Al/Si=1.26	-27.8	-23.1	-17.3	-11.6	-10.0	-12.5	-15.0	-16.8	-25.8	-20.9	-17.9	-11.1	-13.8	-16.4		
Allophane_Al/Si=1.64	-26.3	-21.6	-15.7	-10.1	-8.3	-10.8	-13.3	-15.1	-24.4	-19.4	-16.1	-9.4	-12.1	-14.7		
Allophane_Al/Si=2.02	-25.6	-20.9	-15.0	-9.4	-7.5	-10.0	-12.6	-14.3	-23.7	-18.7	-15.3	-8.6	-11.3	-13.9		
Analcime_0.96	-29.7	-27.0	-23.6	-20.3	-16.2	-16.9	-16.3	-16.6	-28.8	-26.6	-25.5	-16.4	-16.6	-16.5		
Analcime	-30.1	-27.3	-23.7	-20.3	-16.0	-16.6	-16.1	-16.3	-29.1	-26.8	-25.6	-16.1	-16.4	-16.2		
Ca-stilbite	-69.6	-63.9	-56.6	-48.1	-42.8	-44.2	-42.9	-44.0	-66.2	-61.0	-113.1	-42.7	-42.6	-43.5		
Chalcedony	-2.1	-2.2	-2.3	-2.2	-2.6	-2.5	-2.5	-2.7	-1.9	-2.2	-3.0	-2.7	-2.7	-2.7		
Heulandite	-69.8	-64.1	-56.8	-48.3	-43.0	-44.4	-43.1	-44.2	-66.4	-61.2	-113.2	-42.8	-42.8	-43.7		
Laumontite	-41.4	-35.1	-27.8	-19.5	-13.2	-14.4	-13.3	-13.8	-38.8	-32.8	-84.2	-12.9	-12.8	-13.7		
mic-gibbsite	-10.2	-7.7	-4.7	-2.0	-0.9	-2.1	-3.4	-4.2	-9.3	-6.7	-4.6	-1.4	-2.7	-4.0		
Quartz	-5.2	-5.4	-5.5	-5.4	-5.7	-5.8	-5.7	-5.9	-5.0	-5.3	-6.1	-5.8	-5.8	-5.8		
Scolectite	-48.2	-41.8	-34.4	-26.2	-19.5	-20.7	-19.6	-19.9	-45.8	-39.4	-89.7	-19.0	-19.0	-19.8		
Thomsonite	-113.9	-97.6	-79.1	-59.5	-40.8	-43.7	-41.3	-41.5	-109	-92.8	-133.7	-39.8	-39.9	-41.3		
An18_low	-38.0	-34.5	-30.1	-25.6	-21.0	-21.8	-21.2	-21.5	-36.4	-33.4	-85.9	-21.0	-21.2	-21.2		

Labradorite	Experiments run in series										Experiments run individually				
	La-acid-2	La-acid-3	La-acid-4	La-acid-5	La-alk-8	La-alk-9	La-alk-10	La-alk-11	La-2	La-3	La-4	La-9	La-10	La-11	
Albite	-31.3	-31.1	-28.4	-26.0	-21.9	-22.2	-19.0	-19.1	-30.9	-32.1	-26.3	-23.7	-23.1	-23.1	
Anorthite	-43.7	-38.8	-33.1	-26.8	-19.2	-18.0	-17.3	-41.9	-39.9	-30.2	-19.3	-19.3	-20.2		
Albite_high	-22.1	-21.9	-19.2	-16.8	-12.7	-13.0	-9.8	-9.9	-21.8	-23.0	-17.2	-14.6	-14.0	-14.0	
Albite_low	-20.7	-20.5	-17.8	-15.4	-11.3	-11.7	-8.4	-8.5	-20.5	-21.7	-15.9	-13.3	-12.6	-12.6	
Gibbsite	-7.8	-5.5	-3.2	-0.9	0.2	-0.8	-2.7	-2.5	-7.2	-5.7	-2.4	-0.6	-2.0	-2.9	
Diaspore	-6.6	-4.3	-1.9	0.3	1.4	0.4	-1.5	-1.3	-6.0	-4.5	-1.2	0.5	-0.8	-1.7	
Boehmite	-7.0	-4.7	-2.3	-0.1	1.0	0.0	-1.9	-1.7	-6.4	-4.9	-1.6	0.1	-1.2	-2.1	
Kaolinite	-15.4	-12.1	-8.0	-3.8	-2.0	-4.1	-5.7	-6.1	-14.7	-13.7	-6.0	-4.5	-7.0	-8.6	
SiO ₂ (am)	-2.2	-2.8	-3.2	-3.3	-3.5	-3.6	-2.4	-2.8	-2.4	-3.4	-2.9	-3.9	-3.8	-3.7	
Al(OH) ₃ (am)	-10.0	-7.8	-5.4	-3.1	-2.0	-3.0	-4.9	-4.8	-9.5	-8.0	-4.6	-2.9	-4.2	-5.1	
Allophane_Al/Si=1.26	-23.2	-19.6	-15.4	-11.0	-9.1	-11.3	-13.3	-13.6	-22.3	-20.8	-13.3	-11.5	-14.0	-15.6	
Allophane_Al/Si=1.64	-22.0	-18.2	-13.9	-9.5	-7.5	-9.6	-12.1	-12.2	-21.1	-19.2	-11.9	-9.7	-12.3	-13.9	
Allophane_Al/Si=2.02	-21.6	-17.6	-13.2	-8.8	-6.8	-8.9	-11.5	-11.6	-20.5	-18.5	-11.3	-8.9	-11.4	-13.1	
Analcime_0.96	-26.0	-25.3	-22.4	-20.0	-15.9	-16.2	-14.0	-13.8	-25.5	-25.9	-20.7	-17.4	-16.9	-16.9	
Analcime	-26.3	-25.6	-22.5	-20.0	-15.6	-15.9	-13.8	-13.5	-25.8	-26.1	-20.7	-17.1	-16.6	-16.7	
Ca-stilbite	-59.3	-57.3	-53.5	-47.8	-41.2	-42.2	-34.7	-35.9	-58.8	-61.7	-49.5	-43.7	-43.0	-43.6	
Chalcedony	-1.2	-1.8	-2.1	-2.2	-2.4	-2.5	-1.8	-1.4	-1.4	-2.3	-1.9	-2.9	-2.7	-2.7	
Heulandite	-59.5	-57.5	-53.6	-48.0	-41.4	-42.4	-34.9	-36.1	-59.0	-61.9	-49.7	-43.8	-43.1	-43.8	
Laumontite	-33.6	-30.0	-25.1	-19.1	-12.0	-12.7	-8.5	-8.6	-33.0	-33.0	-22.2	-13.4	-13.1	-13.9	
mic-gibbsite	-8.6	-6.3	-3.9	-1.7	-0.6	-1.6	-3.5	-3.3	-8.0	-6.5	-3.1	-1.4	-2.8	-3.7	
Quartz	-4.4	-4.9	-5.3	-5.4	-5.6	-5.7	-4.6	-4.9	-4.5	-5.5	-5.0	-6.0	-5.9	-5.8	
Scolecite	-41.4	-37.2	-31.9	-25.8	-18.4	-19.1	-16.0	-15.7	-40.4	-39.5	-29.1	-19.3	-19.1	-20.0	
Thomsonite	-99.0	-88.1	-73.5	-58.4	-38.8	-40.1	-35.2	-33.2	-91.6	-67.0	-40.9	-40.3	-42.3		
An66_low	-38.6	-35.5	-30.9	-26.0	-19.7	-20.2	-17.8	-17.4	-37.6	-36.8	-28.4	-20.5	-20.3	-20.9	

Bytownite	Experiments run in series											Experiments run individually				
	By-acid-2	By-acid-3	By-acid-4	By-acid-5	By-acid-6	By-alk-8	By-alk-9	By-alk-10	By-alk-11	By-2	By-3	By-4	By-9	By-10	By-11	
Albite	-27.8	-25.4	-24.0	-24.2	-21.9	-20.7	-21.4	-25.7	-27.8	-26.0	-22.3	-20.3	-19.0	-19.0	-19.0	
Anorthite	-40.6	-34.4	-28.7	-25.9	-18.8	-18.6	-17.9	-18.4	-37.6	-36.5	-30.7	-19.6	-18.0	-17.1	-17.1	
Albite_high	-18.6	-16.1	-14.7	-15.0	-12.7	-12.7	-11.4	-12.2	-16.5	-16.8	-13.1	-11.1	-9.8	-9.8	-9.8	
Albite_low	-17.2	-14.7	-13.4	-13.7	-11.4	-11.4	-10.1	-10.8	-15.2	-17.2	-15.5	-11.8	-9.8	-8.5	-8.5	
Gibbsite	-7.3	-4.7	-2.1	-0.8	-0.1	-0.9	-1.8	-2.7	-6.6	-5.3	-2.9	-0.5	-1.1	-1.7	-1.7	
Diaspore	-6.0	-3.5	-0.8	0.4	1.1	0.3	-0.6	-1.4	-5.4	-4.1	-1.7	0.7	0.1	-0.5	-0.5	
Boehmite	-6.5	-3.9	-1.3	0.0	0.7	-0.1	-1.0	-1.9	-5.8	-4.5	-2.1	0.3	-0.3	-0.9	-0.9	
Kaolinite	-12.8	-8.2	-4.2	-3.1	-2.5	-4.2	-5.7	-8.0	-10.8	-10.2	-6.2	-3.9	-3.9	-4.5	-4.5	
SiO ₂ (am)	-1.5	-1.8	-2.3	-3.1	-3.5	-3.5	-3.3	-3.6	-1.1	-2.1	-2.5	-3.7	-3.1	-2.8	-2.8	
Al(OH) ₃ (am)	-9.5	-6.9	-4.3	-3.0	-2.3	-3.1	-4.1	-4.9	-8.8	-7.6	-5.2	-2.8	-3.3	-4.0	-4.0	
Allophane_Al/Si=1.26	-20.9	-16.2	-11.9	-10.5	-9.7	-11.4	-13.0	-15.2	-18.9	-18.0	-13.8	-11.0	-11.2	-12.0	-12.0	
Allophane_Al/Si=1.64	-20.0	-15.2	-10.7	-9.0	-8.1	-9.8	-11.5	-13.5	-18.2	-16.9	-12.6	-9.3	-9.7	-10.6	-10.6	
Allophane_Al/Si=2.02	-19.7	-14.9	-10.2	-8.3	-7.4	-9.0	-10.7	-12.7	-18.0	-16.5	-12.0	-8.5	-9.0	-10.0	-10.0	
Analcime_0.96	-23.3	-20.7	-18.9	-18.5	-16.0	-15.9	-14.9	-15.3	-21.6	-22.8	-20.7	-16.1	-14.7	-13.7	-13.7	
Analcime	-23.6	-20.8	-18.9	-18.4	-15.7	-15.7	-14.6	-15.0	-21.9	-23.0	-20.8	-15.8	-14.4	-13.5	-13.5	
Ca-stilbite	-52.3	-47.6	-44.9	-45.9	-40.8	-40.6	-39.0	-41.1	-47.7	-51.4	-47.7	-42.9	-38.3	-35.8	-35.8	
Chalcedony	-0.4	-0.7	-1.3	-2.0	-2.4	-2.5	-2.3	-2.6	-0.1	-1.0	-1.4	-2.7	-2.1	-1.8	-1.8	
Heulandite	-52.5	-47.8	-45.1	-46.1	-40.9	-40.8	-39.2	-41.3	-47.9	-51.6	-47.9	-43.1	-38.4	-36.0	-36.0	
Laumontite	-29.0	-23.4	-19.0	-17.9	-11.6	-11.3	-10.1	-11.3	-25.7	-26.5	-21.5	-13.0	-10.1	-8.5	-8.5	
mic-gibbsite	-8.0	-5.4	-2.8	-1.5	-0.9	-1.7	-2.6	-3.4	-7.4	-6.1	-3.7	-1.3	-1.9	-2.5	-2.5	
Quartz	-3.6	-3.9	-4.5	-5.2	-5.6	-5.6	-5.5	-5.8	-3.2	-4.2	-4.6	-5.8	-5.2	-4.9	-4.9	
Scolecite	-37.5	-31.7	-26.6	-24.7	-18.0	-17.7	-16.8	-17.6	-34.5	-34.3	-29.0	-19.2	-16.9	-15.6	-15.6	
Thomsonite	-91.0	-75.5	-61.8	-55.2	-38.0	-37.3	-34.8	-35.9	-84.2	-82.2	-68.0	-39.7	-35.5	-32.9	-32.9	
An78_high	-38.1	-32.8	-28.1	-26.0	-20.0	-19.7	-18.9	-19.4	-35.5	-35.1	-30.2	-20.7	-19.0	-18.0	-18.0	
An76_low	-36.8	-31.6	-27.1	-25.1	-19.3	-19.1	-18.2	-18.7	-34.2	-33.9	-29.2	-20.0	-18.3	-17.2	-17.2	

Anorthite	Experiments run in series										Experiments run individually			
	An- acid-2	An- acid-3	An- acid-4	An- acid-5	An-alk-8	An-alk-9	An-alk-10	An-alk-11	An-3	An-4	An-5	An-9	An-10	
Albite	-27.0	-27.4	-27.2	-26.2	-22.7	-21.4	-21.0	-21.8	-22.9	-23.2	-24.2	-21.3	-24.2	
Anorthite	-40.1	-36.7	-33.0	-28.0	-19.8	-19.2	-18.5	-19.2	-30.8	-27.2	-25.6	-19.2	-25.6	
Albite_high	-17.8	-18.2	-17.9	-17.0	-13.5	-12.2	-11.8	-12.6	-13.7	-14.0	-14.9	-12.1	-14.9	
Albite_low	-16.4	-16.9	-16.6	-15.7	-12.1	-10.8	-10.5	-11.2	-12.4	-12.7	-13.6	-10.8	-13.6	
Gibbsite	-7.5	-5.7	-3.5	-0.9	0.4	-0.3	-1.7	-2.9	-3.9	-1.7	-0.3	-0.8	-0.3	
Diaspore	-6.3	-4.5	-2.3	0.3	1.6	0.9	-0.4	-1.7	-2.6	-0.5	0.9	0.4	0.9	
Boehmite	-6.7	-4.9	-2.7	-0.1	1.2	0.5	-0.8	-2.1	-3.1	-0.9	0.5	0.0	0.5	
Kaolinite	-12.4	-10.2	-7.5	-4.3	-1.4	-2.5	-5.5	-8.8	-5.6	-3.1	-2.5	-3.8	-2.5	
SiO ₂ (am)	-1.0	-1.7	-2.6	-3.5	-3.4	-3.2	-3.4	-3.8	-1.2	-2.2	-3.3	-3.4	-3.3	
Al(OH) ₃ (am)	-9.8	-8.0	-5.7	-3.2	-1.8	-2.6	-3.9	-5.2	-6.1	-4.0	-2.5	-3.0	-2.5	
Allophane_Al/Si=1.26	-20.6	-18.1	-15.1	-11.5	-8.6	-9.8	-12.7	-15.9	-13.7	-10.9	-9.8	-11.0	-9.8	
Allophane_Al/Si=1.64	-20.0	-17.2	-13.9	-9.9	-7.1	-8.3	-11.1	-14.2	-13.0	-9.8	-8.2	-9.4	-8.2	
Allophane_Al/Si=2.02	-19.8	-16.9	-13.3	-9.1	-6.3	-7.6	-10.4	-13.4	-12.7	-9.3	-7.5	-8.7	-7.5	
Analcime_0.96	-22.9	-22.7	-21.7	-20.1	-16.8	-15.7	-15.2	-15.6	-18.8	-18.3	-18.3	-15.4	-18.3	
Analcime	-23.3	-23.0	-21.8	-20.0	-16.5	-15.4	-14.9	-15.3	-18.9	-18.3	-18.3	-15.2	-18.2	
Ca-stilbite	-49.4	-49.6	-50.4	-50.0	-41.3	-39.9	-40.0	-42.5	-41.5	-42.5	-46.4	-40.9	-46.4	
Chalcedony	0.1	-0.6	-1.5	-2.5	-2.4	-2.2	-2.3	-2.7	-0.2	-1.1	-2.2	-2.3	-2.2	
Heulandite	-49.6	-49.8	-50.5	-50.2	-41.5	-40.1	-40.2	-42.7	-41.7	-42.7	-46.6	-41.1	-46.6	
Laumontite	-27.6	-25.8	-23.8	-20.7	-12.3	-11.3	-11.0	-12.4	-19.0	-17.2	-17.8	-12.1	-17.8	
mic-gibbsite	-8.3	-6.5	-4.3	-1.7	-0.4	-1.1	-2.4	-3.7	-4.6	-2.5	-1.0	-1.6	-1.0	
Quartz	-3.1	-3.8	-4.7	-5.6	-5.5	-5.4	-5.5	-5.9	-3.4	-4.3	-5.4	-5.5	-5.4	
Scolecite	-36.6	-34.1	-31.1	-27.1	-18.9	-18.0	-17.6	-18.6	-27.7	-25.0	-24.5	-18.6	-24.5	
Thomsonite	-90.2	-82.9	-73.0	-60.4	-40.8	-38.4	-36.6	-37.8	-67.3	-58.5	-54.0	-38.9	-54.0	
An78_high	-37.6	-35.1	-32.1	-28.0	-20.9	-20.1	-19.5	-20.2	-29.5	-26.7	-25.7	-20.3	-25.7	
An89_high	-38.3	-35.5	-32.1	-27.7	-20.2	-19.4	-18.8	-19.4	-29.7	-26.6	-25.4	-19.6	-25.4	

8.3 Appendix 4

Snorri Gudbrandsson, Vasileios Mavromatis, Eric H. Oelkers (2013)
“*Precipitation of gibbsite at pH 11 at 22°C and pH 9 at 80°C*” (Manuscript to be submitted upon completion of work).

Supporting information, thirteen pages, containing four tables.

Annex A

S1: Measured values from R-series

S2: Measured values from H-series

Annex B

S3: Calculated values from R-series

S4: Calculated values from H-series

Annex A

Table S1 - Time, Al conc., pH, reactive fluid mass and saturation indexes for selected phases during experiments at 22 °C.

Exp. No	pH	Elapsed time	M_r (kg)	$C_{Al} \times 10^3$ mol/kg	S.I.			Log (IAP)
	22 °C	(hours)			Gibbsite	Boehmite	Diaspore	
G-R1-01	10.90	1	0.498	0.10	-0.05	1.14	1.55	8.9
G-R1-02	10.70	291	0.488	0.09	0.08	1.27	1.68	9.0
G-R1-03	10.68	623	0.477	0.08	0.09	1.27	1.68	9.0
G-R1-04	10.69	1175	0.467	0.08	0.05	1.24	1.65	9.0
G-R1-05	10.62	1535	0.457	0.07	0.09	1.28	1.69	9.0
G-R1-06	10.56	1970	0.446	0.07	0.14	1.33	1.74	9.1
G-R1-07	10.69	2352	0.435	0.07	-0.02	1.17	1.58	8.9
G-R1-08	10.39	2979	0.425	0.06	0.26	1.45	1.86	9.2
G-R1-09	10.43	3483	0.414	0.06	0.19	1.38	1.79	9.1
G-R1-10	10.53	3815	0.404	0.06	0.07	1.25	1.66	9.0
G-R1-11	10.30	4466	0.394	0.06	0.29	1.48	1.89	9.2
G-R1-12	10.46	5139	0.383	0.05	0.12	1.30	1.71	9.1
G-R2-1	10.88	1	0.497	0.16	0.16	1.35	1.76	9.1
G-R2-2	10.81	291	0.487	0.14	0.17	1.36	1.77	9.1
G-R2-3	10.77	623	0.476	0.10	0.06	1.25	1.65	9.0
G-R2-4	10.86	1175	0.466	0.08	-0.11	1.08	1.48	8.8
G-R2-5	10.84	1535	0.456	0.07	-0.14	1.05	1.46	8.8
G-R2-6	10.79	1970	0.446	0.07	-0.13	1.06	1.47	8.8
G-R2-7	10.73	2352	0.435	0.06	-0.09	1.10	1.50	8.9
G-R2-8	10.62	2979	0.425	n.m.	n.a.	n.a.	n.a.	n.c.
G-R2-9	10.58	3483	0.415	0.07	0.10	1.29	1.69	9.0
G-R2-10	10.57	3815	0.404	0.06	0.07	1.26	1.67	9.0
G-R2-11	10.46	4466	0.394	0.06	0.16	1.35	1.76	9.1
G-R2-12	10.54	5139	0.383	0.05	0.05	1.23	1.64	9.0

Table S1 (continued) - Time, Al conc., pH, reactive fluid mass and saturation indexes for selected phases during experiments at 22 °C.

Exp. No	pH 22 °C	Elapsed time (hours)	M_r (kg)	C_{Al} $\times 10^3$ mol/kg	S.I.			Log (IAP)
					Gibbsite	Boehmite	Diaspore	
G-R3-1	10.87	1	0.495	0.33	0.75	1.94	2.34	9.4
G-R3-2	10.92	291	0.485	0.22	0.33	1.52	1.93	9.2
G-R3-3	10.91	623	0.474	0.14	0.15	1.34	1.75	9.0
G-R3-4	11.00	1175	0.464	0.12	-0.07	1.12	1.52	8.9
G-R3-5	10.99	1535	0.454	0.11	-0.08	1.11	1.52	8.8
G-R3-6	11.11	1970	0.443	0.11	-0.07	1.12	1.52	8.7
G-R3-7	10.88	2352	0.432	0.10	-0.03	1.16	1.57	8.9
G-R3-8	10.79	2979	0.422	0.10	n.a.	n.a.	n.a.	9.0
G-R3-9	10.76	3483	0.411	0.10	0.05	1.24	1.65	9.0
G-R3-10	10.83	3815	0.401	0.10	-0.04	1.15	1.56	9.0
G-R3-11	10.63	4466	0.390	0.08	0.19	1.37	1.78	9.1
G-R3-12	10.73	5139	0.380	0.08	0.03	1.22	1.63	9.0
G-R4-1	10.92	1	0.497	0.67	0.49	1.67	2.08	9.7
G-R4-2	11.08	291	0.487	0.37	0.26	1.44	1.85	9.3
G-R4-3	11.08	623	0.476	0.24	0.08	1.26	1.67	9.1
G-R4-4	11.17	1175	0.466	0.18	-0.06	1.13	1.53	8.9
G-R4-5	11.16	1535	0.456	0.17	-0.12	1.07	1.47	8.9
G-R4-6	11.12	1970	0.445	0.16	-0.23	0.96	1.36	8.9
G-R4-7	11.06	2352	0.435	0.15	-0.03	1.16	1.57	8.9
G-R4-8	10.97	2979	0.424	n.m.	0.06	1.25	1.66	n.c.
G-R4-9	10.94	3483	0.413	0.14	0.10	1.29	1.69	9.0
G-R4-10	10.99	3815	0.403	0.13	0.02	1.21	1.62	8.9
G-R4-11	10.82	4466	0.392	0.14	0.12	1.30	1.71	9.1
G-R4-12	10.93	5139	0.381	0.13	0.01	1.19	1.60	9.0

Table S1 (continued) - Time, Al conc., pH, reactive fluid mass and saturation indexes for selected phases during experiments at 22 °C.

Exp. No	pH 22 °C	Elapsed time (hours)	M_r (kg)	C_{Al} $\times 10^3$ mol/kg	S.I.			Log (IAP)
					Gibbsite	Boehmite	Diaspore	
G-R5-1	10.91	1	0.498	1.51	1.11	2.30	2.71	10.1
G-R5-2	11.33	291	0.488	0.80	0.41	1.60	2.01	9.4
G-R5-3	11.33	623	0.477	0.51	0.22	1.41	1.82	9.2
G-R5-4	11.45	1175	0.467	0.39	-0.02	1.17	1.58	8.9
G-R5-5	11.41	1535	0.456	0.35	-0.02	1.17	1.58	8.9
G-R5-6	11.32	1970	0.446	0.36	0.08	1.26	1.67	9.0
G-R5-7	11.33	2352	0.436	0.33	0.03	1.21	1.62	9.0
G-R5-8	11.22	2979	0.425	n.m.	0.13	1.32	1.73	9.1
G-R5-9	11.21	3483	0.414	0.32	0.14	1.33	1.74	9.1
G-R5-10	11.27	3815	0.404	0.32	0.07	1.26	1.67	9.0
G-R5-11	11.09	4466	0.393	0.31	0.24	1.43	1.83	9.2
G-R5-12	11.20	5139	0.383	0.29	0.10	1.29	1.69	9.0
G-R5-13	11.33	5737	0.373	0.25	-0.09	1.10	1.51	9.1

Table S2 -Time, Al conc., pH, reactive fluid mass and saturation indexes for selected phases during experiments at 80 °C.

Exp. No	pH	Elapsed time (hours)	M_r (kg)	C_{Al} $\times 10^3$ mol/kg	S.I.			$\log(IAP)$
	80 °C				Gibbsite	Boehmite	Diaspore	
G-H6-1	9.38	1	0.395	0.25	-0.33	0.73	1.05	5.2
G-H6-2	8.92	291	0.384	0.23	0.09	1.15	1.48	5.6
G-H6-3	8.98	623	0.373	0.21	0.00	1.06	1.38	5.5
G-H6-4	8.84	1175	0.362	0.18	0.06	1.12	1.44	5.6
G-H6-5	8.72	1535	0.352	0.17	0.17	1.23	1.55	5.7
G-H6-6	7.96	1970	0.341	0.16	0.87	1.94	2.26	6.4
G-H6-7	7.99	2352	0.330	0.13	0.75	1.81	2.13	6.3
G-H6-8	6.73	2979	0.319	0.12	1.71	2.77	3.09	7.2
G-H6-9	6.18	3483	0.308	0.07	1.93	2.99	3.31	7.4
G-H6-10	5.26	3815	0.298	0.09	2.62	3.68	4.00	8.1
G-H6-11	6.34	4466	0.286	0.05	1.67	2.73	3.05	7.2
G-H6-12	6.41	5139	0.274	0.04	1.56	2.62	2.94	7.1
G-H7-1	9.43	1	0.401	0.39	-0.19	0.87	1.19	5.3
G-H7-2	9.19	291	0.390	0.28	-0.09	0.98	1.30	5.4
G-H7-3	9.21	623	0.379	0.26	-0.14	0.92	1.24	5.4
G-H7-4	9.16	1175	0.368	0.23	-0.15	0.91	1.23	5.4
G-H7-5	9.01	1535	0.358	0.21	-0.04	1.02	1.34	5.5
G-H7-6	8.83	1970	0.347	0.21	0.14	1.20	1.52	5.7
G-H7-7	8.63	2352	0.336	0.17	0.26	1.32	1.64	5.8
G-H7-8	8.30	2979	0.325	0.17	0.58	1.64	1.96	6.1
G-H7-9	8.08	3483	0.314	0.12	0.66	1.72	2.04	6.2
G-H7-10	7.96	3815	0.304	0.12	0.75	1.81	2.13	6.3
G-H7-11	7.53	4466	0.293	0.10	1.05	2.11	2.43	6.6
G-H7-12	7.37	5139	0.281	0.08	1.10	2.16	2.48	6.6

Table S2 (continued) -Time, Al conc., pH, reactive fluid mass and saturation indexes for selected phases during experiments at 80 °C.

Exp. No	pH 80 °C	Elapsed time (hours)	M_r (kg)	C_{Al} $\times 10^3$ mol/kg	S.I.			Log (IAP)
					Gibbsite	Boehmite	Diaspore	
G-H8-1	9.39	1	0.399	0.77	0.14	1.20	1.52	5.7
G-H8-2	10.1	291	0.388	0.55	-0.73	0.33	0.65	4.8
G-H8-3	9.49	623	0.377	0.49	-0.15	0.91	1.23	5.4
G-H8-4	9.47	1175	0.366	0.44	-0.18	0.88	1.20	5.3
G-H8-5	9.34	1535	0.356	0.43	-0.06	1.00	1.32	5.4
G-H8-6	9.30	1970	0.345	0.41	-0.03	1.03	1.35	5.5
G-H8-7	9.18	2352	0.334	0.34	-0.01	1.05	1.37	5.5
G-H8-8	8.98	2979	0.324	0.37	0.23	1.29	1.61	5.7
G-H8-9	8.91	3483	0.305	0.31	0.23	1.29	1.61	5.7
G-H8-10	8.73	3815	0.302	0.29	0.38	1.44	1.76	5.9
G-H8-11	8.58	4466	0.291	0.26	0.49	1.55	1.87	6.0
G-H8-12	8.40	5139	0.280	0.23	0.61	1.67	1.99	6.1
G-H9-1	9.39	1	0.399	1.34	0.38	1.44	1.76	5.9
G-H9-2	9.65	291	0.388	1.00	-0.01	1.05	1.37	5.5
G-H9-3	9.73	623	0.378	0.81	-0.17	0.89	1.21	5.3
G-H9-4	9.74	1175	0.366	0.79	-0.19	0.87	1.19	5.3
G-H9-5	9.62	1535	0.356	0.64	-0.17	0.89	1.21	5.3
G-H9-6	9.61	1970	0.345	0.75	-0.09	0.97	1.29	5.4
G-H9-7	9.49	2352	0.334	0.59	-0.07	0.99	1.31	5.4
G-H9-8	9.35	2979	0.323	0.57	0.05	1.12	1.44	5.6
G-H9-9	9.36	3483	0.312	0.56	0.03	1.10	1.42	5.5
G-H9-10	9.19	3815	0.301	0.54	0.19	1.25	1.57	5.7
G-H9-11	9.09	4466	0.290	0.52	0.27	1.33	1.65	5.8
G-H9-12	8.99	5139	0.279	0.47	0.33	1.39	1.71	5.8

Table S2 (continued) -Time, Al conc., pH, reactive fluid mass and saturation indexes for selected phases during experiments at 80 °C.

Exp. No	pH 80 °C	Elapsed time (hours)	M_r (kg)	C_{Al} $\times 10^3$ mol/kg	S.I.			$\log(IAP)$
					Gibbsite	Boehmite	Diaspore	
G-H10-1	9.38	1	0.408	2.68	0.69	1.75	2.07	6.2
G-H10-2	9.42	291	0.397	2.40	0.60	1.66	1.98	6.1
G-H10-3	10.0	623	0.386	2.23	-0.06	1.00	1.33	5.5
G-H10-4	10.1	1175	0.375	1.99	-0.14	0.92	1.24	5.4
G-H10-5	9.99	1535	0.364	1.54	-0.16	0.90	1.22	5.4
G-H10-6	10.0	1970	0.353	1.90	-0.10	0.96	1.28	5.4
G-H10-7	9.91	2352	0.342	1.58	-0.08	0.99	1.31	5.4
G-H10-8	9.82	2979	0.332	1.53	0.01	1.07	1.39	5.5
G-H10-9	9.82	3483	0.321	1.44	-0.02	1.04	1.36	5.5
G-H10-10	9.72	3815	0.310	1.42	0.08	1.14	1.46	5.6
G-H10-11	9.66	4466	0.300	1.38	0.12	1.19	1.51	5.6
G-H10-12	9.63	5139	0.288	1.31	0.13	1.19	1.51	5.6

Annex B

Table S3 - Time, calculated conc., av. pH and saturation indexes for selected phases during experiments at 22 °c.

Exp. No	pH 22 °C	Elapsed time (hours)	M_r (kg)	C Al $\times 10^3$ mol/kg	S.I.			Log (IAP)
	Gibbsite	Boehmite	Diaspore					
G-R1-01	10.58	1	0.498	0.10	0.25	1.44	1.85	8.6
G-R1-02	10.58	291	0.488	0.09	0.23	1.42	1.83	8.6
G-R1-03	10.58	623	0.477	0.09	0.21	1.40	1.80	8.5
G-R1-04	10.58	1175	0.467	0.08	0.17	1.36	1.76	8.5
G-R1-05	10.58	1535	0.457	0.08	0.15	1.33	1.74	8.5
G-R1-06	10.58	1970	0.446	0.07	0.12	1.31	1.72	8.4
G-R1-07	10.58	2352	0.435	0.07	0.10	1.29	1.70	8.4
G-R1-08	10.58	2979	0.425	0.06	0.07	1.26	1.67	8.4
G-R1-09	10.58	3483	0.414	0.06	0.05	1.24	1.65	8.4
G-R1-10	10.58	3815	0.404	0.06	0.04	1.23	1.64	8.4
G-R1-11	10.58	4466	0.394	0.06	0.03	1.21	1.62	8.3
G-R1-12	10.58	5139	0.383	0.06	0.01	1.20	1.61	8.3
G-R2-1	10.70	1	0.497	0.16	0.35	1.53	1.94	8.7
G-R2-2	10.70	291	0.487	0.13	0.24	1.43	1.84	8.6
G-R2-3	10.70	623	0.476	0.10	0.15	1.34	1.75	8.5
G-R2-4	10.70	1175	0.466	0.08	0.04	1.23	1.64	8.4
G-R2-5	10.70	1535	0.456	0.07	0.00	1.19	1.59	8.3
G-R2-6	10.70	1970	0.446	0.07	-0.04	1.15	1.56	8.3
G-R2-7	10.70	2352	0.435	0.06	-0.05	1.13	1.54	8.3
G-R2-8	10.70	2979	0.425	0.06	-0.07	1.12	1.53	8.3
G-R2-9	10.70	3483	0.415	0.06	-0.08	1.11	1.52	8.2
G-R2-10	10.70	3815	0.404	0.06	-0.08	1.11	1.52	8.2
G-R2-11	10.70	4466	0.394	0.06	-0.08	1.11	1.52	8.2
G-R2-12	10.70	5139	0.383	0.06	-0.08	1.11	1.52	8.2

Table S3 (continued) - Time, calculated conc., av. pH and saturation indexes for selected phases during experiments at 22 °C.

Exp. No	pH	Elapsed time	M_r (kg)	$C_{Al} \times 10^3$ mol/kg	S.I.			$\log(IAP)$
	22 °C	(hours)		Gibbsite	Boehmite	Diaspore		
G-R3-1	10.87	1	0.495	0.33	0.49	1.67	2.08	8.8
G-R3-2	10.87	291	0.485	0.21	0.30	1.48	1.89	8.6
G-R3-3	10.87	623	0.474	0.15	0.14	1.33	1.74	8.5
G-R3-4	10.87	1175	0.464	0.11	0.01	1.20	1.61	8.3
G-R3-5	10.87	1535	0.454	0.10	-0.02	1.17	1.58	8.3
G-R3-6	10.87	1970	0.443	0.10	-0.03	1.15	1.56	8.3
G-R3-7	10.87	2352	0.432	0.10	-0.04	1.15	1.56	8.3
G-R3-8	10.87	2979	0.422	0.10	-0.04	1.15	1.55	8.3
G-R3-9	10.87	3483	0.411	0.10	-0.04	1.15	1.55	8.3
G-R3-10	10.87	3815	0.401	0.10	-0.04	1.15	1.55	8.3
G-R3-11	10.87	4466	0.390	0.10	-0.04	1.15	1.55	8.3
G-R3-12	10.87	5139	0.380	0.10	-0.04	1.15	1.55	8.3
G-R4-1	11.02	1	0.497	0.66	0.64	1.83	2.24	9.0
G-R4-2	11.02	291	0.487	0.38	0.41	1.59	2.00	8.7
G-R4-3	11.02	623	0.476	0.24	0.21	1.40	1.81	8.5
G-R4-4	11.02	1175	0.466	0.17	0.05	1.24	1.65	8.4
G-R4-5	11.02	1535	0.456	0.16	0.01	1.20	1.61	8.3
G-R4-6	11.02	1970	0.445	0.15	0.00	1.19	1.60	8.3
G-R4-7	11.02	2352	0.435	0.15	-0.01	1.18	1.59	8.3
G-R4-8	11.02	2979	0.424	0.15	-0.01	1.18	1.59	8.3
G-R4-9	11.02	3483	0.413	0.15	-0.01	1.18	1.59	8.3
G-R4-10	11.02	3815	0.403	0.15	-0.01	1.18	1.59	8.3
G-R4-11	11.02	4466	0.392	0.15	-0.01	1.18	1.59	8.3
G-R4-12	11.02	5139	0.381	0.15	-0.01	1.18	1.59	8.3

Table S3 (continued) - Time, calculated conc., av. pH and saturation indexes for selected phases during experiments at 22 °C.

Exp. No	pH	Elapsed time	M_r (kg)	$C_{Al} \times 10^3$ mol/kg	S.I.			$\log(IAP)$
	22 °C	(hours)		Gibbsite	Boehmite	Diaspore		
G-R5-1	11.26	1	0.498	1.50	0.75	1.94	2.35	9.07
G-R5-2	11.26	291	0.488	0.81	0.49	1.68	2.09	8.81
G-R5-3	11.26	623	0.477	0.50	0.28	1.47	1.88	8.6
G-R5-4	11.26	1175	0.467	0.35	0.13	1.31	1.72	8.44
G-R5-5	11.26	1535	0.456	0.33	0.10	1.28	1.69	8.41
G-R5-6	11.26	1970	0.446	0.32	0.08	1.27	1.68	8.4
G-R5-7	11.26	2352	0.436	0.32	0.08	1.27	1.68	8.4
G-R5-8	11.26	2979	0.425	0.32	0.08	1.27	1.68	8.4
G-R5-9	11.26	3483	0.414	0.32	0.08	1.27	1.68	8.4
G-R5-10	11.26	3815	0.404	0.32	0.08	1.27	1.68	8.4
G-R5-11	11.26	4466	0.393	0.32	0.08	1.27	1.68	8.4
G-R5-12	11.26	5139	0.383	0.32	0.08	1.27	1.68	8.4
G-R5-13	11.26	5737	0.373	0.32	0.08	1.27	1.68	8.4

Table S4 - Time, calculated conc., av. pH and saturation indexes for selected phases during experiments at 80 °C.

Exp. No	pH	Elapsed time (hours)	M_r (kg)	C_{Al} $\times 10^3$ mol/kg	S.I.			$\log(IAP)$
	80 °C				Gibbsite	Boehmite	Diaspore	
G-H6-1	7.70	1	0.395	0.25	1.36	2.42	2.74	6.6
G-H6-2	7.70	291	0.384	0.23	1.32	2.38	2.70	6.6
G-H6-3	7.70	623	0.373	0.21	1.27	2.33	2.65	6.6
G-H6-4	7.70	1175	0.362	0.17	1.18	2.24	2.56	6.5
G-H6-5	7.70	1535	0.352	0.15	1.12	2.18	2.50	6.4
G-H6-6	7.70	1970	0.341	0.12	1.04	2.11	2.43	6.3
G-H6-7	7.70	2352	0.330	0.10	0.97	2.03	2.35	6.3
G-H6-8	7.70	2979	0.319	0.07	0.82	1.89	2.21	6.1
G-H6-9	7.70	3483	0.308	0.05	0.68	1.74	2.06	6.0
G-H6-10	7.70	3815	0.298	0.04	0.56	1.62	1.94	5.8
G-H6-11	7.70	4466	0.286	0.02	0.20	1.27	1.59	5.5
G-H6-12	7.70	5139	0.274	0.00	n.a.	n.a.	n.a.	n.v.
G-H7-1	8.80	1	0.401	0.35	0.40	1.46	1.78	5.7
G-H7-2	8.80	291	0.390	0.32	0.36	1.42	1.74	5.6
G-H7-3	8.80	623	0.379	0.28	0.31	1.37	1.69	5.6
G-H7-4	8.80	1175	0.368	0.24	0.23	1.29	1.61	5.5
G-H7-5	8.80	1535	0.358	0.21	0.18	1.24	1.56	5.5
G-H7-6	8.80	1970	0.347	0.18	0.12	1.19	1.51	5.5
G-H7-7	8.80	2352	0.336	0.16	0.08	1.14	1.46	5.4
G-H7-8	8.80	2979	0.325	0.14	0.00	1.06	1.38	5.3
G-H7-9	8.80	3483	0.314	0.12	-0.06	1.00	1.32	5.2
G-H7-10	8.80	3815	0.304	0.11	-0.09	0.97	1.29	5.2
G-H7-11	8.80	4466	0.293	0.10	-0.16	0.90	1.22	5.1
G-H7-12	8.80	5139	0.281	0.08	-0.21	0.85	1.17	5.1

Table S4 (continued) - Time, calculated conc., av. pH and saturation indexes for selected phases during experiments at 80 °c.

Exp. No	pH	Elapsed time	M_r (kg)	$C_{Al} \times 10^3$ mol/kg	S.I.			$\log(IAP)$
	80 °C	(hours)		Gibbsite	Boehmite	Diaspore		
G-H8-1	9.10	1	0.399	0.70	0.41	1.47	1.79	5.7
G-H8-2	9.1	291	0.388	0.62	0.35	1.42	1.74	5.6
G-H8-3	9.10	623	0.377	0.55	0.30	1.36	1.68	5.6
G-H8-4	9.10	1175	0.366	0.46	0.22	1.28	1.60	5.5
G-H8-5	9.10	1535	0.356	0.42	0.18	1.24	1.56	5.5
G-H8-6	9.10	1970	0.345	0.38	0.14	1.20	1.52	5.4
G-H8-7	9.10	2352	0.334	0.35	0.11	1.17	1.49	5.4
G-H8-8	9.10	2979	0.324	0.32	0.07	1.13	1.45	5.4
G-H8-9	9.10	3483	0.305	0.31	0.05	1.11	1.43	5.3
G-H8-10	9.10	3815	0.302	0.30	0.03	1.09	1.41	5.3
G-H8-11	9.10	4466	0.291	0.29	0.02	1.08	1.40	5.3
G-H8-12	9.10	5139	0.280	0.28	0.01	1.07	1.39	5.3
G-H9-1	9.43	1	0.399	1.28	0.33	1.39	1.71	5.6
G-H9-2	9.43	291	0.388	1.06	0.25	1.31	1.63	5.5
G-H9-3	9.43	623	0.378	0.89	0.17	1.23	1.55	5.5
G-H9-4	9.43	1175	0.366	0.72	0.08	1.14	1.46	5.4
G-H9-5	9.43	1535	0.356	0.66	0.04	1.10	1.42	5.3
G-H9-6	9.43	1970	0.345	0.61	0.01	1.07	1.39	5.3
G-H9-7	9.43	2352	0.334	0.59	-0.01	1.05	1.37	5.3
G-H9-8	9.43	2979	0.323	0.56	-0.03	1.03	1.35	5.3
G-H9-9	9.43	3483	0.312	0.55	-0.03	1.03	1.35	5.2
G-H9-10	9.43	3815	0.301	0.55	-0.04	1.02	1.34	5.2
G-H9-11	9.43	4466	0.290	0.55	-0.04	1.02	1.34	5.2
G-H9-12	9.43	5139	0.279	0.54	-0.04	1.02	1.34	5.2

Table S4 (continued) - Time, calculated conc., av. pH and saturation indexes for selected phases during experiments at 80 °c.

Exp. No	pH	Elapsed time	M_r (kg)	$C_{Al} \times 10^3$ mol/kg	S.I.			$\log(IAP)$
	80 °C	(hours)		Gibbsite	Boehmite	Diaspore		
G-H10-1	9.79	1	0.408	2.660	0.29	1.35	1.67	5.6
G-H10-2	9.79	291	0.397	2.444	0.25	1.32	1.64	5.5
G-H10-3	9.8	623	0.386	2.238	0.22	1.28	1.60	5.5
G-H10-4	9.8	1175	0.375	1.975	0.16	1.22	1.54	5.4
G-H10-5	9.79	1535	0.364	1.844	0.13	1.19	1.51	5.4
G-H10-6	9.8	1970	0.353	1.720	0.10	1.16	1.48	5.4
G-H10-7	9.79	2352	0.342	1.635	0.08	1.14	1.46	5.4
G-H10-8	9.79	2979	0.332	1.531	0.05	1.11	1.43	5.3
G-H10-9	9.79	3483	0.321	1.472	0.04	1.10	1.42	5.3
G-H10-10	9.79	3815	0.310	1.442	0.03	1.09	1.41	5.3
G-H10-11	9.79	4466	0.300	1.397	0.01	1.07	1.39	5.3
G-H10-12	9.79	5139	0.288	1.366	0.00	1.06	1.38	5.3

8.4 Appendix 5

Snorri Gudbrandsson, Vasileios Mavromatis, Quentin Gautier, Nicolas Bovet, Jacques Schott, Eric H. Oelkers (2013) “*An experimental study of kaolinite precipitation kinetics as a function of fluid saturation state at pH 4 and 25 °C*” (Manuscript to be submitted upon completion of work).

Supporting information, thirteen pages, containing sixteen tables.

Annex A

Measured values from published experiments.

Annex B

Calculated values from published experiments given at 120 hours interval with calculated saturation states of noted minerals.

Annex A: Measured values from published experiments.

Sample name	Time (h)	Conc. mmol/Kg	
		Al	Si
		pH	
FKB-0	0	0.18	0.11
FKB-1	27	0.24	0.17
FKB-2	51	0.29	0.19
FKB-3	77	0.36	0.25
FKB-4	101	0.45	3.9
FKB-5	123	0.41	0.36
FKB-6	151	0.51	0.41
FKB-7	173	0.53	0.46
FKB-8	196	0.56	0.51
FKB-9	222	0.58	0.56
FKB-10	245	0.59	0.59
FKB-11	268	0.60	0.63
FKB-12	293	0.62	0.67
FKB-13	320	0.63	0.72
FKB-14	342	0.64	0.75
FKB-15	366	0.67	0.78
FKB-16	416	0.68	0.83
FKB-17	440	0.69	0.85
FKB-18	463	0.70	0.87
FKB-19	488	0.69	0.89
FKB-20	511	0.65	0.88
FKB-21	536	0.59	0.87
FKB-22	560	0.46	0.86
FKB-23	584	0.54	0.86
FKB-24	604	0.55	0.88
FKB-25	632	0.58	0.90
FKB-26	656	0.59	0.92
FKB-27	680	0.60	0.95
FKB-28	727	0.64	0.92
FKB-29	753	0.56	1.02
FKB-30	776	0.67	1.04
FKB-31	795	0.64	1.03
FKB-32	825	0.57	1.07
FKB-33	848	0.62	1.07
FKB-34	873	0.52	1.10
FKB-35	892	0.65	1.11
FKB-36	914	0.68	1.13
FKB-37	943	0.74	1.14
FKB-38	969	0.61	1.15
FKB-39	992	0.80	1.17
FKB-40	1016	0.83	1.12
FKB-41	1040	0.74	1.08
FKB-42	1113	0.96	1.22
FKB-43	1151	0.97	1.27
FKB-44	1179	0.98	1.24
FKB-45	1280	1.00	1.27
FKB-46	1304	1.00	1.30
FKB-47	1325	1.10	1.28
FKB-48	1377	1.06	1.28
FKB-49	1470	1.09	1.30
FKB-50	1639	1.16	1.25
FKB-51	1664	1.17	1.23
FKB-52	1713	0.90	1.30
FKB-53	1783	1.18	1.26
FKB-54	1896	1.22	1.28
FKB-55	2190	1.22	1.23
FKB-56	2215	1.21	1.31
FKC-0	0	0.13	0.14
FKC-1	44	0.11	0.16
FKC-2	120	0.17	0.23
FKC-3	146	0.18	0.25
FKC-4	169	0.20	0.27
FKC-5	191	0.21	0.29
FKC-6	214	0.23	0.30
FKC-7	243	0.23	0.30
FKC-8	269	0.24	0.33
FKC-9	291	0.28	0.33
FKC-10	315	0.29	0.35
FKC-11	333	0.29	0.36
FKC-12	362	0.31	0.38
FKC-13	385	0.32	0.39
FKC-14	411	0.33	0.40
FKC-15	435	0.34	0.42
FKC-16	457	0.35	0.43
FKC-17	481	0.36	0.44
FKC-18	502	0.38	0.45
FKC-19	526	0.39	0.46
FKC-20	550	0.40	0.48
FKC-21	575	0.40	0.47
FKC-22	595	0.43	0.48
FKC-23	633	0.42	0.50
FKC-24	648	0.42	0.51
FKC-25	672	0.43	0.51
FKC-26	698	0.43	0.52
FKC-27	718	0.45	0.53
FKC-28	749	0.45	0.58
FKC-29	765	0.46	0.54
FKC-30	793	0.47	0.76
FKC-31	817	0.47	0.56
FKC-32	845	0.47	0.57
FKC-33	868	0.48	0.58
FKC-34	891	0.48	0.58
FKC-35	912	0.48	0.59
FKC-36	941	0.49	0.59
FKC-37	980	0.48	0.61
FKC-38	989	0.49	0.60
FKC-39	1036	0.49	0.61
FKC-40	1063	0.50	0.62
FKC-41	1107	0.51	0.63
FKC-42	1132	0.51	0.63
FKC-43	1174	0.51	0.64
FKC-44	1223		0.62
FKC-45	1267		0.64
FKC-46	1324	0.51	0.63
FKC-47	1347	0.51	0.63
FKC-48	1370	0.51	0.64
FKC-49	1419	0.43	0.64
FKC-50	1466	0.42	0.64
FKC-51	1510	0.49	0.65
FKC-52	1588	0.49	0.64
FKC-53	1659	0.45	0.66
FKC-54	1771	0.53	0.68
FKC-55	1853	0.54	0.67
FKC-56	1925	0.45	0.69
FKC-57	1947	0.55	0.70
FKC-58	1971	0.54	0.68

Chapter 8 Appendices

Sample name	Time (h)	Conc. mmol/Kg		pH
		Al	Si	
FKE-0	0	0.17	0.16	4.0
FKE-1	30	0.18	0.19	4.0
FKE-2	55	0.19	0.20	3.9
FKE-3	78	0.22	0.22	3.9
FKE-4	101	0.24	0.24	3.9
FKE-5	127	0.27	0.26	3.9
FKE-6	152	0.29	0.28	3.8
FKE-7	171	0.31	0.30	4.0
FKE-8	196	0.33	0.31	0.0
FKE-9	217	0.35	0.33	3.9
FKE-10	244	0.37	0.32	
FKE-11	287	0.39	0.35	3.8
FKE-12	315	0.41	0.36	
FKE-13	342	0.43	0.38	3.8
FKE-14	383	0.45	0.39	3.8
FKE-15	406	0.46	0.41	3.8
FKE-16	430	0.47	0.42	3.8
FKE-17	459	0.49	0.43	
FKE-18	478	0.50	0.44	
FKE-19	511	0.52	0.46	3.9
FKE-20	534	0.53	0.46	3.8
FKE-21	554	0.49	0.48	3.8
FKE-22	577	0.51	0.48	3.8
FKE-23	602	0.52	0.49	3.9
FKE-24	624	0.53	0.50	3.8
FKE-25	649	0.52	0.52	3.8
FKE-26	675	0.53	0.52	3.8
FKE-27	697	0.72	0.69	3.8
FKE-28	721	0.73	0.69	3.8
FKE-29	750			
FKE-30	794	0.77	0.73	3.8
FKE-31	822	0.77	0.74	
FKE-32	842	0.78	0.75	3.8
FKE-33	869	0.80	0.76	3.8
FKE-34	891	0.80	0.76	3.8
FKE-35	918	0.81	0.77	
FKE-36	939	0.83	0.78	3.8
FKE-37	962	0.84	0.79	3.8
FKE-38	986	0.83	0.79	3.8
FKE-39	1010			
FKE-40	1034	0.85	0.80	3.8
FKE-41	1058	0.85	0.80	3.8
FKE-42	1079	0.88	0.82	3.8
FKE-43	1108	0.89	0.83	
FKE-44	1136	0.90	0.84	
FKE-45	1162	0.91	0.85	
FKE-46	1182	0.90	0.83	
FKE-47	1207			
FKE-48	1223	0.89	0.83	3.8
FKE-49	1253	0.91	0.85	
FKE-50	1273	0.94	0.87	3.8
FKE-51	1297	0.94	0.92	
FKE-52	1325	0.91	0.85	3.8
FKE-53	1345	0.93	0.88	3.8
FKE-54	1376	0.92	0.86	
FKE-55	1393	0.93	0.87	3.7
FKE-56	1417	0.93	0.87	
FKE-57	1441	0.94	0.88	3.8
FKE-58	1493	0.94	0.88	3.8
FKE-59	1514	0.96	0.89	
FKE-60	1542	0.95	0.89	
FKE-61	1563	0.94	0.89	3.8
FKE-62	1584	0.95	0.90	3.8

Sample name	Time (h)	Conc. mmol/Kg		pH
		Al	Si	
FKF-0	0	0.10	0.09	4.0
FKF-1	30	0.10	0.11	4.0
FKF-2	55	0.11	0.12	3.9
FKF-3	78	0.13	0.13	3.9
FKF-4	101	0.14	0.14	3.9
FKF-5	127	0.16	0.16	3.9
FKF-6	152	0.17	0.17	7.2
FKF-7	171	0.19	0.17	3.9
FKF-8	196	0.20	0.18	
FKF-9	217	0.21	0.19	3.9
FKF-10	244	0.20	0.19	
FKF-11	287	0.23	0.20	3.9
FKF-12	315	0.24	0.21	
FKF-13	342	0.25	0.22	3.9
FKF-14	383	0.27	0.23	3.8
FKF-15	406	0.28	0.24	3.8
FKF-16	430	0.30	0.24	3.8
FKF-17	459	0.31	0.25	
FKF-18	478	0.31	0.26	
FKF-19	511	0.32	0.27	3.9
FKF-20	534	0.32	0.27	3.9
FKF-21	554	0.31	0.29	3.9
FKF-22	577	0.32	0.30	4.0
FKF-23	602	0.33	0.30	3.9
FKF-24	624	0.34	0.31	3.9
FKF-25	649	0.34	0.31	3.9
FKF-26	675	0.35	0.32	3.9
FKF-27	697	0.36	0.32	3.8
FKF-28	721	0.36	0.33	3.8
FKF-29	750	0.38	0.34	
FKF-30	794	0.38	0.34	3.9
FKF-31	822	0.39	0.34	0.0
FKF-32	842	0.39	0.35	3.9
FKF-33	869	0.41	0.37	3.9
FKF-34	891	0.41	0.37	3.9
FKF-35	918	0.42	0.38	
FKF-36	939	0.42	0.37	3.9
FKF-37	962	0.43	0.38	3.9
FKF-38	986	0.43	0.38	3.9
FKF-39	1010			7.1
FKF-40	1034	0.43	0.39	3.9
FKF-41	1058	0.44	0.39	3.9
FKF-42	1079			
FKF-43	1108	0.43	0.36	
FKF-44	1136			
FKF-45	1162	0.45	0.40	
FKF-46	1182	0.46	0.41	
FKF-47	1207			
FKF-48	1223	0.46	0.41	3.9
FKF-49	1253	0.47	0.41	0.0
FKF-50	1273	0.47	0.42	3.9
FKF-51	1297	0.47	0.42	
FKF-52	1325	0.47	0.42	3.9
FKF-53	1345	0.47	0.42	3.9
FKF-54	1376	0.47	0.42	
FKF-55	1393	0.48	0.42	3.8
FKF-56	1417	0.48	0.42	
FKF-57	1441	0.48	0.43	3.9
FKF-58	1493	0.48	0.43	3.9
FKF-59	1514	0.49	0.43	
FKF-60	1542	0.49	0.43	
FKF-61	1563	0.49	0.44	3.9
FKF-62	1584	0.49	0.44	3.9

Sample name	Time (h)	Conc. mmol/Kg	
		Al	Si
		pH	
FKG-0	0	0.10	0.09
FKG-1	30	0.08	0.11
FKG-2	55	0.10	0.13
FKG-3	78	0.12	0.14
FKG-4	101	0.13	0.15
FKG-5	127	0.15	0.17
FKG-6	152	0.16	0.18
FKG-7	171	0.17	0.19
FKG-8	196	0.19	0.20
FKG-9	217	0.20	0.21
FKG-10	244	0.20	0.20
FKG-11	287	0.22	0.22
FKG-12	315	0.25	0.23
FKG-13	342	0.25	0.23
FKG-14	383	0.26	0.24
FKG-15	406	0.28	0.25
FKG-16	430	0.29	0.26
FKG-17	459	0.30	0.26
FKG-18	478	0.30	0.27
FKG-19	511	0.33	0.28
FKG-20	534	0.33	0.28
FKG-21	554	0.32	0.29
FKG-22	577	0.33	0.30
FKG-23	602	0.33	0.30
FKG-24	624	0.34	0.30
FKG-25	649	0.34	0.31
FKG-26	675	0.34	0.32
FKG-27	697	0.38	0.34
FKG-28	721	0.38	0.34
FKG-29	750	0.39	0.35
FKG-30	794	0.40	0.36
FKG-31	822	0.40	0.36
FKG-32	842	0.41	0.36
FKG-33	869	0.41	0.37
FKG-34	891	0.44	0.40
FKG-35	918	0.42	0.37
FKG-36	939	0.42	0.37
FKG-37	962	0.43	0.38
FKG-38	986	0.43	0.38
FKG-39	1010	0.43	0.38
FKG-40	1034	0.44	0.38
FKG-41	1058	0.44	0.39
FKG-42	1079	0.44	0.39
FKG-43	1108	0.45	0.39
FKG-44	1136	0.45	0.40
FKG-45	1162	0.45	0.40
FKG-46	1182	0.46	0.41
FKG-47	1207		3.9
FKG-48	1223	0.46	0.40
FKG-49	1253	0.46	0.40
FKG-50	1273	0.47	0.41
FKG-51	1297	0.47	0.41
FKG-52	1325	0.47	0.41
FKG-53	1345	0.47	0.41
FKG-54	1376	0.48	0.42
FKG-55	1393	0.48	0.42
FKG-56	1417	0.48	0.42
FKG-57	1441	0.49	0.42
FKG-58	1493	0.49	0.42
FKG-59	1514	0.48	0.43
FKG-60	1542	0.49	0.43
FKG-61	1563	0.49	0.43
FKG-62	1584	0.49	0.43

Sample name	Time (h)	Conc. mmol/Kg	
		Al	Si
		pH	
FKH-0	0	0.10	0.09
FKH-1	30	0.08	0.12
FKH-2	55	0.09	0.14
FKH-3	78	0.10	0.15
FKH-4	101	0.11	0.17
FKH-5	127	0.13	0.18
FKH-6	152	0.14	0.19
FKH-7	171	0.16	0.20
FKH-8	196	0.17	0.21
FKH-9	217	0.19	0.22
FKH-10	244	0.18	0.21
FKH-11	287	0.21	0.21
FKH-12	315	0.23	0.21
FKH-13	342	0.24	0.22
FKH-14	383	0.26	0.23
FKH-15	406	0.28	0.25
FKH-16	430	0.29	0.25
FKH-17	459	0.31	0.25
FKH-18	478	0.31	0.26
FKH-19	511	0.33	0.27
FKH-20	534	0.34	0.27
FKH-21	554	0.33	0.28
FKH-22	577	0.33	0.30
FKH-23	602	0.34	0.28
FKH-24	624	0.35	0.29
FKH-25	649	0.35	0.29
FKH-26	675	0.33	0.30
FKH-27	697	0.37	0.33
FKH-28	721	0.38	0.33
FKH-29	750	0.39	0.34
FKH-30	794	0.40	0.35
FKH-31	822	0.40	0.35
FKH-32	842	0.40	0.36
FKH-33	869	0.41	0.36
FKH-34	891	0.41	0.36
FKH-35	918	0.42	0.36
FKH-36	939	0.42	0.37
FKH-37	962	0.43	0.37
FKH-38	986	0.43	0.38
FKH-39	1010	0.44	0.38
FKH-40	1034	0.44	0.38
FKH-41	1058	0.44	0.38
FKH-42	1079	0.44	0.38
FKH-43	1108	0.45	0.39
FKH-44	1136	0.45	0.39
FKH-45	1162	0.45	0.39
FKH-46	1182	0.46	0.40
FKH-47	1207		3.8
FKH-48	1223	0.46	0.40
FKH-49	1253	0.46	0.40
FKH-50	1273	0.47	0.40
FKH-51	1297	0.47	0.41
FKH-52	1325	0.47	0.41
FKH-53	1345	0.48	0.41
FKH-54	1376	0.48	0.41
FKH-55	1393	0.47	0.41
FKH-56	1417	0.48	0.41
FKH-57	1441	0.49	0.42
FKH-58	1493	0.49	0.42
FKH-59	1514	0.49	0.42
FKH-60	1542	0.49	0.42
FKH-61	1563	0.49	0.42
FKH-62	1584	0.49	0.42

Sample name	Time (h)	Conc. mmol/Kg	
		Al	Si
			pH
FKI-0	0	0.15	0.13
FKI-1	43	0.13	0.13
FKI-2	71	0.14	0.14
FKI-3	98	0.14	0.14
FKI-4	139	0.15	0.14
FKI-5	162	0.15	0.14
FKI-6	186	0.16	0.15
FKI-7	215	0.17	0.15
FKI-8	234	0.17	0.15
FKI-9	267	0.18	0.15
FKI-10	290	0.18	0.15
FKI-11	309	0.20	0.16
FKI-12	334	0.20	0.16
FKI-13	356	0.20	0.16
FKI-14	381	0.21	0.16
FKI-15	407	0.20	0.16
FKI-16	429	0.21	0.18
FKI-17	453	0.21	0.18
FKI-18	478	0.22	0.18
FKI-19	526	0.22	0.18
FKI-20	554	0.00	0.18
FKI-21	574	0.22	0.18
FKI-22	601	0.22	0.18
FKI-23	623	0.22	0.18
FKI-24	650	0.23	0.19
FKI-25	671	0.24	0.20
FKI-26	694	0.23	0.18
FKI-27	718	0.24	0.19
FKI-28	742	0.24	0.19
FKI-29	766	0.24	0.17
FKI-30	790	0.25	0.17
FKI-31	811	0.24	0.19
FKI-32	840	0.24	0.19
FKI-33	868	0.25	0.19
FKI-34	894	0.27	0.18
FKI-35	914	0.26	0.18
FKI-36	939	0.25	0.19
FKI-37	955	0.25	0.20
FKI-38	985	0.26	0.18
FKI-39	1005	0.00	0.00
FKI-40	1029	0.27	0.18
FKI-41	1057	0.26	0.20
FKI-42	1077	0.26	0.20
FKI-43	1108	0.27	0.18
FKI-44	1125	0.26	0.19
FKI-45	1149	0.00	0.18
FKI-46	1173	0.26	0.19
FKI-47	1225	0.26	0.19
FKI-48	1246	0.27	0.20
FKI-49	1274	0.26	0.19
FKI-50	1295	0.27	0.20
FKI-51	1316	0.27	0.19

Sample name	Time (h)	Conc. mmol/Kg	
		Al	Si
			pH
FKJ-0	0	0.15	0.12
FKJ-1	43	0.09	0.13
FKJ-2	71	0.07	0.13
FKJ-3	98	0.11	0.13
FKJ-4	139	0.13	0.13
FKJ-5	162	0.10	0.13
FKJ-6	234	0.12	0.14
FKJ-7	267	0.16	0.14
FKJ-8	290	0.16	0.14
FKJ-9	309	0.18	0.15
FKJ-10	334	0.18	0.15
FKJ-11	356	0.18	0.15
FKJ-12	381	0.18	0.15
FKJ-13	407	0.19	0.15
FKJ-14	429	0.00	0.15
FKJ-15	453	0.20	0.15
FKJ-16	502	0.21	0.16
FKJ-17	530	0.21	0.16
FKJ-18	550	0.21	0.16
FKJ-19	577	0.22	0.16
FKJ-20	599	0.22	0.17
FKJ-21	626	0.22	0.18
FKJ-22	647	0.22	0.18
FKJ-23	670	0.23	0.18
FKJ-24	694	0.25	0.17
FKJ-25	718	0.25	0.17
FKJ-26	742	0.24	0.19
FKJ-27	766	0.24	0.18
FKJ-28	787	0.00	0.00
FKJ-29	816	0.24	0.18
FKJ-30	844	0.24	0.19
FKJ-31	870	0.25	0.19
FKJ-32	890	0.25	0.19
FKJ-33	915	0.24	0.19
FKJ-34	931	0.26	0.18
FKJ-35	961	0.24	0.19
FKJ-36	981	0.26	0.19
FKJ-37	1005	0.25	0.19
FKJ-38	1033	0.25	0.19
FKJ-39	1053	0.26	0.18
FKJ-40	1084	0.25	0.19
FKJ-41	1101	0.26	0.20
FKJ-42	1125	0.25	0.20
FKJ-43	1149	0.25	0.19
FKJ-44	1173	0.26	0.20
FKJ-45	1225	0.25	0.00
FKJ-46	1246	0.26	0.20
FKJ-47	1274	0.26	0.20
FKJ-48	1295	0.26	0.20
FKJ-49	1316	0.26	0.20

Annex B. Calculated values of elemental concentration given at 120 hours interval. Best line pH, best fit concentration curve in mmol/kg. From these calculations saturation indexes for Gibbsite, Kaolinite and amorphous silica.

FKB Time	pH	conc. mmol/kg		Saturation index		
		Al	Si	Gibbsite	Kaolinite	SiO ₂ (am)
0	4.0	0.27	0.08	0.3	1.2	-1.4
120	3.9	0.41	0.37	0.3	2.4	-0.7
240	4.0	0.54	0.59	0.5	3.2	-0.5
360	4.0	0.64	0.76	0.6	3.7	-0.4
480	4.0	0.73	0.89	0.8	4.2	-0.3
600	4.1	0.80	0.99	1.0	4.7	-0.3
720	4.0	0.87	1.07	0.8	4.5	-0.2
840	4.0	0.92	1.13	0.7	4.3	-0.2
960	3.9	0.97	1.18	0.6	4.2	-0.2
1080	3.9	1.01	1.22	0.6	4.0	-0.2
1200	3.9	1.04	1.24	0.5	4.0	-0.2
1320	3.9	1.07	1.27	0.5	3.9	-0.2
1440	3.8	1.09	1.28	0.4	3.8	-0.1
1560	3.8	1.11	1.30	0.4	3.8	-0.1
1680	3.8	1.13	1.31	0.4	3.7	-0.1
1800	3.8	1.15	1.31	0.3	3.7	-0.1
1920	3.8	1.16	1.32	0.3	3.7	-0.1
2040	3.8	1.17	1.32	0.3	3.7	-0.1
2160	3.8	1.18	1.33	0.3	3.6	-0.1
2232	3.8	1.18	1.33	0.3	3.6	-0.1

FKC Time	pH	conc. mmol/kg		Saturation index		
		Al	Si	Gibbsite	Kaolinite	SiO ₂ (am)
0	4.1	0.04	0.13	-0.4	0.3	-1.1
120	4.0	0.15	0.23	0.1	1.8	-0.9
240	4.0	0.24	0.32	0.3	2.3	-0.8
360	4.0	0.31	0.39	0.3	2.6	-0.7
480	4.0	0.37	0.45	0.4	2.8	-0.6
600	4.0	0.41	0.49	0.4	2.9	-0.6
720	4.0	0.44	0.53	0.4	3.0	-0.5
840	4.0	0.47	0.56	0.4	3.0	-0.5
960	3.9	0.49	0.59	0.4	3.1	-0.5
1080	3.9	0.50	0.61	0.4	3.1	-0.5
1200	3.9	0.52	0.63	0.4	3.1	-0.5
1320	3.9	0.53	0.64	0.4	3.1	-0.4
1440	3.9	0.53	0.66	0.4	3.1	-0.4
1560	3.9	0.54	0.67	0.4	3.2	-0.4
1680	3.9	0.54	0.67	0.4	3.2	-0.4
1800	3.9	0.55	0.68	0.4	3.2	-0.4
1920	3.9	0.55	0.69	0.4	3.2	-0.4
2040	3.9	0.55	0.69	0.4	3.2	-0.4

FKE Time	pH	conc. mmol/kg		Saturation index		
		Al	Si	Gibbsite	Kaolinite	SiO ₂ (am)
0	4.0	0.12	0.12	-0.1	0.7	-1.2
120	3.9	0.27	0.26	0.0	1.5	-0.8
240	3.8	0.39	0.38	0.0	1.9	-0.7
360	3.8	0.50	0.48	0.0	2.2	-0.6
480	3.8	0.59	0.56	0.1	2.4	-0.5
600	3.8	0.66	0.63	0.1	2.6	-0.5
720	3.8	0.73	0.69	0.2	2.8	-0.4
840	3.8	0.78	0.74	0.2	2.9	-0.4
960	3.8	0.82	0.78	0.2	3.0	-0.4
1080	3.8	0.86	0.81	0.2	3.0	-0.3
1200	3.8	0.89	0.84	0.2	3.1	-0.3
1320	3.8	0.92	0.86	0.3	3.1	-0.3
1440	3.8	0.94	0.88	0.3	3.2	-0.3
1560	3.8	0.96	0.90	0.3	3.2	-0.3

FKF Time	pH	conc. mmol/kg		Saturation index		
		Al	Si	Gibbsite	Kaolinite	SiO ₂ (am)
0	4.0	0.09	0.10	-0.2	0.3	-1.3
120	3.9	0.16	0.16	-0.3	0.6	-1.1
240	3.9	0.21	0.20	-0.2	1.1	-1.0
360	3.9	0.26	0.24	-0.1	1.4	-0.9
480	3.9	0.30	0.28	0.0	1.6	-0.8
600	3.9	0.34	0.31	0.0	1.8	-0.8
720	3.9	0.37	0.34	0.1	1.9	-0.7
840	3.9	0.40	0.36	0.1	2.1	-0.7
960	3.9	0.42	0.38	0.1	2.1	-0.7
1080	3.9	0.44	0.39	0.1	2.2	-0.7
1200	3.9	0.45	0.41	0.1	2.3	-0.6
1320	3.9	0.47	0.42	0.2	2.3	-0.6
1440	3.9	0.48	0.43	0.2	2.4	-0.6
1560	3.9	0.49	0.44	0.2	2.4	-0.6

FKG Time	pH	conc. mmol/kg		Saturation index		
		Al	Si	Gibbsite	Kaolinite	SiO ₂ (am)
0	4.0	0.06	0.10	-0.3	0.1	-1.3
120	3.9	0.14	0.16	-0.2	0.7	-1.0
240	3.9	0.20	0.21	-0.2	1.0	-0.9
360	3.9	0.26	0.26	-0.1	1.3	-0.8
480	3.9	0.30	0.29	-0.1	1.5	-0.8
600	3.9	0.34	0.32	0.0	1.7	-0.8
720	3.9	0.37	0.34	0.0	1.8	-0.7
840	3.8	0.40	0.36	0.0	1.9	-0.7
960	3.8	0.42	0.38	0.0	2.0	-0.7
1080	3.8	0.44	0.39	0.1	2.1	-0.7
1200	3.8	0.46	0.40	0.1	2.1	-0.7
1320	3.8	0.47	0.41	0.1	2.2	-0.6
1440	3.8	0.48	0.42	0.1	2.2	-0.6
1560	3.8	0.49	0.42	0.1	2.2	-0.6

FKH Time	pH	conc. mmol/kg		Saturation index		
		Al	Si	Gibbsite	Kaolinite	SiO ₂ (am)
0	4.1	0.04	0.11	-0.3	0.2	-1.2
120	4.0	0.12	0.17	-0.2	0.8	-1.0
240	3.9	0.19	0.21	-0.2	1.1	-0.9
360	3.9	0.25	0.25	-0.2	1.2	-0.9
480	3.8	0.30	0.28	-0.2	1.4	-0.8
600	3.8	0.34	0.31	-0.1	1.5	-0.8
720	3.8	0.37	0.33	-0.1	1.6	-0.7
840	3.8	0.40	0.35	-0.1	1.7	-0.7
960	3.8	0.42	0.37	-0.1	1.7	-0.7
1080	3.8	0.44	0.38	-0.1	1.8	-0.7
1200	3.8	0.46	0.39	-0.1	1.8	-0.7
1320	3.8	0.47	0.40	0.0	1.9	-0.7
1440	3.8	0.48	0.41	0.0	1.9	-0.6
1560	3.8	0.49	0.42	0.0	1.9	-0.6

FKI Time	pH	conc. mmol/kg		Saturation index		
		Al	Si	Gibbsite	Kaolinite	SiO ₂ (am)
0	4.0	0.11	0.13	-0.1	0.8	-1.1
120	4.0	0.14	0.14	-0.1	0.9	-1.1
240	4.0	0.17	0.15	0.0	1.1	-1.1
360	4.0	0.19	0.16	0.0	1.2	-1.0
480	4.0	0.21	0.17	0.1	1.3	-1.0
600	4.0	0.22	0.18	0.1	1.4	-1.0
720	4.0	0.24	0.18	0.1	1.5	-1.0
840	4.0	0.24	0.18	0.1	1.5	-1.0
960	4.0	0.25	0.19	0.1	1.6	-1.0
1080	4.0	0.26	0.19	0.1	1.6	-1.0
1200	4.0	0.26	0.19	0.1	1.6	-1.0
1320	4.0	0.27	0.20	0.2	1.7	-1.0

FKJ Time	pH	conc. mmol/kg		Saturation index		
		Al	Si	Gibbsite	Kaolinite	SiO ₂ (am)
0	4.0	0.07	0.12	-0.4	0.2	-1.2
120	4.0	0.12	0.13	-0.1	0.7	-1.1
240	4.0	0.16	0.14	0.0	1.0	-1.1
360	4.0	0.19	0.15	0.0	1.2	-1.1
480	4.0	0.21	0.16	0.1	1.3	-1.1
600	4.0	0.22	0.17	0.1	1.4	-1.0
720	4.0	0.23	0.17	0.1	1.5	-1.0
840	4.0	0.24	0.18	0.2	1.6	-1.0
960	4.0	0.25	0.19	0.2	1.6	-1.0
1080	4.0	0.26	0.19	0.2	1.7	-1.0
1200	4.0	0.26	0.20	0.2	1.7	-1.0
1320	4.0	0.26	0.20	0.2	1.7	-1.0